

7-11-2013

Dual Neutral Particle Beam Interrogation of Intermodal Shipping Containers for Special Nuclear Material

Rodney Keith

Follow this and additional works at: https://digitalrepository.unm.edu/ne_etds

Recommended Citation

Keith, Rodney. "Dual Neutral Particle Beam Interrogation of Intermodal Shipping Containers for Special Nuclear Material." (2013). https://digitalrepository.unm.edu/ne_etds/5

This Dissertation is brought to you for free and open access by the Engineering ETDs at UNM Digital Repository. It has been accepted for inclusion in Nuclear Engineering ETDs by an authorized administrator of UNM Digital Repository. For more information, please contact disc@unm.edu.

Rodney Lyman Keith

Candidate

Nuclear Engineering

Department

This dissertation is approved, and it is acceptable in quality and form for publication:

Approved by the Dissertation Committee:

Dr. Cassiano R. E. de Oliveira, Chairperson

Dr. Adam Hecht

Dr. Edward Arthur

Dr. Timothy Ross

Dr. Bobby Middleton

Dual Neutral Particle Beam Interrogation of Intermodal Shipping Containers for Special Nuclear Material

by

Rodney Lyman Keith

B.S., Chemical Engineering, University of Arizona, 1992

M.S., Toxicology, University of Arizona, 1997

DISSERTATION

Submitted in Partial Fulfillment of the
Requirements for the Degree of

**Doctor of Philosophy
Engineering**

The University of New Mexico
Albuquerque, New Mexico

May 2013

© 2013, Rodney Lyman Keith

ACKNOWLEDGEMENTS

I would like to thank my advisor, Dr. Cassiano R. E. de Oliveira, for his thoughtful guidance and support during my time with his group. I would also like to recognize the members of my Committee - Dr. Arthur, Dr. Hecht, Dr. Middleton and Dr. Ross - and thank them as well for the time and effort they have expended on my behalf.

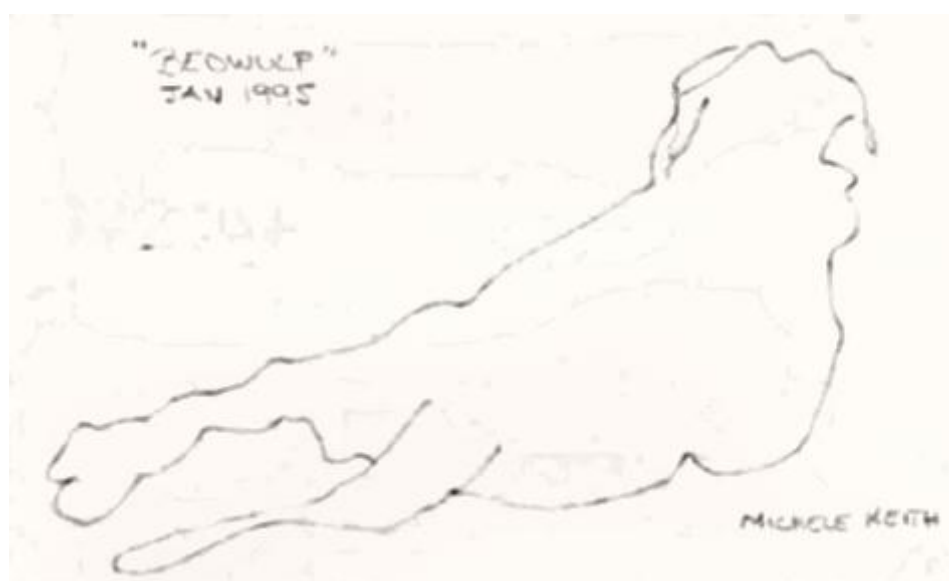
I am particularly indebted to Billy Martin for his help and advice, Marc Krubsack for patiently enduring my endless diatribes and Jamie Cash for his excellent taste.

My gratitude to Dr. Cooper, Dr. Prinja, Elliott Leonard, Ms. Jocelyn White and Ms. Jasmine Torres for all their assistance.

Finally, I would like to thank Ann, Malcolm and Hadrian for their love and support.

This work was partially supported by contract DTRA01-03-D-0009-0025 from the Defense Threat Reduction Agency, Department of Defense.

DEDICATION



R. I. P.

Dual Neutral Particle Beam Interrogation of Intermodal Shipping Containers for Special Nuclear Material

by

Rodney Lyman Keith

B.S., Chemical Engineering, University of Arizona, 1992

M.S., Toxicology, University of Arizona, 1997

Ph.D., Engineering, University of New Mexico, 2013

ABSTRACT

Intermodal shipping containers entering the United States provide an avenue to smuggle unsecured or stolen special nuclear material (SNM). The only direct method fielded to indicate the presence of SNM is by passive photon/neutron radiation detection. Active interrogation using neutral particle beams to induce fission in SNM is a method under consideration. One by-product of fission is the creation of fragments that undergo radioactive decay over a time period on the order of tens of seconds after the initial event. The “delayed” gamma-rays emitted from these fragments over this period are considered a hallmark for the

presence of SNM. A fundamental model is developed using homogenized cargos with a SNM target embedded at the center and computationally interrogated using simultaneous neutron and photon beams. Findings from analysis of the delayed gamma emissions from these experiments are intended to mitigate the effects of poor quality information about the composition and disposition of suspect cargo before examination in an active interrogation portal.

TABLE OF CONTENTS

LIST OF FIGURES.....	xiii
LIST OF TABLES.....	xliv
INTRODUCTION.....	1
I. Forward.....	1
A. Special Nuclear Materials.....	1
B. Intermodal Shipping Containers.....	2
C. Active Interrogation.....	3
II. Hypothesis and Chronological Aims.....	3
A. Hypothesis.....	3
B. Chronological Aims.....	3
BACKGROUND.....	5
I. Special Nuclear Materials.....	5
A. Definition.....	5
B. Quantities of Significance.....	5
II. Intermodal Shipping Containers.....	6
A. History.....	6
B. Materials of Construction.....	7
C. Dimensions.....	9
D. Capacities.....	9
III. The Inspection System.....	10
A. Container Traffic.....	10
B. History.....	12
C. Special Nuclear Materials Detection.....	14

IV. Active Interrogation.....	15
A. Neutron Experiments.....	15
B. Photon Experiments.....	16
C. Simulations.....	18
D. Work by the University of New Mexico.....	18
MODELS AND METHODS.....	20
I. Delayed Gamma Production.....	20
A. Neutron Induced Fission.....	20
B. Photon Induced Fission.....	20
C. Delayed Gamma Detection.....	23
D. Detection System Performance.....	25
II. Neutral Particle Interrogation.....	26
III. Simulation Outline.....	28
A. Operational Scenario.....	30
B. Threat Source Signature.....	30
C. Nuisance Source Population.....	30
1. Nuisance.....	31
2. Noise.....	33
D. Ambient Background.....	35
E. Radiation Transport.....	35
F. Detection System Hardware.....	36
G. Alarm Algorithm.....	36
H. Performance Evaluation.....	37
IV. Simulation Model.....	38
A. Basis.....	38
B. Container.....	38
C. Surrogate Cargo.....	42

D. Threat Target.....	44
E. Nuisance Signal.....	44
F. Noise Target.....	45
G. Fundamental Model.....	45
H. Neutral Particle Beams.....	47
I. Detector.....	51
J. Detection Figure-of-Merit.....	53
1. Definition.....	53
2. Application.....	55
V. Simulation Flow.....	60
A. Time Scales.....	62
B. Delayed Gamma Current Tally.....	62
C. Delayed Gamma Pulse Height Tally.....	63
D. Computing Systems.....	63
RESULTS.....	65
I. Anticipated Outcomes.....	65
II. Trial Simulations.....	65
III. Delayed Gamma Current Results.....	71
A. Celotex, Aluminum and Iron.....	73
B. Tungsten.....	76
E. Clay and Thorium-232.....	79
F. Five Material Summary.....	82
IV. Plastic Detector Implementation.....	84
A. Detector Efficiency.....	84
B. Gaussian Energy Broadening.....	87
V. Delayed Gamma Detection Results.....	90
VI. Fluorine Interference.....	96

A. Nitrogen-16.....	96
B. Teflon Target.....	101
VII. Detection System Performance.....	109
A. Celotex.....	111
B. Aluminum.....	114
C. Clay.....	117
D. Iron.....	120
E. Summary.....	123
DISCUSSION.....	124
I. Fundamental Model and Code Suite.....	124
A. Fundamental Model.....	124
B. Code Suite.....	124
II. Model Implementation.....	125
A. Linearity.....	125
B. Target Detection.....	125
III. Dual-Beam Interrogation.....	126
A. Additivity of Beam Results.....	126
B. Photon Beam Contribution.....	131
C. Teflon.....	134
IV. On-Site Modeling.....	134
V. Uncertainty Quantification.....	139
A. Reducing σ	139
B. Cargo Composition.....	140
C. 4-Box Approach.....	143
VI. Future Studies.....	147
A. Other Photon Beam Energies.....	147
B. Phosphogypsum.....	147

C. Exploiting Poor Data.....	148
VII.Conclusion.....	149
APPENDIX A: Simulated Detector Responses with U_3O_8 Target in Air.....	153
APPENDIX B: Simulated Detector Responses with U_3O_8 Target in Celotex.....	157
APPENDIX C: Simulated Detector Responses with U_3O_8 Target in Aluminum.....	182
APPENDIX D: Simulated Detector Responses with U_3O_8 Target in Clay....	207
APPENDIX E: Simulated Detector Responses with U_3O_8 Target in Iron.....	232
APPENDIX F: EJ-200 Plastic Scintillator.....	257
APPENDIX G: Sample Input Decks – U_3O_8 Target in 0.1 g/cc Aluminum.....	258
REFERENCES.....	265

LIST OF FIGURES

Figure 1. Intermodal shipping container, steel, 20' (1 TEU), exterior and interior. (www.containertech.com , http://20foothouse.com)	8
Figure 2. TEU traffic, ~20 million containers (from USDOT, 2009).....	11
Figure 3. The importation process (from PTG, 2010).	13
Figure 4. Experimental delayed gamma energy spectrum resulting from photofission of uranium-238 using 15 MeV photons, top trace (from Proctor, et al., 2012).....	17
Figure 5. Photofission cross sections for uranium-235, uranium-238 and thorium-232. The largest cross sections are realized with photons at energies of ~14 MeV (from Jones et al., 2000).	22
Figure 6. A remote alarm monitor unit used with pedestrian, vehicle and train portal monitors. The unit provides both audible and visual indications for gamma and neutron radiation alarms (from TSA, 2012).....	24
Figure 7. A neutral particle active interrogation system showing delayed particle production resulting from fission product decay alone (from de Oliveira et al., 2009).	27
Figure 8. General components to define when simulating a detection system. (from Nelson & Sokkappa, 2008).....	29

- Figure 9. Dry freight trailer loaded with tires (quasi-homogeneous). The resolution observed here is more than adequate for the purposes of sectioning (red area) and homogenization (from Stevenson, 2005). 40
- Figure 10. Combined neutron and x-ray image of an aluminum unit load device (ULD) used for air cargo (~ 5' x 5' x 5'). This ULD contains computer monitors, a vase, bottles, and a sack of chemicals (left), air conditioners and gas cylinders (middle), and vegetables (right) (from Buffler & Tickner, 2010 and Cutmore et al., 2010). 41
- Figure 11. Distribution of average cargo density collected via shipping manifests on 14 days distributed over 12 months (from Descalle et al., 2006). 43
- Figure 12. The fundamental model with PVT detector (not to scale). 46
- Figure 13. A 7 MeV penetrating neutron beam interacting in the Celotex cargo surrogate model ($\rho = 0.1$ g/cc). The image on the left shows the beam entering from the bottom; the viewpoint on the right is from above looking down. The U_3O_8 target can be seen clearly in the center of each image. A total of 1000 neutrons were injected. The colors reflect subjective collision event energies with red being "high" and blue being "low." 48
- Figure 14. A 12.2 MeV penetrating gamma-ray beam interacting in the celotex cargo surrogate model (0.1 g/cc). The shot on the left shows the beam entering from the bottom; the viewpoint on the right is from above looking down. The U_3O_8 target can be seen clearly in the center of each image. A

total of 1000 photons were injected. The colors reflect subjective collision event energies with red being “high” and blue being “low.” 50

Figure 15. Response to independent monoenergetic photons of 3, 4, 5 and 6 MeV isotropically broadcast from the center of the surrogate model filled with air at ISA..... 52

Figure 16. Generic ROC curves for $F_s = 3$ (pink), $F_s = 5$ (green) and $F_s = 7$ (blue). With $F_s = 5$ at the minimum detection probability (P_d) of 0.9833, the false positive rate (P_{fp}) is < 0.005 and the DNDO performance requirements are met (adapted from Prussin et al., 2005). 58

Figure 17. Generic ROC curves for $F_s = 1$ to 6. The goal set for the “Nuclear Car Wash” was a minimum detection probability (P_d) of 0.95 and a false alarm rate (P_{fA}) of 0.001. This performance is achieved with $F_s = 5$ as well (“ROC curve for $F_b = 10$ ” from Slaughter et al., 2007b)..... 59

Figure 18. The flow of the simulation. The TINDER wrapper controls the entire process by initially calling MCNPX twice to transport each interrogating beam to the target. The resulting target cell fluxes are added and CINDER is called for the first time step. The delayed gammas produced in the target are then transported out using MCNPX. The CINDER-MCNPX process is repeated for as many time steps as specified by the user. 61

Figure 19. Instantaneous delayed gamma emission ($E_\gamma = 3\text{-}6$ MeV) rate 6-100 seconds post-irradiation from target alone after 30 second interrogation with 7 MeV neutron and 12.2 MeV photon beams. 95% enriched uranium sphere ($d=8$ cm, 5 kg) in a cube of homogenized Celotex at a density of 0.4 g/cc... 67

Figure 20. Instantaneous delayed gamma emission ($E_\gamma = 3-7$ MeV) rate 6-100 seconds post-irradiation from target alone after 30 second interrogation with 7 MeV neutron and 12.2 MeV photon beams. Plutonium-239 sphere (d=10 cm, 8.27 kg) in a cube of homogenized Celotex at a density of 0.4 g/cc. 68

Figure 21. Cumulative (7-100 seconds post-irradiation) delayed gamma emission ($E_\gamma = 3-6$ MeV) through one vertical side of surrogate container cube after 30 second interrogation with 7 MeV neutron and 12.2 MeV photon beams. Plutonium-239 sphere (d=10 cm, 8.27 kg) in homogenized Celotex at a density of 0.4 g/cc..... 70

Figure 22. Cumulative (7-100 seconds post-irradiation) delayed gamma emission (3-6 MeV window) through one vertical side of surrogate container cube after 30 second interrogation with 7 MeV neutron (N) or 7 MeV neutron and 12.2 MeV photon (N & P) beams. Rapiscan Test Object "E" in homogenized Celotex at densities of 0.05-0.65 g/cc. 74

Figure 23. Cumulative (7-100 seconds post-irradiation) delayed gamma emission (3-6 MeV window) through one vertical side of surrogate container cube after 30 second interrogation with 7 MeV neutron (N) or 7 MeV neutron and 12.2 MeV photon (N & P) beams. Rapiscan Test Object "E" in homogenized aluminum at densities of 0.05-0.65 g/cc. 75

Figure 24. Cumulative (7-100 seconds post-irradiation) delayed gamma emission (3-6 MeV window) through one vertical side of surrogate container cube after 30 second interrogation with 7 MeV neutron (N) or 7 MeV neutron and 12.2 MeV photon (N & P) beams. Rapiscan Test Object "E" in homogenized iron at densities of 0.05-0.65 g/cc. 77

Figure 25. Cumulative (7-100 seconds post-irradiation) delayed gamma emission (3-6 MeV window) through one vertical side of surrogate container cube after 30 second interrogation with 7 MeV neutron (N) or 7 MeV neutron and 12.2 MeV photon (N & P) beams. Rapiscan Test Object “E” in homogenized tungsten at densities of 0.05-0.65 g/cc..... 78

Figure 26. Cumulative (7-100 seconds post-irradiation) delayed gamma emission (3-6 MeV window) through one vertical side of surrogate container cube after 30 second interrogation with 7 MeV neutron and 12.2 MeV photon (N & P) beams. Rapiscan Test Object “E” in homogenized clay, with and without thorium, at densities of 0.05-0.65 g/cc..... 81

Figure 27. Cumulative (7-100 seconds post-irradiation) delayed gamma emission (3-6 MeV window) through one vertical side of surrogate container cube after 30 second interrogation with 7 MeV neutron and 12.2 MeV photon (N & P) beams. Rapiscan Test Object “E” in five materials at densities of 0.05-0.65 g/cc..... 83

Figure 28. Delayed gamma emission (3-6 MeV window) at seven seconds post-irradiation through one vertical side of surrogate container cube and adjacent PVT detector after 30 second interrogation with 7 MeV neutron and 12.2 MeV photon beams. Rapiscan Test Object “E” in homogenized Celotex at a density of 0.05 g/cc..... 86

Figure 29. Simulated detector response to delayed gamma emission at one second intervals from 7-10 seconds and five second intervals from 10-40 seconds after 30 second interrogation with 7 MeV neutron and 12.2 MeV photon beams. PVT detector is adjacent to one vertical side of surrogate

container cube. Rapiscan Test Object “E” in air at ISA. No Gaussian energy broadening (GEB) is used. 88

Figure 30. Simulated detector response to delayed gamma emission at one second intervals from 7-10 seconds and five second intervals from 10-40 seconds after 30 second interrogation with 7 MeV neutron and 12.2 MeV photon beams. PVT detector is adjacent to one vertical side of surrogate container cube. Rapiscan Test Object “E” in air at ISA. Gaussian energy broadening is applied. 89

Figure 31. Simulated detector response to delayed gamma emission at one second intervals from 7-10 seconds and five second intervals from 10-40 seconds after 30 second interrogation with 7 MeV neutron and 12.2 MeV photon beams. PVT detector adjacent to one vertical side of surrogate container cube. Rapiscan Test Object “E” in Celotex at 0.65 g/cc. 92

Figure 32. Simulated detector response to delayed gamma emission at one second intervals from 7-10 seconds and five second intervals from 10-40 seconds after 30 second interrogation with 7 MeV neutron beam. PVT detector adjacent to one vertical side of surrogate container cube. Rapiscan Test Object “E” in Celotex at 0.65 g/cc. 93

Figure 33. Simulated detector response to delayed gamma emission at one second intervals from 7-10 seconds and five second intervals from 10-40 seconds after 30 second interrogation with 12.2 MeV photon beam. PVT detector adjacent to one vertical side of surrogate container cube. Rapiscan Test Object “E” in Celotex at 0.65 g/cc. 94

Figure 34. Neutron activation cross section for the $^{19}\text{F} (n,\alpha) ^{16}\text{N}$ reaction. The 7 MeV neutron interrogation energy used for this work is nearly ideal (from NNDC, 2012)..... 97

Figure 35. Simulated detector response to gamma emission at one second intervals from 7-10 seconds and five second intervals from 10-40 seconds after 30 second interrogation with 7 MeV neutron beam. PVT detector adjacent to one vertical side of surrogate container cube. Teflon at 0.03624 g/cc.....99

Figure 36. Smoothed experimental energy-counts profile of a nitrogen-16 source (irradiated Teflon, mass unknown) at 2, 7, and 12 seconds (from Luu et al., 2007)..... 100

Figure 37. Simulated detector response to gamma emission at one second intervals from 7-10 seconds and five second intervals from 10-40 seconds after 30 second interrogation with 7 MeV neutron beam. PVT detector adjacent to one vertical side of surrogate container cube. Teflon target (600 g puck) in air at 0.001275 g/cc (ISA). 102

Figure 38. Simulated detector response to gamma emission at one second intervals from 7-10 seconds and five second intervals from 10-40 seconds after 30 second interrogation with 7 MeV neutron beam. PVT detector adjacent to one vertical side of surrogate container cube. Teflon target (600 g puck) in Celotex at 0.4 g/cc. 103

Figure 39. Simulated detector response to gamma emission at one second intervals from 7-10 seconds and five second intervals from 10-40 seconds

after 30 second interrogation with 7 MeV neutron beam. PVT detector adjacent to one vertical side of surrogate container cube. Teflon target (600 g puck) in aluminum at 0.4 g/cc. 104

Figure 40. Simulated detector response to gamma emission at one second intervals from 7-10 seconds and five second intervals from 10-40 seconds after 30 second interrogation with 7 MeV neutron beam. PVT detector adjacent to one vertical side of surrogate container cube. Teflon target (600 g puck) in clay at 0.4 g/cc. 105

Figure 41. Simulated detector response to gamma emission at one second intervals from 7-10 seconds and five second intervals from 10-40 seconds after 30 second interrogation with 7 MeV neutron beam. PVT detector adjacent to one vertical side of surrogate container cube. Teflon target (600 g puck) in iron at 0.4 g/cc. 106

Figure 42. Simulated detector response to gamma-ray emission 7-40 seconds (cumulative) after 30 second interrogation with 7 MeV neutron and/or 12.2 MeV photon beams. PVT detector adjacent to one vertical side of surrogate container cube. Rapiscan Test Object "E" in Teflon at 0.2 g/cc. 108

Figure 43. Simulated detection system performance based on delayed gamma emission ($E_\gamma = 3-6$ Mev) after 30 second interrogation with a 7 MeV neutron beam. Rapiscan Test Object "E" in homogenized Celotex at densities of 0.05-0.65 g/cc. 112

Figure 44. Simulated detection system performance based on delayed gamma emission ($E_\gamma = 3-6$ Mev) after 30 second interrogation with 7 MeV neutron

and 12.2 MeV photon beams. Rapiscan Test Object “E” in homogenized Celotex at densities of 0.05-0.65 g/cc..... 113

Figure 45. Simulated detection system performance based on delayed gamma emission ($E_\gamma = 3-6$ Mev) after 30 second interrogation with a 7 MeV neutron beam. Rapiscan Test Object “E” in homogenized aluminum at densities of 0.05-0.65 g/cc..... 115

Figure 46. Simulated detection system performance based on delayed gamma emission ($E_\gamma = 3-6$ Mev) after 30 second interrogation with 7 MeV neutron and 12.2 MeV photon beams. Rapiscan Test Object “E” in homogenized aluminum at densities of 0.05-0.65 g/cc. 116

Figure 47. Simulated detection system performance based on delayed gamma emission ($E_\gamma = 3-6$ Mev) after 30 second interrogation with a 7 MeV neutron beam. Rapiscan Test Object “E” in homogenized clay at densities of 0.05-0.65 g/cc. 118

Figure 48. Simulated detection system performance based on delayed gamma emission ($E_\gamma = 3-6$ Mev) after 30 second interrogation with 7 MeV neutron and 12.2 MeV photon beams. Rapiscan Test Object “E” in homogenized clay at densities of 0.05-0.65 g/cc..... 119

Figure 49. Simulated detection system performance based on delayed gamma emission ($E_\gamma = 3-6$ Mev) after 30 second interrogation with a 7 MeV neutron beam. Rapiscan Test Object “E” in homogenized iron at densities of 0.05-0.65 g/cc. 121

- Figure 50. Simulated detection system performance based on delayed gamma emission ($E_\gamma = 3\text{-}6\text{ MeV}$) after 30 second interrogation with 7 MeV neutron and 12.2 MeV photon beams. Rapiscan Test Object “E” in homogenized iron at densities of 0.05-0.65 g/cc..... 122
- Figure 51. Smoothed beam contributions to cumulative delayed gamma signal after interrogation with 7 MeV neutron and 12.2 MeV photon beams. Rapiscan Test Object “E” in homogenized Celotex, aluminum, clay or iron at densities of 0.05-0.65 g/cc..... 133
- Figure 52. What about when general homogenization is not feasible (from Reed, 2007)?..... 137
- Figure 53. Load weight estimation reference example for use in determining the density of MCNPX macrobodies when general homogenization is not feasible (from WRRRC, 1990)..... 138
- Figure 54. The 4-box approach depicting various descriptions and contents of each box and the six inference connections (from de Oliveira et al., 2011).....144
- Figure 55. Simulated detector response to delayed gamma emission at one second intervals from 7-10 seconds and five second intervals from 10-40 seconds after 30 second interrogation with 7 MeV neutron and 12.2 MeV photon beams. PVT detector adjacent to one vertical side of surrogate container cube. Rapiscan Test Object “E” in air at 0.001275 g/cc (ISA)..... 154

- Figure 56. Simulated detector response to delayed gamma emission at one second intervals from 7-10 seconds and five second intervals from 10-40 seconds after 30 second interrogation with 7 MeV neutron beam. PVT detector adjacent to one vertical side of surrogate container cube. Rapiscan Test Object "E" in air at 0.001275 g/cc (ISA). 155
- Figure 57. Simulated detector response to delayed gamma emission at one second intervals from 7-10 seconds and five second intervals from 10-40 seconds after 30 second interrogation with 12.2 MeV photon beam. PVT detector adjacent to one vertical side of surrogate container cube. Rapiscan Test Object "E" in air at 0.001275 g/cc (ISA). 156
- Figure 58. Simulated detector response to delayed gamma emission at one second intervals from 7-10 seconds and five second intervals from 10-40 seconds after 30 second interrogation with 7 MeV neutron and 12.2 MeV photon beams. PVT detector adjacent to one vertical side of surrogate container cube. Rapiscan Test Object "E" in Celotex at 0.05 g/cc..... 158
- Figure 59. Simulated detector response to delayed gamma emission at one second intervals from 7-10 seconds and five second intervals from 10-40 seconds after 30 second interrogation with 7 MeV neutron beam. PVT detector adjacent to one vertical side of surrogate container cube. Rapiscan Test Object "E" in Celotex at 0.05 g/cc. 159
- Figure 60. Simulated detector response to delayed gamma emission at one second intervals from 7-10 seconds and five second intervals from 10-40 seconds after 30 second interrogation with 12.2 MeV photon beam. PVT detector adjacent to one vertical side of surrogate container cube. Rapiscan Test Object "E" in Celotex at 0.05 g/cc. 160

Figure 61. Simulated detector response to delayed gamma emission at one second intervals from 7-10 seconds and five second intervals from 10-40 seconds after 30 second interrogation with 7 MeV neutron and 12.2 MeV photon beams. PVT detector adjacent to one vertical side of surrogate container cube. Rapiscan Test Object "E" in Celotex at 0.1 g/cc..... 161

Figure 62. Simulated detector response to delayed gamma emission at one second intervals from 7-10 seconds and five second intervals from 10-40 seconds after 30 second interrogation with 7 MeV neutron beam. PVT detector adjacent to one vertical side of surrogate container cube. Rapiscan Test Object "E" in Celotex at 0.1 g/cc. 162

Figure 63. Simulated detector response to delayed gamma emission at one second intervals from 7-10 seconds and five second intervals from 10-40 seconds after 30 second interrogation with 12.2 MeV photon beam. PVT detector adjacent to one vertical side of surrogate container cube. Rapiscan Test Object "E" in Celotex at 0.1 g/cc. 163

Figure 64. Simulated detector response to delayed gamma emission at one second intervals from 7-10 seconds and five second intervals from 10-40 seconds after 30 second interrogation with 7 MeV neutron and 12.2 MeV photon beams. PVT detector adjacent to one vertical side of surrogate container cube. Rapiscan Test Object "E" in Celotex at 0.2 g/cc..... 164

Figure 65. Simulated detector response to delayed gamma emission at one second intervals from 7-10 seconds and five second intervals from 10-40 seconds after 30 second interrogation with 7 MeV neutron beam. PVT

detector adjacent to one vertical side of surrogate container cube. Rapiscan
Test Object "E" in Celotex at 0.2 g/cc. 165

Figure 66. Simulated detector response to delayed gamma emission at one
second intervals from 7-10 seconds and five second intervals from 10-40
seconds after 30 second interrogation with 12.2 MeV photon beam. PVT
detector adjacent to one vertical side of surrogate container cube. Rapiscan
Test Object "E" in Celotex at 0.2 g/cc. 166

Figure 67. Simulated detector response to delayed gamma emission at one
second intervals from 7-10 seconds and five second intervals from 10-40
seconds after 30 second interrogation with 7 MeV neutron and 12.2 MeV
photon beams. PVT detector adjacent to one vertical side of surrogate
container cube. Rapiscan Test Object "E" in Celotex at 0.3 g/cc. 167

Figure 68. Simulated detector response to delayed gamma emission at one
second intervals from 7-10 seconds and five second intervals from 10-40
seconds after 30 second interrogation with 7 MeV neutron beam. PVT
detector adjacent to one vertical side of surrogate container cube. Rapiscan
Test Object "E" in Celotex at 0.3 g/cc. 168

Figure 69. Simulated detector response to delayed gamma emission at one
second intervals from 7-10 seconds and five second intervals from 10-40
seconds after 30 second interrogation with 12.2 MeV photon beam. PVT
detector adjacent to one vertical side of surrogate container cube. Rapiscan
Test Object "E" in Celotex at 0.3 g/cc. 169

Figure 70. Simulated detector response to delayed gamma emission at one second intervals from 7-10 seconds and five second intervals from 10-40 seconds after 30 second interrogation with 7 MeV neutron and 12.2 MeV photon beams. PVT detector adjacent to one vertical side of surrogate container cube. Rapiscan Test Object “E” in Celotex at 0.4 g/cc..... 170

Figure 71. Simulated detector response to delayed gamma emission at one second intervals from 7-10 seconds and five second intervals from 10-40 seconds after 30 second interrogation with 7 MeV neutron beam. PVT detector adjacent to one vertical side of surrogate container cube. Rapiscan Test Object “E” in Celotex at 0.4 g/cc. 171

Figure 72. Simulated detector response to delayed gamma emission at one second intervals from 7-10 seconds and five second intervals from 10-40 seconds after 30 second interrogation with 12.2 MeV photon beam. PVT detector adjacent to one vertical side of surrogate container cube. Rapiscan Test Object “E” in Celotex at 0.4 g/cc. 172

Figure 73. Simulated detector response to delayed gamma emission at one second intervals from 7-10 seconds and five second intervals from 10-40 seconds after 30 second interrogation with 7 MeV neutron and 12.2 MeV photon beams. PVT detector adjacent to one vertical side of surrogate container cube. Rapiscan Test Object “E” in Celotex at 0.5 g/cc..... 173

Figure 74. Simulated detector response to delayed gamma emission at one second intervals from 7-10 seconds and five second intervals from 10-40 seconds after 30 second interrogation with 7 MeV neutron beam. PVT

detector adjacent to one vertical side of surrogate container cube. Rapiscan
Test Object "E" in Celotex at 0.5 g/cc. 174

Figure 75. Simulated detector response to delayed gamma emission at one
second intervals from 7-10 seconds and five second intervals from 10-40
seconds after 30 second interrogation with 12.2 MeV photon beam. PVT
detector adjacent to one vertical side of surrogate container cube. Rapiscan
Test Object "E" in Celotex at 0.5 g/cc. 175

Figure 76. Simulated detector response to delayed gamma emission at one
second intervals from 7-10 seconds and five second intervals from 10-40
seconds after 30 second interrogation with 7 MeV neutron and 12.2 MeV
photon beams. PVT detector adjacent to one vertical side of surrogate
container cube. Rapiscan Test Object "E" in Celotex at 0.6 g/cc. 176

Figure 77. Simulated detector response to delayed gamma emission at one
second intervals from 7-10 seconds and five second intervals from 10-40
seconds after 30 second interrogation with 7 MeV neutron beam. PVT
detector adjacent to one vertical side of surrogate container cube. Rapiscan
Test Object "E" in Celotex at 0.6 g/cc. 177

Figure 78. Simulated detector response to delayed gamma emission at one
second intervals from 7-10 seconds and five second intervals from 10-40
seconds after 30 second interrogation with 12.2 MeV photon beam. PVT
detector adjacent to one vertical side of surrogate container cube. Rapiscan
Test Object "E" in Celotex at 0.6 g/cc. 178

Figure 79. Simulated detector response to delayed gamma emission at one second intervals from 7-10 seconds and five second intervals from 10-40 seconds after 30 second interrogation with 7 MeV neutron and 12.2 MeV photon beams. PVT detector adjacent to one vertical side of surrogate container cube. Rapiscan Test Object “E” in Celotex at 0.65 g/cc..... 179

Figure 80. Simulated detector response to delayed gamma emission at one second intervals from 7-10 seconds and five second intervals from 10-40 seconds after 30 second interrogation with 7 MeV neutron beam. PVT detector adjacent to one vertical side of surrogate container cube. Rapiscan Test Object “E” in Celotex at 0.65 g/cc. 180

Figure 81. Simulated detector response to delayed gamma emission at one second intervals from 7-10 seconds and five second intervals from 10-40 seconds after 30 second interrogation with 12.2 MeV photon beam. PVT detector adjacent to one vertical side of surrogate container cube. Rapiscan Test Object “E” in Celotex at 0.65 g/cc. 181

Figure 82. Simulated detector response to delayed gamma emission at one second intervals from 7-10 seconds and five second intervals from 10-40 seconds after 30 second interrogation with 7 MeV neutron and 12.2 MeV photon beams. PVT detector adjacent to one vertical side of surrogate container cube. Rapiscan Test Object “E” in aluminum at 0.05 g/cc. 183

Figure 83. Simulated detector response to delayed gamma emission at one second intervals from 7-10 seconds and five second intervals from 10-40 seconds after 30 second interrogation with 7 MeV neutron beam. PVT

detector adjacent to one vertical side of surrogate container cube. Rapiscan
Test Object "E" in aluminum at 0.05 g/cc..... 184

Figure 84. Simulated detector response to delayed gamma emission at one
second intervals from 7-10 seconds and five second intervals from 10-40
seconds after 30 second interrogation with 12.2 MeV photon beam. PVT
detector adjacent to one vertical side of surrogate container cube. Rapiscan
Test Object "E" in aluminum at 0.05 g/cc..... 185

Figure 85. Simulated detector response to delayed gamma emission at one
second intervals from 7-10 seconds and five second intervals from 10-40
seconds after 30 second interrogation with 7 MeV neutron and 12.2 MeV
photon beams. PVT detector adjacent to one vertical side of surrogate
container cube. Rapiscan Test Object "E" in aluminum at 0.1 g/cc. 186

Figure 86. Simulated detector response to delayed gamma emission at one
second intervals from 7-10 seconds and five second intervals from 10-40
seconds after 30 second interrogation with 7 MeV neutron beam. PVT
detector adjacent to one vertical side of surrogate container cube. Rapiscan
Test Object "E" in aluminum at 0.1 g/cc..... 187

Figure 87. Simulated detector response to delayed gamma emission at one
second intervals from 7-10 seconds and five second intervals from 10-40
seconds after 30 second interrogation with 12.2 MeV photon beam. PVT
detector adjacent to one vertical side of surrogate container cube. Rapiscan
Test Object "E" in aluminum at 0.1 g/cc..... 188

Figure 88. Simulated detector response to delayed gamma emission at one second intervals from 7-10 seconds and five second intervals from 10-40 seconds after 30 second interrogation with 7 MeV neutron and 12.2 MeV photon beams. PVT detector adjacent to one vertical side of surrogate container cube. Rapiscan Test Object "E" in aluminum at 0.2 g/cc. 189

Figure 89. Simulated detector response to delayed gamma emission at one second intervals from 7-10 seconds and five second intervals from 10-40 seconds after 30 second interrogation with 7 MeV neutron beam. PVT detector adjacent to one vertical side of surrogate container cube. Rapiscan Test Object "E" in aluminum at 0.2 g/cc..... 190

Figure 90. Simulated detector response to delayed gamma emission at one second intervals from 7-10 seconds and five second intervals from 10-40 seconds after 30 second interrogation with 12.2 MeV photon beam. PVT detector adjacent to one vertical side of surrogate container cube. Rapiscan Test Object "E" in aluminum at 0.2 g/cc..... 191

Figure 91. Simulated detector response to delayed gamma emission at one second intervals from 7-10 seconds and five second intervals from 10-40 seconds after 30 second interrogation with 7 MeV neutron and 12.2 MeV photon beams. PVT detector adjacent to one vertical side of surrogate container cube. Rapiscan Test Object "E" in aluminum at 0.3 g/cc. 192

Figure 92. Simulated detector response to delayed gamma emission at one second intervals from 7-10 seconds and five second intervals from 10-40 seconds after 30 second interrogation with 7 MeV neutron beam. PVT

detector adjacent to one vertical side of surrogate container cube. Rapiscan
Test Object "E" in aluminum at 0.3 g/cc..... 193

Figure 93. Simulated detector response to delayed gamma emission at one
second intervals from 7-10 seconds and five second intervals from 10-40
seconds after 30 second interrogation with 12.2 MeV photon beam. PVT
detector adjacent to one vertical side of surrogate container cube. Rapiscan
Test Object "E" in aluminum at 0.3 g/cc..... 194

Figure 94. Simulated detector response to delayed gamma emission at one
second intervals from 7-10 seconds and five second intervals from 10-40
seconds after 30 second interrogation with 7 MeV neutron and 12.2 MeV
photon beams. PVT detector adjacent to one vertical side of surrogate
container cube. Rapiscan Test Object "E" in aluminum at 0.4 g/cc. 195

Figure 95. Simulated detector response to delayed gamma emission at one
second intervals from 7-10 seconds and five second intervals from 10-40
seconds after 30 second interrogation with 7 MeV neutron beam. PVT
detector adjacent to one vertical side of surrogate container cube. Rapiscan
Test Object "E" in aluminum at 0.4 g/cc..... 196

Figure 96. Simulated detector response to delayed gamma emission at one
second intervals from 7-10 seconds and five second intervals from 10-40
seconds after 30 second interrogation with 12.2 MeV photon beam. PVT
detector adjacent to one vertical side of surrogate container cube. Rapiscan
Test Object "E" in aluminum at 0.4 g/cc..... 197

Figure 97. Simulated detector response to delayed gamma emission at one second intervals from 7-10 seconds and five second intervals from 10-40 seconds after 30 second interrogation with 7 MeV neutron and 12.2 MeV photon beams. PVT detector adjacent to one vertical side of surrogate container cube. Rapiscan Test Object "E" in aluminum at 0.5 g/cc. 198

Figure 98. Simulated detector response to delayed gamma emission at one second intervals from 7-10 seconds and five second intervals from 10-40 seconds after 30 second interrogation with 7 MeV neutron beam. PVT detector adjacent to one vertical side of surrogate container cube. Rapiscan Test Object "E" in aluminum at 0.5 g/cc..... 199

Figure 99. Simulated detector response to delayed gamma emission at one second intervals from 7-10 seconds and five second intervals from 10-40 seconds after 30 second interrogation with 12.2 MeV photon beam. PVT detector adjacent to one vertical side of surrogate container cube. Rapiscan Test Object "E" in aluminum at 0.5 g/cc..... 200

Figure 100. Simulated detector response to delayed gamma emission at one second intervals from 7-10 seconds and five second intervals from 10-40 seconds after 30 second interrogation with 7 MeV neutron and 12.2 MeV photon beams. PVT detector adjacent to one vertical side of surrogate container cube. Rapiscan Test Object "E" in aluminum at 0.6 g/cc. 201

Figure 101. Simulated detector response to delayed gamma emission at one second intervals from 7-10 seconds and five second intervals from 10-40 seconds after 30 second interrogation with 7 MeV neutron beam. PVT

detector adjacent to one vertical side of surrogate container cube. Rapiscan
Test Object "E" in aluminum at 0.6 g/cc..... 202

Figure 102. Simulated detector response to delayed gamma emission at one
second intervals from 7-10 seconds and five second intervals from 10-40
seconds after 30 second interrogation with 12.2 MeV photon beam. PVT
detector adjacent to one vertical side of surrogate container cube. Rapiscan
Test Object "E" in aluminum at 0.6 g/cc..... 203

Figure 103. Simulated detector response to delayed gamma emission at one
second intervals from 7-10 seconds and five second intervals from 10-40
seconds after 30 second interrogation with 7 MeV neutron and 12.2 MeV
photon beams. PVT detector adjacent to one vertical side of surrogate
container cube. Rapiscan Test Object "E" in aluminum at 0.65 g/cc. 204

Figure 104. Simulated detector response to delayed gamma emission at one
second intervals from 7-10 seconds and five second intervals from 10-40
seconds after 30 second interrogation with 7 MeV neutron beam. PVT
detector adjacent to one vertical side of surrogate container cube. Rapiscan
Test Object "E" in aluminum at 0.65 g/cc..... 205

Figure 105. Simulated detector response to delayed gamma emission at one
second intervals from 7-10 seconds and five second intervals from 10-40
seconds after 30 second interrogation with 12.2 MeV photon beam. PVT
detector adjacent to one vertical side of surrogate container cube. Rapiscan
Test Object "E" in aluminum at 0.65 g/cc..... 206

Figure 106. Simulated detector response to delayed gamma emission at one second intervals from 7-10 seconds and five second intervals from 10-40 seconds after 30 second interrogation with 7 MeV neutron and 12.2 MeV photon beams. PVT detector adjacent to one vertical side of surrogate container cube. Rapiscan Test Object "E" in clay at 0.05 g/cc..... 208

Figure 107. Simulated detector response to delayed gamma emission at one second intervals from 7-10 seconds and five second intervals from 10-40 seconds after 30 second interrogation with 7 MeV neutron beam. PVT detector adjacent to one vertical side of surrogate container cube. Rapiscan Test Object "E" in clay at 0.05 g/cc..... 209

Figure 108. Simulated detector response to delayed gamma emission at one second intervals from 7-10 seconds and five second intervals from 10-40 seconds after 30 second interrogation with 12.2 MeV photon beam. PVT detector adjacent to one vertical side of surrogate container cube. Rapiscan Test Object "E" in clay at 0.05 g/cc..... 210

Figure 109. Simulated detector response to delayed gamma emission at one second intervals from 7-10 seconds and five second intervals from 10-40 seconds after 30 second interrogation with 7 MeV neutron and 12.2 MeV photon beams. PVT detector adjacent to one vertical side of surrogate container cube. Rapiscan Test Object "E" in clay at 0.1 g/cc..... 211

Figure 110. Simulated detector response to delayed gamma emission at one second intervals from 7-10 seconds and five second intervals from 10-40 seconds after 30 second interrogation with 7 MeV neutron beam. PVT

detector adjacent to one vertical side of surrogate container cube. Rapiscan
Test Object "E" in clay at 0.1 g/cc..... 212

Figure 111. Simulated detector response to delayed gamma emission at one
second intervals from 7-10 seconds and five second intervals from 10-40
seconds after 30 second interrogation with 12.2 MeV photon beam. PVT
detector adjacent to one vertical side of surrogate container cube. Rapiscan
Test Object "E" in clay at 0.1 g/cc..... 213

Figure 112. Simulated detector response to delayed gamma emission at one
second intervals from 7-10 seconds and five second intervals from 10-40
seconds after 30 second interrogation with 7 MeV neutron and 12.2 MeV
photon beams. PVT detector adjacent to one vertical side of surrogate
container cube. Rapiscan Test Object "E" in clay at 0.2 g/cc..... 214

Figure 113. Simulated detector response to delayed gamma emission at one
second intervals from 7-10 seconds and five second intervals from 10-40
seconds after 30 second interrogation with 7 MeV neutron beam. PVT
detector adjacent to one vertical side of surrogate container cube. Rapiscan
Test Object "E" in clay at 0.2 g/cc..... 215

Figure 114. Simulated detector response to delayed gamma emission at one
second intervals from 7-10 seconds and five second intervals from 10-40
seconds after 30 second interrogation with 12.2 MeV photon beam. PVT
detector adjacent to one vertical side of surrogate container cube. Rapiscan
Test Object "E" in clay at 0.2 g/cc..... 216

Figure 115. Simulated detector response to delayed gamma emission at one second intervals from 7-10 seconds and five second intervals from 10-40 seconds after 30 second interrogation with 7 MeV neutron and 12.2 MeV photon beams. PVT detector adjacent to one vertical side of surrogate container cube. Rapiscan Test Object "E" in clay at 0.3 g/cc..... 217

Figure 116. Simulated detector response to delayed gamma emission at one second intervals from 7-10 seconds and five second intervals from 10-40 seconds after 30 second interrogation with 7 MeV neutron beam. PVT detector adjacent to one vertical side of surrogate container cube. Rapiscan Test Object "E" in clay at 0.3 g/cc..... 218

Figure 117. Simulated detector response to delayed gamma emission at one second intervals from 7-10 seconds and five second intervals from 10-40 seconds after 30 second interrogation with 12.2 MeV photon beam. PVT detector adjacent to one vertical side of surrogate container cube. Rapiscan Test Object "E" in clay at 0.3 g/cc..... 219

Figure 118. Simulated detector response to delayed gamma emission at one second intervals from 7-10 seconds and five second intervals from 10-40 seconds after 30 second interrogation with 7 MeV neutron and 12.2 MeV photon beams. PVT detector adjacent to one vertical side of surrogate container cube. Rapiscan Test Object "E" in clay at 0.4 g/cc..... 220

Figure 119. Simulated detector response to delayed gamma emission at one second intervals from 7-10 seconds and five second intervals from 10-40 seconds after 30 second interrogation with 7 MeV neutron beam. PVT

detector adjacent to one vertical side of surrogate container cube. Rapiscan
Test Object "E" in clay at 0.4 g/cc..... 221

Figure 120. Simulated detector response to delayed gamma emission at one
second intervals from 7-10 seconds and five second intervals from 10-40
seconds after 30 second interrogation with 12.2 MeV photon beam. PVT
detector adjacent to one vertical side of surrogate container cube. Rapiscan
Test Object "E" in clay at 0.4 g/cc..... 222

Figure 121. Simulated detector response to delayed gamma emission at one
second intervals from 7-10 seconds and five second intervals from 10-40
seconds after 30 second interrogation with 7 MeV neutron and 12.2 MeV
photon beams. PVT detector adjacent to one vertical side of surrogate
container cube. Rapiscan Test Object "E" in clay at 0.5 g/cc..... 223

Figure 122. Simulated detector response to delayed gamma emission at one
second intervals from 7-10 seconds and five second intervals from 10-40
seconds after 30 second interrogation with 7 MeV neutron beam. PVT
detector adjacent to one vertical side of surrogate container cube. Rapiscan
Test Object "E" in clay at 0.5 g/cc..... 224

Figure 123. Simulated detector response to delayed gamma emission at one
second intervals from 7-10 seconds and five second intervals from 10-40
seconds after 30 second interrogation with 12.2 MeV photon beam. PVT
detector adjacent to one vertical side of surrogate container cube. Rapiscan
Test Object "E" in clay at 0.5 g/cc..... 225

Figure 124. Simulated detector response to delayed gamma emission at one second intervals from 7-10 seconds and five second intervals from 10-40 seconds after 30 second interrogation with 7 MeV neutron and 12.2 MeV photon beams. PVT detector adjacent to one vertical side of surrogate container cube. Rapiscan Test Object "E" in clay at 0.6 g/cc..... 226

Figure 125. Simulated detector response to delayed gamma emission at one second intervals from 7-10 seconds and five second intervals from 10-40 seconds after 30 second interrogation with 7 MeV neutron beam. PVT detector adjacent to one vertical side of surrogate container cube. Rapiscan Test Object "E" in clay at 0.6 g/cc..... 227

Figure 126. Simulated detector response to delayed gamma emission at one second intervals from 7-10 seconds and five second intervals from 10-40 seconds after 30 second interrogation with 12.2 MeV photon beam. PVT detector adjacent to one vertical side of surrogate container cube. Rapiscan Test Object "E" in clay at 0.6 g/cc..... 228

Figure 127. Simulated detector response to delayed gamma emission at one second intervals from 7-10 seconds and five second intervals from 10-40 seconds after 30 second interrogation with 7 MeV neutron and 12.2 MeV photon beams. PVT detector adjacent to one vertical side of surrogate container cube. Rapiscan Test Object "E" in clay at 0.65 g/cc..... 229

Figure 128. Simulated detector response to delayed gamma emission at one second intervals from 7-10 seconds and five second intervals from 10-40 seconds after 30 second interrogation with 7 MeV neutron beam. PVT

detector adjacent to one vertical side of surrogate container cube. Rapiscan
Test Object "E" in clay at 0.65 g/cc..... 230

Figure 129. Simulated detector response to delayed gamma emission at one
second intervals from 7-10 seconds and five second intervals from 10-40
seconds after 30 second interrogation with 12.2 MeV photon beam. PVT
detector adjacent to one vertical side of surrogate container cube. Rapiscan
Test Object "E" in clay at 0.65 g/cc..... 231

Figure 130. Simulated detector response to delayed gamma emission at one
second intervals from 7-10 seconds and five second intervals from 10-40
seconds after 30 second interrogation with 7 MeV neutron and 12.2 MeV
photon beams. PVT detector adjacent to one vertical side of surrogate
container cube. Rapiscan Test Object "E" in iron at 0.05 g/cc..... 233

Figure 131. Simulated detector response to delayed gamma emission at one
second intervals from 7-10 seconds and five second intervals from 10-40
seconds after 30 second interrogation with 7 MeV neutron beam. PVT
detector adjacent to one vertical side of surrogate container cube. Rapiscan
Test Object "E" in iron at 0.05 g/cc. 234

Figure 132. Simulated detector response to delayed gamma emission at one
second intervals from 7-10 seconds and five second intervals from 10-40
seconds after 30 second interrogation with 12.2 MeV photon beam. PVT
detector adjacent to one vertical side of surrogate container cube. Rapiscan
Test Object "E" in iron at 0.05 g/cc. 235

Figure 133. Simulated detector response to delayed gamma emission at one second intervals from 7-10 seconds and five second intervals from 10-40 seconds after 30 second interrogation with 7 MeV neutron and 12.2 MeV photon beams. PVT detector adjacent to one vertical side of surrogate container cube. Rapiscan Test Object "E" in iron at 0.1 g/cc. 236

Figure 134. Simulated detector response to delayed gamma emission at one second intervals from 7-10 seconds and five second intervals from 10-40 seconds after 30 second interrogation with 7 MeV neutron beam. PVT detector adjacent to one vertical side of surrogate container cube. Rapiscan Test Object "E" in iron at 0.1 g/cc. 237

Figure 135. Simulated detector response to delayed gamma emission at one second intervals from 7-10 seconds and five second intervals from 10-40 seconds after 30 second interrogation with 12.2 MeV photon beam. PVT detector adjacent to one vertical side of surrogate container cube. Rapiscan Test Object "E" in iron at 0.1 g/cc. 238

Figure 136. Simulated detector response to delayed gamma emission at one second intervals from 7-10 seconds and five second intervals from 10-40 seconds after 30 second interrogation with 7 MeV neutron and 12.2 MeV photon beams. PVT detector adjacent to one vertical side of surrogate container cube. Rapiscan Test Object "E" in iron at 0.2 g/cc. 239

Figure 137. Simulated detector response to delayed gamma emission at one second intervals from 7-10 seconds and five second intervals from 10-40 seconds after 30 second interrogation with 7 MeV neutron beam. PVT

detector adjacent to one vertical side of surrogate container cube. Rapiscan
Test Object “E” in iron at 0.2 g/cc. 240

Figure 138. Simulated detector response to delayed gamma emission at one
second intervals from 7-10 seconds and five second intervals from 10-40
seconds after 30 second interrogation with 12.2 MeV photon beam. PVT
detector adjacent to one vertical side of surrogate container cube. Rapiscan
Test Object “E” in iron at 0.2 g/cc. 241

Figure 139. Simulated detector response to delayed gamma emission at one
second intervals from 7-10 seconds and five second intervals from 10-40
seconds after 30 second interrogation with 7 MeV neutron and 12.2 MeV
photon beams. PVT detector adjacent to one vertical side of surrogate
container cube. Rapiscan Test Object “E” in iron at 0.3 g/cc. 242

Figure 140. Simulated detector response to delayed gamma emission at one
second intervals from 7-10 seconds and five second intervals from 10-40
seconds after 30 second interrogation with 7 MeV neutron beam. PVT
detector adjacent to one vertical side of surrogate container cube. Rapiscan
Test Object “E” in iron at 0.3 g/cc. 243

Figure 141. Simulated detector response to delayed gamma emission at one
second intervals from 7-10 seconds and five second intervals from 10-40
seconds after 30 second interrogation with 12.2 MeV photon beam. PVT
detector adjacent to one vertical side of surrogate container cube. Rapiscan
Test Object “E” in iron at 0.3 g/cc. 244

Figure 142. Simulated detector response to delayed gamma emission at one second intervals from 7-10 seconds and five second intervals from 10-40 seconds after 30 second interrogation with 7 MeV neutron and 12.2 MeV photon beams. PVT detector adjacent to one vertical side of surrogate container cube. Rapiscan Test Object "E" in iron at 0.4 g/cc. 245

Figure 143. Simulated detector response to delayed gamma emission at one second intervals from 7-10 seconds and five second intervals from 10-40 seconds after 30 second interrogation with 7 MeV neutron beam. PVT detector adjacent to one vertical side of surrogate container cube. Rapiscan Test Object "E" in iron at 0.4 g/cc. 246

Figure 144. Simulated detector response to delayed gamma emission at one second intervals from 7-10 seconds and five second intervals from 10-40 seconds after 30 second interrogation with 12.2 MeV photon beam. PVT detector adjacent to one vertical side of surrogate container cube. Rapiscan Test Object "E" in iron at 0.4 g/cc. 247

Figure 145. Simulated detector response to delayed gamma emission at one second intervals from 7-10 seconds and five second intervals from 10-40 seconds after 30 second interrogation with 7 MeV neutron and 12.2 MeV photon beams. PVT detector adjacent to one vertical side of surrogate container cube. Rapiscan Test Object "E" in iron at 0.5 g/cc. 248

Figure 146. Simulated detector response to delayed gamma emission at one second intervals from 7-10 seconds and five second intervals from 10-40 seconds after 30 second interrogation with 7 MeV neutron beam. PVT

detector adjacent to one vertical side of surrogate container cube. Rapiscan
Test Object "E" in iron at 0.5 g/cc. 249

Figure 147. Simulated detector response to delayed gamma emission at one
second intervals from 7-10 seconds and five second intervals from 10-40
seconds after 30 second interrogation with 12.2 MeV photon beam. PVT
detector adjacent to one vertical side of surrogate container cube. Rapiscan
Test Object "E" in iron at 0.5 g/cc. 250

Figure 148. Simulated detector response to delayed gamma emission at one
second intervals from 7-10 seconds and five second intervals from 10-40
seconds after 30 second interrogation with 7 MeV neutron and 12.2 MeV
photon beams. PVT detector adjacent to one vertical side of surrogate
container cube. Rapiscan Test Object "E" in iron at 0.6 g/cc. 251

Figure 149. Simulated detector response to delayed gamma emission at one
second intervals from 7-10 seconds and five second intervals from 10-40
seconds after 30 second interrogation with 7 MeV neutron beam. PVT
detector adjacent to one vertical side of surrogate container cube. Rapiscan
Test Object "E" in iron at 0.6 g/cc. 252

Figure 150. Simulated detector response to delayed gamma emission at one
second intervals from 7-10 seconds and five second intervals from 10-40
seconds after 30 second interrogation with 12.2 MeV photon beam. PVT
detector adjacent to one vertical side of surrogate container cube. Rapiscan
Test Object "E" in iron at 0.6 g/cc. 253

Figure 151. Simulated detector response to delayed gamma emission at one second intervals from 7-10 seconds and five second intervals from 10-40 seconds after 30 second interrogation with 7 MeV neutron and 12.2 MeV photon beams. PVT detector adjacent to one vertical side of surrogate container cube. Rapiscan Test Object "E" in iron at 0.65 g/cc. 254

Figure 152. Simulated detector response to delayed gamma emission at one second intervals from 7-10 seconds and five second intervals from 10-40 seconds after 30 second interrogation with 7 MeV neutron beam. PVT detector adjacent to one vertical side of surrogate container cube. Rapiscan Test Object "E" in iron at 0.65 g/cc. 255

Figure 153. Simulated detector response to delayed gamma emission at one second intervals from 7-10 seconds and five second intervals from 10-40 seconds after 30 second interrogation with 12.2 MeV photon beam. PVT detector adjacent to one vertical side of surrogate container cube. Rapiscan Test Object "E" in iron at 0.65 g/cc. 256

LIST OF TABLES

Table 1. Activity Concentrations of NORM in Building Materials.....	32
Table 2. Neutron Activation Products of Concern.....	34
Table 3. Delayed Gamma Tally, 3-4 MeV.....	128
Table 4. Delayed Gamma Tally, 4-5 MeV.....	129
Table 5. Delayed Gamma Tally, 5-6 MeV.....	130
Table 6. Contribution of Neutron vs. Photon Beam to the Total Delayed Gamma Signal.....	132
Table 7. MINE Statistics Example.....	141

INTRODUCTION

I. Foreword

A. Special Nuclear Materials

The formal ushering in of the Atomic Age began on July 16, 1945 with the Trinity test in the high desert of New Mexico and concluded with the destruction of the cities of Hiroshima and Nagasaki in Japan less than one month later. Isotopes of two elements hitherto unknown to the general population, accompanied by astounding engineering prowess, were each used as key ingredients to capstone the Second World War. Uranium-235 and plutonium-239 are now widely recognized as valuable materials for use in both power generation and as weapon components. This dual nature has made the production and/or enrichment of these isotopes a necessary and closely guarded process. For approximately 50 years, a delicate balance had been maintained to control their proliferation while at the same time assisting responsible nations in generating energy from these materials. The collapse of the Soviet Union and the onset of the “War on Terror” have changed the nature of this balance with the revelation of poorly controlled stockpiles of both isotopes and an unremitting pursuit of raw materials and technology by rogue states to create their own weapons. Monitoring inventories and tracking the movements of these very “special” materials has now become a science and engineering challenge of its own.

B. Intermodal Shipping Containers

Nearly one million intermodal shipping containers enter the United States per month by sea (USDOT, 2009). These containers can be used to smuggle illicit or illegal materials, animals, or people into (or out of) the country and may include unsecured or stolen special nuclear material (Lichtenwald et al., 2009). Every container cannot be comprehensively examined due to the impact on the speed of commerce. As a result, a complex scheme to identify containers for intensive scrutiny is in place (Kelly, 2007). These layers of defense are built around various factors including gathered intelligence from manifests, x-ray inspection, portal monitoring and cursory physical examination. If the container triggers additional interest, it may be moved to a Customs exam site for a more extensive inspection, including complete unloading. The only direct method available to indicate the possible presence of special nuclear material (SNM) is through passive photon/neutron detection of the comparatively weak signals produced by natural radioactive decay. These decay signatures can be shielded with relative ease and may allow small quantities (< 1 kg) to pass undetected (Myers, et al., 2004).

C. Active Interrogation

The catastrophic consequences of reprobate weapon use has driven research into active approaches that induce nuclear reactions, namely fission, in SNM and then attempt to detect the unique particle signatures produced from the events. Initially, neutron beams alone were considered, but the combination of cargo beam attenuation and neutron activation are problematic (Slaughter et al., 2007a; Pruett et al., 2005). The dual-beam active interrogation concept applies both neutrons and gamma-rays to irradiate containers simultaneously and takes advantage of the penetrating ability of photons in hydrogenous materials to produce photofission events.

II. Hypothesis and Chronological Aims

A. Hypothesis

Interrogating a suspect shipping container for special nuclear material with both neutron and photon beams at appropriate energies is superior to neutron beam interrogation alone.

B. Chronological Aims

1. Develop a fundamental container model to accommodate combinations of low, medium and high density homogenized materials as surrogate cargo using an SNM test object of practical composition.

2. Demonstrate that the application of an additional photon beam yields a useful signal increase from photofission as opposed to interrogation using a neutron beam alone.
3. Apply an appropriate measure based on delayed gamma emission ($E_\gamma = 3\text{-}6$ MeV) using a plastic scintillator added to the fundamental model to validate the general performance of a system designed to detect SNM in the presence of background interference.

BACKGROUND

I. Special Nuclear Materials

A. Definition

Special Nuclear Materials (SNM) are generally categorized in the context of weapon applications as “direct-use” or “indirect-use.” Direct-use is clear. Indirect-use refers to the materials’ precursor potential and requires a significant amount of enrichment or conversion effort. Direct-use nuclear materials are plutonium (element), uranium-233 and uranium-235 of $\geq 20\%$ enrichment. Indirect-use nuclear materials are thorium (element) and uranium-235 of $< 20\%$ enrichment (Cochran and Paine, 1995).

B. Quantities of Significance

The International Atomic Energy Agency (IAEA) defines a “significant quantity” as “the approximate quantity of nuclear material in respect of which, taking into account any conversion process involved, the possibility of manufacturing a nuclear explosive device cannot be excluded (IAEA, 1993).” With regard to illicit movements, the IAEA specifically “...aims to have a high level of assurance that the safeguards system would detect the diversion of a significant quantity of nuclear material (8 kg of plutonium, 25 kg of uranium-235 in highly enriched uranium, 75 kg of uranium-235 in natural or low enriched uranium).” The

remaining significant quantities are 8 kg of uranium-233 and 20,000 kg of thorium (Cochran and Paine, 1995).

II. Intermodal Shipping Containers

A. History

Containerization is defined as “the utilizing, grouping or consolidating of multiple units into a larger container for more efficient movement” and has existed for over half a century (Rath, 1973, quoting The Containerization Institute, now “The Containerization & Intermodal Institute”). The concept of unitized cargo conveyed seamlessly across truck, ship and railcar as recognized today appears intuitive on the surface. However, as with most innovations that have increased the speed of commerce, intermodal containerization took a winding road to fruition. Opposition from labor unions, challenges in systems engineering and the negotiation of cost distribution throughout the transportation chain all impeded progress. Ultimately, the economy of scale triumphed and unitized cargo, realized as “intermodal shipping containers,” now dominate the movement of global commerce.

B. Materials of Construction

Containerization implies standardization. This is only generally true for the intermodal container. Intermodal shipping containers are rectangular in shape, structurally robust and weather resistant (Figure 1). Materials of construction are not as diverse as they once were as manufacture is now primarily done overseas. Steel, with plywood flooring, is the construction material of choice due to cost despite its poor corrosion resistance. Containers made of steel are easily identified by their corrugated sides. Aluminum and fiberglass-reinforced plywood (FRP) may still be found (Rath, 1973).



Figure 1. Intermodal shipping container, steel, 20' (1 TEU), exterior and interior. (www.containertech.com, <http://20foothouse.com>)

C. Dimensions

The standard unit of measure is the “20-foot equivalent unit” (TEU) and refers to the length of a container. This measure is independent of height or width. The term was initially introduced to describe containers with a nominal dimension of 20' x 8' x 8' (L x W x H). There are now several different combinations of length (40', 48' and 53') and height (4', 8 ½' and 9 ½'), including an 8 ½' width that is primarily seen in Europe. These differing lengths are referenced in multiples and fractions of TEUs. For example, a nominal 40-foot container (40' x 8' x 8') is equal to 2 TEU; a 48' container is equal to 2.4 TEU.

D. Capacities

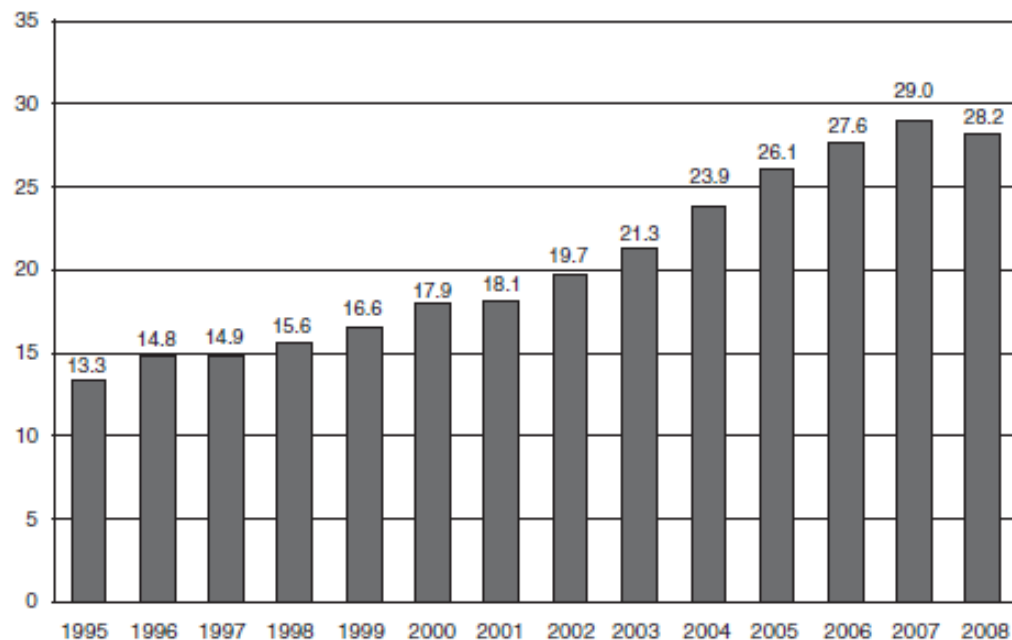
Payload varies depending on manufacturer. Generally, a nominal 20-foot container (1 TEU) has an internal volume on the order of 1200 ft³ (34 m³) and a payload capacity of ~48,000 lbs. (~22,000 kg). A nominal 40-foot container (2 TEU) has an internal volume on the order of 2400 ft³ (68 m³) and a payload capacity of ~60,000 lbs. (~27,000 kg). Note that doubling the volume does not equate to a doubling in payload capacity. To provide some idea of their value, used shipping containers in good condition are available for sale on the internet from ~\$2000 (20') to ~\$3000 (40') (ELG, 2012).

III. The Inspection System

A. Container Traffic

Container traffic is measured in TEUs. In 2010, 114.3 million loaded TEUs worldwide were exported (WSC, 2012). Total loaded traffic including import, export and transshipments with respect to the United States now approaches 30 million TEUs (Figure 2). This equates to approximately 20 million boxes of mixed lengths, presenting a challenging number to inspect.

U.S. International Maritime Containerized Activity: 1995-2008
(Millions of loaded TEUs)



KEY: TEUs = twenty-foot equivalent units. One 20-foot container equals one TEU, and one 40-foot container equals two TEUs.

NOTES: Totals are for all container ports in all 50 states and Puerto Rico. The data in this figure include only loaded containers in U.S. international maritime activity and cover U.S. imports, exports, and transshipments.

Figure 2. TEU traffic, ~20 million containers (from USDOT, 2009).

B. History

The current inspection scheme for containers entering the United States consists of a “layered system of layers” (Kelly, 2007). It begins with the 24 Hour Advanced Cargo Rule. An accurate cargo manifest with valid consignee addresses must be submitted to a clearinghouse 24 hours before loading on a vessel bound for the United States. The Automated Targeting System (ATS) uses algorithms to analyze data from the manifests to identify containers for additional scrutiny on arrival to a U.S. port, including physical inspections. The Container Security Initiative (CSI) program is applied outside the United States. It employs U.S. personnel stationed at ports around the world to identify “high risk” containers on-site, using the aforementioned 24 Hour Rule manifests, and includes limited use of some imaging and radiation detection technologies. The emphasis is on curbing the impact to the speed of commerce; consequently, less than one percent of the containers are scanned in any fashion, and only a fraction of these are actually opened. In contrast, within the United States “the selection and physical examination of cargo amounts to 3% - 5% of all merchandise being imported and exported” (PTG, 2010). A schema of the process is provided in Figure 3.

The Importation Process

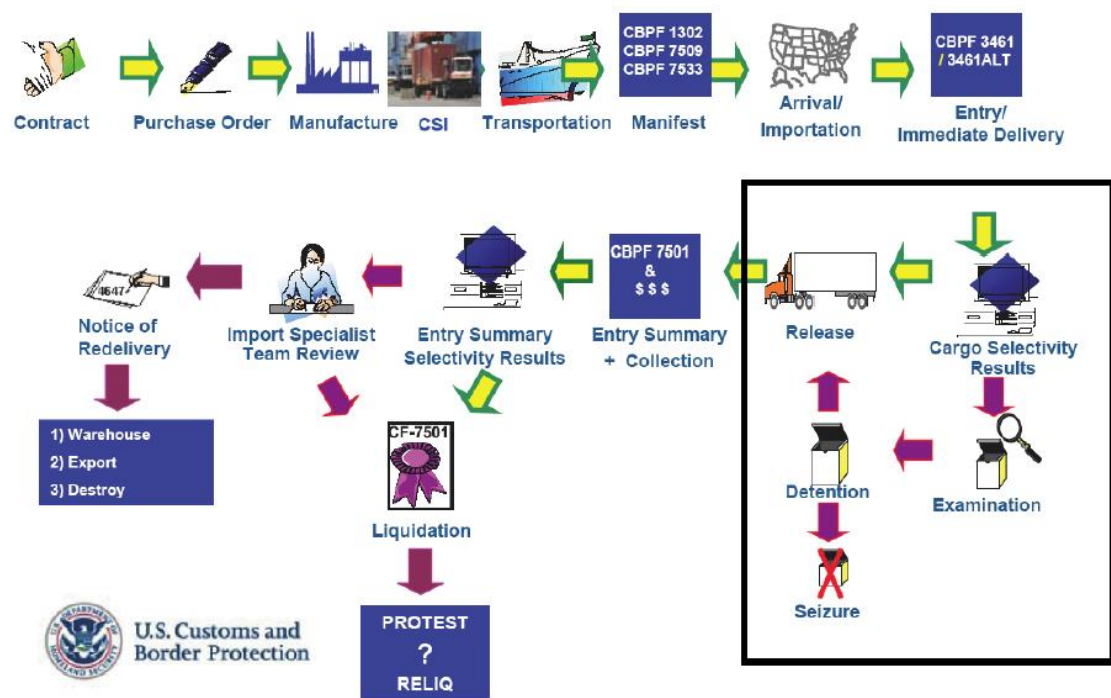


Figure 3. The importation process (from PTG, 2010).

The Megaports Initiative is also an overseas program, but looks specifically for illicit nuclear materials, including SNM, with National Nuclear Security Administration (NNSA) radiation portal monitors (RPMs). Handheld devices are also employed in the form of radioisotope identification devices (RIIDs), standard survey meters and high performance germanium (HPGe) detectors. The Initiative is active in over 27 foreign ports and scans all inbound, outbound and transshipped cargo (Reynolds & Dusina, 2010). It is important to note that, aside from x-ray imaging and fast neutron and gamma-ray radiography (FNRR), the search for SNM applies passive methods (Sowerby et al., 2009, Bjorkholm, 2003).

C. Special Nuclear Materials Detection

Passive radiation detection takes many forms and can be very sensitive. This sensitivity can lead to false alarms from naturally occurring radioactive material (NORM) such as potassium-40 found in bananas (Hosenball, 2008). The additional inspection required to clear a container containing NORM or other approved man-made source results in a delay that may be monetarily significant. A false alarm rate of $\leq 0.5\%$ in practice appears to be tolerable (Port of Oakland, 2005). The number of threat items that pass undetected is unknown. This lack of information and the associated potentially catastrophic consequences has driven research into active approaches that induce nuclear reactions, namely fission, in

SNM and then attempt to detect the unique particle signatures produced from the events. Initially, fast neutron beams alone were considered because of their ability to induce fission at essentially any incident energy. However, the combination of beam scattering by low Z hydrogenous materials and interference(s) resulting from neutron activation of the cargo are problematic (Slaughter et al., 2007a; Pruett et al., 2005). More recently, the notion of increasing the energy and magnitude of existing photon imaging beam systems to induce photofission in SNM is being seriously considered (Danagoulian et al., 2010). Energetic photon beams can penetrate low Z elements easily. The dual-beam active interrogation concept applies both of these techniques simultaneously to meaningfully penetrate a larger scope of cargo. Unlike the radiation portal monitor that is deployed to passively survey nearly everything, any active interrogation technique would apply to only a small fraction of the container traffic currently selected for physical examination in the first place.

IV. Active Interrogation

A. Neutron Experiments

A substantial experimental effort was undertaken at Lawrence Livermore National Laboratory (LLNL) using neutron beams to interrogate surrogate cargos and SNM targets (Hall et al., 2007; Slaughter et al., 2007b). This program commonly referred to as the “Nuclear Car Wash” investigated particle signatures

produced by interrogating highly enriched uranium targets buried within steel or plywood matrices. They confirmed that neutron beams are adept at penetrating high Z substances such as iron, but scatter considerably in the presence of hydrogenous (low Z) material. These characteristics make it challenging to penetrate cargo, such as coffee, to induce fission events using these neutrons. In addition, it was found that the potential creation of noise signatures from cargo activation dictates that neutron beam energies must be 10 MeV or less (Slaughter et al., 2007b). A less energetic beam reduces its effective penetration, but this trade-off is well worth the cost, particularly when the maximum penetration distances of concern are only on the order ~48" (~122 cm) or roughly half the height/width of a shipping container.

B. Photon Experiments

A number of relevant photofission experiments have been conducted (Proctor et al., 2012, Rennhofer et al., 2010, Myers et al., 2004, Jones et al., 2000, Gmar & Capdevila, 1999, Hollas et al., 1987). Several of these experiments measured delayed particle emissions. An excellent example of a delayed gamma spectrum from the photofission of uranium-238 is provided in Figure 4. The shape of this delayed spectrum is very similar to that of neutron induced fission as nearly the same chain of decay products, and consequently β -delayed gammas, are produced.

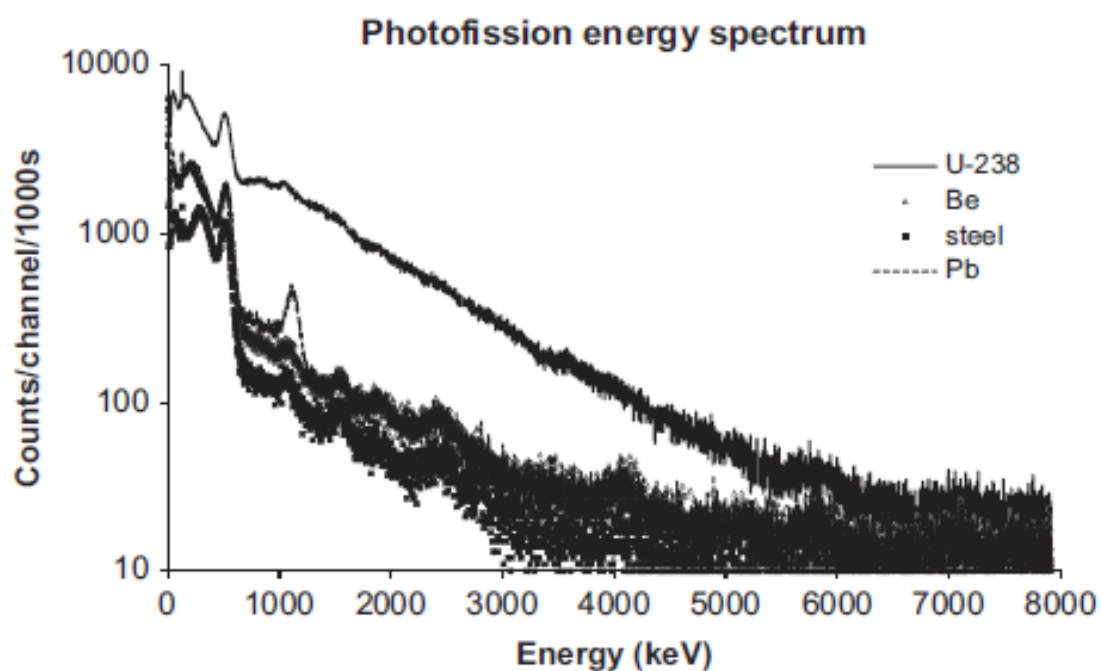


Figure 4. Experimental delayed gamma energy spectrum resulting from photofission of uranium-238 using 15 MeV photons, top trace (from Proctor, et al., 2012).

C. Simulations

Interrogation experiments such as those described in the previous sections are time consuming and expensive to conduct and consequently have limited scope. Unsurprisingly, there appears to be no experimental evidence available in the public realm at this time with regard to near simultaneous neutron and photon beam interrogation. Clearly, low cost simulations using code suites developed with this explicit task in mind are needed to help fill the gap and smooth the way for better informed experimental designs.

There are several neutron interrogation simulations of SNM targets in the literature. The LLNL COG effort is the most relevant for this work (Prussin et al., 2006, Buck et al., 2002, Buck & Hall, 1999). An interesting set of benchmarking exercises involving delayed gamma simulation in MCNPX has also been conducted (Durkee et al., 2009). There are no published dual-beam simulation efforts available. This is likely due to the complexity and unrealized need to seriously consider photofission contributions and there is limited work to mitigate this deficiency (Verbeke et al., 2010).

D. Work by the University of New Mexico

The Defense Threat Reduction Agency (DTRA) continues to fund initiatives exploring civil and military applications for active interrogation (also referred to as

“standoff detection systems”), beam sources and improvements to computational transport solvers and associated nuclear data (i.e. cross section libraries). Research was recently concluded for one of these DTRA programs under the direction of Professor Cassiano R.E. de Oliveira at the University of New Mexico (de Oliveira et al., 2009). The proposal called for:

- Improvement and extension of particle transport methods and codes to be used for testing and validation of proposed standoff detection systems.
- Improvement of key nuclear data necessary for unambiguous detection of concealed nuclear material and incorporation of results into simulation tools.
- Application of a suite of particle transport codes for benchmarking against relevant experimental data and for examining and evaluating potential DTRA-funded systems applications.

The resultant code suite developments from this endeavor were successfully benchmarked against the aforementioned LLNL “Nuclear Car Wash” set of experiments investigating the detection of shielded SNM inside a shipping container surrogate using neutron beam interrogation (Martin, 2012; Hall et al., 2007, Church et al., 2006). This enhanced code suite will be applied in part to achieve the research aims of this dissertation, which also serves as a natural continuation to the contracted DTRA work.

MODELS AND METHODS

I. Delayed Gamma Production

A. Neutron Induced Fission

Neutron induced fission can occur when a neutron (at essentially any energy) interacts with fissile material. For example, if a uranium-235 nucleus absorbs a neutron, the resulting compound nucleus quickly breaks into two primary fragments and releases ~200 MeV of energy. Most of the energy is kinetic with a large fraction (173 MeV) retained by the unstable primary fission fragments and resulting prompt neutrons. Prompt gamma-rays and neutinos make up another 16 MeV. The remaining 11 MeV of energy is distributed down the decay chain of fission fragment daughters in the form of beta particles and delayed gamma-rays produced from beta decay.

B. Photon Induced Fission

If an incident photon is energetic enough (> 5 MeV), it may also induce fission events in SNM through the process of photofission (Gallmeier, 2005, Haxby et al., 1941). This photonuclear course tends to be less efficient as the excited nucleus may undergo other de-excitation processes instead. If fission does occur, the result produces a family of prompt and delayed decay products considered nearly identical to that produced by neutron induced fission (Verbeke

et al., 2010). An incident photon energy of 14 MeV appears ideal (Figure 5). As an aside, a practical upper limit of 16 MeV may be considered due to the photonuclear reaction $O^{18}(\gamma,p)N^{17}$ that results in a neutron emission similar to that of the delayed neutron signature from SNM (Jones et al., 2007). Although not addressed here, it is conceivable that delayed neutron measurements will be included in any active interrogation method deployed.

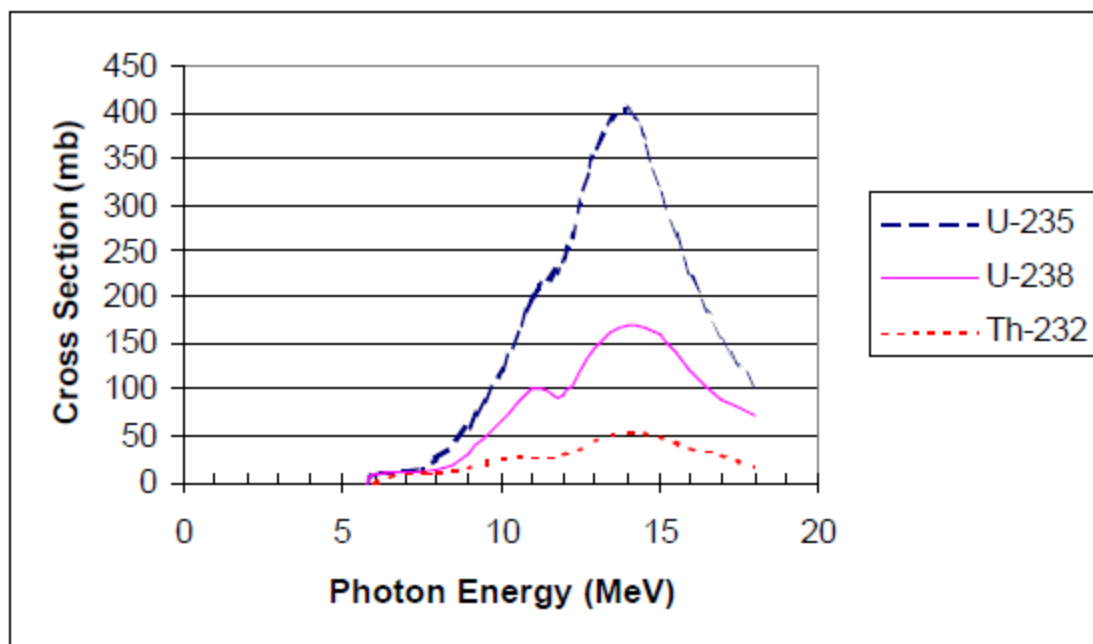
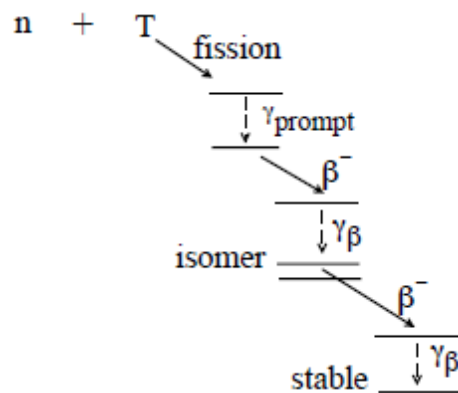


Figure 5. Photofission cross sections for uranium-235, uranium-238 and thorium-232. The largest cross sections are realized with photons at energies of ~14 MeV (from Jones et al., 2000).

C. Delayed Gamma Detection

The hallmarks for detection of irradiated uranium-235 and plutonium-239 are the creation of large numbers of beta-delayed gamma-rays ($E_\gamma \geq 3$ MeV) from fission product decay with a short effective half-life of ~ 25 seconds (Norman et al., 2004).



(from Pruet et al., 2005)

The method of detection is based on tallying the delayed gamma-ray emission ($E_\gamma = 3-7$ MeV) from fission product decay produced from concealed SNM. The measurements take place near the surface of the container over approximately 90 seconds post interrogation. A signal interface to indicate the SNM status of a container is required and should follow the same simple paradigm as that used for generic portal alarm monitors (Figure 6).



Figure 6. A remote alarm monitor unit used with pedestrian, vehicle and train portal monitors. The unit provides both audible and visual indications for gamma and neutron radiation alarms (from TSA, 2012).

D. Detection System Performance

Alarm threshold values may not be crisp, and would be determined partially through modeling (as proposed here), experimental testing and lessons learned from deployed systems. When added to the myriad of other sources of uncertainty that may be encountered (NORM, detector performance, operator error, etc.), the inevitable result is “false positive” and “false negative” outcomes. A “false positive” is defined as an indication by the instrument that a radioactive source is present when the source is not present; a “false negative” is defined as a lack of indication by the instrument to a radioactive source that is present (DNDO, 2011). With respect to SNM, false positives would trigger profound (and costly) emergency responses and one false negative could have catastrophic consequences (Aloise, 2009). Clearly, false signals should be minimized. Because dual-beam active interrogation research is in its infancy, initial markers for allowable false signal rates may be borrowed from an appropriate field. The Domestic Nuclear Detection Office’s (DNDO) now-defunct Cargo Advanced Automated Radiography System (CAARS) had an allowable false positive rate of 1 in 200 (0.5%) and an allowable false negative rate of 1 in 60 (1.67%) for detecting shielded 100 cc cubes of high atomic number elemental materials ($Z \geq 72$) (Quiter et al., 2008). Since the properties and dimensions of the CAARS objects of interest are similar to what is considered here, those rates will be adopted for this work.

II. Neutral Particle Interrogation

Active interrogation systems using neutral particles are intended for identification of concealed special nuclear material. If a neutron, or gamma-ray with a high enough energy, interacts with SNM and produces fission events, prompt and delayed neutrons and gamma-rays will be emitted (Figure 7). Fast neutron beams are adept at penetrating high Z substances such as iron, but scatter considerably in the presence of hydrogenous (low Z) material. Neutrons may also be significantly attenuated if there is a high degree of non-uniformity, or “clumpiness,” in the cargo regardless of the material (Pruet et al., 2005). These characteristics make it challenging to penetrate cargo, such as wood, to induce fission events using these neutrons. The creation of nuisance signatures dictates that neutron beam energies must be < 10 MeV, which also limits penetration (Slaughter et al., 2007b). On the other hand, any delayed gammas produced as a result of fission events are poorly attenuated and therefore easier to detect. The lack of attenuation can be exploited in reverse by generating a gamma-ray beam and using it to penetrate the cargo.

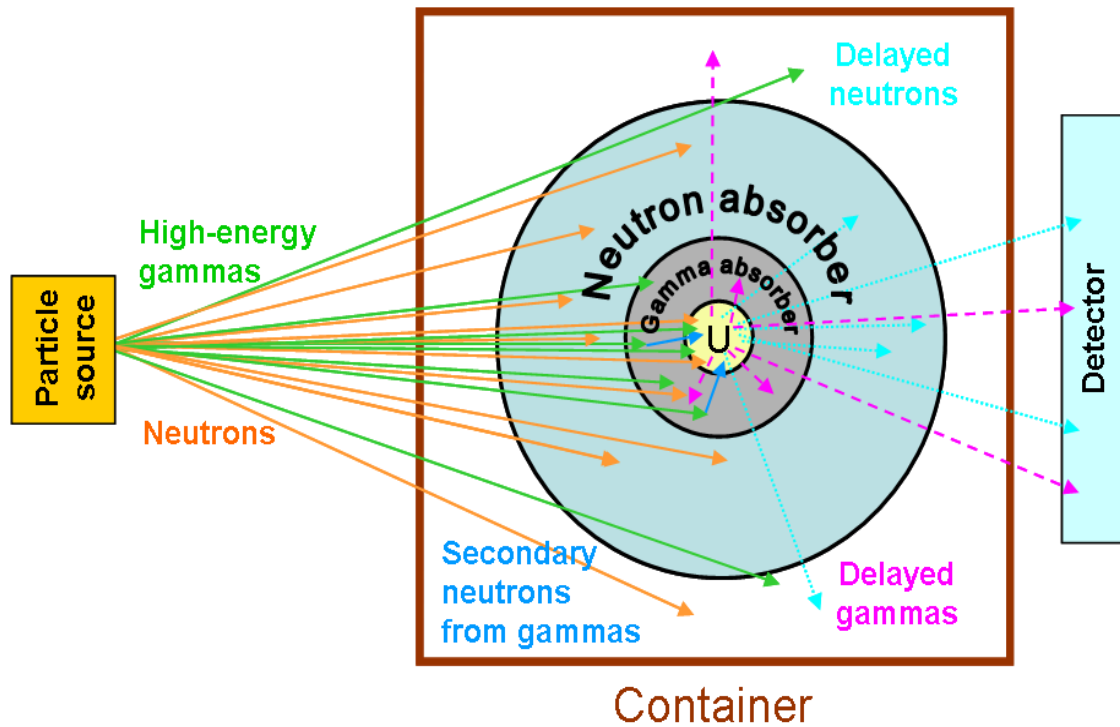


Figure 7. A neutral particle active interrogation system showing delayed particle production resulting from fission product decay alone (from de Oliveira et al., 2009).

An additional benefit of using a photon beam is that it is “mostly sensitive to average opacities” at the densities of interest, thereby providing an advantage over neutrons in penetration when non-uniform, or “clumpy,” cargos are encountered (Pruet et al., 2005). This technique also provides an avenue to penetrate low-Z engineered shielding such as polyethylene and creates essentially no interfering activation products.

III. Simulation Outline

A template adopted from Nelson & Sökkappa, 2008, is provided in Figure 8. To summarize, this research involves:

- an operational scenario examining sections of loaded intermodal shipping containers;
- modeling threat and nuisance (or noise) sources;
- addressing the ambient background range;
- the computational radiation transport of neutrons and photons;
- the tracking and detection of delayed gammas using a plastic scintillation detector and/or current tallies through a surface;
- the application of an alarm algorithm based on S/N ratio;
- establishing performance benchmarks based on industry standards.

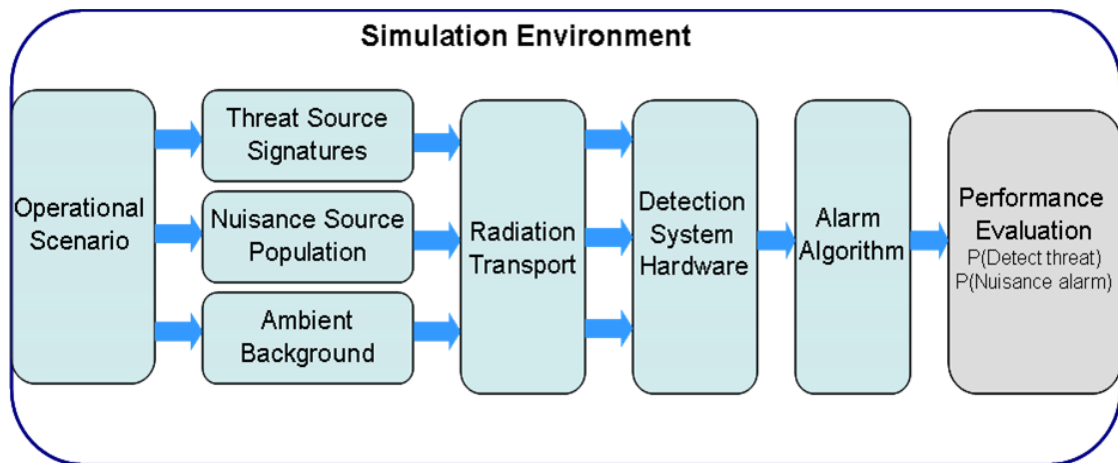


Figure 8. General components to define when simulating a detection system.
(from Nelson & Sökkappa, 2008).

The research addresses the components in Figure 8 as follows:

A. Operational Scenario

Surrogate models comprised of 0.4 TEU sections filled with a variety of homogenized materials at differing densities representative of those imported into the United States and subjected to interrogation by a neutron beam or neutron and photon beams simultaneously.

B. Threat Source Signature

An object requested by Rapiscan Systems of Torrance, CA to be fabricated by the Y-12 National Security Complex and referred to as Test Object “E” in a letter to the Nuclear Regulatory Commission (Shahabidin, 2011). The threat source is 600g of uranium oxide (U_3O_8) containing 100g of uranium-235 (19.75% enrichment). The object is in the shape of a puck that is 12.1 cm (4.75”) in diameter and 2.54 cm (1”) thick with a density of 2.05 g/cc.

C. Nuisance Source Population

The definition of the “nuisance source population” is better served by dividing those signals that are produced as a by-product of scission, but not of interest, as a “nuisance” and anything else as “noise.” Noise includes detector signals

registered by photons or facsimiles produced by neutron activation, cosmic rays, line voltage spikes, etc.

1. Nuisance

Thorium is one of the most prevalent passive NORM signatures encountered and is associated with shipments of building materials like cement, tiles and plasterboard (Kouzes et al., 2006, Sökkappa et al., 2009). Along with fission, photofission can also take place in thorium-232 with photon $E > 6$ MeV, thereby producing its own delayed gamma signature on interrogation (Haxby et al., 1941). A concentration of 240 Bq/kg of cargo (a mass fraction of $\sim 0.006\%$) represents a practical value for thorium-232 in these materials (Table 1). It is noteworthy to point out that, although radium-226 and potassium-40 have activities of the same magnitude as thorium, the physical mass of these isotopes is miniscule in comparison. The nuisance source model used here is clay ($\text{AlSi}_2\text{O}_5(\text{OH})_4$) doped with thorium-232 at 240 Bq/kg of cargo.

Table 1: Activity Concentrations of NORM in Building Materials (Bq/kg)*Source: IAEA 2003 Tech Report 419, pg. 104*

Material	Ra-226	Th-232	K-40
Concrete	1-250	1-190	5-1570
Aerated concrete	109818	<1-220	180-1600
Clay bricks	1-200	1-200	60-2000
Sand-lime bricks and sandstone	18415	10959	5-700
Natural building stones	1-500	1-310	767011
Natural gypsum	<1-70	<1-100	7-280
Cement	7-180	7-240	24-850
Tiles	30-200	20-200	160-1410
Phosphogypsum	4-700	19360	25-120
Blast furnace slag stone and cement	30-120	30-220	-

Activity concentrations (Bq/kg) of naturally occurring radioactive materials (NORM) in building materials. Reproduced from the World Nuclear Association (NORM, 2011).

2. Noise

There are a host of neutron activation products to avoid. Many are eliminated by selecting neutron interrogation energies below their respective activation energy thresholds or by delaying the start of counting by a few seconds post interrogation to limit or eliminate the impact of short-lived activation products (Table 2). At a neutron interrogation $E_n = 7$ MeV, only fluorine is of real concern as an interference source (Church et al., 2007a). A post interrogation delay of six seconds prior to the start of signal collection is incorporated based on past experimental work. In addition, there will be activation products created outside the cargo container by the interrogation process such as the portal structure or underlying pavement. These anomalous photon sources may be shielded to some extent, for example, by wrapping the detector(s) in thin lead sheeting. Actual values for noise would have to be measured using the deployed system (Nelson & Sokkappa, 2008). Therefore, a range of background noise from 10-10000 counts/sec in the $E = 3$ -5 MeV range is applied during post-processing to simulate system performance.

Table 2: Neutron Activation Products of Concern

Z	Target	(%)	Reaction	Threshold (MeV)	Product	Half-life (sec)
8	¹⁶ O	99.8	(n,p)	11	¹⁶ N	7.1
9	¹⁹ F	100	(n,α)	2	¹⁶ N	7.1
5	¹¹ B	80	(n,p)	11.8	¹¹ Be	13.8
14	³⁰ Si	3.1	(n,p)	8.3	³⁰ Al	3.68
7	¹⁵ N	0.37	(n,p)	10.1	¹⁵ C	2.45
12	²⁶ Mg	11	(n,p)	9	²⁶ Na	1.07
17	³⁷ Cl	24.2	(n,α)	6.97	³⁴ P	12.4
8	¹⁸ O	0.2	(n,α)	7.7	¹⁵ C	2.45
40	⁹⁶ Zr	2.8	(n,p)	7	⁹⁶ Y	9.6
20	⁴⁸ Ca	0.187	(n,γ)	0	⁴⁹ Ca	523.2
16	³⁴ S	4.2	(n,p)	4.7	³⁴ P	47
11	²³ Na	100	(n,α)	6	²⁰ F	11
24	⁵⁴ Cr	2.38	(n,p)	7.5	⁵⁴ V	49.8

Activation products of concern including incident neutron activation threshold energies (from Slaughter et al., 2007a).

D. Ambient Background

The maximum energy of terrestrial background radiation is 2.6 MeV (Slaughter et al., 2007b). This is below the delayed gamma energy of interest ($E_\gamma \geq 3$ MeV). There is measurable cosmic ray activity. Again, all of this passive background information would have to be empirically determined on site by counting so that it can be compensated for prior to interrogation (Nelson & Sökkappa, 2008).

E. Radiation Transport

Radiation transport is modeled with the solver MCNPX2.7.0 coupled to CINDER2008g using TINDER. MCNPX is a Monte Carlo radiation transport computer code that “transports nearly all particles at nearly all energies for nearly all applications” (Pelowitz et al., 2011, Pelowitz, 2011). CINDER is a transmutation code that uses Markovian chains to determine temporal densities of nuclides in a radiation environment. The program follows “all paths of nuclide transmutation,” defined as the conversion of a nuclide to a different nuclide by particle absorption and/or radioactive decay (Holloway et al., 2011, Wilson et al., 2007). CINDER2008g is a modified version (“g” for gamma) to include a photofission capability (Martin, 2012). TINDER is a generalized code for coupling transport solvers to CINDER with a substantial degree of automation (Id.). MCNPX, CINDER and TINDER are all written in the Fortran90 language. TINDER also utilizes Perl scripts as needed.

F. Detection System Hardware

Plastic scintillator modeled after the Eljen Technology EJ-200 as used by the “Nuclear Car Wash” (Hall et al., 2007a). The EJ-200 specification sheet is reproduced in Appendix F. Polyvinyltoluene (PVT) is the most common type of plastic scintillator material used in radiation portal monitors for screening vehicles. It is an environmentally robust and cost effective product for creating large cross sectional detection areas (Ely et al., 2006).

G. Alarm Algorithm

In the cases considered here, the alarm algorithm is based on some applicable form of signal-to-noise (S/N) ratio to identify photons in the energy range of 3-6 MeV. The photons of interest are born as decay chain by-products of fission events in SNM and constitute the “signal.” Photons or facsimiles resulting from activation of the cargo and its surroundings, cosmic ray interactions and anything else that would trigger a signal in the detection equipment in that energy window are considered “noise.” Measurements taken before interrogation constitute the passive background and may or may not contribute to the definition of noise. More precisely, depending on the active background produced by each cargo from neutron interrogation (empirically determined) threshold values for sensed delayed gamma-rays would specify a response of either detected (detectable), undetected (undetectable) or indeterminate based on the performance

requirement(s) for the detection system. It is important to note that, unlike passive background, active background cannot be measured and then simply subtracted, but rather takes on a complex role in defining the noise in any signal detection algorithm.

H. Performance Evaluation

What is desired is a set of performance requirements that any detection system must achieve in order to be considered successful in identifying the presence of a minimum quantity of SNM. These performance requirements are commonly defined using terms such as “false positive rate” and “rate of detection.” Ideally, a detection system would successfully identify the target quantity (or more) 100% of the time it is present, and never alarm when it is not. This is possibly achievable in a controlled environment, but not practically achievable at a container terminal.

This study should provide some insight for one critical question: What are the conditions for which a neutron beam alone is sufficient for interrogation? This is an important consideration as the ALARA (As Low As Reasonably Achievable) concept can be logically extended from personal exposure to the treatment of commercial cargo.

There will also be an attempt to incorporate DNDO-derived allowable false positive and negative rate targets ($\leq 0.5\%$ and $\leq 1.67\%$ respectively) for this simulated system in a meaningful way (Bjorkholm & Boeh, 2006). A generic figure-of-merit developed by LLNL and based on a generic receiver operating characteristic (ROC) curve for the rates above will be modified to incorporate signals produced from photofission (Slaughter et al., 2007b).

IV. Simulation Model

A. Basis

The fundamental design for these computational simulations is primarily based on previous models and conclusions from Moss et al., 2006, Slaughter et al., 2007a, and from work performed for DTRA at the University of New Mexico under Professor de Oliveira by Rodney Keith, Billy Martin and Elliot Leonard (de Oliveira et al., 2009).

B. Container

The container model is an 8' x 8' x 8' (244 cm x 244 cm x 244 cm) box with an inclusive 3/16" (4.76 mm) carbon steel wall (Moss et al., 2006). This is equivalent to 0.4 TEU and allows a full size container to be modeled in sections. This represents an accurate reproduction of what would actually occur in an interrogation portal as the entire container would probably not be surveyed, only

one or two sections of interest and not all at once. When combined with the imaging resolution now quickly and routinely obtained by current hardware, the distribution of cargo can be easily ascertained for possible homogenization and/or precise identification of a section or sections to interrogate. The method is not limited to shipping containers and could be used for any cuboidal (Figures 9 and 10).

Note that the carbon steel wall in the model is unrealistically thick due of its mass; this is to compensate for particle attenuation by insulation and/or interior walls found in actual containers. Steel dry cargo shipping containers have outer wall thicknesses of 1.6mm to 2 mm ($1/16''$ - $5/64''$) (Steinecker, 2010).

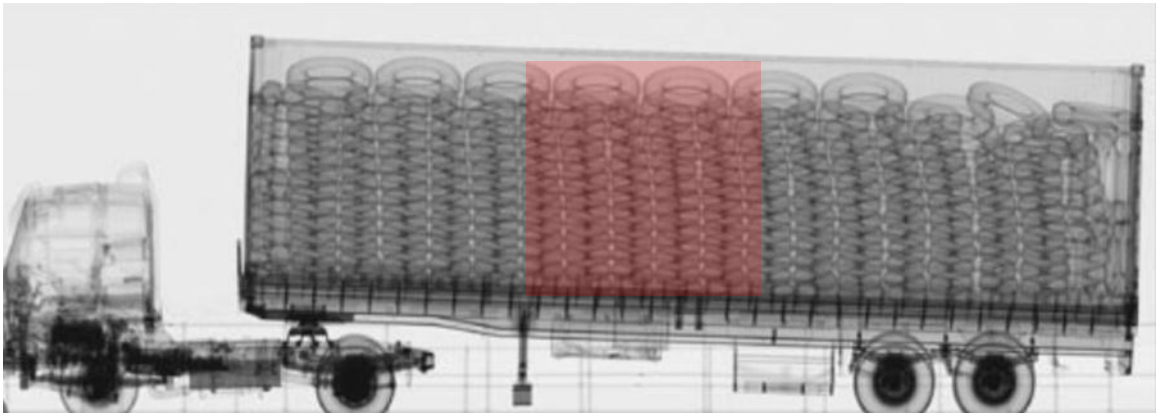


Figure 9. Dry freight trailer loaded with tires (quasi-homogeneous). The resolution observed here is more than adequate for the purposes of sectioning (red area) and homogenization (from Stevenson, 2005).

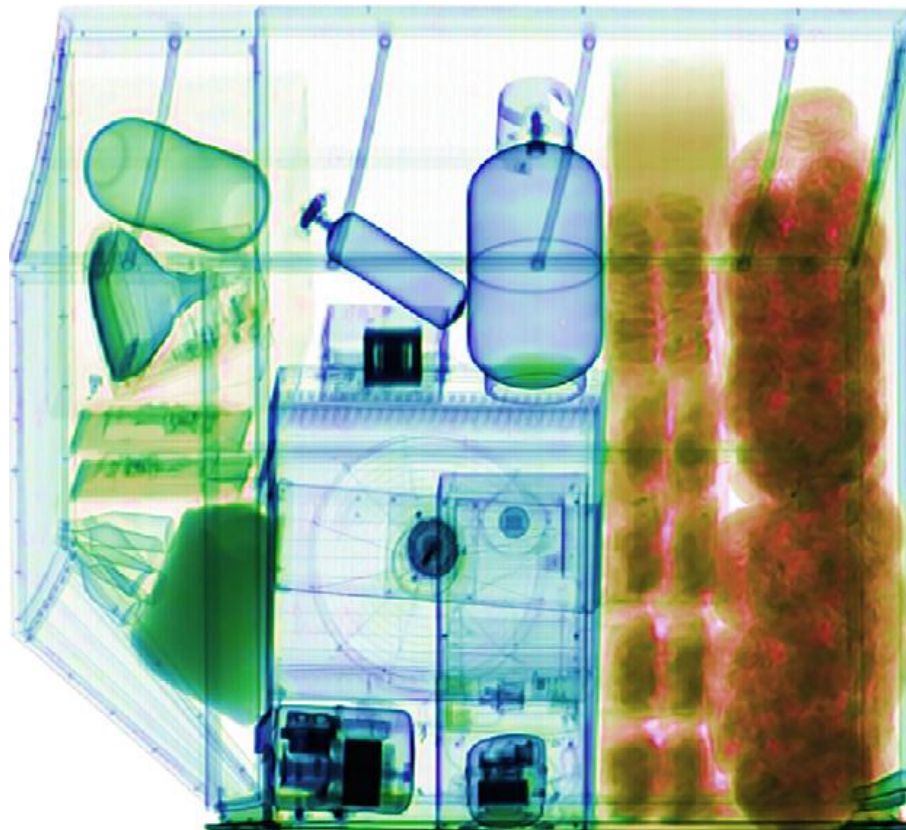


Figure 10. Combined neutron and x-ray image of an aluminum unit load device (ULD) used for air cargo (~ 5' x 5' x 5'). This ULD contains computer monitors, a vase, bottles, and a sack of chemicals (left), air conditioners and gas cylinders (middle), and vegetables (right) (from Buffler & Tickner, 2010 and Cutmore et al., 2010).

C. Surrogate Cargo

Surrogate cargoes have been selected that initially span three classes of average atomic numbers (Z) and densities (g/cc) associated with importations. The surrogates are homogenized representations. These cargo classes are in part based on the Z recommendations of Slaughter et al., 2007a, and the key density distributions were obtained through manifests analyzed by Descalle et al., 2006 (Figure 11).

Homogenized surrogate cargos are composed of Low, Medium or High Z materials:

- Low = Celotex® (cellulose, wood fiberboard), $C_6H_{10}O_5$ per LANL
- Medium = aluminum, Al
- Medium = clay, $AlSi_2O_5(OH)_4$ (also used in the NORM investigation)
- High = iron, Fe
- Very High = tungsten, W (current only)

The surrogates are evaluated at several densities, with the following Low, Medium, High and Very High densities being the initial placeholders (refer to Figure 11):

- Low = 0.10 g/cc (most prevalent)
- Medium = 0.30 g/cc (80% of all cargo falls below this figure)
- High = 0.50 g/cc
- Very High = 0.60 g/cc ("most challenging," Slaughter, et al., 2007a)

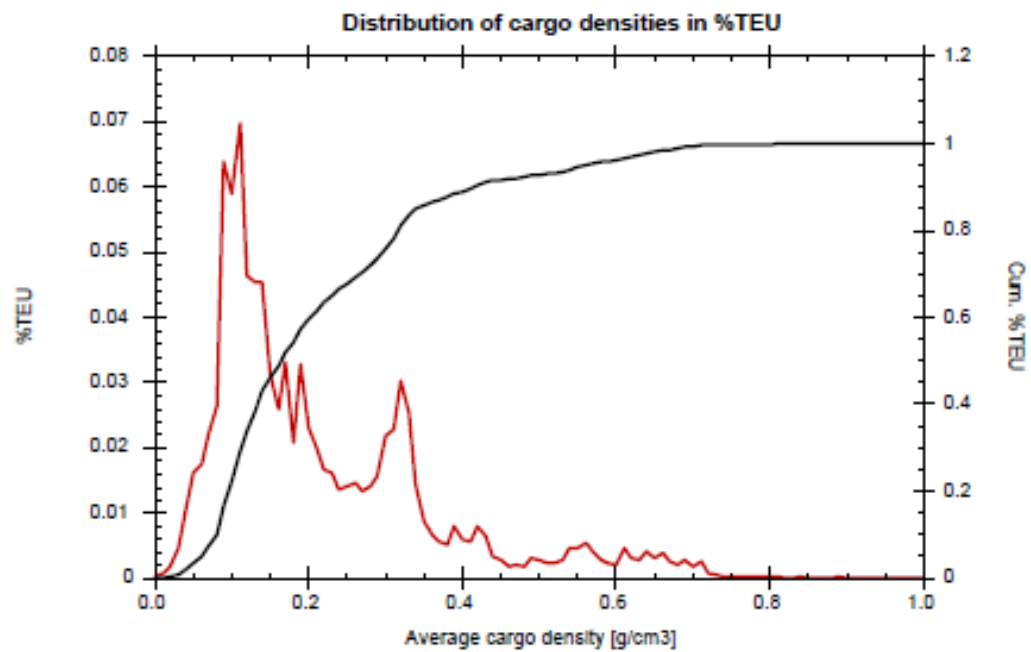


Figure 11. Distribution of average cargo density collected via shipping manifests on 14 days distributed over 12 months (from Descalle et al., 2006).

Three other densities of interest:

- Maximum (20 ft container) = 0.65 g/cc (theoretical load maximum)
- Maximum (40 ft container) = 0.40 g/cc (theoretical load maximum)
- Average = 0.20 g/cc (cargo average)
- Very Low = 0.05 g/cc (for consistency)

There is also an “empty container” model that is filled with air at the International Standard Atmosphere (ISA), 0.001275 g/cc at sea level and 15°C. A series was also done with tungsten, representing a very high Z material.

D. Threat Target

The threat target is 600g of uranium oxide (U_3O_8) containing 100g of uranium-235 (19.75% enrichment) and approved by the DNDO (Shahabidin, 2011). The object is in the shape of a puck that is 12.1 cm (4.75”) in diameter and 2.54 cm (1”) thick with a density of 2.05 g/cc.

E. Nuisance Signal

The nuisance signal is produced by the fission of thorium-232 at a concentration of 240 Bq/kg in the homogenized clay matrix. This was achieved in the model by replacing an equivalent mass of oxygen (~0.01%) with thorium in the clay matrix for each homogenized density.

F. Noise Target

The noise target is 600g of polytetrafluoroethylene (Teflon® PTFE). The object is in the shape of a puck that is 12.1 cm (4.75”) in diameter and 2.54 cm (1”) thick with a density of 2.05 g/cc. The dimensions are identical to the threat target. The nominal density of PTFE is 2.15 g/cc (DuPont, 2012).

G. Fundamental Model

A visualization of the fundamental model with a detector (described below) is provided in Figure 12. A deployed system would place detectors on more than one face with a stand-off of a few centimeters and neutral particle beams (described below) may not enter from the same face.

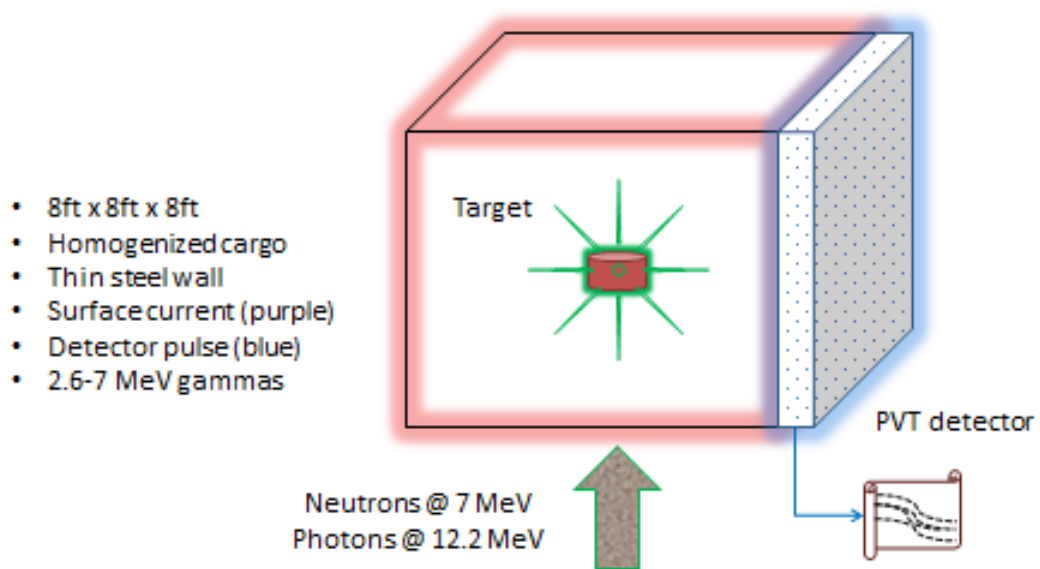


Figure 12. The fundamental model with PVT detector (not to scale).

H. Neutral Particle Beams

A neutron and a photon beam are employed for this study. The beams are modeled as monodirectional disk sources on the surface of the container, radiating inward, with a diameter equal to the targets (12.1 cm). The 7 MeV neutron beam energy is based on findings from the “Nuclear Car Wash” experiments (Slaughter et al., 2007b, Hall et al., 2007). This neutron beam was selected because it is attainable and at a low enough energy (< 10 MeV) to avoid creating strong activation backgrounds from common low-Z materials, particularly the $^{16}\text{O} (n,p) ^{16}\text{N}$ reaction, but still energetic enough to adequately penetrate cargo (Gozani, 2009). A visual representation of neutron beam interaction in the challenging Celotex matrix is provided in Figure 13. The uranium oxide target can be seen clearly in the center of each image.

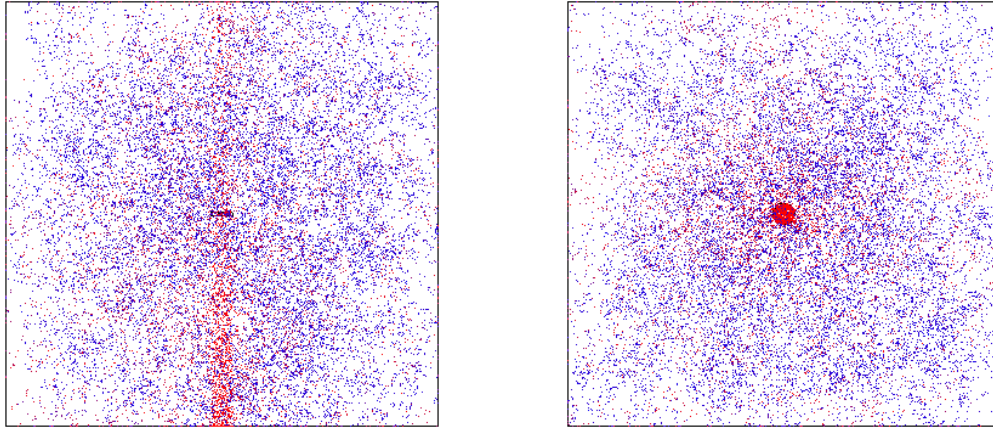


Figure 13. A 7 MeV penetrating neutron beam interacting in the Celotex cargo surrogate model ($\rho = 0.1$ g/cc). The image on the left shows the beam entering from the bottom; the viewpoint on the right is from above looking down. The U_3O_8 target can be seen clearly in the center of each image. A total of 1000 neutrons were injected. The colors reflect subjective collision event energies with red being “high” and blue being “low.”

The gamma-ray beam energy of 12.2 MeV was selected from a scoping study because it was attainable and well within the energy range to induce photofission in SNM (Moss et al., 2006). A visual representation of photon beam penetration is provided in Figure 14. The images in Figures 13 and 14 were produced using the MCNPX visual editor program Vised24E (Schwarz et al., 2011).

The efficacies of both neutral particle beams in a simulation environment were confirmed using strengths of 2×10^8 particles/sec each (Martin, 2012). The beam strengths used for these simulations are 5×10^8 particles/sec each on the model surface (115 cm^2 spot = 4.35×10^6 particles/ cm^2/sec) and reflect the lower bound of what would be expected for a working interrogation portal.

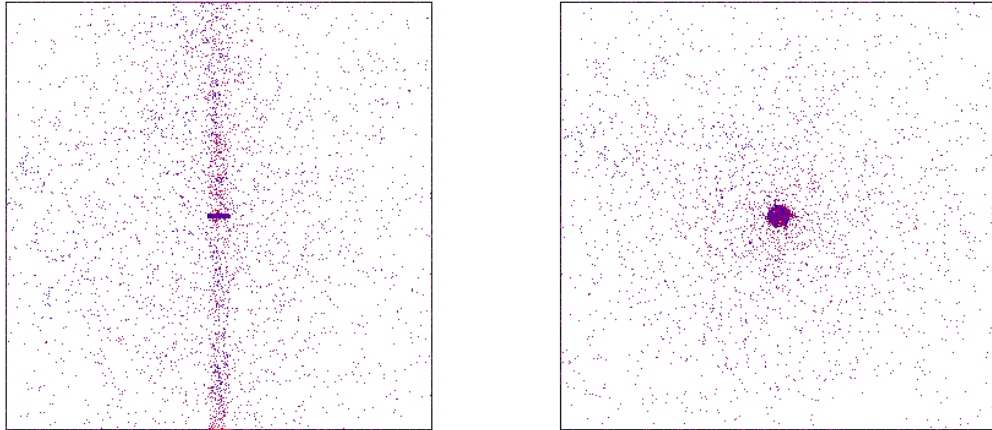


Figure 14. A 12.2 MeV penetrating gamma-ray beam interacting in the celotex cargo surrogate model (0.1 g/cc). The shot on the left shows the beam entering from the bottom; the viewpoint on the right is from above looking down. The U_3O_8 target can be seen clearly in the center of each image. A total of 1000 photons were injected. The colors reflect subjective collision event energies with red being “high” and blue being “low.”

I. Detector

The detector is modeled after the EJ-200 Plastic Scintillator and is composed of polyvinyltoluene (PVT) with physical dimensions (L x W x H) of 96" x 10" x 96" (244 cm x 25.4 cm x 244 cm) and a density of 1.023 g/cc. Details from the manufacturer, Eljen Technology, can be found in Appendix F. Gaussian energy broadening was applied in the detector model using $FWHM = 0.35$ MeV (see Results chapter). The detection response was examined using monoenergetic photons in the delayed gamma range energy of interest ($E_\gamma = 3\text{-}6$ MeV) independently by isotropic broadcast from the center of the fundamental model in the presence of air at ISA. Simulated detector response to monoenergetic photon sources of $E = 3, 4, 5$ and 6 MeV are plotted together in Figure 15.

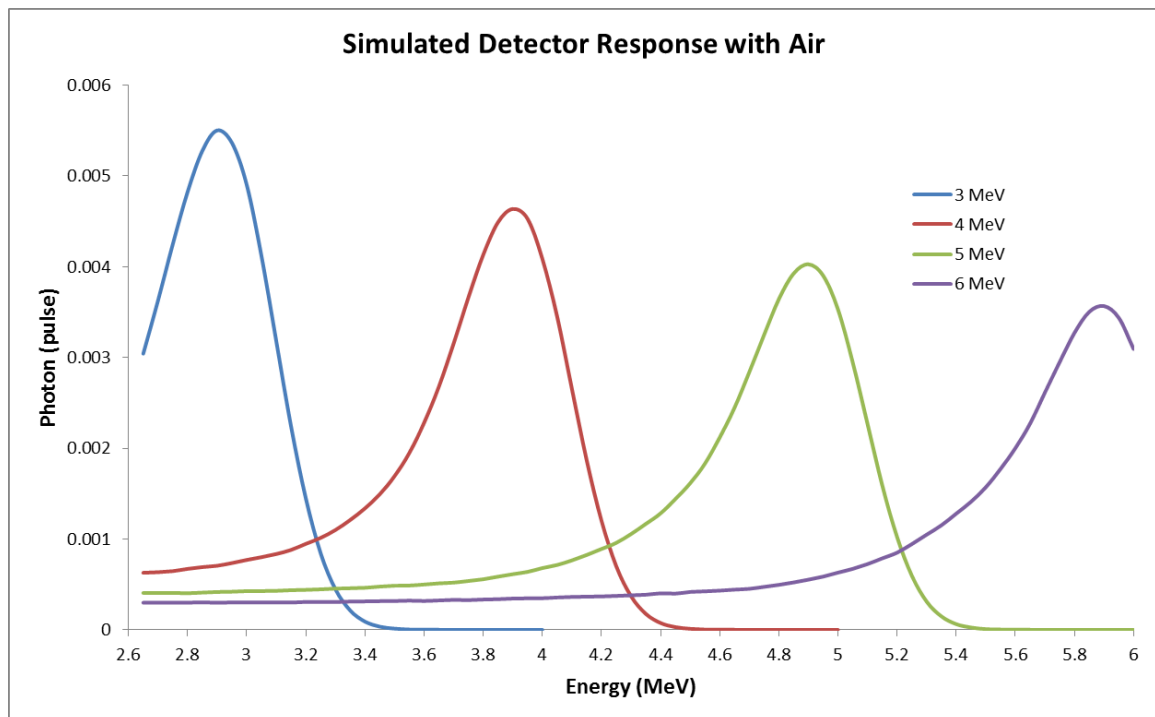


Figure 15. Response to independent monoenergetic photons of 3, 4, 5 and 6 MeV isotropically broadcast from the center of the surrogate model filled with air at ISA.

J. Detection Figure-of-Merit

1. Definition

A figure-of-merit was appropriated from the “Nuclear Car Wash” to judge the performance of a detection system utilizing dual-beam interrogation and delayed gamma-ray measurement (Slaughter et al., 2007a; 2007b). The figure-of-merit (F_s) statistic is rephrased here to indicate delayed gamma signals as a result of neutron-induced fission and photofission separately as well:

$$F_s = \frac{S}{\sigma} \text{ or } \frac{S_n + S_p}{\sigma}$$

with,

$$\sigma \approx 2\sqrt{S + 2B} \text{ or } 2\sqrt{S_n + S_p + 2B}$$

where,

S = delayed gamma signal (3-6 MeV) from interrogation

S_n = delayed gamma signal (3-6 MeV) from neutron interrogation

S_p = delayed gamma signal (3-6 MeV) from photon interrogation

B = mean background (3-5 MeV) captured by late counting (> 85 sec)

σ = expression for standard deviation term

This approximate value of σ was proposed by Slaughter as a “rule-of-thumb” to reasonably bound variations in the background count from a plethora of sources including detection system drift, repeated activation of the environment and

diurnal changes in the cosmic ray flux. This makes the figure-of-merit calculation considerably more conservative and unavoidable with regard to computational modeling due to the inability to make the empirical measurements necessary to determine σ directly. Therefore this “rule-of-thumb” is applied here for estimating F_s . If systematic variations are found to be small through experiment, improved nuclear data, or uncertainty analyses then the factor of two can be reduced (or ideally eliminated) and the standard deviation term would approach that for a Poisson distribution:

$$\sigma = \sqrt{S + 2B}$$

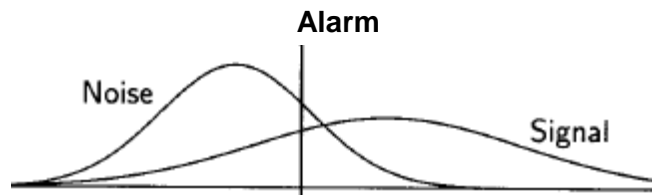
Note that the measurement of B is over a narrower energy range, $E = 3\text{-}5$ MeV, rather than the signal range $E_\gamma = 3\text{-}6$ MeV. The general background contribution at $E > 5$ MeV is insignificant (Luu et al., 2007). Truncating the energy range also eliminates the possibly large B -skewing spike in ~ 6 MeV photons resulting from fluorine activation. Lastly, if the signals are considered separately (i.e. $S = S_n + S_p$) the additional signal produced by the photon beam (S_p) should have a disproportionate impact on F_s as there would be little, if any, contribution to B for a deployed system.

The primary time integrated signal(s) and active background (essentially zero for the homogenized materials used here) for the calculation of F_s are determined

over the period of 7-40 seconds post-irradiation (34 seconds total). The F_s threshold value for reliable system operation is based on DNDO performance requirements of a maximum false negative rate of 1.67% and 0.5% maximum false positive rate and determined by examining a set of relevant receiver operating characteristic curves.

2. Application

Slaughter constructed generic receiver operating characteristic (ROC) curves using Gaussian assumptions for signal and noise shapes with the probability of detection (P_d) and probability of false positive (P_{fp}) defined as:



$$P_d = \frac{1}{2} \left[1 + \operatorname{erf} \left(\frac{F_s + F_b - \frac{L}{\sigma}}{\sqrt{2}} \right) \right]$$

$$P_{fp} = \frac{1}{2} \left[1 + \operatorname{erf} \left(\frac{\frac{L}{\sigma} - F_b}{\sqrt{2}} \right) \right]$$

with,

$$Fs = \frac{S}{\sigma}$$

$$Fb = \frac{B}{\sigma}$$

and,

$$\sigma = \sqrt{S + 2B}$$

where,

Fs = figure-of-merit

Fb = background factor

S = delayed gamma signal from interrogation

B = mean background (noise)

L = alarm threshold

σ = standard deviation

The ROC curves (Fs) represent these probabilities as a function of L as shown in Figures 16 and 17. Examination of these plots together reveal a broad range in error rates for $Fs = 1$ to $Fs = 7$. As an aside, it was found that “large variations in Fb have no observable effect on error rates;” in other words, the ROC curves look essentially the same regardless of the background factor (Slaughter et al., 2007b). Tracing the curve for $Fs = 5$ to the minimum detection probability (Pd) of 98.33%, the corresponding false positive rate (Pfp) is < 0.5% and the DNDO

performance requirements are met. In other words, the system is predicted to perform as designed against any cargo threats where the detected delayed gamma-ray signal exceeds the mean background rate by five standard deviations as defined. An example of declining, but possibly acceptable, system performance can be illustrated by tracing $F_s = 3$, where $P_d = 95\%$ yields a false positive rate of nearly 10%. If examination frequency is suitably low, the high number of false alarms may be tolerable. To summarize:

- $F_s \geq 5$, good system performance (meets DNDO goals)
- $5 > F_s > 2$, declining system performance (increasing false alarm rates)
- $F_s \leq 2$, poor system performance (unreliable)

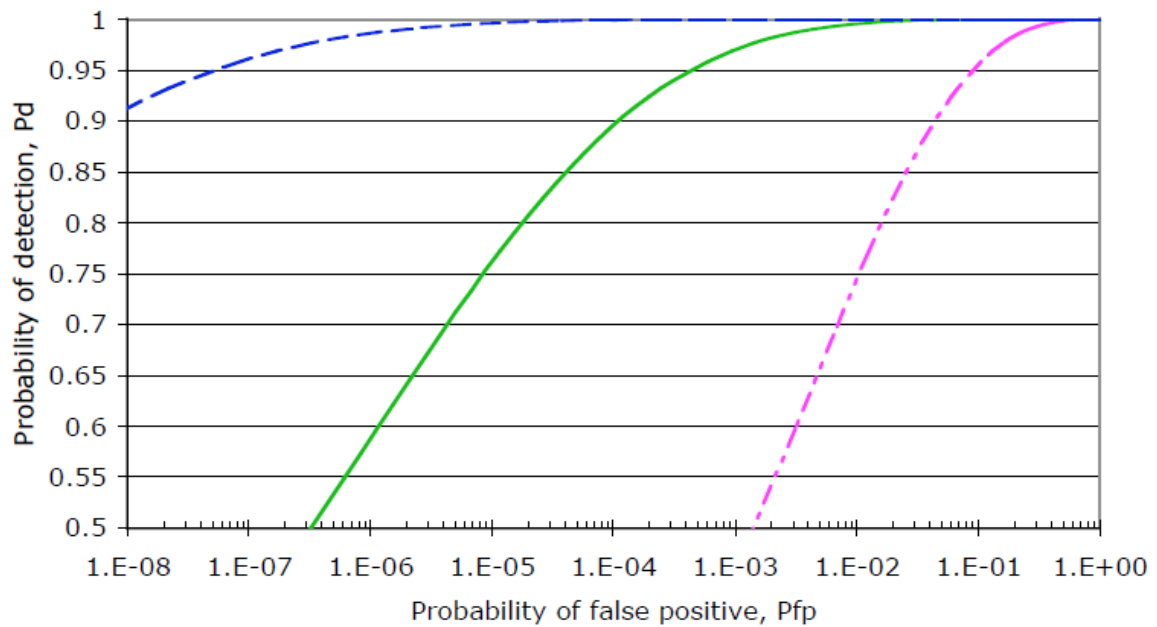


Figure 16. Generic ROC curves for $F_s = 3$ (pink), $F_s = 5$ (green) and $F_s = 7$ (blue). With $F_s = 5$ at the minimum detection probability (P_d) of 0.9833, the false positive rate (P_{fp}) is < 0.005 and the DNDO performance requirements are met (adapted from Prussin et al., 2005).

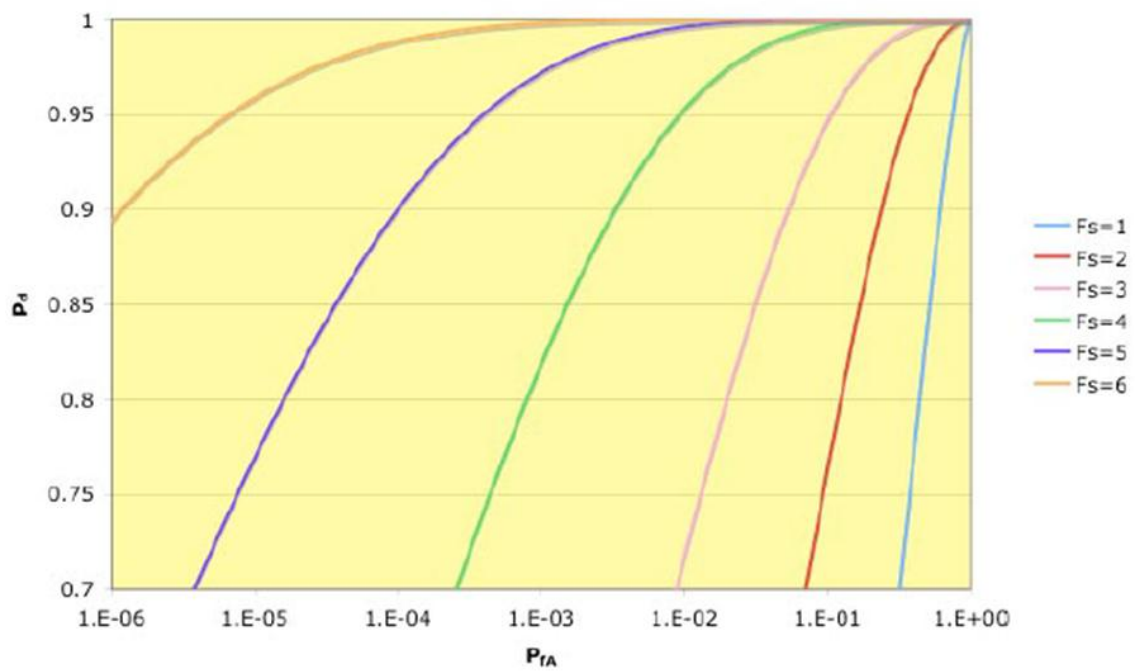


Figure 17. Generic ROC curves for $F_s = 1$ to 6. The goal set for the “Nuclear Car Wash” was a minimum detection probability (P_d) of 0.95 and a false alarm rate (P_{fa}) of 0.001. This performance is achieved with $F_s = 5$ as well (“ROC curve for $F_b = 10$ ” from Slaughter et al., 2007b).

V. Simulation Flow

Experimental sampling is performed on surrogate models with the radiation transport code MCNPX2.7.0 coupled to the transmutation code CINDER2008g using the generalized wrapper TINDER. The TINDER wrapper controls the process by initially calling MCNPX twice to transport interrogating beams of neutrons or photons to the target. The resulting neutron and photon fluxes created in the target cell from neutron and photon induced fission events are added and supplied to CINDER for the first transmutation time step. The delayed gammas produced in the target are then transported out using MCNPX again. The CINDER-MCNPX process is repeated for as many time steps as specified. Two text files are created and continuously updated from the standard voluminous output produced with every user-defined time step calculation. One file contains the energy binned instantaneous delayed gamma tally crossing one surface of the surrogate container cube (MCNPX “F1” tally). The other file contains the energy binned instantaneous pulse height tally created from delayed gamma-ray interaction within the PVT detector (MCNPX “F8” pulse height tally). The detector is adjacent to the F1-tallied surface to provide a coarse estimate of its efficiency. Both tallies are multiplied by the CINDER-derived total number of gamma-rays created, based on the original particle flux at the target, to produce a notional count. The flow of the simulation is presented in Figure 18.

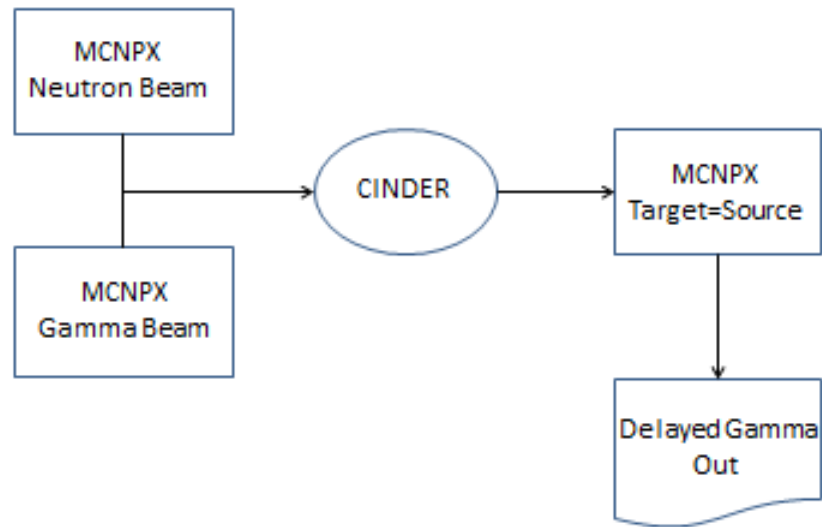


Figure 18. The flow of the simulation. The TINDER wrapper controls the entire process by initially calling MCNPX twice to transport each interrogating beam to the target. The resulting target cell fluxes are added and CINDER is called for the first time step. The delayed gammas produced in the target are then transported out using MCNPX. The CINDER-MCNPX process is repeated for as many time steps as specified by the user.

A. Time Scales

In the fundamental model, particle beam(s) are switched on for 30 seconds (“interrogating”). The beam(s) are switched off, and tallying for effect begins six seconds later; this would allow a large quantity of low energy photons (< 3 MeV) from short-lived activation products to die away in a deployed system. Fission products have decay times ranging from 5–150 seconds (Slaughter et al., 2004). Instantaneous tallies are recorded immediately after irradiation (time zero) and at one-second intervals starting with six and ending with ten seconds post-irradiation. Subsequent steps are taken in five second intervals out to 100 seconds post-irradiation (only 40 seconds post-irradiation with the detector present). Time steps are user-defined; the schedule here is based on the “Nuclear Car Wash” experiments and is sufficient for this work. Time-integration of the delayed gammas is easily accomplished using Microsoft Works 9.0 Spreadsheet to achieve the final energy binned result.

B. Delayed Gamma Current Tally

All delayed gamma-rays created up to $E_\gamma = 30$ MeV are tracked and transported through the back end (CINDER-MCNPX) of the code suite. The instantaneous delayed gamma current tally produced in the final output of the simulation is expressed in five bins: < 2.6 MeV, 2.6-3 MeV, 3-4 MeV, 4-5 MeV, 5-6 MeV, 6-7 MeV and > 7 MeV. The energy bins are defined by the user; this level of fidelity is

more than sufficient. The delayed gammas of interest for detecting SNM are captured in the three bins that define a 3-6 MeV window. The narrow window extends a reasonable degree of conservatism to any ultimate finding.

C. Delayed Gamma Pulse Height Tally

All delayed gammas created up to $E_\gamma = 30$ MeV are tracked and transported through the back end (CINDER-MCNPX) of the code suite. The instantaneous delayed gamma pulse height tally produced in the final output of the simulation is expressed in 99 uniform energy bins (50 KeV width) from 2-7 MeV. The energy bins are defined by the user; this level of fidelity is more than sufficient. The delayed gammas of interest for detecting SNM are captured in the bins that define a 3-6 MeV window. There are comparatively few events above $E_\gamma = 6$ MeV and narrowing the window at a deployed interrogation portal would help eliminate spurious signals, for example, from cosmic rays. Note that the binning reported extends down to $E_\gamma = 2.6$ MeV for contemplation and it may prove useful in the future for looking only at photon beam interrogation results.

D. Computing Systems

Code suite simulations related to delayed gamma current determinations alone (the fundamental model without the PVT detector) were performed on a Toshiba Satellite A505 laptop computer with 4 GB of RAM and an Intel Core 2 Duo CPU

(2 x 2.20 GHz) running the Windows 7 (64-bit) operating system. A PNY SDHC flash card (16 GB, Class 10) was employed to host the primary working directory for each sampling experiment as the ultimate file size was ~1 GB.

Simulations including the PVT detector are computationally more expensive and were performed on a Dell Precision T5500 desktop computer with 24 GB of RAM and an Intel Xeon X5550 CPU (8 x 2.66 GHz) running the Red Hat Enterprise Linux Version 6.3 (64-bit) operating system. This allowed MCNPX to be executed in parallel (MPI) and reduced the wall clock time required to produce statistically significant pulse height tallies. The CINDER code has not been parallelized as yet, but consumes an insignificant amount of CPU time during its execution (on the order of seconds) for the type of problems considered here.

RESULTS

I. Anticipated Outcomes

Interrogating a homogenized section of a suspect shipping container with both neutron and photon beams at the appropriate energies should:

- Yield an increased delayed gamma signal, if SNM is encountered, over a neutron beam alone.
- Extend the system performance envelope in the presence of background noise for any given cargo by increasing the delayed gamma signal from SNM.
- Further reduce the amount of prior information needed about the makeup of the cargo without compromising the interrogation result.

II. Trial Simulations

Several trial simulations of the fundamental model using plutonium or 95% enriched uranium spheres in Celotex were run to get an idea of the delayed gamma production in significant quantities of ideal threat materials. These studies did not include a detector. Neutron transport was initially accomplished using 2×10^6 histories for neutron transport and all photon transport (interrogating beam and subsequent delayed gamma-rays) set at 1×10^7 histories. No variance reduction techniques were applied.

Figures 19 and 20 demonstrate simulations of instantaneous delayed gamma emission over 100 seconds (1.67 minutes) induced by dual-beam interrogation of a large spheres of uranium (8 cm) or plutonium (10 cm) in Celotex ($\rho = 0.4$ g/cc, maximum for a 40' container). The top two time points in the chart legends, 0.000 seconds (blue) and 30.000 seconds (red), denote the gamma-ray emission due to natural decay and immediately following interrogation respectively. Figure 19 shows the instantaneous delayed gamma ($E_\gamma = 3-6$ MeV) emission rate 6-100 seconds post-irradiation from the uranium sphere alone after a 30 second interrogation with 7 MeV neutron and 12.2 MeV photon beams. The emission rate ($E_\gamma = 3-7$ MeV) for the plutonium sphere is provided in Figure 20 under identical circumstances. Beam strengths for both cases remained the same (5×10^8 particles/sec) with the spot sizes on the surrogate surface equaling the diameter of the spheres. The magnitudes of the delayed gamma rates from each target alone strongly imply that 1) neither target would represent much of an identification challenge, and 2) plutonium is less challenging to detect than uranium. Both of these observations tend to support the general industry consensus, particularly with regard to plutonium.

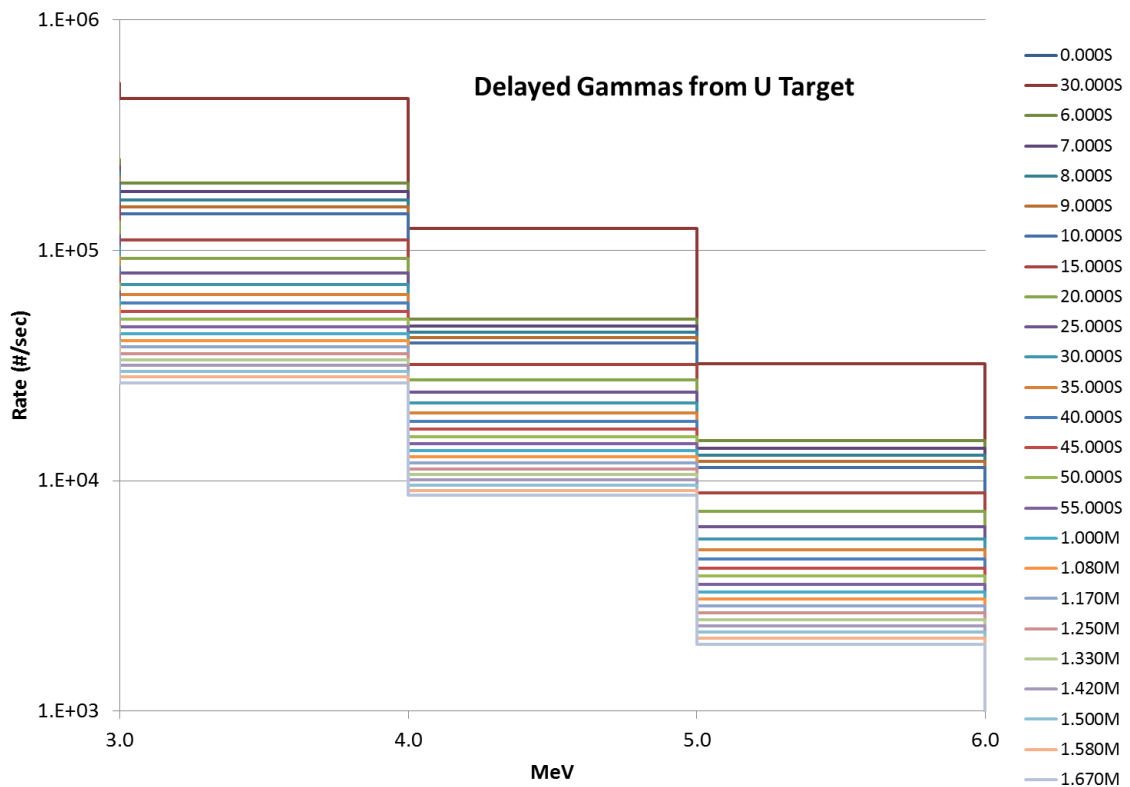


Figure 19. Instantaneous delayed gamma emission ($E_\gamma = 3\text{-}6$ MeV) rate 6-100 seconds post-irradiation from target alone after 30 second interrogation with 7 MeV neutron and 12.2 MeV photon beams. 95% enriched uranium sphere ($d=8$ cm, 5 kg) in a cube of homogenized Celotex at a density of 0.4 g/cc.

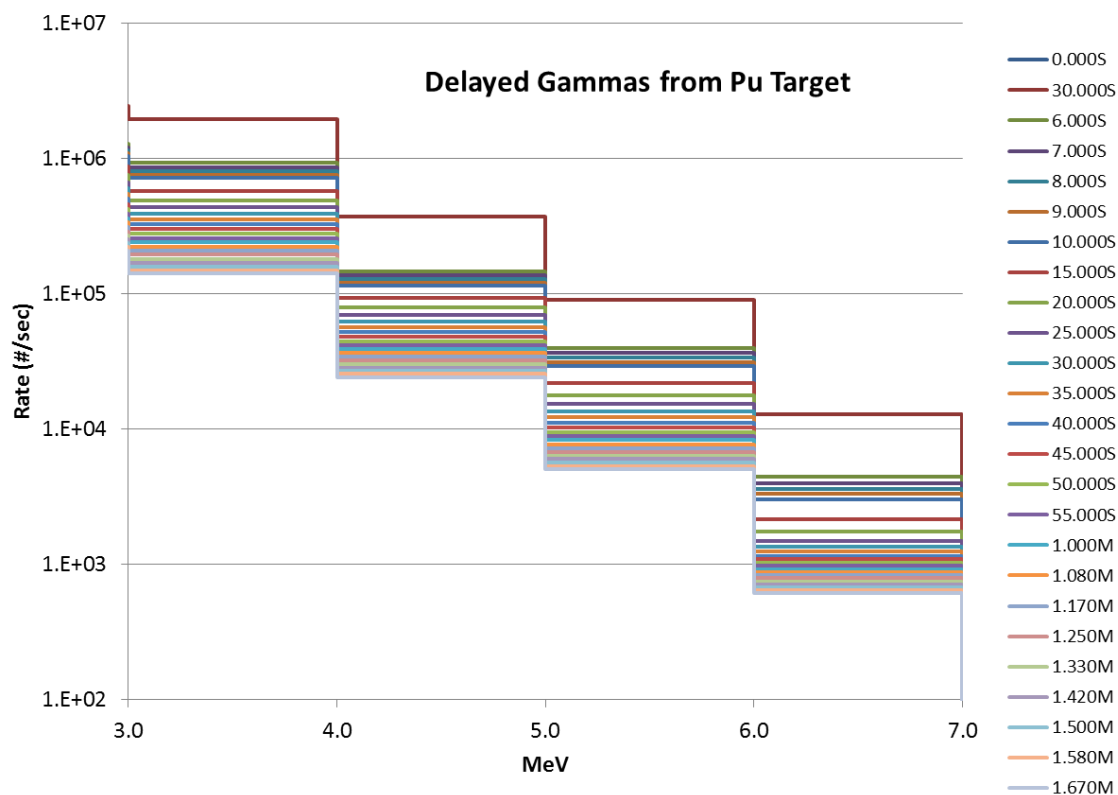


Figure 20. Instantaneous delayed gamma emission ($E_\gamma = 3\text{-}7$ MeV) rate 6-100 seconds post-irradiation from target alone after 30 second interrogation with 7 MeV neutron and 12.2 MeV photon beams. Plutonium-239 sphere ($d=10$ cm, 8.27 kg) in a cube of homogenized Celotex at a density of 0.4 g/cc.

Figure 21 describes the binned cumulative delayed gamma emission current ($E_\gamma = 3\text{-}6\text{ MeV}$) from the same plutonium sphere exiting one side of the cube over 94 seconds of counting ($T + 7$ to 100 seconds post-interrogation). This indicates that nearly one million delayed gamma-rays would be available for detection after passing through a comparatively dense matrix.

These simulations were the only experiments conducted using plutonium. Plutonium and highly enriched uranium (HEU) are difficult to acquire legally, much less illegally. One of the key reasons why only a uranium target of low enrichment was considered for this research is because kilogram quantities of oxides are obtainable for physical testing (Shahabidin, 2011). Enrichment is also largely unimportant from the standpoint of active interrogation because only the mass of fissionable material illuminated by the beam matters (Slaughter et al., 2007a). Finally, unescorted smuggling of plutonium or HEU through avenues of transport subject to routine inspection (ship, train, plane or truck) is highly unlikely because of the value of the material. Instead, meaningful quantities can and have been transported in person (Smalling, 2004).

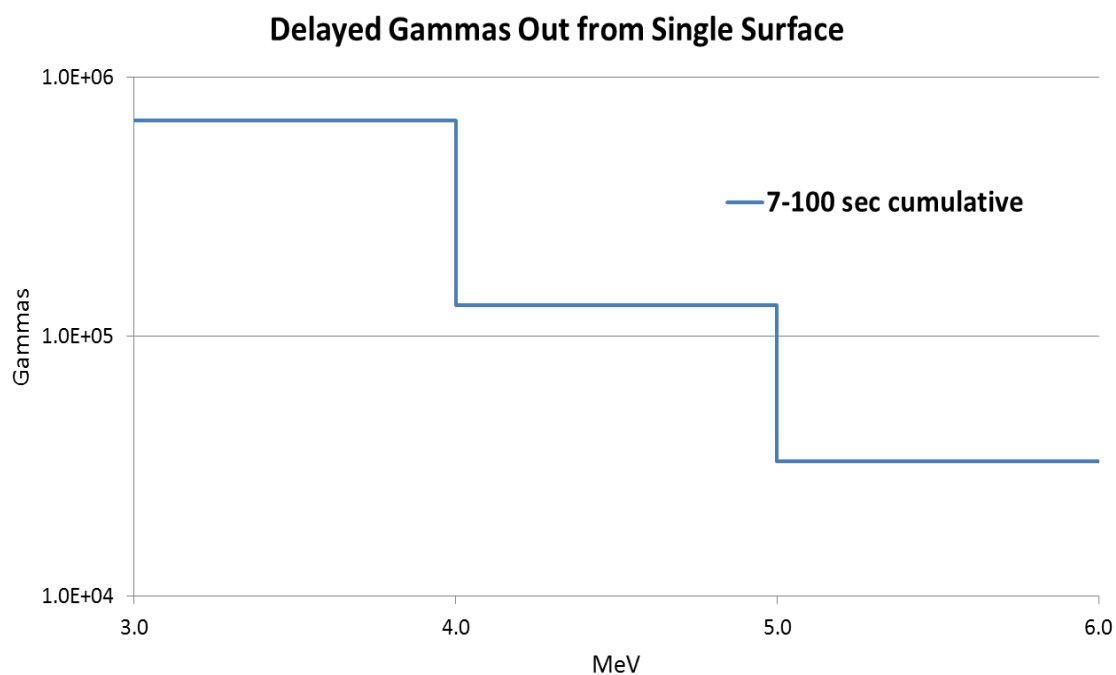


Figure 21. Cumulative (7-100 seconds post-irradiation) delayed gamma emission ($E_\gamma = 3-6$ MeV) through one vertical side of surrogate container cube after 30 second interrogation with 7 MeV neutron and 12.2 MeV photon beams. Plutonium-239 sphere ($d=10$ cm, 8.27 kg) in homogenized Celotex at a density of 0.4 g/cc.

III. Delayed Gamma Current Results

Cubes of homogeneous materials with the Rapiscan-derived target embedded at the center were interrogated with a single neutron beam, or a neutron and photon beam simultaneously. The resulting cumulative delayed gamma emissions ($E_\gamma = 3\text{-}6\text{ MeV}$) exiting one vertical side of the cube were plotted against increasing density from 48 sampling experiments (16 per material). The results are presented in Figures 22-24 for Celotex, aluminum, and iron, respectively. These three materials represent a foundation for studies in active interrogation as they reflect the key Z values (atomic number) for typical cargos, with Celotex considered a low Z material ($Z_{\text{avg}} \approx 4$), aluminum an intermediate ($Z = 13$), and iron a high Z material ($Z = 26$).

These investigations were carried out with Monte Carlo neutron transport set at 256×10^3 histories and all photon transport (interrogating beam and subsequent delayed gamma-ray re-transport) set at 640×10^3 histories. These parameters produced statistically germane flux and current tallies in a timely manner.

Two more interrogation experiments were conducted on a model of an empty box containing only air (density = 0.001275 g/cc) and the threat target to provide a maximum gamma-ray current value. The resulting yields of 527×10^3 delayed gammas for the neutron beam alone and 618×10^3 delayed gammas using both

beams are plotted on each figure as a purple triangle and a green square, respectively, straddling the y-axis.

Finally, a series of simulations were done using tungsten and clay. Tungsten represents a very high Z material ($Z = 74$) that may be encountered infrequently. Tungsten is employed as radiation shielding in both commercial and naval nuclear power, for example, as blankets and vests composed of tungsten/polymer blends like those sent to Fukushima Daiichi following the Great East Japan Earthquake (Entergy, 2011; Navy, 2009). Clay ($Z_{\text{avg}} \approx 7$) was added because it contains silicon ($Z = 14$) along with aluminum. Glass (SiO_2) is also considered an intermediate Z material ($Z_{\text{avg}} = 10$) for modeling purposes (Slaughter et al., 2007a). Clay is a suitable representative for ceramics. As thorium-232 is a nuisance source commonly associated with ceramics, a NORM model was designed using thorium-doped clay.

Visual interpretation of the plotted points suggested that the collective result of each simulation series was amenable to regression analysis. A linear fit (semi-log) and accompanying R^2 value are co-located with each series in Figures 22-26.

A. Celotex, Aluminum and Iron

Celotex, being a hydrogenous material, represents the most challenging cargo for a neutron beam to effectively penetrate (Figure 22). Beam scatter is substantial, and the corresponding reduction in the neutron flux on the threat target negatively impacts the number of fission events created. At the highest cargo densities ($\rho > 0.6 \text{ g/cc}$), only a few hundred delayed gamma-rays over the cumulative 94 second counting period exit the single cube surface. The addition of the photon beam nearly doubles the output at these densities when compared to the neutron beam alone. The slope of the fit is visibly flattened using dual-beam interrogation with the net effect that the importance of the homogenized cargo density is reduced.

The results for aluminum are to some extent similar to that of Celotex (Figure 23). The slope of the fit is flatter using dual-beam interrogation and the cumulative signal at all points for both series are improved. The photon beam delivers a noticeably enhanced signal at high densities. The R^2 value is nearly unity over the density range for both series, implying accurate interpolation.

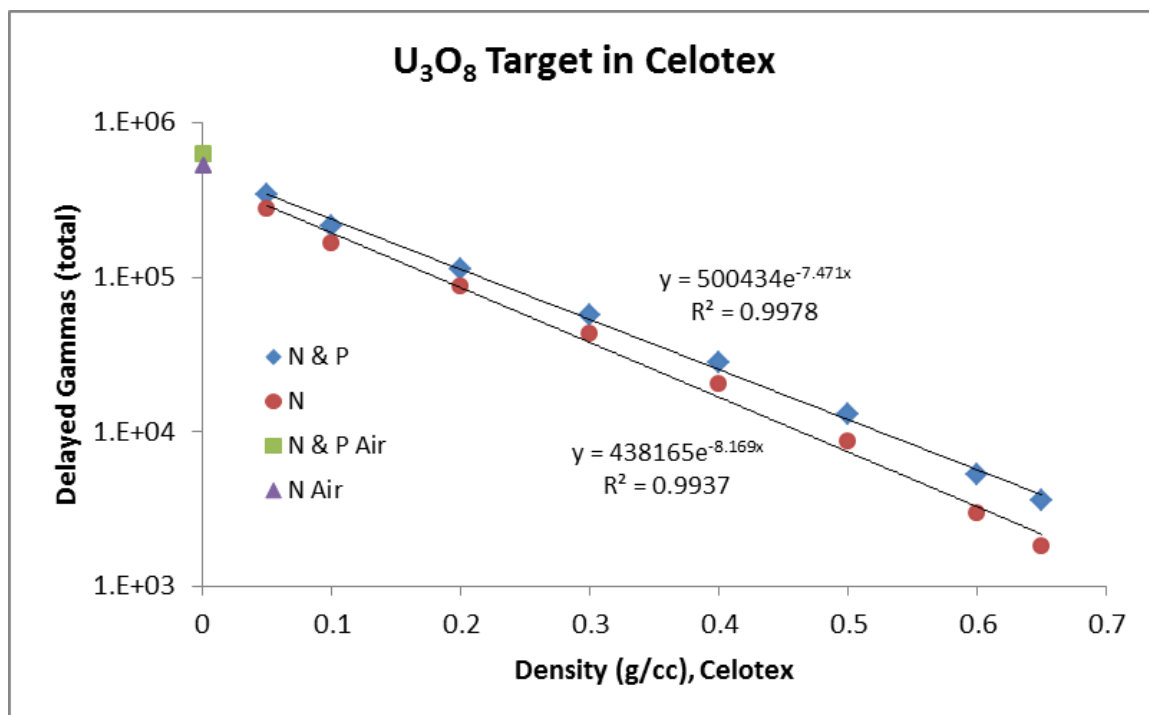


Figure 22. Cumulative (7-100 seconds post-irradiation) delayed gamma emission (3-6 MeV window) through one vertical side of surrogate container cube after 30 second interrogation with 7 MeV neutron (N) or 7 MeV neutron and 12.2 MeV photon (N & P) beams. Rapiscan Test Object “E” in homogenized Celotex at densities of 0.05-0.65 g/cc.

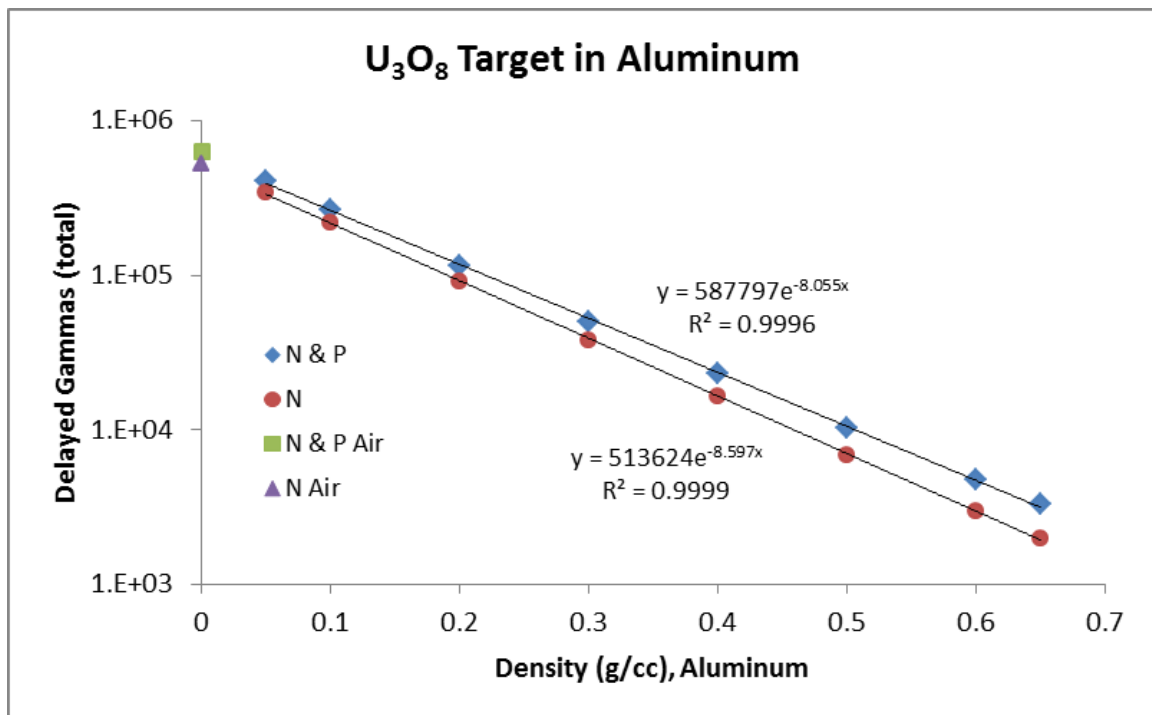


Figure 23. Cumulative (7-100 seconds post-irradiation) delayed gamma emission (3-6 MeV window) through one vertical side of surrogate container cube after 30 second interrogation with 7 MeV neutron (N) or 7 MeV neutron and 12.2 MeV photon (N & P) beams. Rapiscan Test Object “E” in homogenized aluminum at densities of 0.05-0.65 g/cc.

As expected, photon beam attenuation becomes more pronounced in the iron cargo (Figure 24). The photon beam continues to make a contribution, but the slopes of the fits are nearly the same. It is noteworthy that both y-intercept values coincide well with those of the target in air. The R^2 values are again nearly unity over the density range.

B. Tungsten

Tungsten was the highest Z material examined and provides a reasonable upper bound with regard to SNM smuggling. Tungsten may be employed as radiation shielding to thwart primary passive radiation portal monitor (RPM) screening. Dual-beam interrogation produces very little additional delayed gamma current when compared to the neutron beam alone for $\rho > 0.3$ g/cc. As expected, tungsten effectively shields the photon beam from the target at these densities (Figure 25).

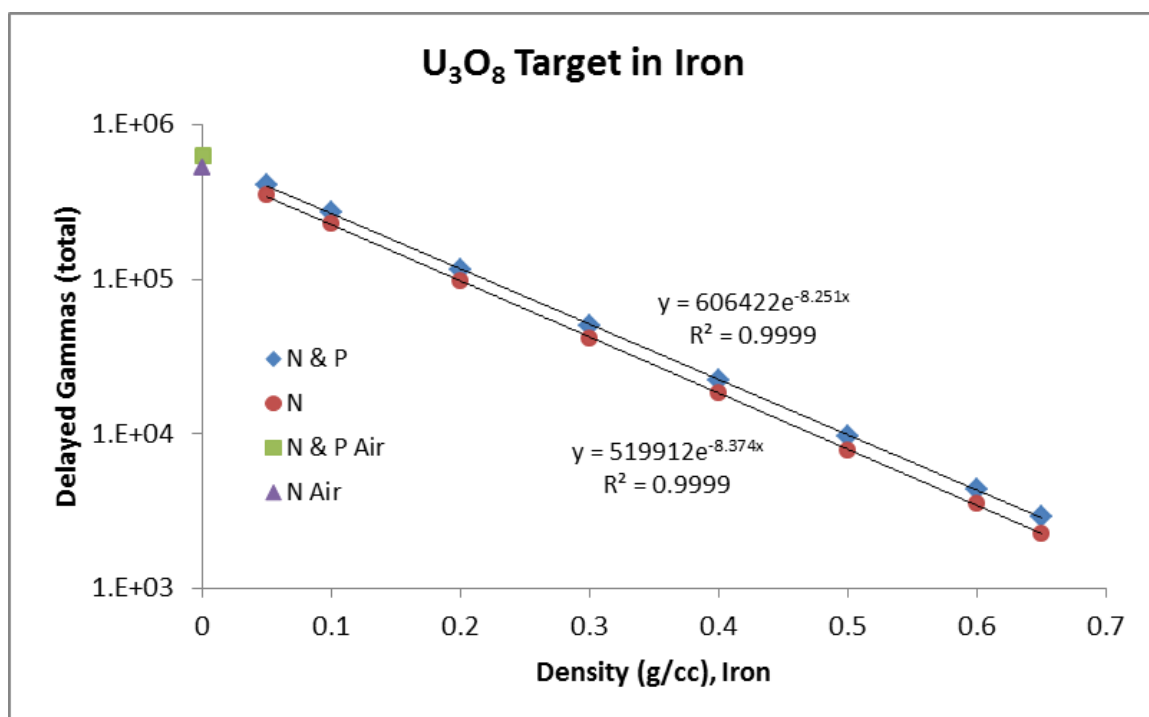


Figure 24. Cumulative (7-100 seconds post-irradiation) delayed gamma emission (3-6 MeV window) through one vertical side of surrogate container cube after 30 second interrogation with 7 MeV neutron (N) or 7 MeV neutron and 12.2 MeV photon (N & P) beams. Rapiscan Test Object “E” in homogenized iron at densities of 0.05-0.65 g/cc.

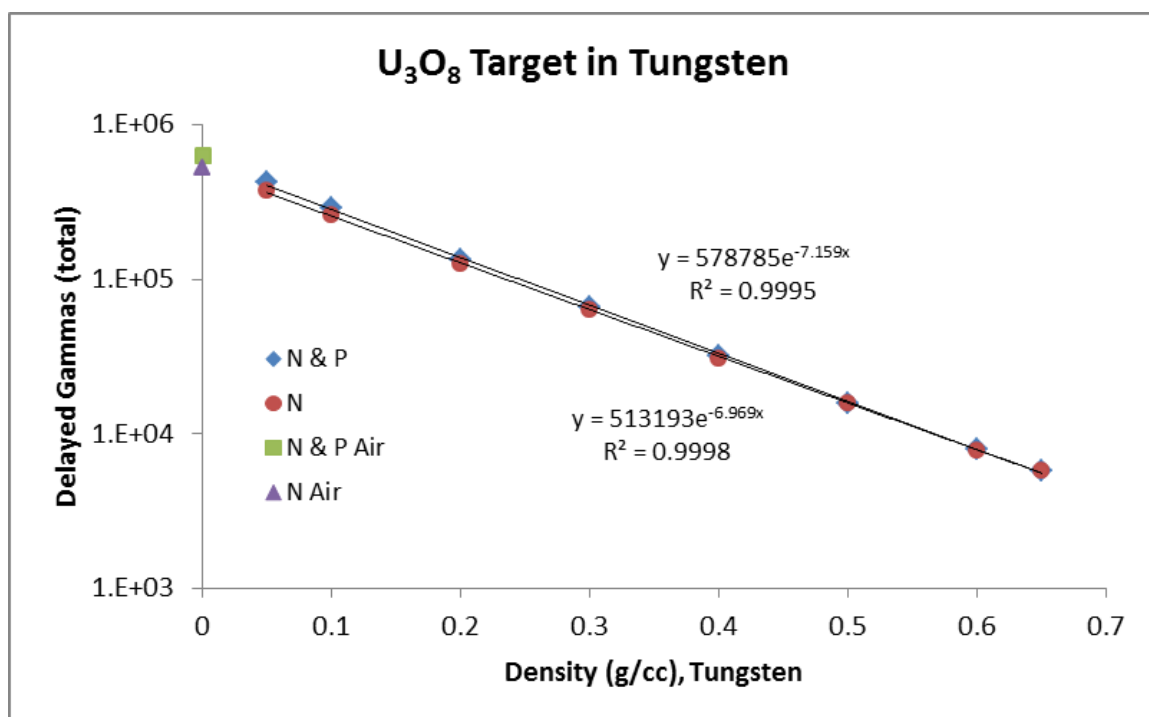


Figure 25. Cumulative (7-100 seconds post-irradiation) delayed gamma emission (3-6 MeV window) through one vertical side of surrogate container cube after 30 second interrogation with 7 MeV neutron (N) or 7 MeV neutron and 12.2 MeV photon (N & P) beams. Rapiscan Test Object “E” in homogenized tungsten at densities of 0.05-0.65 g/cc.

C. Clay and Thorium-232

Clay, like Celotex, is a mixture and is closer in natural composition to a real cargo. Clay was initially introduced as a NORM vehicle for estimating delayed gamma emissions from the fission of thorium-232, and only dual-beam simulations were performed. Figure 26 actually plots two separate studies.

One study compares dual-beam interrogation results for the uranium oxide target in clay alone or clay doped with thorium at 240 Bq/kg. The nuisance signal from the fission of thorium-232 at a typical concentration found in earthenware did not alter the results significantly as shown. This is an important finding that indicates that commercial concentrations of thorium will probably not mask the presence of SNM. However, this may not be true in the case of phosphogypsum (Table 1). Phosphogypsum ($\rho = 0.9\text{-}1.7\text{ g/cc}$) is a by-product of phosphoric acid production and is increasingly regarded as a resource rather than a waste stream (Hilton, 2010). Sacks of this intermediate Z material (for agricultural use, for example), if encountered, could pose a challenge when used to mask/shield SNM from active interrogation. No further simulations involving thorium-232 were deemed necessary at 240 Bq/kg because delayed gammas from thorium fission using dual-beam interrogation did not add appreciably to the active background.

The second study compares dual-beam interrogation results for the threat target in clay alone using ten times the number of Monte Carlo histories (2.56×10^6 for neutron transport, 6.40×10^6 for photon transport) to determine if there were any notable differences between the set numbers in the delayed gamma totals. The additional histories had little impact ("Histories x10"), and not enough to force a change to the set number of histories used for the current tally work described in this section (Figure 26). This bodes well for the possibility of near real-time modeling of suspected threat objects captured from high resolution x-ray images and opens up the possibility of limited modeling on site to estimate detector response prior to interrogation. An outline of this idea will be described in the **Discussion**.

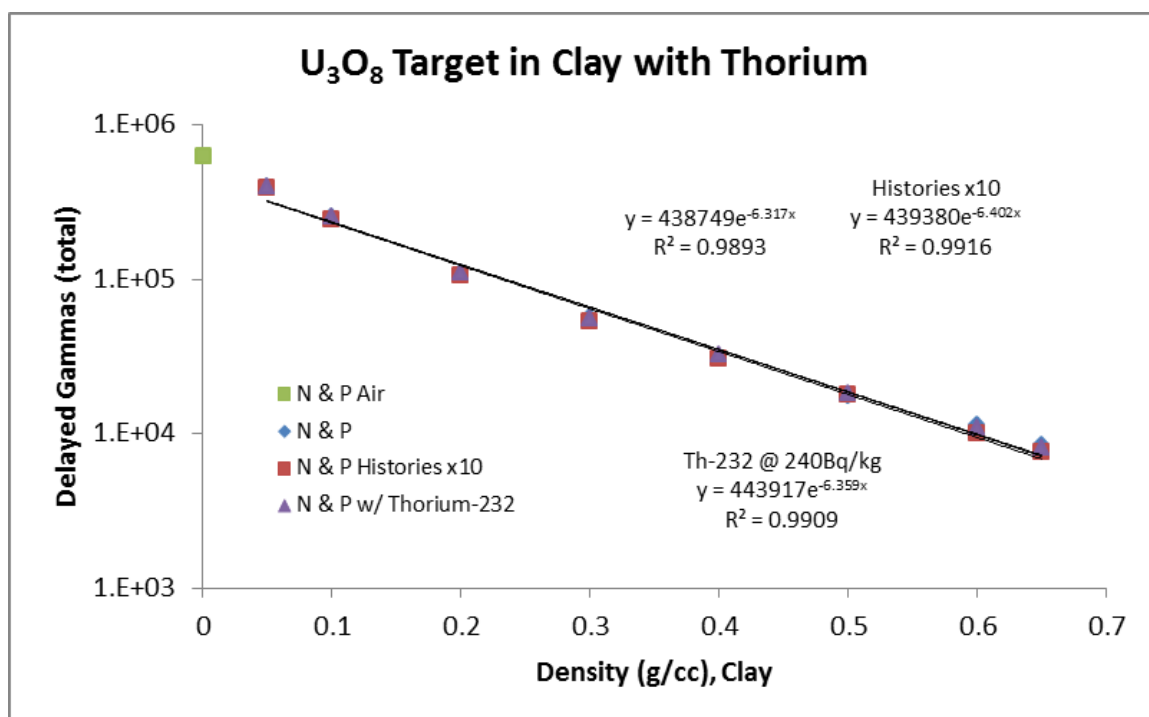


Figure 26. Cumulative (7-100 seconds post-irradiation) delayed gamma emission (3-6 MeV window) through one vertical side of surrogate container cube after 30 second interrogation with 7 MeV neutron and 12.2 MeV photon (N & P) beams. Rapiscan Test Object “E” in homogenized clay, with and without thorium, at densities of 0.05-0.65 g/cc.

D. Five Material Summary

Dual-beam interrogation results for all five materials previously described, plus air, is summarized in Figure 27. The delayed gamma tally is strongly influenced by density, as predicted, and markedly independent of homogeneous cargo composition up to significant densities (Pruett et al., 2005). Keeping in mind that these plots are semi-logarithmic, all five materials demonstrate essentially the same behavior for $\rho < 0.3$ g/cc. In other words, given noise and assuming a detector efficiency of 30%, the cumulative number of delayed gammas exiting one side of the cube is so large that this unique signature for SNM would be clearly exposed. Referring back to the distribution of average cargo density (Figure 11), one sees that 80% of all cargo falls below 0.3 g/cc. This appears to be a critical threshold density for the fundamental model employed here. Material composition is largely irrelevant until this point. The neutron beam does most of the work, but the first indication of the potential efficacy of adding the photon beam in conjunction with high average density (above 0.3 g/cc) cargo - the most challenging - is revealed.

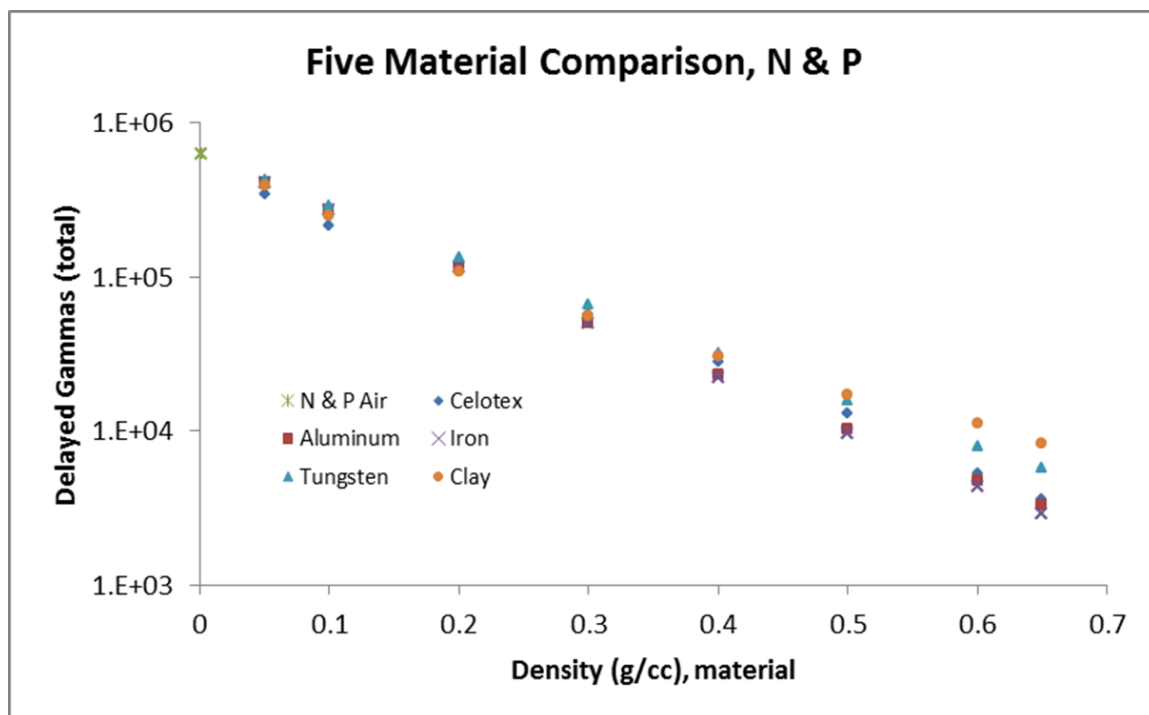


Figure 27. Cumulative (7-100 seconds post-irradiation) delayed gamma emission (3-6 MeV window) through one vertical side of surrogate container cube after 30 second interrogation with 7 MeV neutron and 12.2 MeV photon (N & P) beams. Rapiscan Test Object “E” in five materials at densities of 0.05-0.65 g/cc.

IV. Plastic Detector Implementation

A plastic detector (polyvinyltoluene, PVT) was added to the fundamental model after review of the insightful delayed gamma current evaluations. The addition of the detector transitions the model from a crude counting device to a notional detection system. This in turn allows the application of a number of conservative statistical methods, adding relatable human factors aspects and bridging esoteric calculations to application (Kraemer et al., 2009).

A. Detector Efficiency

The PVT detector was ideally located directly adjacent to the carbon steel wall used for current measurements (Figure 12). An efficiency determination can be made by taking the ratio of the pulse height tally produced in the detector to the current tally through the carbon steel wall. This could also be considered a reasonable estimate of the PVT detector's intrinsic efficiency, ϵ , where:

$$\epsilon = \frac{\text{\# of pulses recorded}}{\text{\# of quanta incident on detector}}$$

for $E_\gamma = 3\text{-}6$ MeV (Knoll, 1989). A typical result is shown in Figure 28, using the dual-beam example of the uranium oxide target in Celotex (0.05 g/cc) at seven seconds post-irradiation, yielding $\epsilon \approx 1/3$. This estimate matches well with

observations from previous experiments and simulations of $\sim 30\%$ for $E_\gamma = 2.5\text{-}6$ MeV (Hall et al. 2007, Slaughter et al., 2007b).

Because the current is being measured, it is important to note that there are low energy photons bouncing back into the container from the detector. The energy of these photons is below 2.6 MeV and has no effect on the estimate of efficiency. The contribution from delayed gammas $E_\gamma > 6$ MeV is comparatively small and their exclusion from the calculation has little impact (see Figure 20).

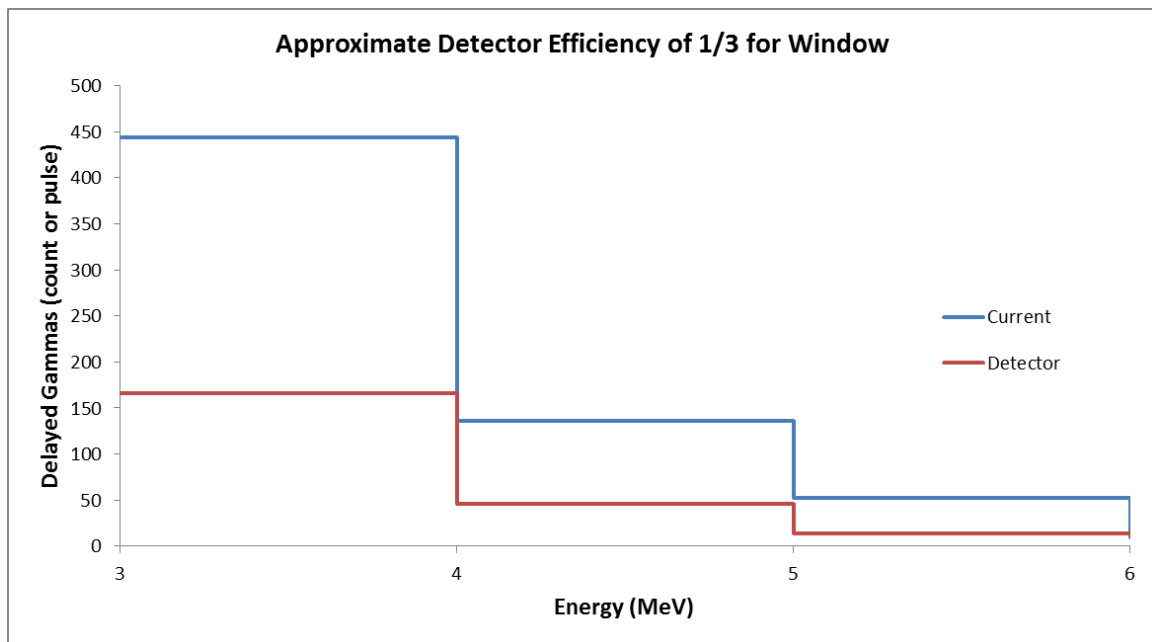


Figure 28. Delayed gamma emission (3-6 MeV window) at seven seconds post-irradiation through one vertical side of surrogate container cube and adjacent PVT detector after 30 second interrogation with 7 MeV neutron and 12.2 MeV photon beams. Rapiscan Test Object “E” in homogenized Celotex at a density of 0.05 g/cc.

B. Gaussian Energy Broadening

MCNPX has a “Special Treatment for Tallies Card” that can apply Gaussian energy broadening (GEB) to the pulse height tally to help mimic the resolution of a physical detector. This is accomplished by defining the full width at half maximum (*FWHM* in MeV) using the expression:

$$FWHM = a + b\sqrt{E + cE^2}$$

where E is the energy of the particle in MeV and the parameters a (in MeV), b (in $\text{MeV}^{1/2}$) and c (in $1/\text{MeV}$) are supplied by the user. Detailed information on observed energy resolution was limited for the EJ-200 detector and consequently only a , and therefore a fixed *FWHM*, was applied. With interest focused on $E_\gamma = 3\text{-}7$ MeV, a conservative (likely over-resolved) $FWHM = 0.35$ MeV was chosen. This spans the energy resolution ($FWHM \div E_\gamma$) range of 5-10% normally associated with scintillation detectors used in gamma-ray spectroscopy (Knoll, 1989).

The bin structure for the delayed gamma-rays supplied by CINDER to MCNPX is very coarse for $E_\gamma > 2$ MeV (see **Appendix G**). This is reflected in the unmodified detector response using the uranium oxide target in air (Figure 29). The identical simulation, with GEB applied, is shown in Figure 30. The broadened plot appears smoother and is a better imitation of a physical detector. GEB was employed for all detector work.

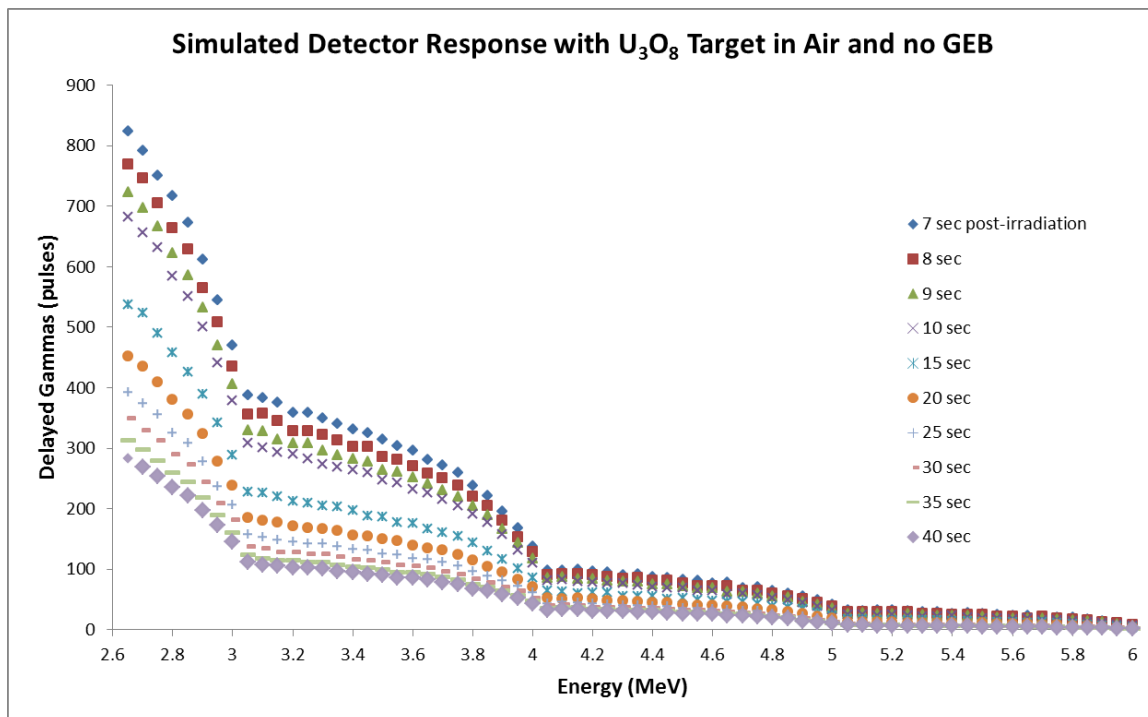


Figure 29. Simulated detector response to delayed gamma emission at one second intervals from 7-10 seconds and five second intervals from 10-40 seconds after 30 second interrogation with 7 MeV neutron and 12.2 MeV photon beams. PVT detector is adjacent to one vertical side of surrogate container cube. Rapiscan Test Object “E” in air at ISA. No Gaussian energy broadening (GEB) is used.

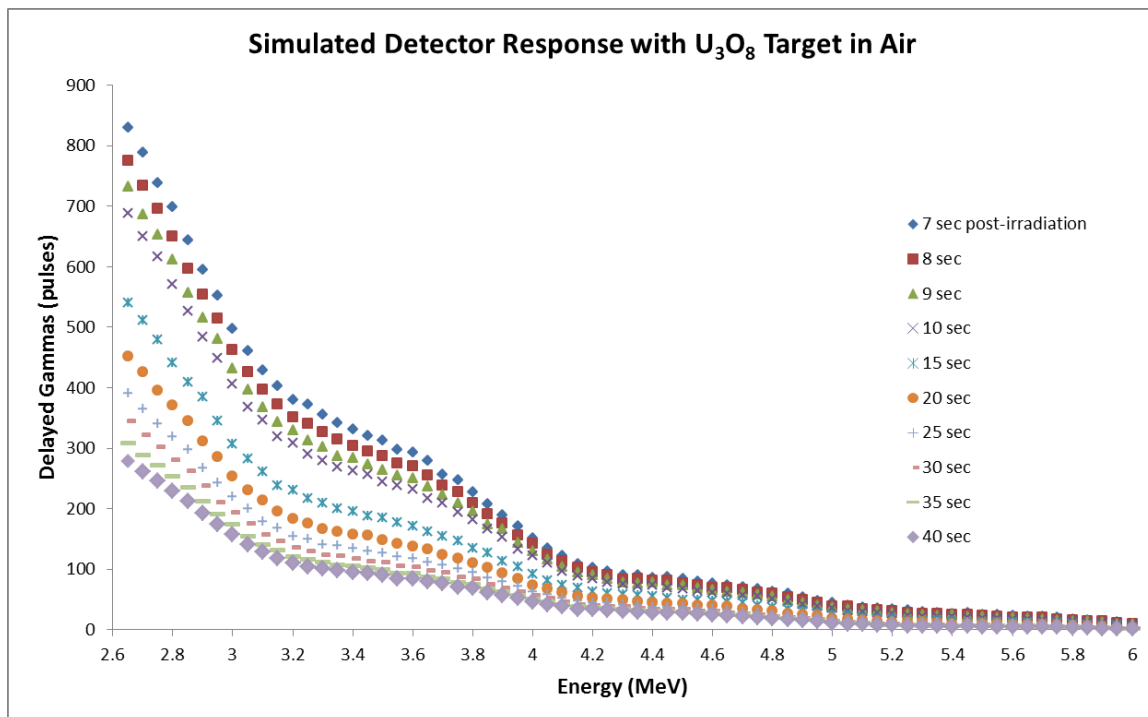


Figure 30. Simulated detector response to delayed gamma emission at one second intervals from 7-10 seconds and five second intervals from 10-40 seconds after 30 second interrogation with 7 MeV neutron and 12.2 MeV photon beams. PVT detector is adjacent to one vertical side of surrogate container cube. Rapiscan Test Object "E" in air at ISA. Gaussian energy broadening is applied.

V. Delayed Gamma Detection Results

After modifying the fundamental model and ancillary post-processing methods, the findings from the delayed gamma current results were comprehensively extended to exercise the detector. Clay was included with the three benchmark surrogate cargos of Celotex, aluminum and iron. Clay was added to the list because it is worth modeling; \$1.21 billion of ceramic tile alone were exported to the United States in 2010 (CTaSC, 2012).

To summarize, delayed gamma results were collected at one second intervals from 7-10 seconds and five second intervals from 10-40 seconds after 30 second interrogation with 7 MeV neutron and/or 12.2 MeV photon beams. The PVT detector is adjacent to one vertical side of surrogate container cube. A signal collection time on the order of 30 seconds is adequate from experiment (Church et al., 2007a). There are a set of three figures for each material at each average density consisting of dual-beam, neutron beam only and photon beam only results. They cover the density range of 0.05-0.65 g/cc at all the points detailed in **Models and Methods**.

There are a total of 24 figures for each surrogate cargo. The delayed gamma detection results are presented in their entirety in the appendices:

- Appendix A: Air
- Appendix B: Celotex
- Appendix C: Aluminum
- Appendix D: Clay
- Appendix E: Iron

The figures as a whole provide a comprehensive look at simulated detector responses to delayed gamma emission ($E_\gamma = 2.6\text{-}6\text{ MeV}$) produced by interrogation of the Rapiscan test object in these representative materials at densities important to the shipping container industry.

The figures of **Appendix B8**, “Simulated Detector Responses with U_3O_8 Target in 0.65 g/cc Celotex,” are reproduced here to highlight some general features (Figures 31-33). This simulation series represents the most challenging surrogate cargo and reinforced by the anemic pulse tallies (less than three for $E_\gamma \geq 3\text{ MeV}$) in each 50 KeV bin. The “default” plot is produced from dual-beam simulations (Figure 31). The individual beam results are noted in the chart title (Figures 32 and 33).

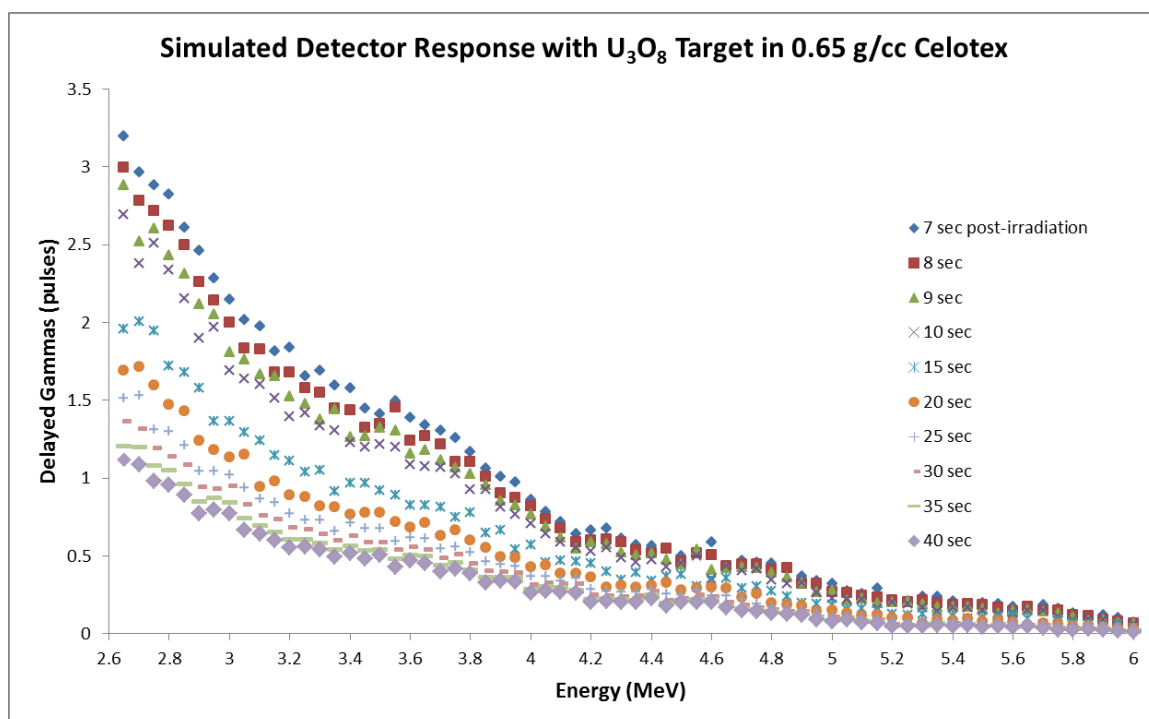


Figure 31. Simulated detector response to delayed gamma emission at one second intervals from 7-10 seconds and five second intervals from 10-40 seconds after 30 second interrogation with 7 MeV neutron and 12.2 MeV photon beams. PVT detector adjacent to one vertical side of surrogate container cube. Rapiscan Test Object "E" in Celotex at 0.65 g/cc.

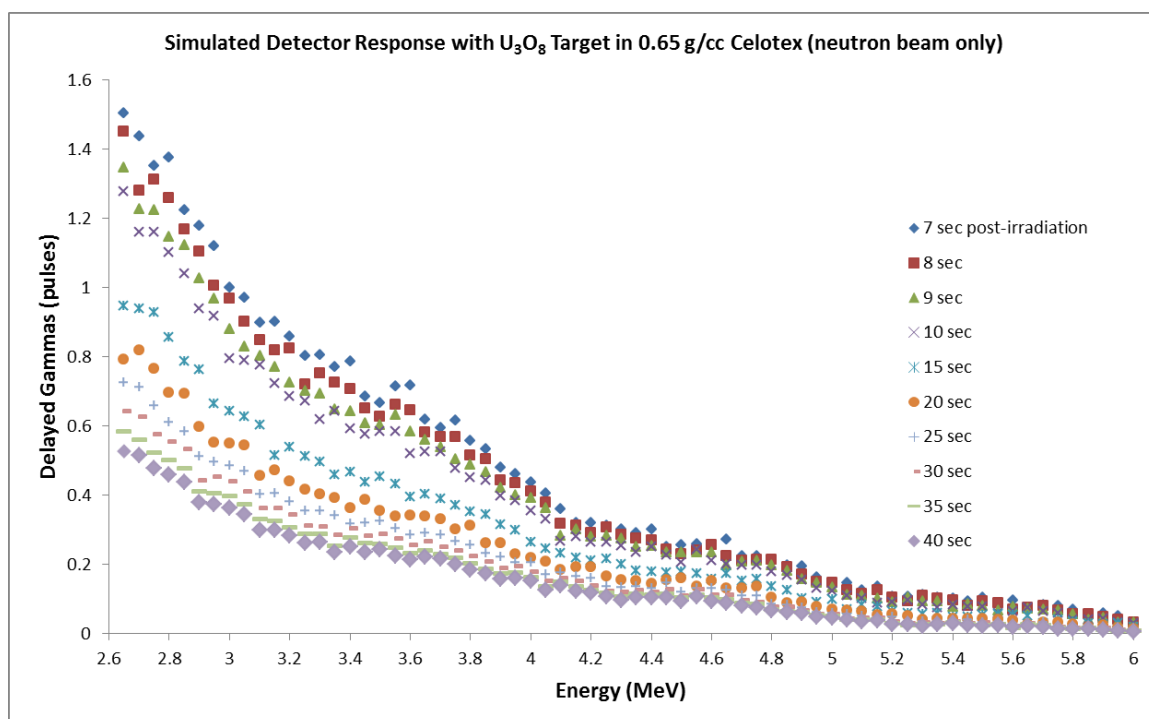


Figure 32. Simulated detector response to delayed gamma emission at one second intervals from 7-10 seconds and five second intervals from 10-40 seconds after 30 second interrogation with 7 MeV neutron beam. PVT detector adjacent to one vertical side of surrogate container cube. Rapiscan Test Object “E” in Celotex at 0.65 g/cc.

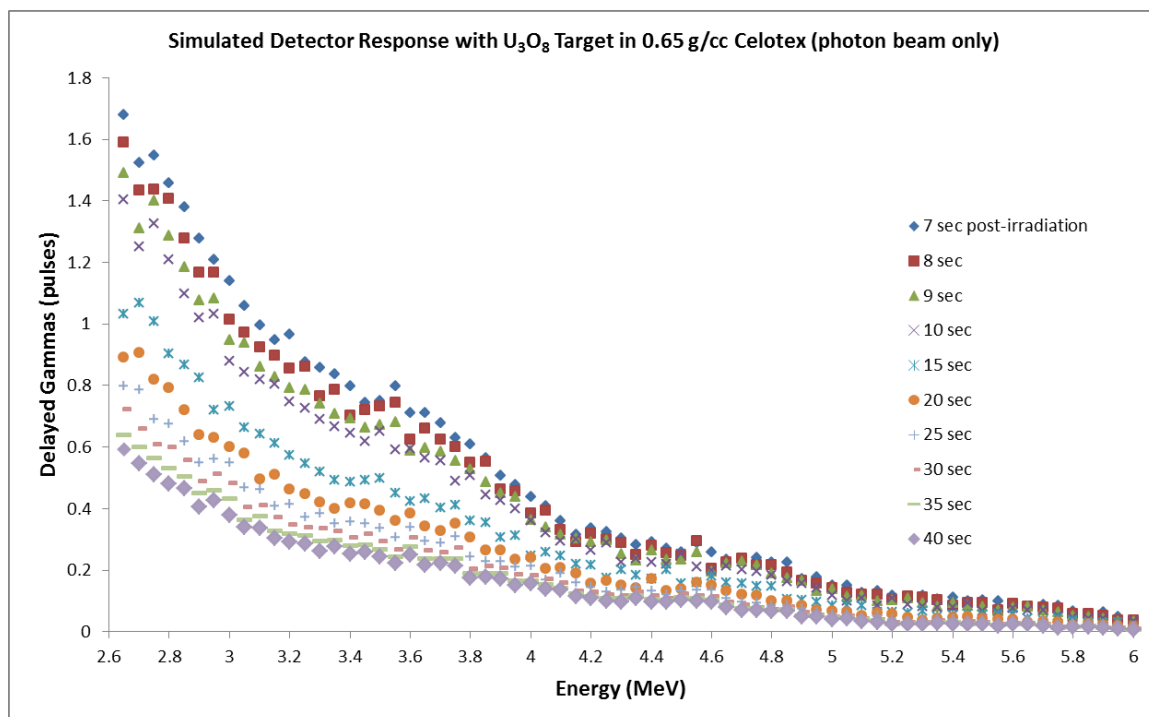


Figure 33. Simulated detector response to delayed gamma emission at one second intervals from 7-10 seconds and five second intervals from 10-40 seconds after 30 second interrogation with 12.2 MeV photon beam. PVT detector adjacent to one vertical side of surrogate container cube. Rapiscan Test Object "E" in Celotex at 0.65 g/cc.

Plotting the detector response by delayed gamma energy allows for detailed visualization of the signal below 3 MeV. Projected detection system performance is based on the cumulative signal for $E_\gamma = 3\text{-}6$ MeV captured over a short period of time (< 2 minutes) as isotopic identification is impossible (Ely et al., 2006). Extending the pulse height tally down to 2.6 MeV, the upper limit for naturally occurring radioactivity, provides additional data in the Compton continuum that could be incorporated to extend the performance envelope. All beam configurations reveal there may be good signals available if background noise can be effectively subtracted.

The five appendices serve as a library. The delayed gamma current data implies that a neutron beam may be sufficient for low average density cargos. The library reveals that there may be some circumstances when a photon beam alone may be appropriate. One clear prospect is when fluorine is encountered.

VI. Fluorine Interference

A. Nitrogen-16

Neutron ($E_n > 1.6$ MeV) activation of fluorine-19 (naturally occurring, 100% isotopic concentration) results in the reaction $^{19}\text{F} (n,\alpha) ^{16}\text{N}$ with subsequent β -decay to oxygen-16 and emission of a 6.128 MeV gamma-ray ($t_{1/2} = 7.13$ seconds) (Church et al., 2007a). This is a critical, but easily identifiable, interference source as it produces a large masking signal in a plastic detector with a clear peak at $E_\gamma \approx 6$ MeV even when comparatively small quantities are present. Unfortunately, useful neutron interrogation energies are ideal for this reaction to occur (Figure 34).

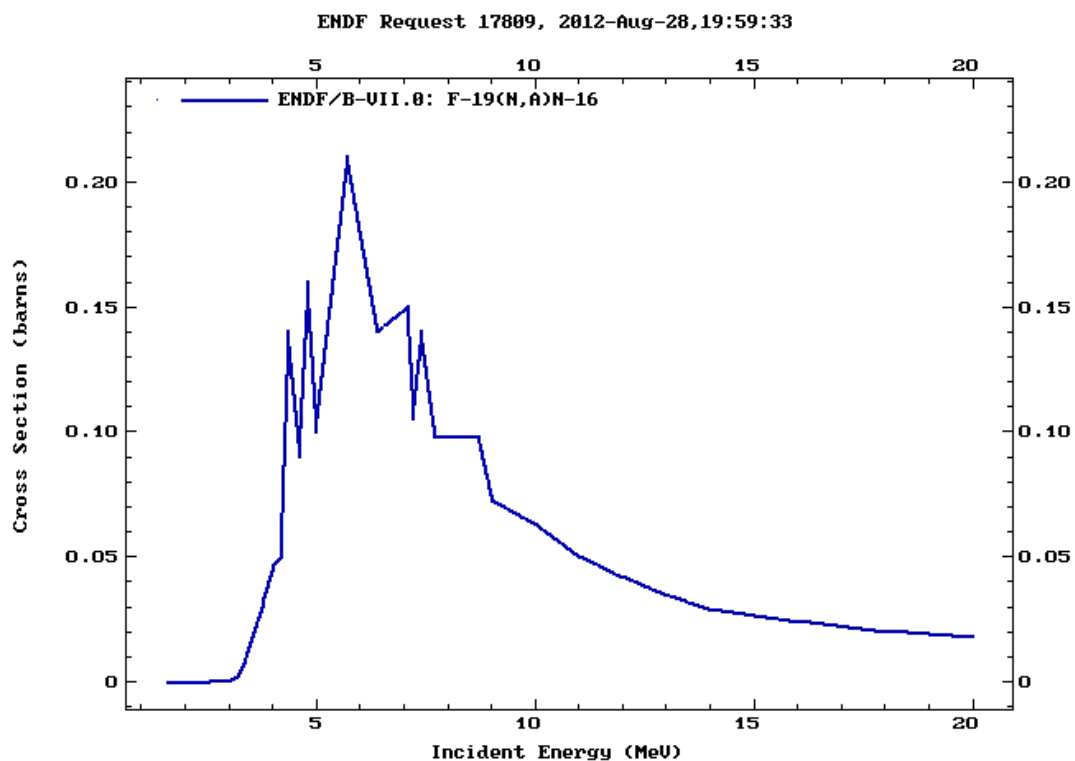


Figure 34. Neutron activation cross section for the $^{19}\text{F} (n,\alpha) ^{16}\text{N}$ reaction. The 7 MeV neutron interrogation energy used for this work is nearly ideal (from NNDC, 2012).

An example of this unique signal is provided in Figure 35 from the fundamental model filled with low density Teflon (400 kg of fluorine-19 total) and interrogated with 7 MeV neutrons using the default beam diameter of 12.1 cm. If one imagines that the beam passes all the way through the surrogate, then ~1 kg of Teflon is illuminated in this column. The noise produced from this small quantity of Teflon is substantial when compared against the signals from the uranium oxide target described in the previous section. The noise signal shape formed by the model matches well with that demonstrated by experiment (Figure 36). Note that the peak produced in the simulation is to the right of 6.1 MeV as compared to the experiment which, as expected, would be shifted to the left. This is a repercussion of the coarse binning structure used by CINDER for $E_\gamma > 2$ MeV.

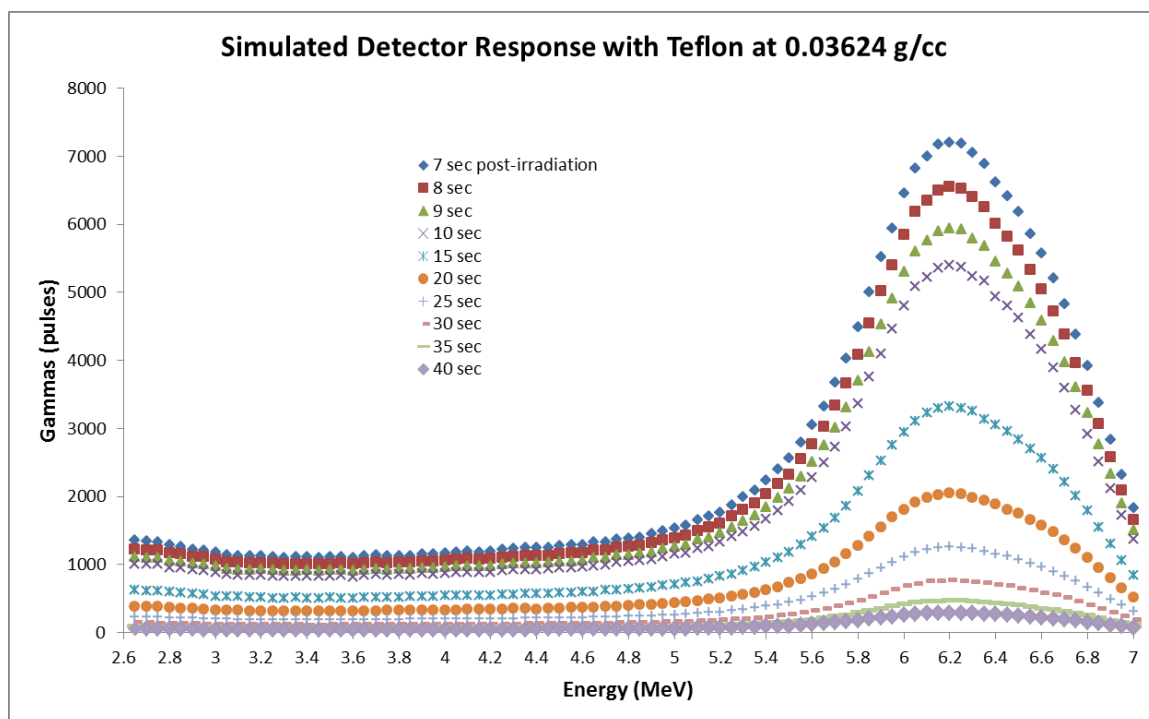


Figure 35. Simulated detector response to gamma emission at one second intervals from 7-10 seconds and five second intervals from 10-40 seconds after 30 second interrogation with 7 MeV neutron beam. PVT detector adjacent to one vertical side of surrogate container cube. Teflon at 0.03624 g/cc.

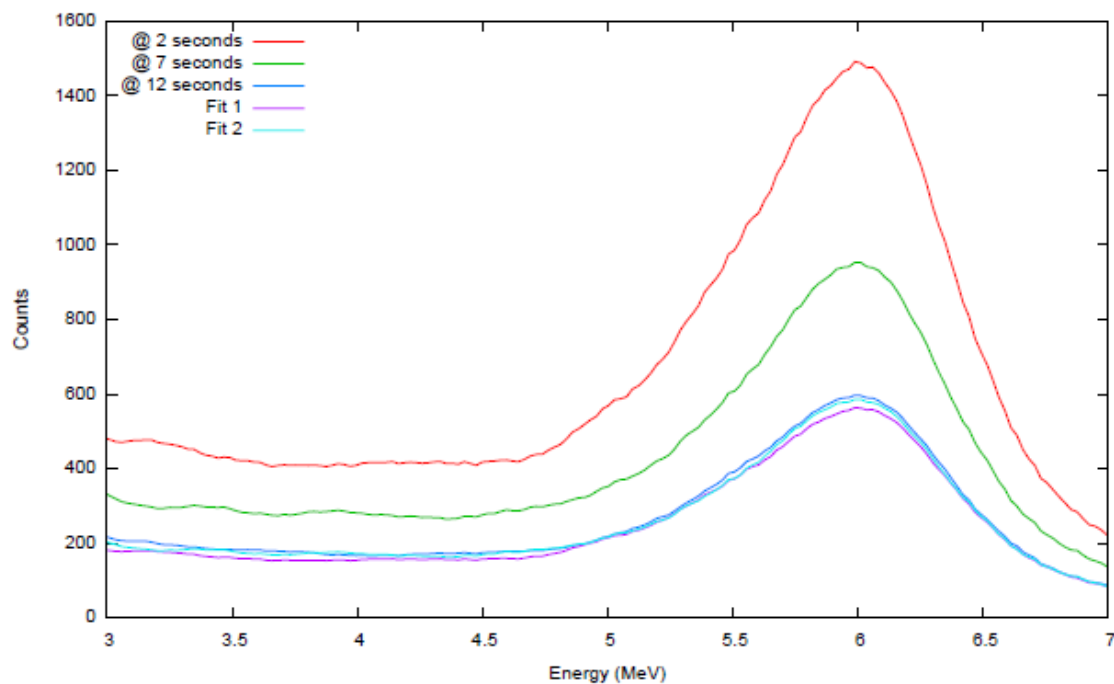


Figure 36. Smoothed experimental energy-counts profile of a nitrogen-16 source (irradiated Teflon, mass unknown) at 2, 7, and 12 seconds (from Luu et al., 2007).

B. Teflon Target

A series of simulations were run substituting the uranium oxide target with a Teflon target of the same dimensions and mass (600 grams). Figure 37 shows the resulting detector response for air, and Figures 38 through 41 show responses for Celotex, aluminum, clay and iron respectively at $\rho = 0.4$ g/cc. This is the maximum average density for a 40' container. As will be outlined below, it is also the critical density at which the neutron beam alone is sufficient to meet detection system performance requirements. However, as these five responses reveal, this may not be possible if even a small amount of Teflon or other fluorinated compounds are present during neutron interrogation. Any real signal from concealed SNM could be effectively masked throughout $E_\gamma = 2.6-7$ MeV when counting for effect. There appears to be no reliable field method for subtracting this active noise even when 1) the source is obviously nitrogen-16, and 2) the half-life is $\sim 1/3$ shorter than the observed average for the fission products ($T_{1/2}$ of 7.13 seconds versus ~ 20 seconds).

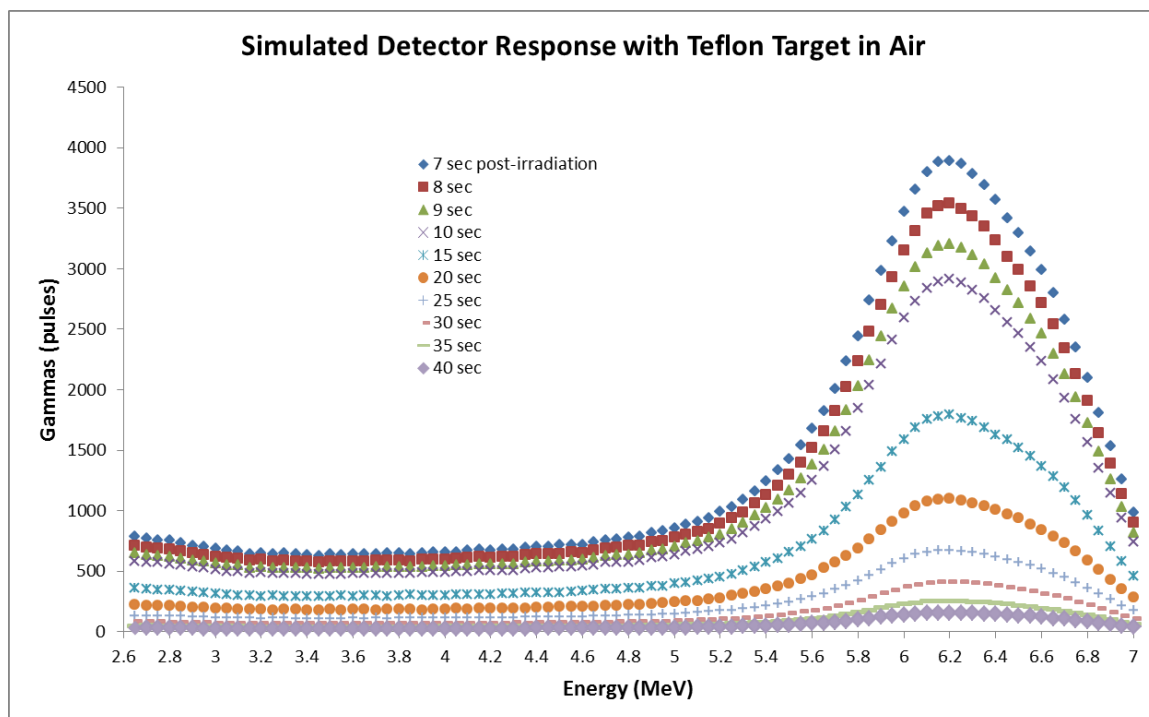


Figure 37. Simulated detector response to gamma emission at one second intervals from 7-10 seconds and five second intervals from 10-40 seconds after 30 second interrogation with 7 MeV neutron beam. PVT detector adjacent to one vertical side of surrogate container cube. Teflon target (600 g puck) in air at 0.001275 g/cc (ISA).

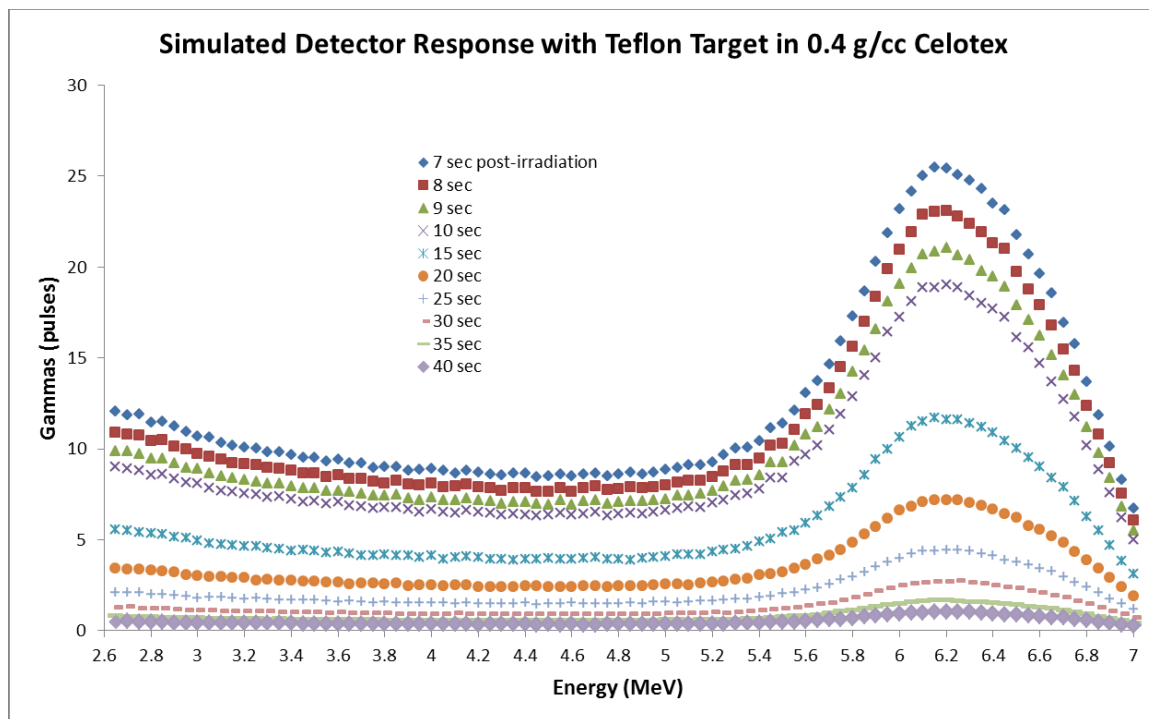


Figure 38. Simulated detector response to gamma emission at one second intervals from 7-10 seconds and five second intervals from 10-40 seconds after 30 second interrogation with 7 MeV neutron beam. PVT detector adjacent to one vertical side of surrogate container cube. Teflon target (600 g puck) in Celotex at 0.4 g/cc.

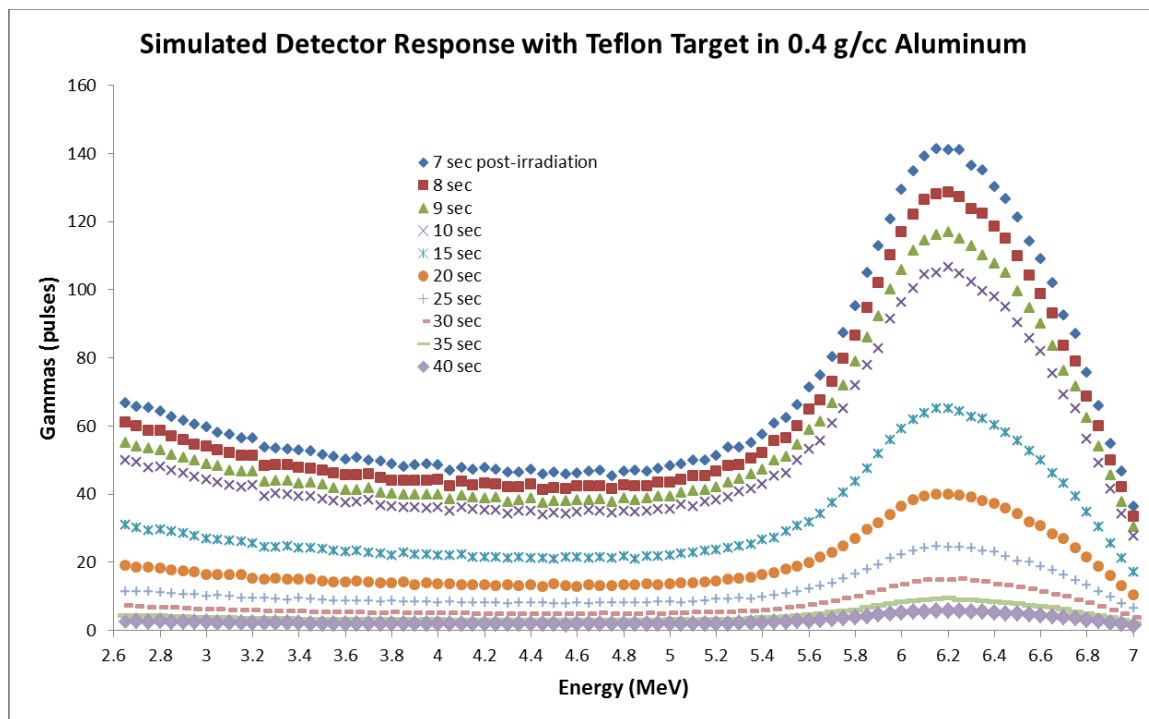


Figure 39. Simulated detector response to gamma emission at one second intervals from 7-10 seconds and five second intervals from 10-40 seconds after 30 second interrogation with 7 MeV neutron beam. PVT detector adjacent to one vertical side of surrogate container cube. Teflon target (600 g puck) in aluminum at 0.4 g/cc.

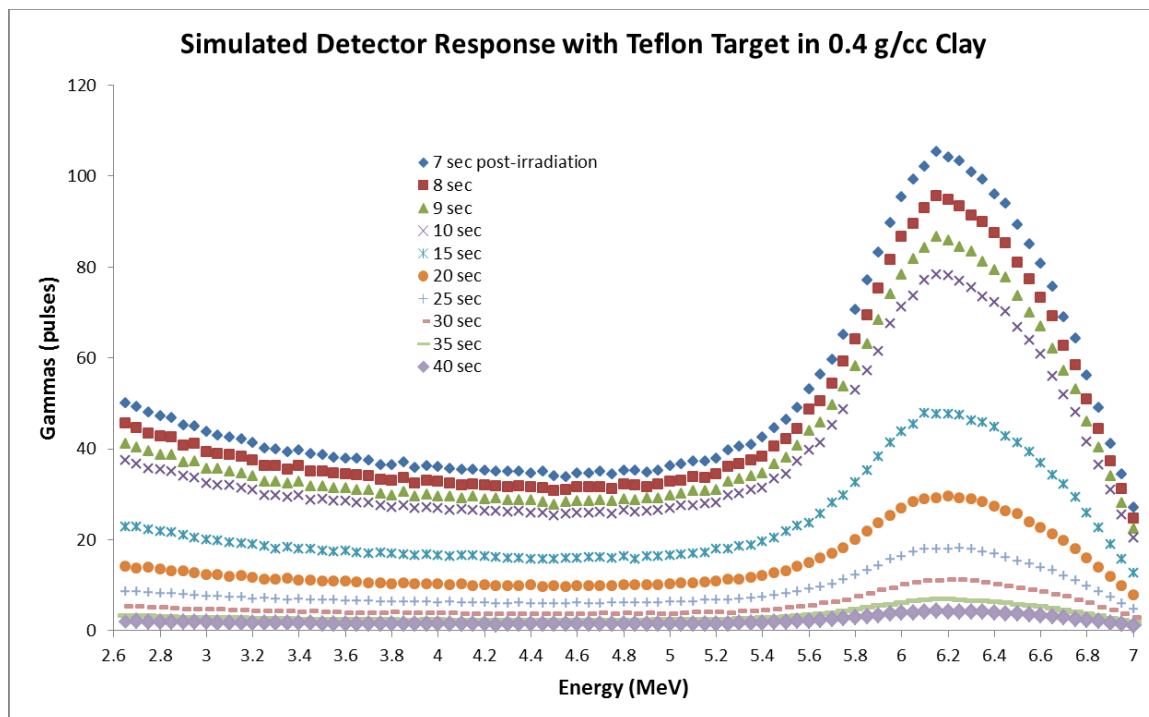


Figure 40. Simulated detector response to gamma emission at one second intervals from 7-10 seconds and five second intervals from 10-40 seconds after 30 second interrogation with 7 MeV neutron beam. PVT detector adjacent to one vertical side of surrogate container cube. Teflon target (600 g puck) in clay at 0.4 g/cc.

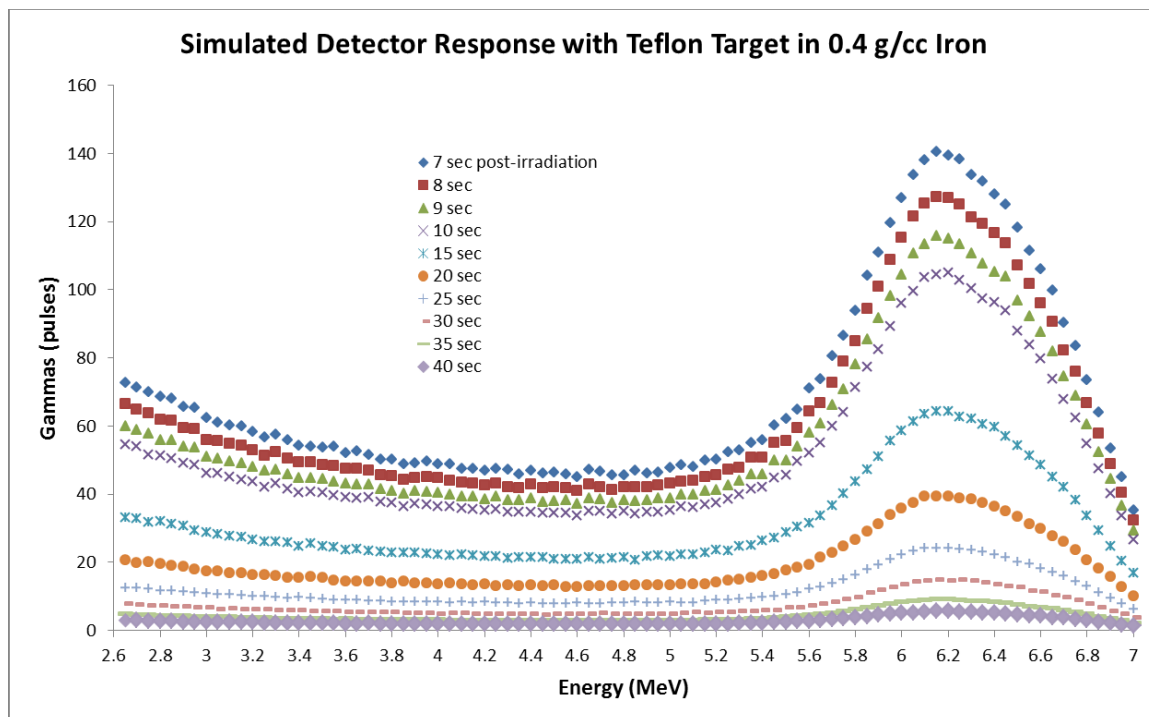


Figure 41. Simulated detector response to gamma emission at one second intervals from 7-10 seconds and five second intervals from 10-40 seconds after 30 second interrogation with 7 MeV neutron beam. PVT detector adjacent to one vertical side of surrogate container cube. Teflon target (600 g puck) in iron at 0.4 g/cc.

Fluorine activation of this nature can be avoided by using photon interrogation alone. Delayed gamma signals resulting from photofission could be substantially less but this may present a partial solution when fluorinated compounds are encountered. Figure 42 highlights the challenge in SNM identification when a fluorinated compound is present. The threat target is virtually indistinguishable from the Teflon cargo signal alone under neutron interrogation, boosting the cumulative pulse count less than 4% and only at low gamma-ray energies. The photon beam produces a clean delayed gamma signal (secondary axis), but only about 1/4 of that produced by neutron beam interaction with the target. Considering the lack of active background produced by the photon beam in general, it may be possible to reliably detect SNM with these weaker signals if system performance requirements are relaxed to allow for a higher rate of false alarms.

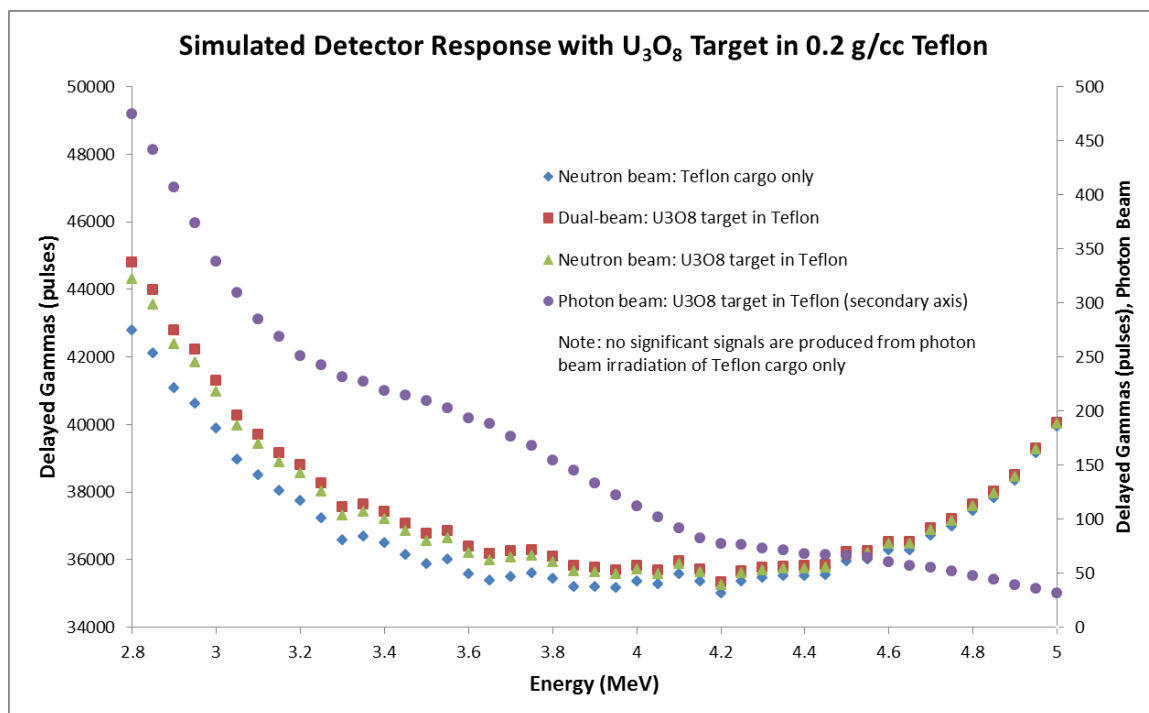


Figure 42. Simulated detector response to gamma-ray emission 7-40 seconds (cumulative) after 30 second interrogation with 7 MeV neutron and/or 12.2 MeV photon beams. PVT detector adjacent to one vertical side of surrogate container cube. Rapiscan Test Object “E” in Teflon at 0.2 g/cc.

VII. Detection System Performance

For a given set of system performance requirements, based on neutron beam interrogation alone, how much does pairing a photon beam extend the performance envelope? All of the data necessary to demonstrate the performance of a dual-beam detection system, based on the idealized fundamental model and surrogate cargos, can be accomplished with the detection library previously established.

To reiterate, detection system performance is estimated using a figure-of-merit (F_s) as a function of the empirically determined average noise background measured at $T \gg 40$ seconds post-irradiation (see **Models and Methods**). The primary time integrated signal(s) for the calculation of F_s are determined over the period of 7-40 seconds post-irradiation (34 seconds total). The F_s threshold values for good, diminishing and unreliable system operation are based on DNDO performance requirements of a maximum false negative rate of 1.67% and 0.5% maximum false positive rate. Values calculated for F_s can be generally categorized for this system as:

- $F_s \geq 5$, good system performance (meets DNDO goals)
- $5 > F_s > 2$, declining system performance (increasing false alarm rates)
- $F_s \leq 2$, poor system performance (unreliable)

By definition, the DNDO performance requirements do not guarantee threat target detection. On the other hand, F_s values somewhat less than five do not necessarily preclude acceptable system performance ($P_d \geq 0.95$) if higher false positive rates are tolerated (Figure 17).

Simulated detection system performances for the threat target in Celotex, aluminum, clay and iron over a mean background range of 10-10000 counts/sec are illustrated in Figures 43 through 50. Following previous convention, the “default” plot is produced from dual-beam simulations and the neutron beam interrogation results are noted in the chart title. Dashed lines at $F_s = 5$ (green, meets DNDO goals) and $F_s = 2$ (red, unreliable) demarcate the diminishing, but potentially useful, system performance area (yellow). Active backgrounds measured from experiment ranged from 50-5000 counts/sec, so a functional threshold of 50 counts/sec is appropriate as well (Slaughter et al., 2007a).

A. Celotex

System performance using neutron beam interrogation with Celotex is shown in Figure 43. The neutron beam alone is sufficient to meet $F_s \geq 5$ at $\rho \leq 0.3$ g/cc (purple curve) for backgrounds up to 10000 counts/sec, and good performance is still achieved at $\rho = 0.4$ g/cc at ~2400 counts/sec (green curve). The system does not meet any detection goal at the highest density of 0.65 g/cc (bottom tan curve). Dual-beam results are presented in Figure 44. Immediate benefit can be seen at the highest density, as the addition of the photon beam allows good system performance to 65 counts/sec and increases the potential performance band by a factor of five.

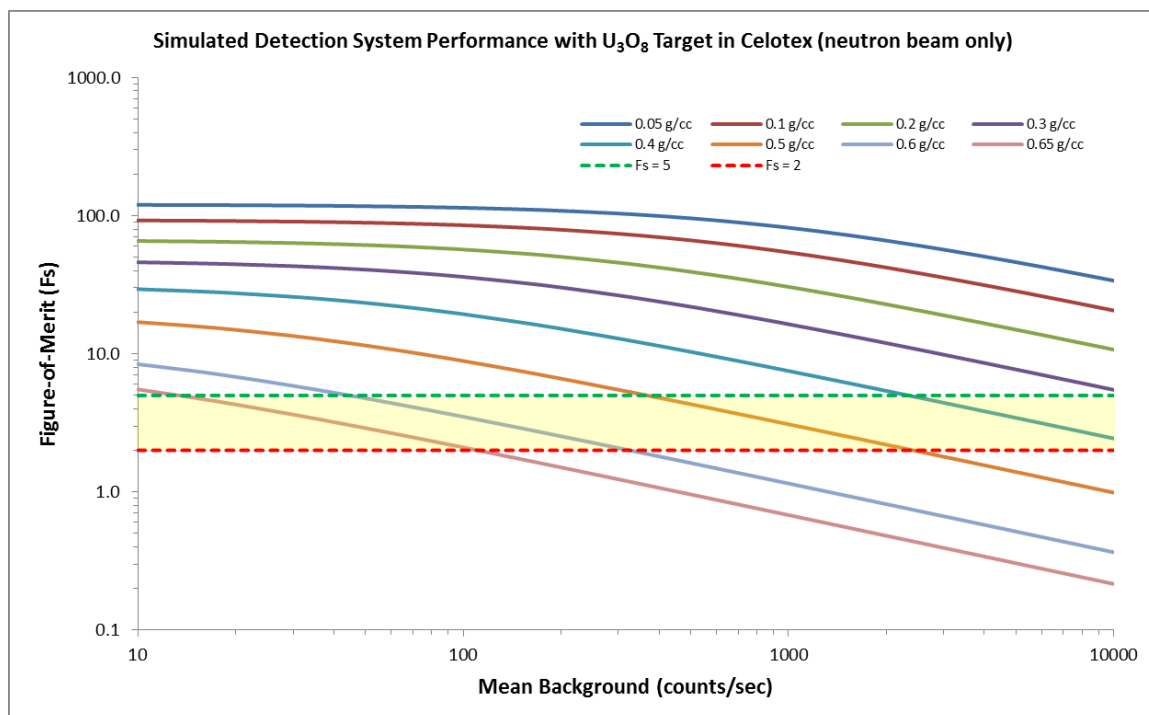


Figure 43. Simulated detection system performance based on delayed gamma emission ($E_\gamma = 3\text{-}6\text{ MeV}$) after 30 second interrogation with a 7 MeV neutron beam. Rapiscan Test Object “E” in homogenized Celotex at densities of 0.05-0.65 g/cc.

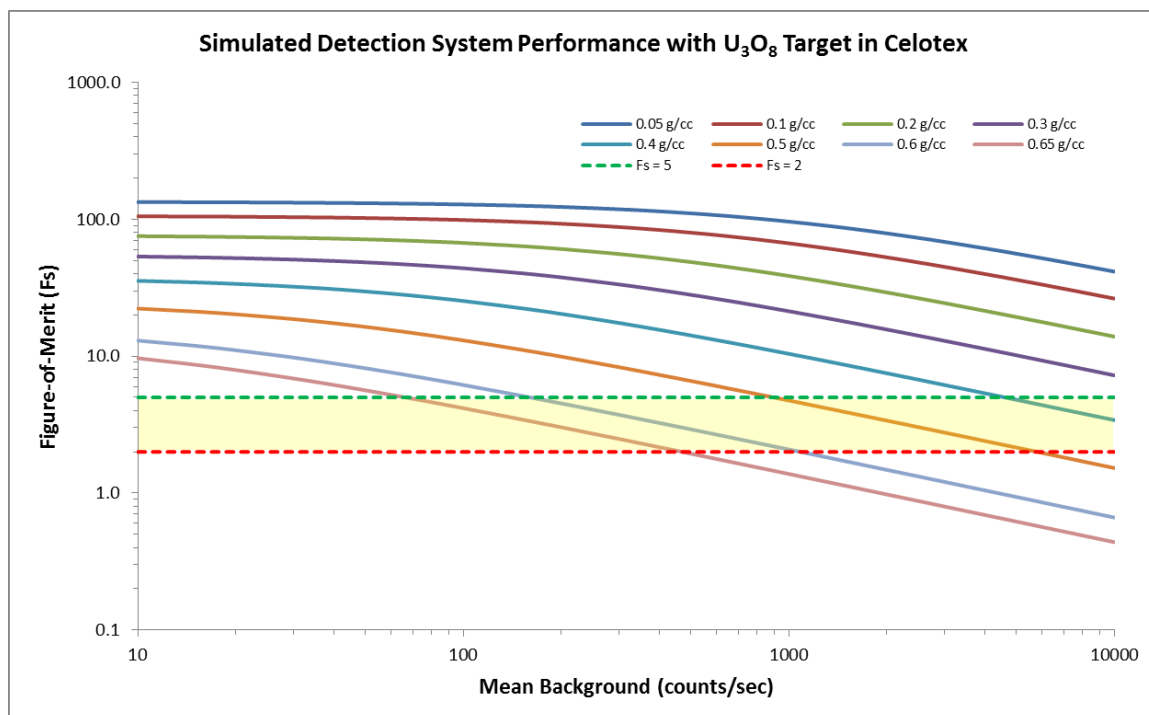


Figure 44. Simulated detection system performance based on delayed gamma emission ($E_\gamma = 3-6$ MeV) after 30 second interrogation with 7 MeV neutron and 12.2 MeV photon beams. Rapiscan Test Object "E" in homogenized Celotex at densities of 0.05-0.65 g/cc.

B. Aluminum

System performance using neutron beam interrogation with aluminum is shown in Figure 45. The neutron beam alone is sufficient to meet $F_s \geq 5$ at $\rho \leq 0.3$ g/cc for backgrounds up to 10000 counts/sec, and good performance is still achieved at $\rho = 0.4$ g/cc at ~1600 counts/sec (green curve). Again, the system does not meet meaningful detection goals at the highest densities 0.6 of 0.65 g/cc (bottom two curves). Dual-beam results are presented in Figure 46. Gain can be seen as well at the highest densities, as the addition of the photon beam allows good system performance up to ~110 counts/sec for $\rho = 0.6$ g/cc.

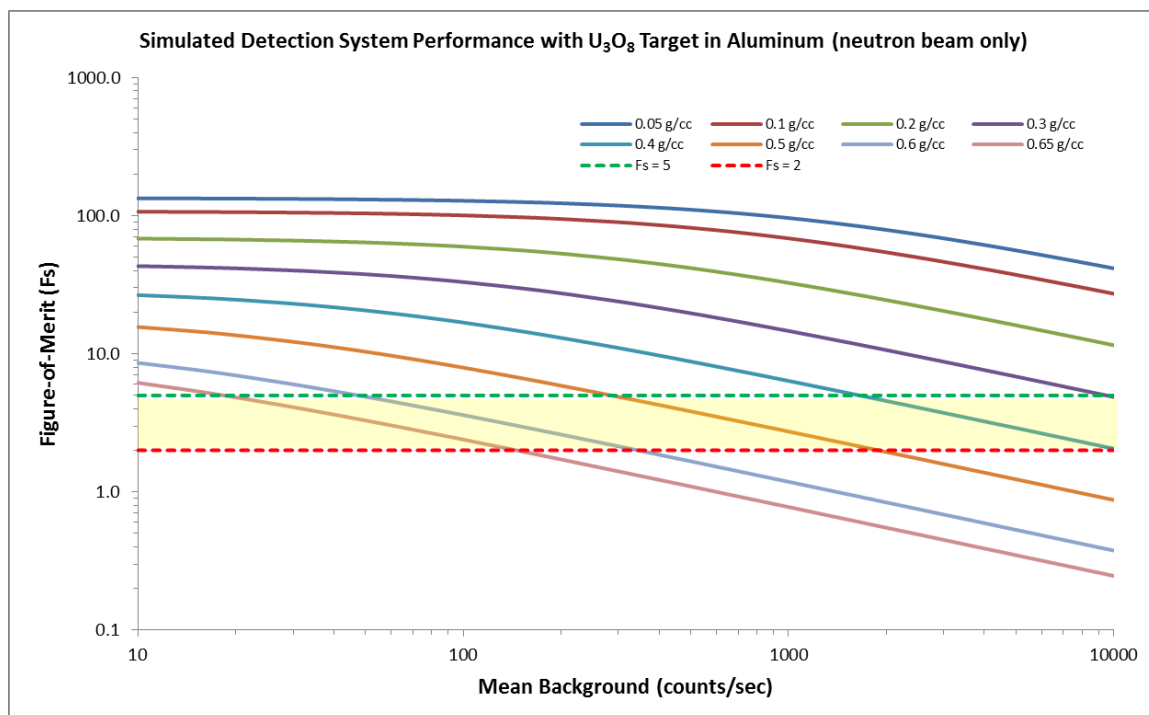


Figure 45. Simulated detection system performance based on delayed gamma emission ($E_\gamma = 3\text{-}6\text{ MeV}$) after 30 second interrogation with a 7 MeV neutron beam. Rapiscan Test Object “E” in homogenized aluminum at densities of 0.05-0.65 g/cc.

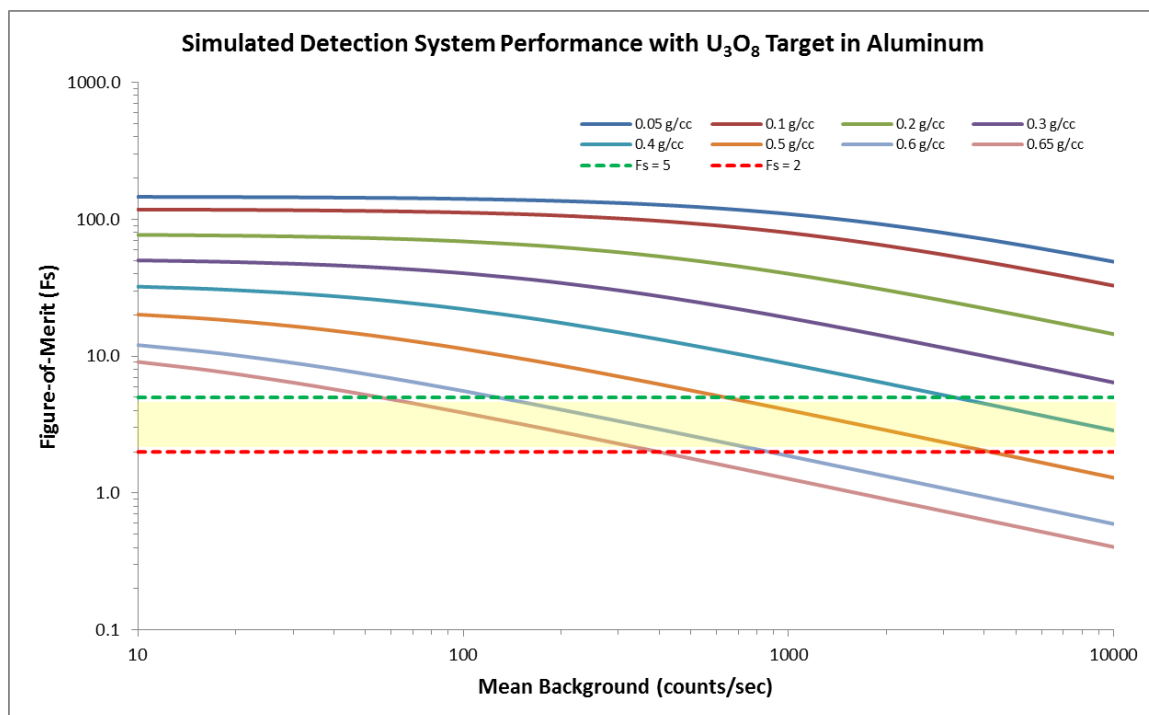


Figure 46. Simulated detection system performance based on delayed gamma emission ($E_\gamma = 3\text{-}6$ MeV) after 30 second interrogation with 7 MeV neutron and 12.2 MeV photon beams. Rapiscan Test Object “E” in homogenized aluminum at densities of 0.05-0.65 g/cc.

C. Clay

System performance using neutron beam interrogation with Clay is shown in Figure 47. The neutron beam alone is sufficient to meet $F_s \geq 5$ at $\rho \leq 0.3$ g/cc for backgrounds up to 10000 counts/sec, and good performance is still achieved at $\rho = 0.5$ g/cc at ~1300 counts/sec (orange curve). The system meets meaningful detection goals at the highest densities 0.6 of 0.65 g/cc at ≥ 250 counts/sec (bottom two curves). Dual-beam results are presented in Figure 48. The addition of the photon beam allows good system performance up to ~650 counts/sec for $\rho = 0.6$ g/cc.

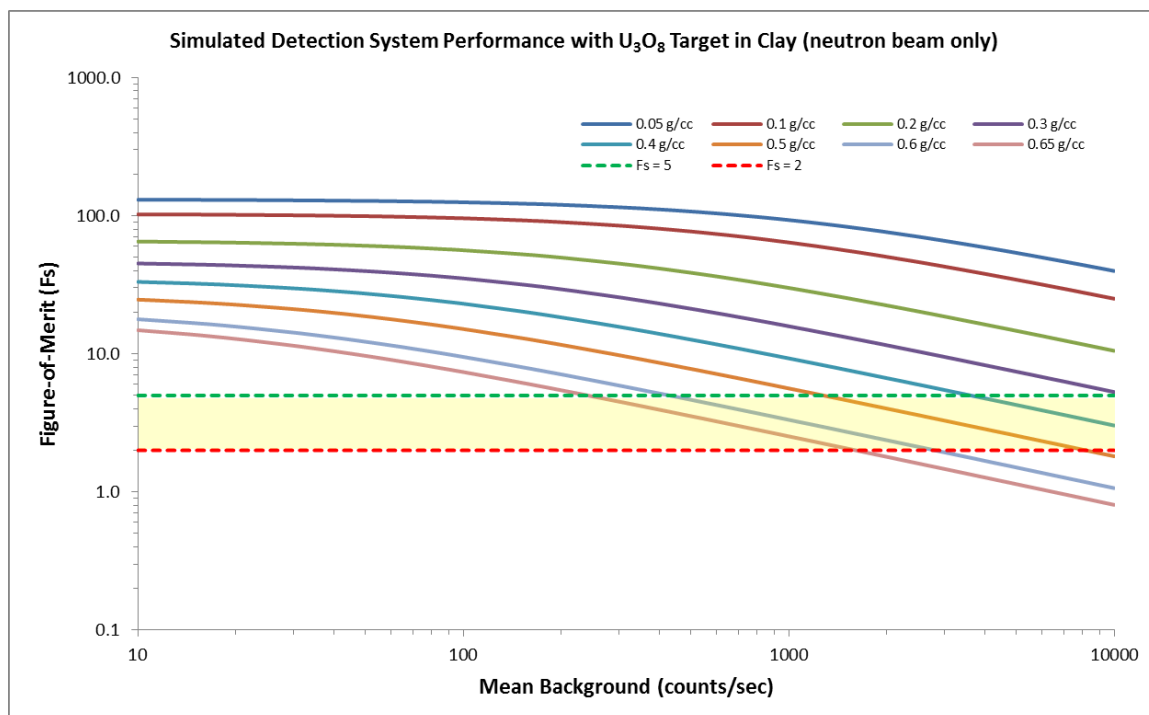


Figure 47. Simulated detection system performance based on delayed gamma emission ($E_\gamma = 3\text{-}6$ MeV) after 30 second interrogation with a 7 MeV neutron beam. Rapiscan Test Object “E” in homogenized clay at densities of 0.05-0.65 g/cc.

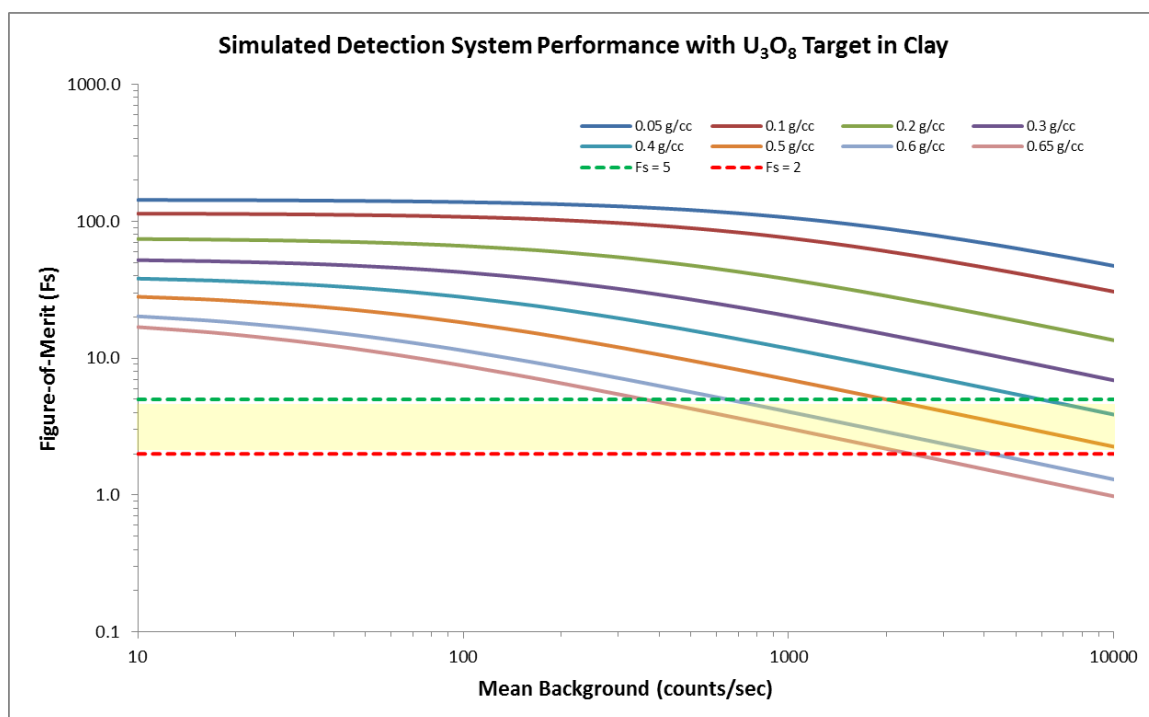


Figure 48. Simulated detection system performance based on delayed gamma emission ($E_\gamma = 3\text{-}6$ MeV) after 30 second interrogation with 7 MeV neutron and 12.2 MeV photon beams. Rapiscan Test Object “E” in homogenized clay at densities of 0.05-0.65 g/cc.

D. Iron

System performance using neutron beam interrogation with iron is shown in Figure 49. The neutron beam alone is sufficient to meet $F_s \geq 5$ at $\rho \leq 0.3$ g/cc for backgrounds up to 10000 counts/sec, and good performance is still achieved at $\rho = 0.4$ g/cc at ~2100 counts/sec (green curve). Again, the system does not meet meaningful detection goals at the highest density of 0.65 g/cc (bottom curve). Dual-beam results are presented in Figure 50. Some gain can be seen, but the photon beam still does not add enough signals for the system to meet detection goals at the highest density.

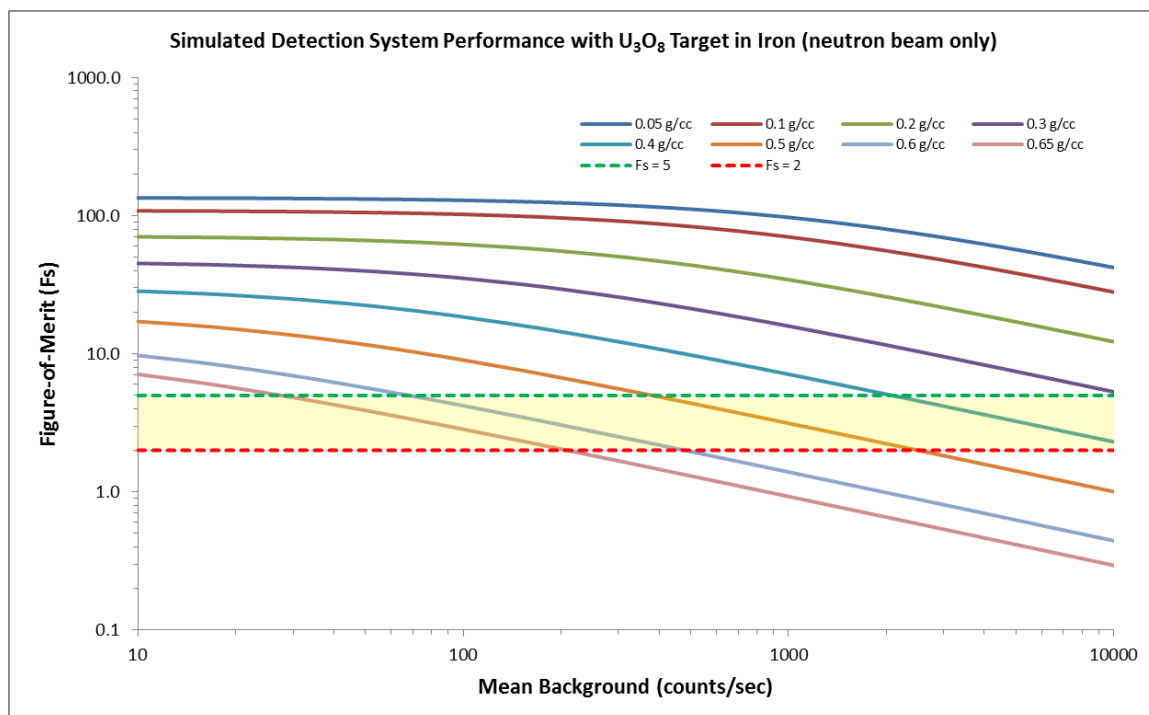


Figure 49. Simulated detection system performance based on delayed gamma emission ($E_\gamma = 3\text{-}6$ MeV) after 30 second interrogation with a 7 MeV neutron beam. Rapiscan Test Object “E” in homogenized iron at densities of 0.05-0.65 g/cc.

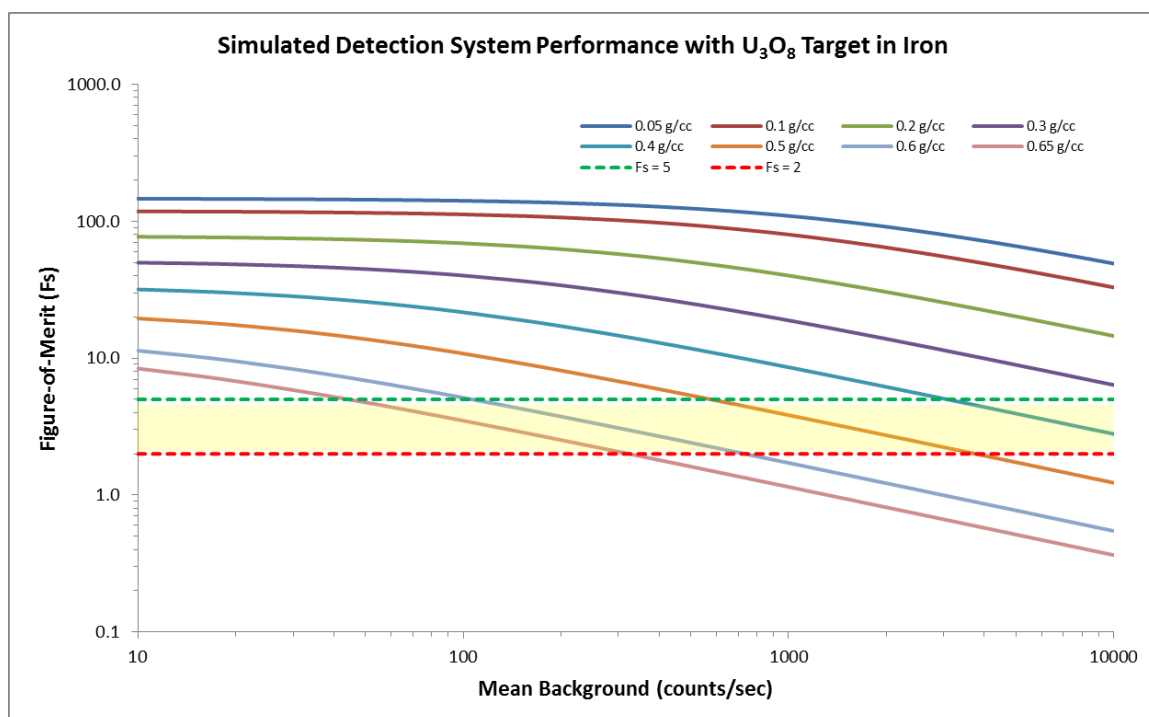


Figure 50. Simulated detection system performance based on delayed gamma emission ($E_\gamma = 3-6$ MeV) after 30 second interrogation with 7 MeV neutron and 12.2 MeV photon beams. Rapiscan Test Object "E" in homogenized iron at densities of 0.05-0.65 g/cc.

E. Summary

The delayed gamma signal produced by neutron beam interrogation met the figure-of-merit goal of $F_s \geq 5$ in all four materials at average densities up to 0.3 g/cc. This finding indicates that neutron beam interrogation alone may be sufficient to confirm the presence of SNM in this system at low average densities, regardless of Z, at active background levels $\leq 10,000$ counts/sec. This covers 80% of all container traffic and could allow for the application of the ALARA concept to commercial shipping without impacting container security. This could be achieved by reducing the beam strength (neutrons/sec) or the irradiation time (less than 30 seconds).

All four sets of figures clearly demonstrate the positive impact of pairing a 12.2 MeV photon beam with an interrogating 7 MeV neutron beam on detection system performance at $\rho > 0.3$ g/cc. The photon beam not only shifts but extends the potentially acceptable performance zone for each density to the right improving the possibility that folding outside information can assist in meeting system performance objectives at increased levels of mean background.

DISCUSSION

I. Fundamental Model and Code Suite

A. Fundamental Model

This work has successfully demonstrated that 8' cubes are reasonable interrogation volumes for modeling. The "Nuclear Car Wash" design anticipated driving entire containers through a neutron beam. This may not be necessary, or even preferred, when considering the amount of avoidable active background produced, ALARA concerns over the container contents, or inadvertent exposure of stowaways (ANSI, 2007). The fundamental model prescribes stationary interrogation of a specific section determined by folding x-ray images, shipping manifest information and other pertinent data into the decision process. The container would be transported into the interrogation portal on a conveyer system, much like that used for air cargo (ULD) screening.

B. Code Suite

The code suite was implemented as described in Martin, 2012, with minor in-suite post processing modifications as requested to ease interpretation of the output. Fission product yields were not available in the existing CINDER library for thorium-232 and were substituted using protactinium-232. On a humorous note, we had not anticipated the case where CINDER supplied zero gamma flux

results to MCNPX, resulting in a program crash. This occurs when no decay gamma-rays are created, as in the cases of the Celotex and clay surrogates without the threat target.

II. Model Implementation

A. Linearity

The preliminary data collected indicates a strong linear (semi-logarithmic) relationship between the homogenized density of the cargo and the number of delayed gammas exiting the surrogate container. This behavior was anticipated and touched upon in Pruet et al., 2005, and may have a positive impact on the ability to predict performance given lower (or higher) beam source strengths (particles/sec). Over the density range involved, it is conceivable that one would only need to ascertain the slopes of the lines for various homogenized materials at fixed beam energies to be able to make accurate predictions of delayed gamma production for differing source strengths from a given target.

B. Target Detection

Due to the unique nature of delayed gamma-ray emission, the beam energies used and their strengths (5×10^8 particles/sec at cargo surface), the modeled system here would certainly identify this uranium oxide target as a potential SNM threat. This statement is further reinforced when considering that the method

used to determine F_s is very conservative. Finally, the beam strengths anticipated for a deployed system would be substantially higher, perhaps 10^9 particles/sec or more. Increased photon beam energy is also possible using bremsstrahlung sources.

III. Dual-Beam Interrogation

A. Additivity of Beam Results

One can assume simple additivity for interrogation results when beams are applied separately for this system. An example using the very low density aluminum surrogate is tabulated in Tables 3, 4 and 5. The signals created by each beam are essentially independent and amenable to simple addition with regard to the figure-of-merit (F_s) calculation using this threat target and homogenized cargos over the density range of 0.05-0.65 g/cc. Further analysis of the cross production of (n,f) and (γ ,f) produced by the beams in the target proper support this observation:

- Dual-beam: (n,f) = 13690/cc-sec, (γ ,f) = 2503/cc-sec
- Neutron beam: (n,f) = 13640/cc-sec, (γ ,f) = 0.1545/cc-sec
- Photon beam: (n,f) = 48.37/cc-sec, (γ ,f) = 2503/cc-sec

The fission (γ ,f) contribution is trivial as $E < 8$ MeV for gamma-rays associated with fission (Maienschein et al., 1958). Follow on (n,f) from photofission yields an increase in the overall rate of just 0.35% to the dual-beam case – not enough to

significantly alter delayed gamma emission as witnessed. This is an important consideration lending itself to the possibility of estimating the contribution from photon beam interrogation when system performance falls into the marginal, or informative, yellow zone after neutron interrogation alone. There should be comparatively little addition to the active background (photonuclear reactions other than photofission appear to contribute little to the active background and are ignored when determining σ). The figure-of-merit could then be estimated assuming the presence of SNM and a determination made as to whether or not the additional delayed gamma signal would cross the threshold for reliable system performance. If not, then an unnecessary irradiation would be avoided and other avenues, such as removal of a portion of the container's contents followed by intensive passive scanning, may be employed.

Table 3: Delayed Gamma Tally, 3-4 MeV

Time (sec)	N	P	N + P	N & P
7	9065	1579	10644	10647
8	8325	1459	9784	9783
9	7693	1356	9050	9051
10	7148	1268	8417	8414
15	5293	962	6255	6253
20	4254	788	5042	5039
25	3600	676	4276	4276
30	3146	596	3742	3742
35	2805	535	3340	3338
40	2533	486	3018	3018

Delayed gamma current ($E = 3\text{-}4\text{ MeV}$) through one vertical side of surrogate container cube at one second intervals from 7-10 seconds and five second intervals from 10-40 seconds after 30 second interrogation with 7 MeV neutron (N), 12.2 MeV photon (P) or both (N & P) beams. Rapiscan Test Object "E" in homogenized aluminum at a density of 0.05 g/cc.

Table 4: Delayed Gamma Tally, 4-5 MeV

Time (sec)	N	P	N + P	N & P
7	2726	496	3222	3223
8	2537	465	3003	3005
9	2374	438	2812	2813
10	2232	414	2647	2648
15	1721	327	2049	2050
20	1423	276	1699	1700
25	1232	242	1474	1475
30	1100	217	1317	1318
35	999	198	1197	1199
40	918	183	1101	1102

Delayed gamma current ($E = 4\text{-}5\text{ MeV}$) through one vertical side of surrogate container cube at one second intervals from 7-10 seconds and five second intervals from 10-40 seconds after 30 second interrogation with 7 MeV neutron (N), 12.2 MeV photon (P) or both (N & P) beams. Rapiscan Test Object “E” in homogenized aluminum at a density of 0.05 g/cc.

Table 5: Delayed Gamma Tally, 5-6 MeV

Time (sec)	N	P	N + P	N & P
7	1031	197	1228	1228
8	937	180	1117	1118
9	854	165	1019	1020
10	782	152	934	934
15	532	106	639	639
20	397	82	478	478
25	322	67	389	390
30	275	59	334	333
35	244	53	296	296
40	221	48	269	268

Delayed gamma current ($E = 5\text{-}6\text{ MeV}$) through one vertical side of surrogate container cube at one second intervals from 7-10 seconds and five second intervals from 10-40 seconds after 30 second interrogation with 7 MeV neutron (N), 12.2 MeV photon (P) or both (N & P) beams. Rapiscan Test Object "E" in homogenized aluminum at a density of 0.05 g/cc.

B. Photon Beam Contribution

In all cases, the addition of the 12.2 MeV interrogating photon beam increased the number of delayed gammas tallied. As expected, the relative increase from the neutron beam experiments declined with increasing Z as the photon beam was more highly attenuated. The increased attenuation led to fewer photons being transported at a reduced average energy to the target, and consequently generating fewer photofission events. The Celotex case exhibited the most improvement, at the highest densities, as the photon beam doubled the delayed gamma signal demonstrating the benefit of the additional photon beam in a hydrogenous low Z cargo. Clay is a transitional material in this respect. A summary of beam contribution ratios is provided in Table 6 for Celotex, aluminum, clay and iron. For dual-beam interrogation of the threat target in air, the neutron beam contributes 85% to the delayed gamma signal versus 15% by the photon beam. A visual explanation of Table 6 is shown in Figure 51.

Table 6: Contribution of Neutron vs. Photon Beam to the Total Delayed**Gamma Signal**(Percentage per **neutron**/**photon** beam)

Density (g/cc)	Celotex Z \approx 4 (%)	Aluminum Z = 13 (%)	Clay Z \approx 7 (%)	Iron Z = 26 (%)
0.05	81/ 19	84/ 16	84/ 16	85/ 15
0.1	78/ 22	83/ 17	81/ 19	85/ 15
0.2	77/ 23	79/ 21	77/ 23	84/ 16
0.3	76/ 24	76/ 24	77/ 23	83/ 17
0.4	71/ 29	72/ 28	78/ 22	82/ 18
0.5	65/ 35	67/ 33	80/ 20	82/ 18
0.6	55/ 45	63/ 37	82/ 18	81/ 19
0.65	49/ 51	61/ 39	82/ 18	81/ 19

Individual beam contributions (neutron/**photon**) to cumulative delayed gamma signal after interrogation with 7 MeV neutron and 12.2 MeV photon beams. Rapiscan Test Object “E” in homogenized Celotex, aluminum, clay or iron at densities of 0.05-0.65 g/cc.

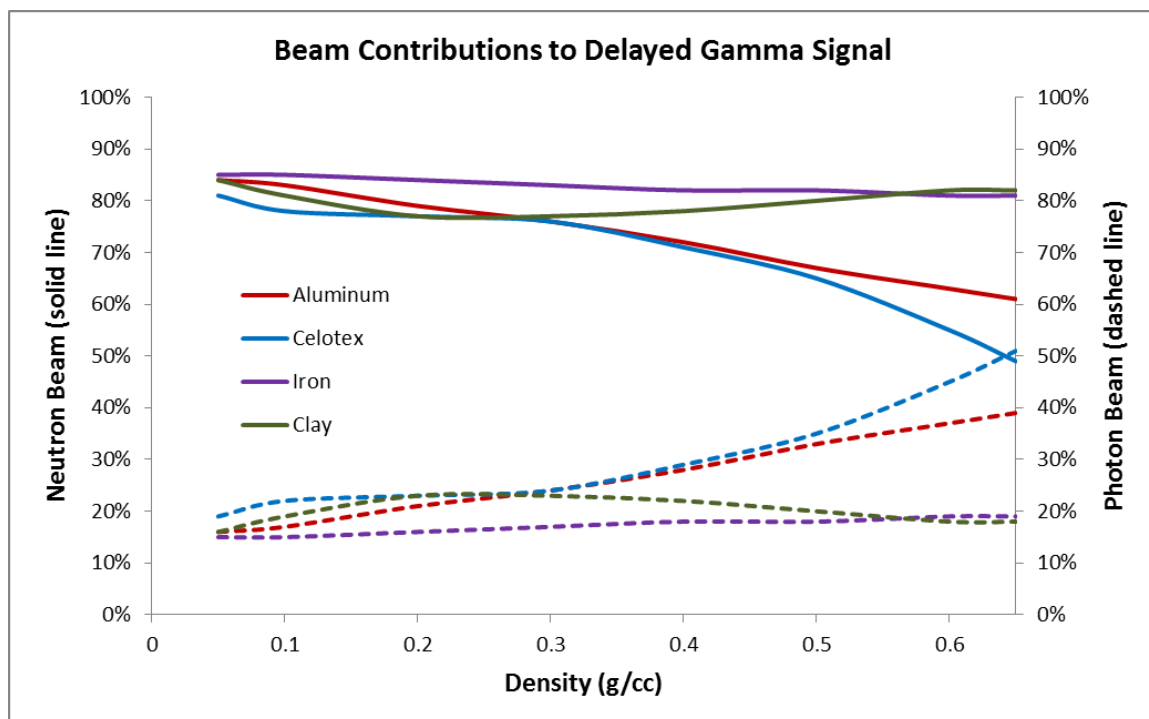


Figure 51. Smoothed beam contributions to cumulative delayed gamma signal after interrogation with 7 MeV neutron and 12.2 MeV photon beams. Rapiscan Test Object “E” in homogenized Celotex, aluminum, clay or iron at densities of 0.05-0.65 g/cc.

C. Teflon

Fluorine is an excellent mask, even though it is easily identified from the nitrogen-16 decay gamma spectrum it produces. The reason is the large, flat signal created in the detector for $E < 5$ MeV. Very little fluorine-19 is needed to generate enough noise to render any signal-to-noise (S/N) measurement in this type of scintillator inconclusive, and it is doubtful that subtracting this noise source could be done reliably. This can be addressed if a single photon beam is used as nitrogen-16 would not be created. Oddly enough, if fluorinated materials were used to attempt to mask SNM signals from neutron interrogation, they may act as an amplifier when photofission is induced. The average energy of fission neutrons is ~ 2 MeV, which is at the threshold energy for fluorine-19 activation (see Table 2).

IV. **On-Site Modeling**

The delayed gamma current results were produced in very reasonable clock times on a laptop computer. A rapid method could be developed to anticipate a detector response from interrogating an 8' section of a shipping container. Below is a trial procedure for modeling a container on-site:

1. Obtain the manifest, net weight and a coarse x-ray of the container contents.

2. Segment the cargo and homogenize, if feasible, based on Z_{avg} (paper, aluminum, brick, steel, etc.); if not, use as few homogenized MCNPX macrobodies as possible (cubes, spheres, etc.).
3. An example of macrobody use would be a challenging cargo such as a car (Figure 52). The engine compartment could be modeled as a cube of medium-high density iron with the balance of the car volume homogenized and presented as a rectangular parallelepiped of low density aluminum.
4. The operator only needs a look-up to define the material Z category based on the manifest.
5. Use rigging/hoisting techniques to determine density estimates of each segment/macrobody (Figure 53).
6. Each segment follows the 8' x 8' x 8' model = 0.4 TEU.
7. Prior information gathered on the container history and contents should limit scanning to one or two segments.
8. If the whole container requires scanning, then a 40' container is divided into five segments and a 20' container is divided into two segments (ignoring the 2' on each end; in fact, anything < 4').
9. Locate a DNDO threat object in the center of mass of each segment.
10. Approximately 10^6 Monte Carlo histories for all particles should be sufficient to achieve one significant figure in the delayed gamma current result.

11. Model using a photon beam alone if fluorine-19 is suspected.
12. Look at the $E_\gamma = 3\text{-}6$ MeV current and multiply by 0.3 for a PVT detector estimate.
13. Now have an idea of the detector response prior to actual interrogation, if something is really there.
14. Inject this information into the decision process to reduce uncertainty in clearing (or condemning) the container.

The resources necessary to deploy an active interrogation system at a port would be considerable, \$1 million+, using the passive Advanced Spectroscopic Portal (ASP) program target of \$822,000 per installed system as a benchmark (GSN, 2011). The computational hardware requirement for fast modeling should be financially practicable and defensible if unnecessary interrogations can be avoided.

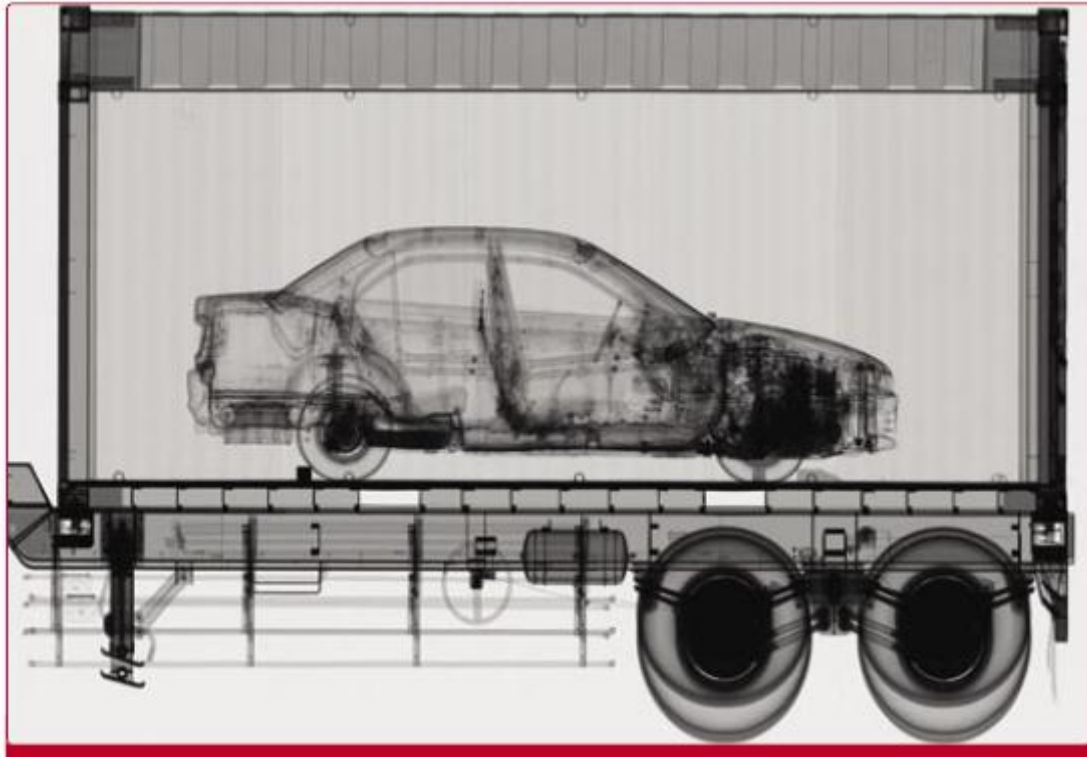


Figure 52. What about when general homogenization is not feasible (from Reed, 2007)?

Load Weights - Calculating

6

Materials and Liquids - Pounds / cu. ft.				Pounds / sq. ft.	Pounds / gal.
Aluminum	165	Iron Casting	450	Steel plate	Gas 6.0
Asbestos	153	Lead	708	• 1/8" 5	Diesel 7.0
Asphalt	81	Lumber - Fir	32	• 1/4" 10	Water 8.3
Brass	524	Lumber - Oak	62	• 1/2" 20	
Brick	120	Lumber - RR Ties	50	• 1" 40	
Bronze	534	Oil, Motor	58	Aluminum plate	• 7.5 gallons of liquid to a cubic foot
Coal	56	Paper	58	• 1/8" 1.75	• 27 cubic feet to a cubic yard
Concrete, Reinf.	150	Portland Cement	94	• 1/4" 3.50	• 2,000 lbs = 1 U.S. ton
Crushed Rock	95	River Sand	120	Lumber	
Diesel	52	Rubber	94	• 3/4" Fir 2	
Dry Earth, Loose	75	Steel	480	• 3/4" Oak 4	
Gasoline	45	Water	63		
Glass	162	Zinc	437		

Formulas and Information			
• H = Height	• W = Width	• L = Length	• d = diameter
• Area of square or rectangle = LW	• Vol. of cube = HWL	• Area of circle = πr^2	• Circumference = πd
• The area of a circle is approx. 80% of its diameter squared (diameter x diameter)			
• Load Weight (to estimate) _____	Volume in cu. ft. x 500 lbs. x density factor .02, .05, .10, .20, .30 etc.		

Figure 53. Load weight estimation reference example for use in determining the density of MCNPX macrobodies when general homogenization is not feasible (from WRRRC, 1990).

V. Uncertainty Quantification

The ability to computationally model a proposed particle interrogation system for detecting SNM requires a comprehensive assessment of both the probabilistic and non-probabilistic uncertainties involved. The interest lies in the ability to achieve realism and to inject the additional information gleaned from these computational models into the overall container security decision chain.

A. Reducing σ

Reducing the value of the standard deviation term, σ , in the F_s calculation is critical. The conservative approach applied, artificially doubling σ , attempts to bound the variations encountered in actual background measurements likely leading to an under-valuation of true system performance in an ideal model. Systematically shrinking σ would be accomplished by identifying and minimizing the sources of uncertainty associated with the mean experimental background measurement, such as instrumentation drift, line voltage noise or changes in ambient temperature, more effectively linking the model to the proposed system. This is a continuous improvement process that begins by establishing an “uncertainty inventory.” This inventory is an accounting of the various kinds of uncertainties involved, ranging from irreducible random noise to reducible lack-of-knowledge (Langenbrunner et al., 2008). The inventory includes a review of the data available and devising ideas for how this information may be quantified

and used to provide estimates for each uncertainty relevant to improving the predictive capability of computational models for active interrogation systems.

B. Cargo Composition

A major leap in detection chain efficiency is realized if only the mass of the cargo and its approximate distribution in the container were required for the interrogation process to determine the presence of SNM. This can be approached through forward uncertainty propagation, or “propagating uncertainties through simulation models using varying parameter settings” (Lin et al., 2012). In fact, this has been carried out to some extent by changing cargo compositions in the fundamental model while all other aspects remained fixed.

Limited analyses of dual-beam computational experiments were piloted using the maximal information-based nonparametric exploration (MINE) statistical package (Reshef et al., 2011). This novel toolkit provides an avenue to identify and explore associations and relationships in the data that are not well modeled by a function through determination of a maximal information coefficient (MIC). The MIC is founded on mutual information, a general measure of dependence between a pair of random variables, initially outlined by Linfoot (1957). In Table 7, MINE is applied to the five material comparison of the delayed gamma current work to exercise the tool and confirm the linear behavior observed in Figure 27.

Table 7: MINE Statistics Example

X var	Y var	MIC (strength)	MAS (non- monotonicity)	MEV (functionality)	MCN (complexity)	Linear regression (p)
density	celotex	1	0	1	2	-0.88204557
density	aluminum	1	0	1	2	-0.8642583
density	iron	1	0	1	2	-0.86429983
density	clay	1	0	1	2	-0.85958856
density	tungsten	1	0	1	2	-0.8806098

MIC - Maximal Information Coefficient



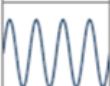
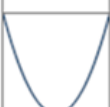



MAS – Maximum Asymmetry Score

MEV – Maximum Edge Value

MCN – Minimum Cell Number

An example applying the MINE statistical package to confirm some linear properties initially observed in the five material comparisons of Figure 27.

Reshef provides a chart of MINE statistics calculated for some ideal sample associations:

Data	MIC	MAS	MEV	MCN
	1.00	0.00	1.00	2.00
	1.00	0.74	1.00	3.00
	1.00	0.89	1.00	4.00
	1.00	0.69	1.00	2.56
	0.79	0.16	0.70	6.91
	0.71	0.03	0.32	6.87
	0.46	0.19	0.22	6.98

- Maximal Information Coefficient (MIC) = relationship strength
- Maximum Asymmetry Score (MAS) = departure from monotonicity
- Maximum Edge Value (MEV) = closeness to being a function
- Minimum Cell Number (MCN) = complexity

Detailed explanation of each measure is beyond the scope of this simple example; it is sufficient to know that an MIC approaching unity is an indicator of a strong relationship between the cargo density and delayed gamma current for

each material. A comparison of the MINE output in Table 7 to the top line of the chart confirms the linear properties observed in the dual-beam current results.

The next logical application is to compare the delayed gamma results from each material in a series of stepped densities between the cargo wall and threat target, gradually moving away from homogeneity. Evaluating a complex series of simulations in this fashion, but still maintaining $\rho = 0.05\text{-}0.65$ g/cc within each step, establishes a basis from which to judge the strength of the association between cargos. This would be principally useful with regard to neutron interrogation because clumpy cargos can be substantially more attenuating than homogeneous ones.

C. 4-Box Approach

With a library of dual-beam simulation results using relevant test objects, attainable sources and general categories of homogenized cargos established, how could this information be incorporated into an evaluation of the entire container security system? One method under investigation is the 4-box approach (Figure 54).

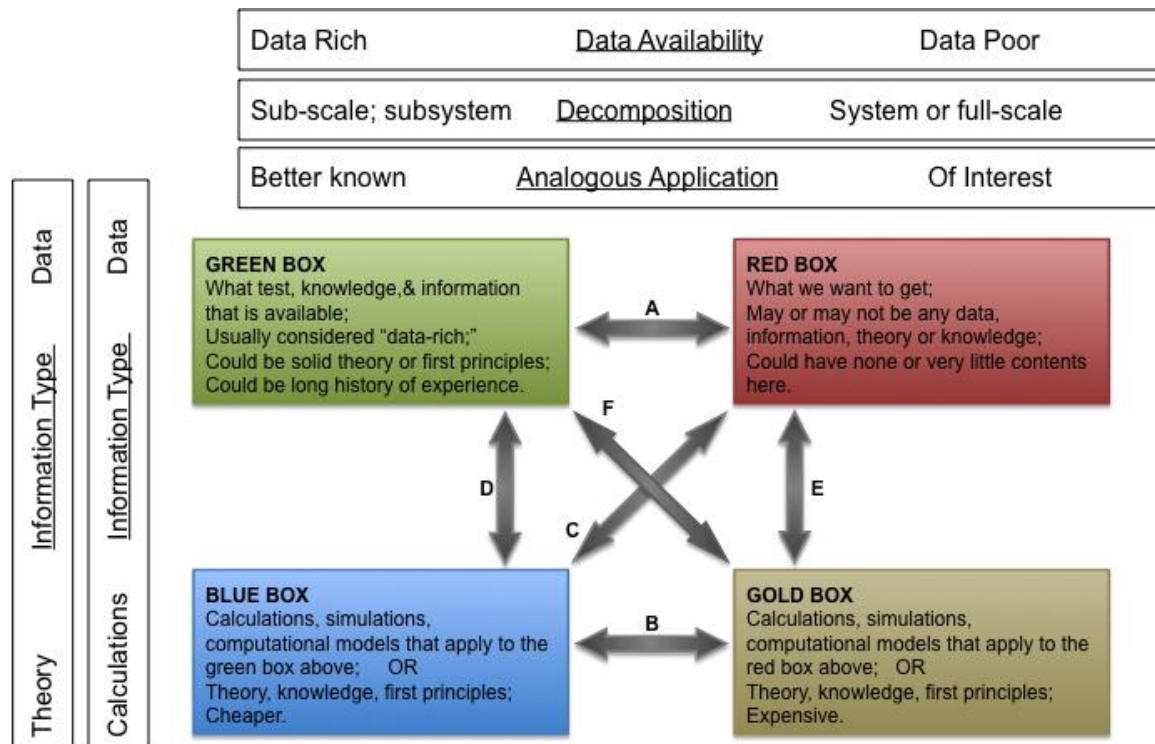


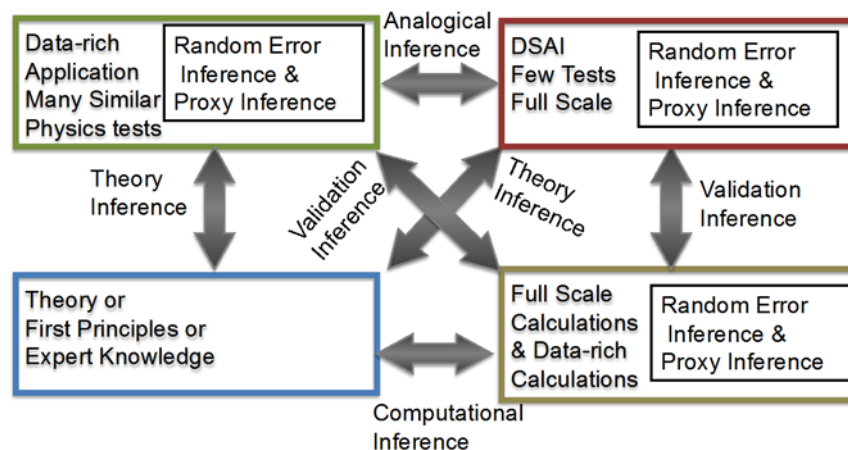
Figure 54. The 4-box approach depicting various descriptions and contents of each box and the six inference connections (from de Oliveira et al., 2011).

The 4-box approach is a tool to quantify “inference uncertainty.” Inference uncertainty is produced when deriving a conclusion about something that is unmeasured or unattainable based on what is known at the time. The 4-box approach is a vehicle that integrates the knowledge available and quantifies and aggregates the various uncertainties involved (Langenbrunner et al., 2008; 2009; 2010a; 2010b). The goal is to infer real world performance from experiments, simulations and theory, particularly at the system level. The four boxes are generally defined as follows:

- The Red Box is the system or problem of interest, which has insufficient data to provide conclusions on its own and must be supported, supplemented, or augmented by the data, knowledge and information contained in the other boxes. This could be the SNM detection success rate for a deployed active interrogation system scanning a container stuffed with consumer electronics.
- The Gold Box contains the calculations or high fidelity computational models corresponding closely to the Red Box application of interest. The level of computation will generally be very expensive.
- The Green Box is a sub-scale, sub-system or analogous version of the Red Box problem. The “Nuclear Car Wash” work conducted at LLNL is a good example of an experimental campaign that falls within this box.

- The Blue Box includes theory, first principles, historical records and knowledge elicited from subject matter experts, and 1-D, 2-D, or simple 3-D calculations or computational models. This dissertation is an excellent example.

The data, information, and knowledge contained in the supporting boxes are combined with that of the Red Box based on Saaty's Analytical Hierarchy Process for decision making (Saaty, 1980). The integration takes place at the "box" level (from de Oliveira et al., 2011):



If the boxes contain the top or system level, then results for the integration are at the same level. The integration methodology quantifies probabilistic and non-probabilistic uncertainties inside each box, plus the inference uncertainties between boxes (the arrows), to produce an integrated uncertainty value for the

real world application in the Red Box. Even applying the 4-box technique, mathematical research and development work will be required to accommodate the integration of different uncertainty theories specific to active interrogation systems based on the uncertainty inventory.

VI. Future Studies

A. Other Photon Beam Energies

The code suite can be easily modified to investigate photon beam energies other than 12.2 MeV. One beam under consideration is a 9.2 MeV monoenergetic source, despite the lower energy, because it is below the 10 MeV x-ray energy limit to inspect food (Moss et al., 2006; FDA, 2001). Another beam could be modeled from a 30 MeV end-point bremsstrahlung source that yields, according to Figure 5, a nearly ideal 14.7 MeV average energy (Jacobs et al., 1979). Neutron beam energy is essentially capped at 10 MeV because of neutron activation issues but energies < 10 MeV, or a spectrum, would be easy to institute as well.

B. Phosphogypsum

Phosphogypsum ($\text{CaSO}_4 \cdot 2\text{H}_2\text{O}$) is a by-product created during the manufacture of phosphoric acid by reacting phosphate ore (apatite) with sulfuric acid. Some phosphate ores can be highly radioactive, and contaminants like radium, uranium

and thorium wind up in this synthetic gypsum rendering it largely useless (Table 1). This characteristic, combined with an intermediate Z_{avg} and ease of acquisition, make it a potentially interesting masking and shielding material for defeating passive and/or active scanning. Reproducing a data set like that done for clay would be time consuming, but not complicated, again demonstrating the flexibility of the fundamental model and code suite.

C. Exploiting Poor Data

The figure-of-merit (F_s) determination for system performance is based on cumulative detector counts in an energy window over a fixed time:

$$F_s = \frac{S}{\sigma}$$

where,

S = delayed gamma signal from interrogation

σ = expression for standard deviation term

Can the figure-of-merit be modified to reflect “poor” information? Preferably the focus would be on modifying the numerator, making a direct addition to the signal without substantively affecting the complex standard deviation term. Any improvement to F_s (e.g. $3 \rightarrow 3.5$) using the data already collected (good, bad or

indeterminate) from the interrogation would be excellent. It may take the form of a simple weighting factor:

$$F_S = \frac{S(1 + \omega)}{\sigma}$$

with ω as a function of the observed decay rate at $T < 6$ seconds post-irradiation, or a measure of $E_\gamma < 3$ MeV, where short-lived low energy activation products make SNM-derived delayed gamma signal counting unreliable. A set of experiments could be devised using a threat target that initially results in F_S very near some target threshold using the original method. Careful examination of the poor data may reveal a reliable trend that would allow a fractional increase in S .

VII. Conclusion

Active interrogation is a powerful tool worth the expense and complexity if confidence in the results is high. When applied to the search for special nuclear material in shipping containers, limiting false positives reduces the overall expenditure on security and the impact on the speed of commerce. On the other hand, eliminating false negatives implies absolute discovery and “the net cost to protect the country from a WMD [Weapon of Mass Destruction] arriving in a container could be negligible” (Bjorkholm and Boeh, 2006).

The intention of this dissertation is to provide practical engineering information and techniques for use in the design and operation of proposed active interrogation portals or related applications. This research has added the following to the active interrogation knowledge base:

- A systematic method to evaluate containers using a novel code suite.
- A dual-beam model incorporating photons and neutrons for active interrogation.
- A body of Monte Carlo results applying the method to evaluate the model and ascertain the efficacy of a photon beam in applicable materials.

The results produced lead to these primary findings:

- Dual-beam interrogation produces a superior delayed gamma-ray signal to neutron beam interrogation in all cases.
- Neutron beam interrogation alone may be sufficient for cargos of average density $< 0.3 \text{ g/cc}$.
- Only a general idea of cargo composition may be needed to effectively model a threat.

The addition of a photon beam to an active interrogation portal should provide the following advantages:

- Photonuclear reactions other than photofission contribute little to the active background. Fluorinated cargo is a key example.
- 12.2 MeV photons demonstrate superior penetration in hydrogenous materials.
- Neutron beam production and shielding concerns make photon beam interrogation an attractive addition.
- ALARA neutron dose considerations to commercial cargo can be reduced if photon beam interrogation can serve as a supplement (subject to its own legal limitations).
- In limited cases, such as encountering fluorinated cargo, if system performance requirements are relaxed (i.e. an increase in the false alarm rate is tolerated) photon interrogation alone may be sufficient to adequately scan and clear a container.

The ability to computationally assess every conceivable container/threat scenario is not currently possible. In the meantime, the careful application of well thought-out, simplifying assumptions to the issue of container security can transform the computer from an adding machine into an “intelligence amplifier” (Weinberg, 1972). In conjunction with data mining devices like MINE, and innovative

uncertainty quantification methods like the 4-box approach, powerful tools are available for exploring (and exploiting) the information from active interrogation research using only modest computational resources. The author has gained many insights by taking a system view of the shipping container industry as a whole and will apply these lessons from the “science of simplification” to future research, regardless of the field.

APPENDIX A

Simulated Detector Responses with U_3O_8 Target in Air

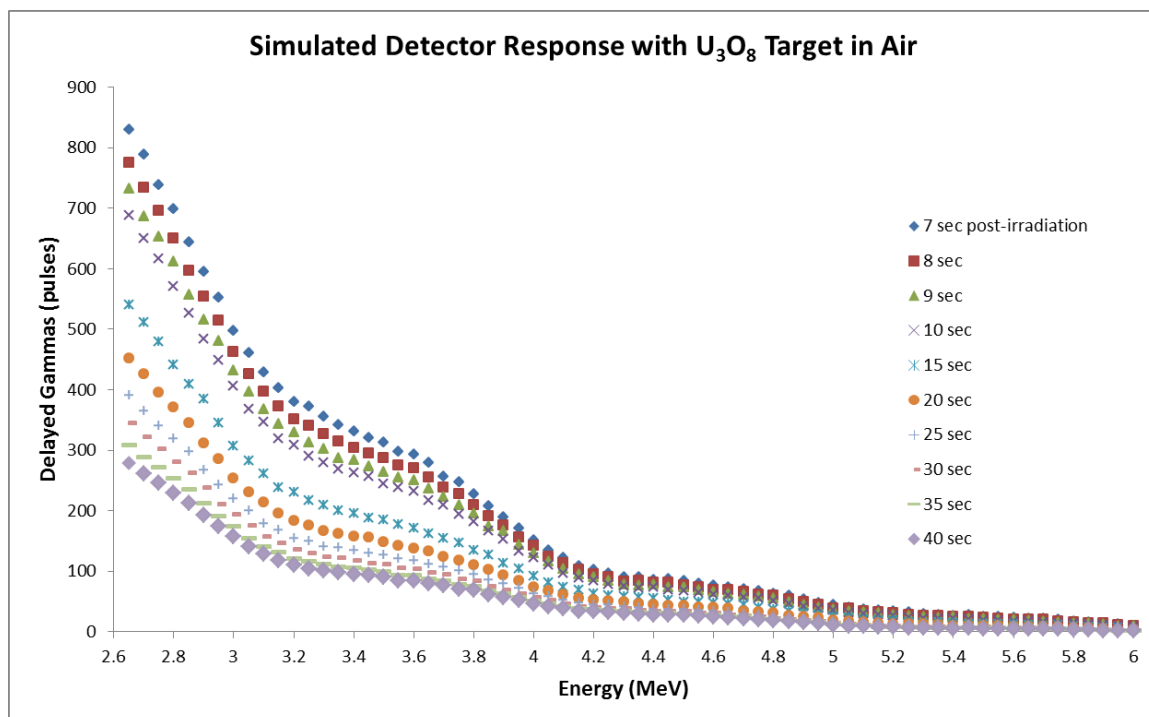


Figure 55. Simulated detector response to delayed gamma emission at one second intervals from 7-10 seconds and five second intervals from 10-40 seconds after 30 second interrogation with 7 MeV neutron and 12.2 MeV photon beams. PVT detector adjacent to one vertical side of surrogate container cube. Rapiscan Test Object “E” in air at 0.001275 g/cc (ISA).

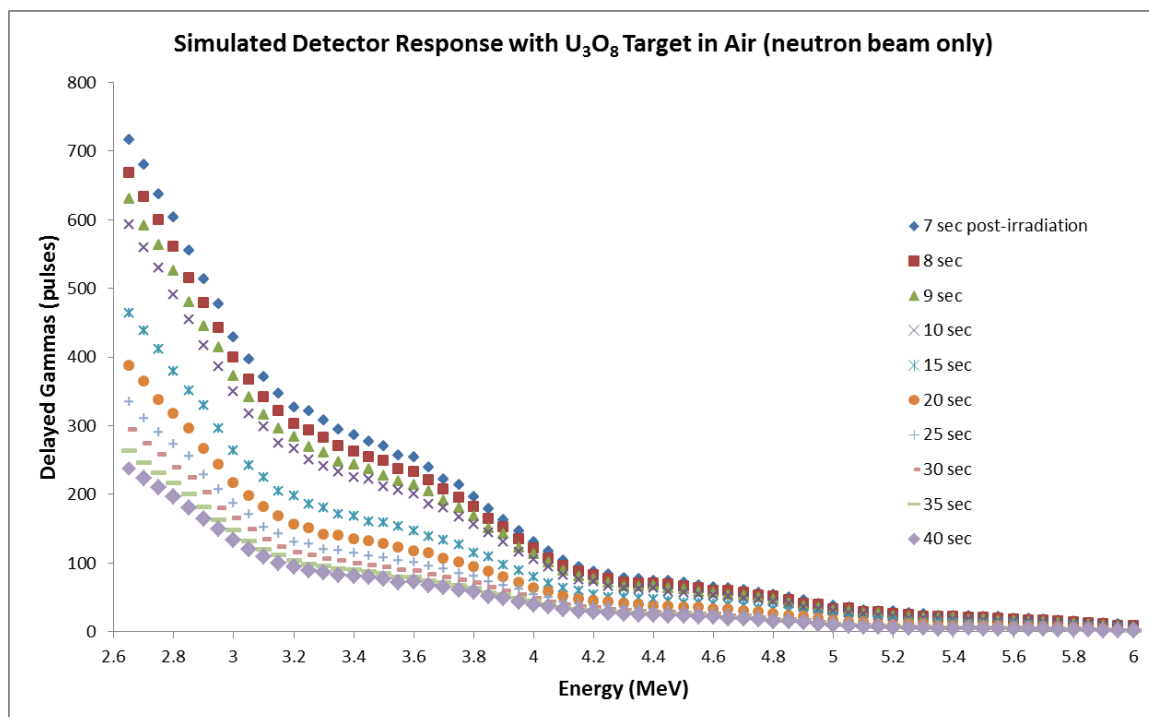


Figure 56. Simulated detector response to delayed gamma emission at one second intervals from 7-10 seconds and five second intervals from 10-40 seconds after 30 second interrogation with 7 MeV neutron beam. PVT detector adjacent to one vertical side of surrogate container cube. Rapiscan Test Object "E" in air at 0.001275 g/cc (ISA).

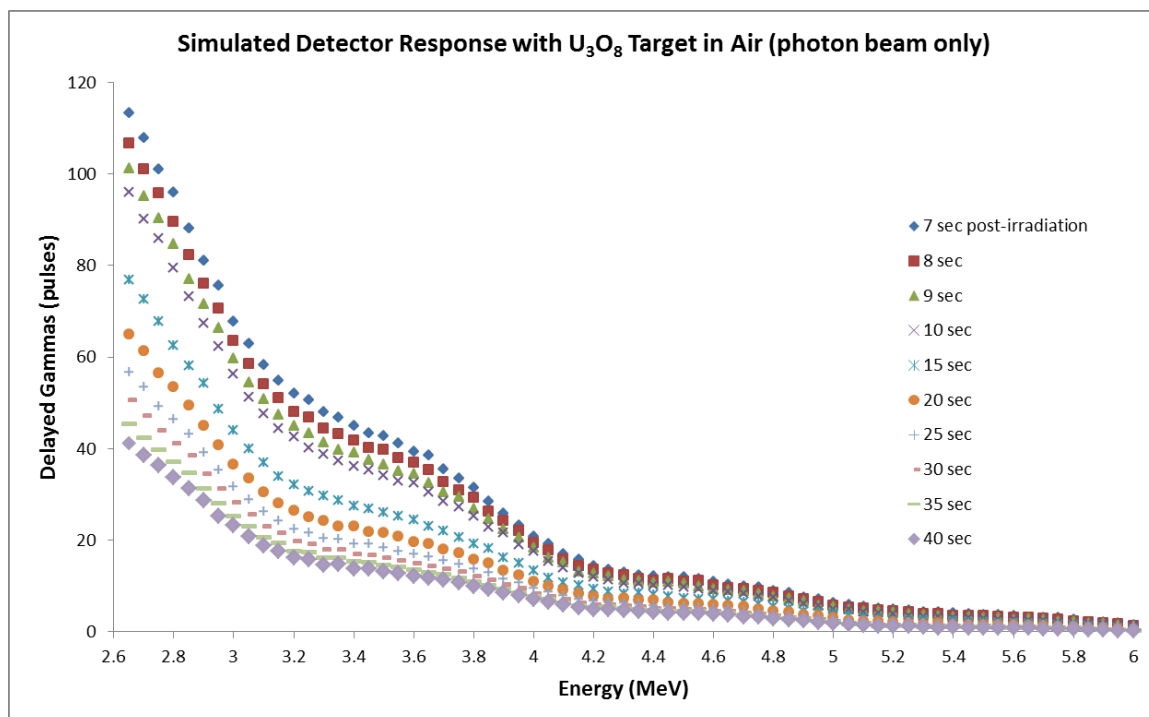


Figure 57. Simulated detector response to delayed gamma emission at one second intervals from 7-10 seconds and five second intervals from 10-40 seconds after 30 second interrogation with 12.2 MeV photon beam. PVT detector adjacent to one vertical side of surrogate container cube. Rapiscan Test Object "E" in air at 0.001275 g/cc (ISA).

APPENDIX B

Simulated Detector Responses with U₃O₈ Target in Celotex

B1. Simulated Detector Responses with U_3O_8 Target in 0.05 g/cc Celotex

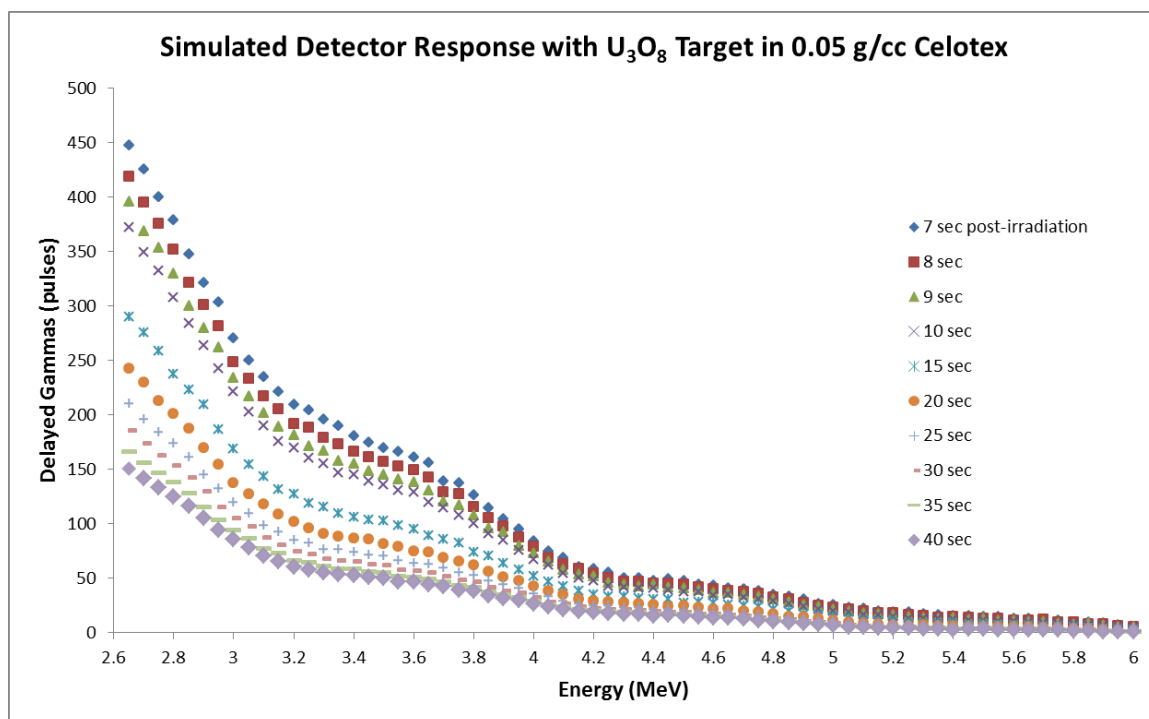


Figure 58. Simulated detector response to delayed gamma emission at one second intervals from 7-10 seconds and five second intervals from 10-40 seconds after 30 second interrogation with 7 MeV neutron and 12.2 MeV photon beams. PVT detector adjacent to one vertical side of surrogate container cube. Rapiscan Test Object "E" in Celotex at 0.05 g/cc.

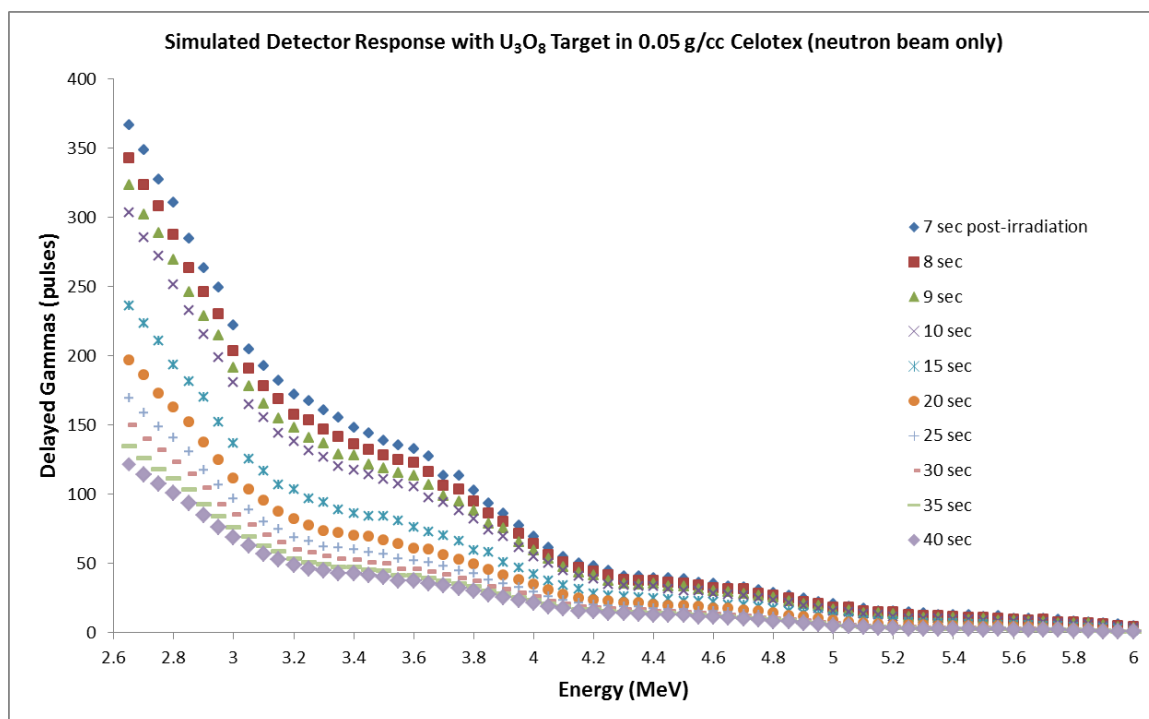


Figure 59. Simulated detector response to delayed gamma emission at one second intervals from 7-10 seconds and five second intervals from 10-40 seconds after 30 second interrogation with 7 MeV neutron beam. PVT detector adjacent to one vertical side of surrogate container cube. Rapiscan Test Object “E” in Celotex at 0.05 g/cc.

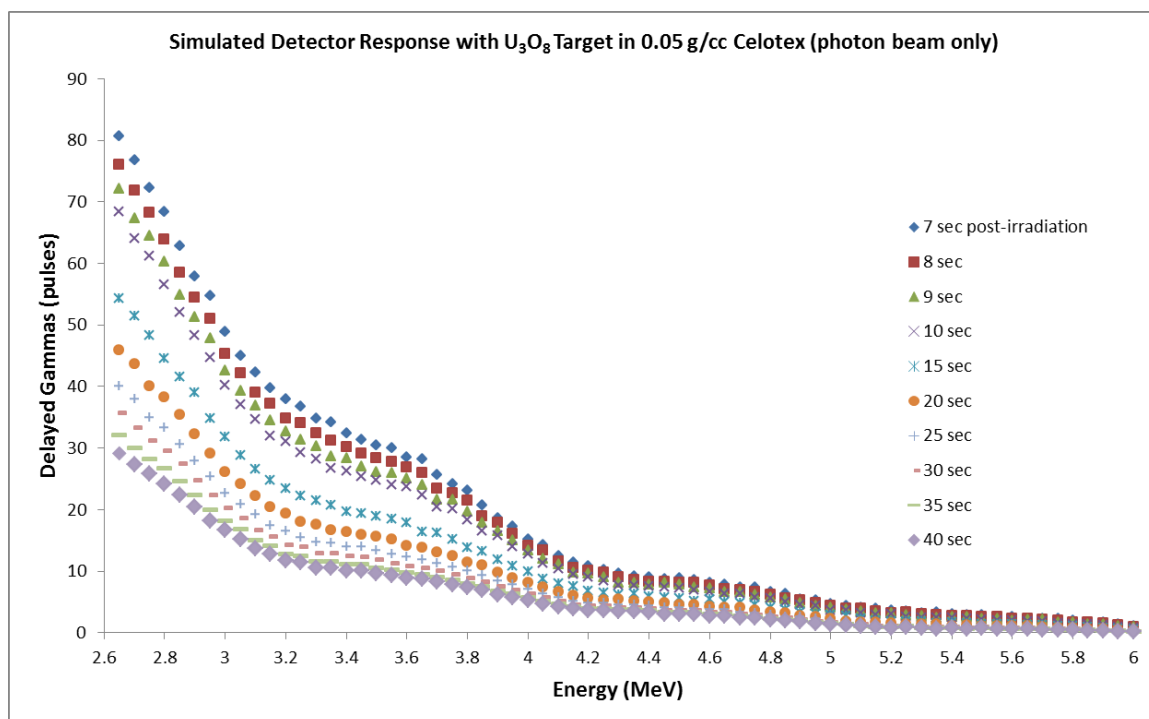


Figure 60. Simulated detector response to delayed gamma emission at one second intervals from 7-10 seconds and five second intervals from 10-40 seconds after 30 second interrogation with 12.2 MeV photon beam. PVT detector adjacent to one vertical side of surrogate container cube. Rapiscan Test Object “E” in Celotex at 0.05 g/cc.

B2. Simulated Detector Responses with U_3O_8 Target in 0.1 g/cc Celotex

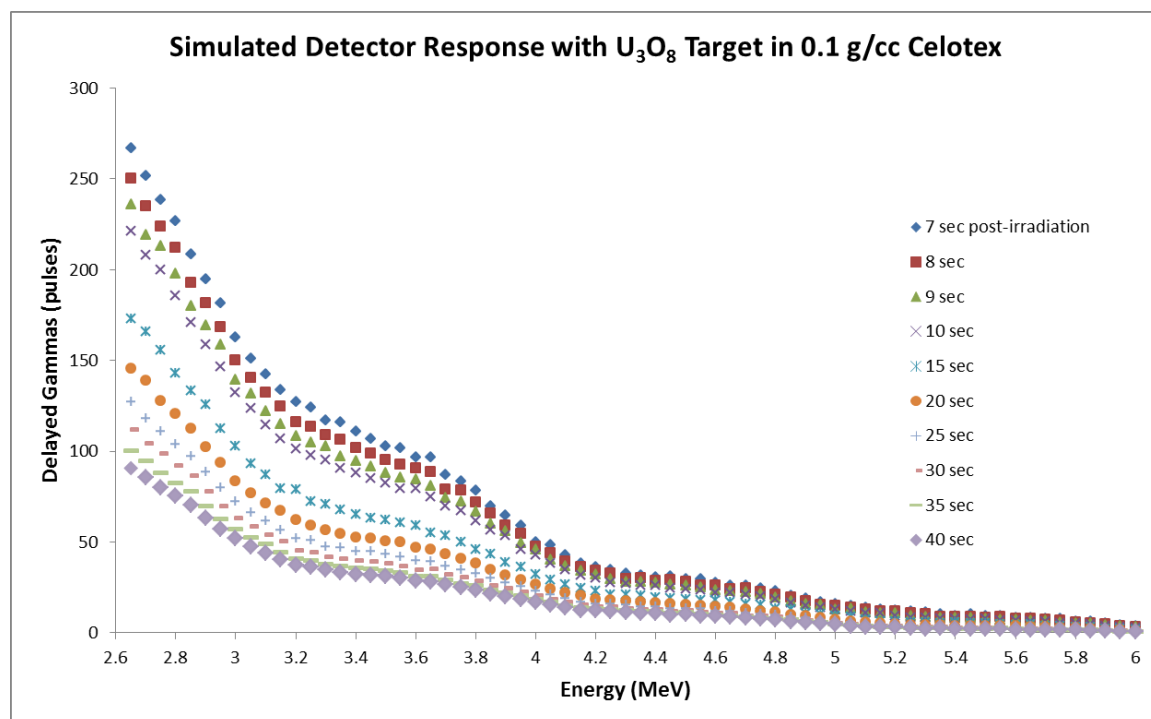


Figure 61. Simulated detector response to delayed gamma emission at one second intervals from 7-10 seconds and five second intervals from 10-40 seconds after 30 second interrogation with 7 MeV neutron and 12.2 MeV photon beams. PVT detector adjacent to one vertical side of surrogate container cube. Rapiscan Test Object "E" in Celotex at 0.1 g/cc.

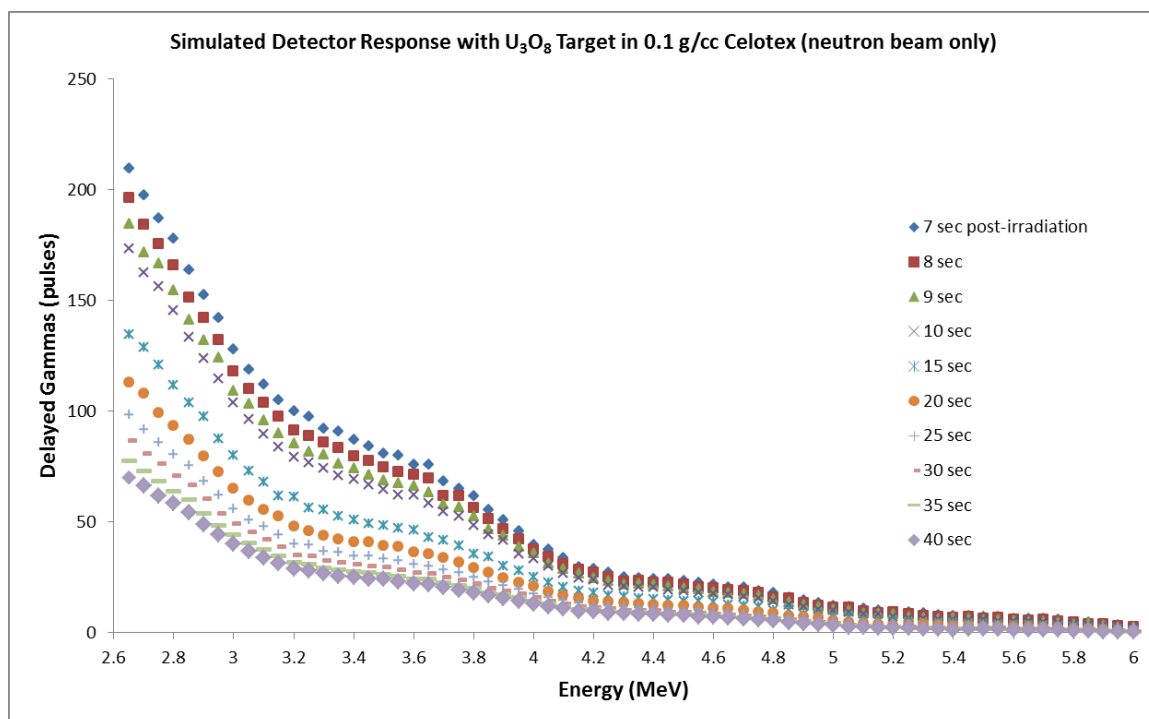


Figure 62. Simulated detector response to delayed gamma emission at one second intervals from 7-10 seconds and five second intervals from 10-40 seconds after 30 second interrogation with 7 MeV neutron beam. PVT detector adjacent to one vertical side of surrogate container cube. Rapiscan Test Object “E” in Celotex at 0.1 g/cc.

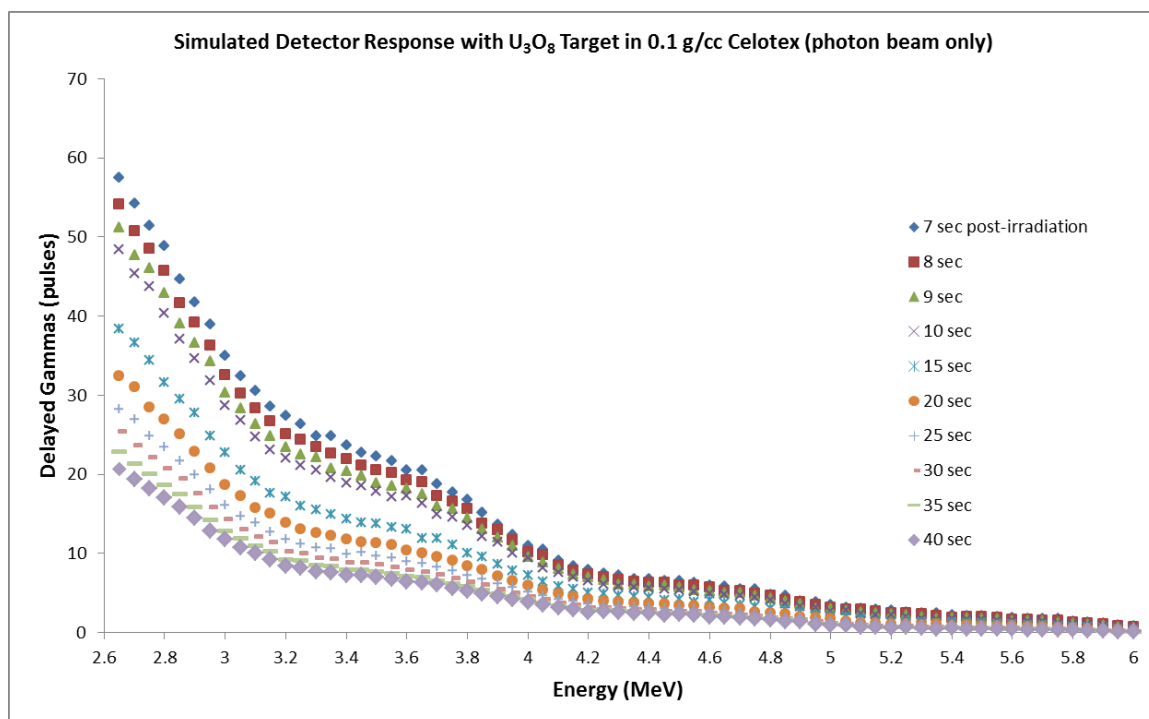


Figure 63. Simulated detector response to delayed gamma emission at one second intervals from 7-10 seconds and five second intervals from 10-40 seconds after 30 second interrogation with 12.2 MeV photon beam. PVT detector adjacent to one vertical side of surrogate container cube. Rapiscan Test Object “E” in Celotex at 0.1 g/cc.

B3. Simulated Detector Responses with U_3O_8 Target in 0.2 g/cc Celotex

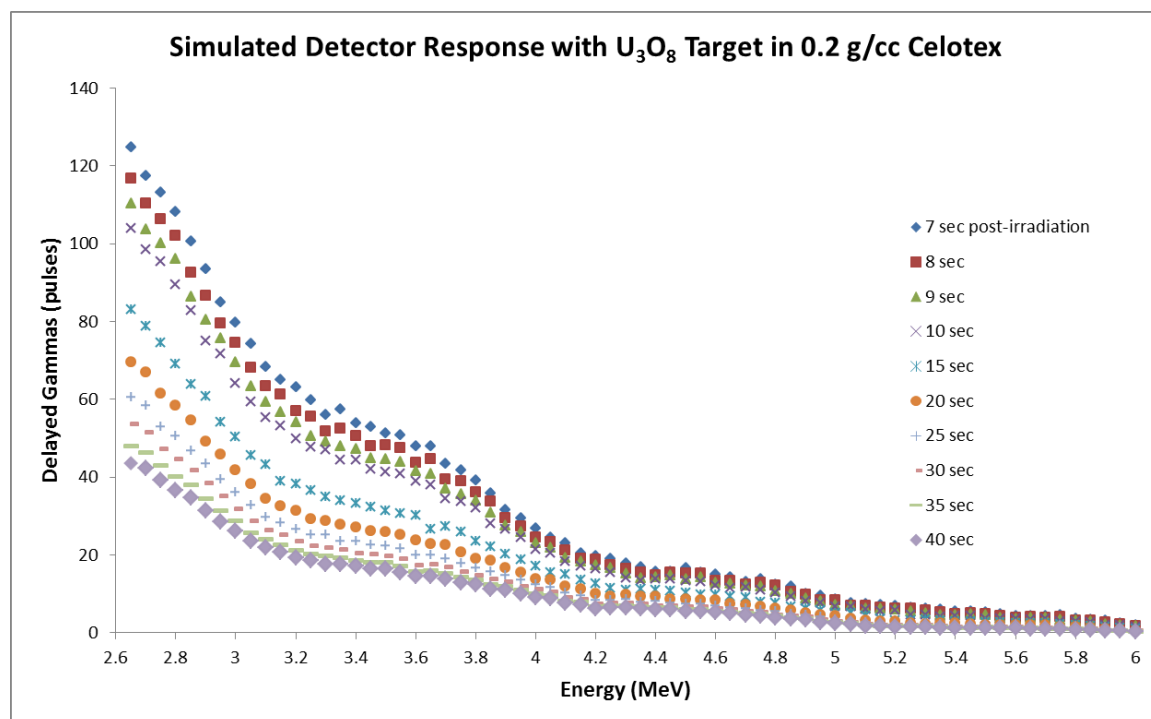


Figure 64. Simulated detector response to delayed gamma emission at one second intervals from 7-10 seconds and five second intervals from 10-40 seconds after 30 second interrogation with 7 MeV neutron and 12.2 MeV photon beams. PVT detector adjacent to one vertical side of surrogate container cube. Rapiscan Test Object "E" in Celotex at 0.2 g/cc.

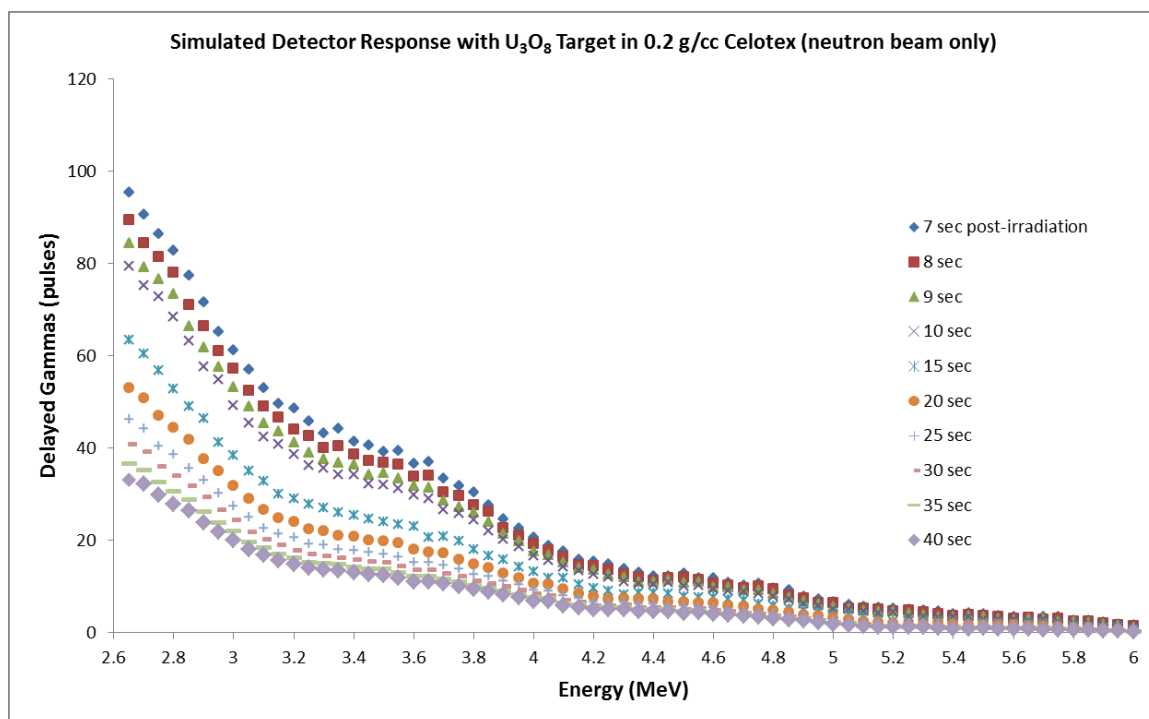


Figure 65. Simulated detector response to delayed gamma emission at one second intervals from 7-10 seconds and five second intervals from 10-40 seconds after 30 second interrogation with 7 MeV neutron beam. PVT detector adjacent to one vertical side of surrogate container cube. Rapiscan Test Object “E” in Celotex at 0.2 g/cc.

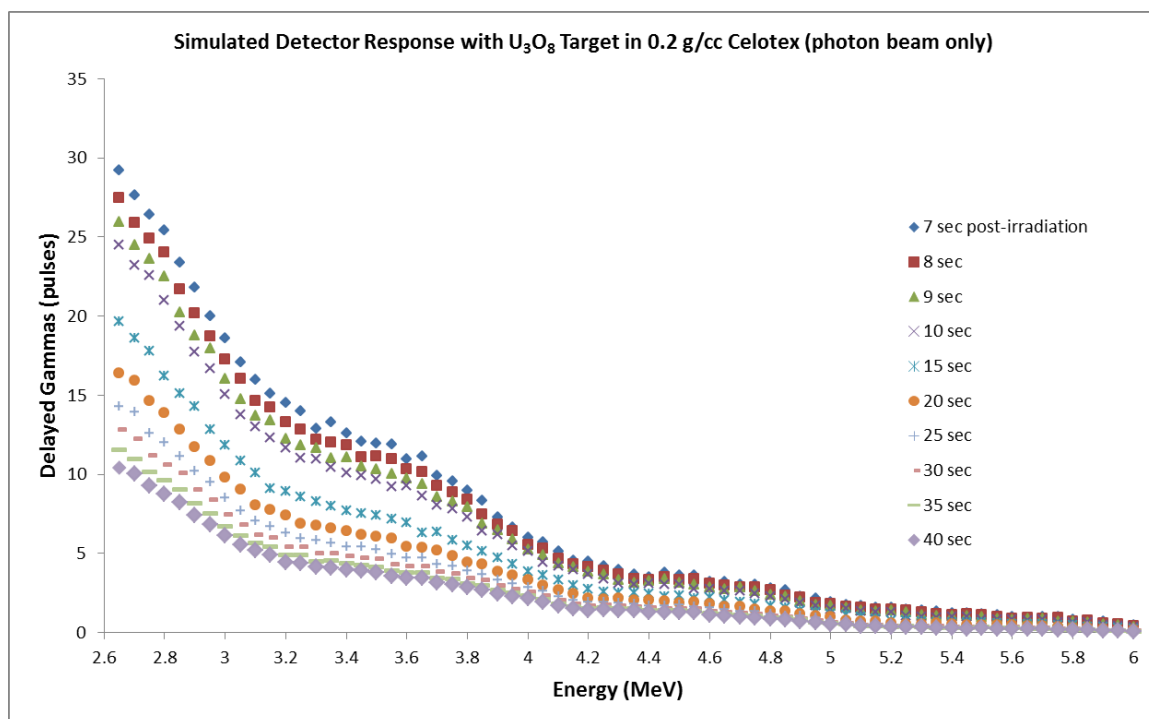


Figure 66. Simulated detector response to delayed gamma emission at one second intervals from 7-10 seconds and five second intervals from 10-40 seconds after 30 second interrogation with 12.2 MeV photon beam. PVT detector adjacent to one vertical side of surrogate container cube. Rapiscan Test Object “E” in Celotex at 0.2 g/cc.

B4. Simulated Detector Responses with U_3O_8 Target in 0.3 g/cc Celotex

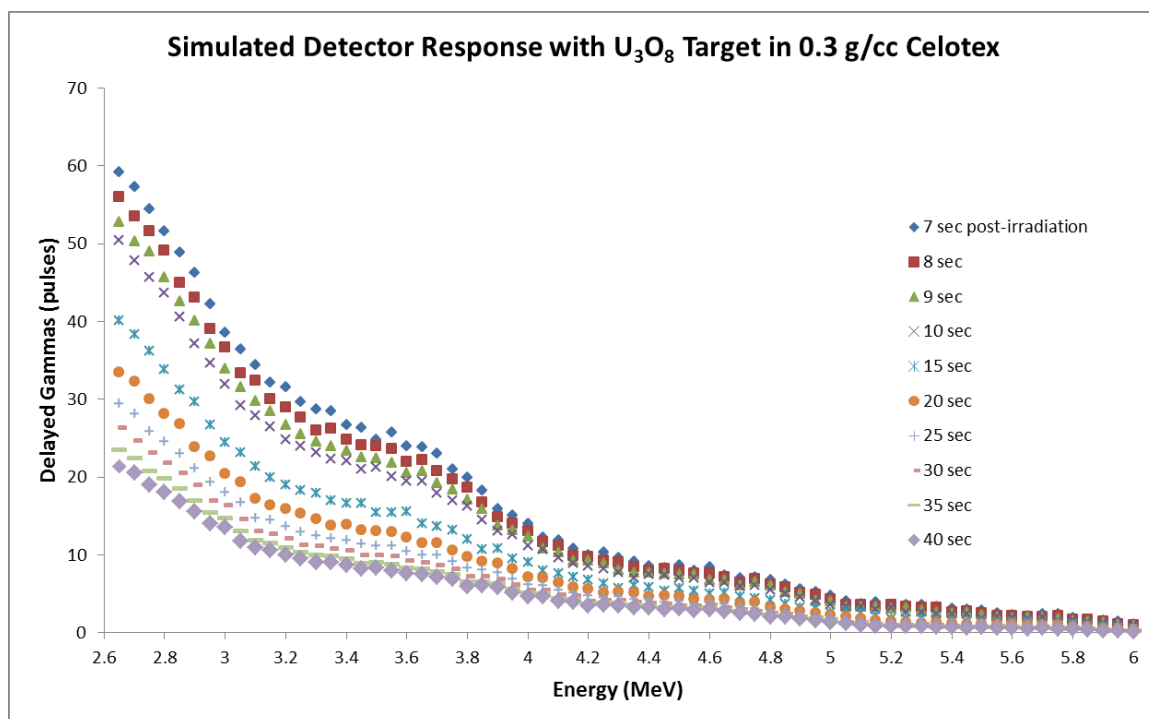


Figure 67. Simulated detector response to delayed gamma emission at one second intervals from 7-10 seconds and five second intervals from 10-40 seconds after 30 second interrogation with 7 MeV neutron and 12.2 MeV photon beams. PVT detector adjacent to one vertical side of surrogate container cube. Rapiscan Test Object "E" in Celotex at 0.3 g/cc.

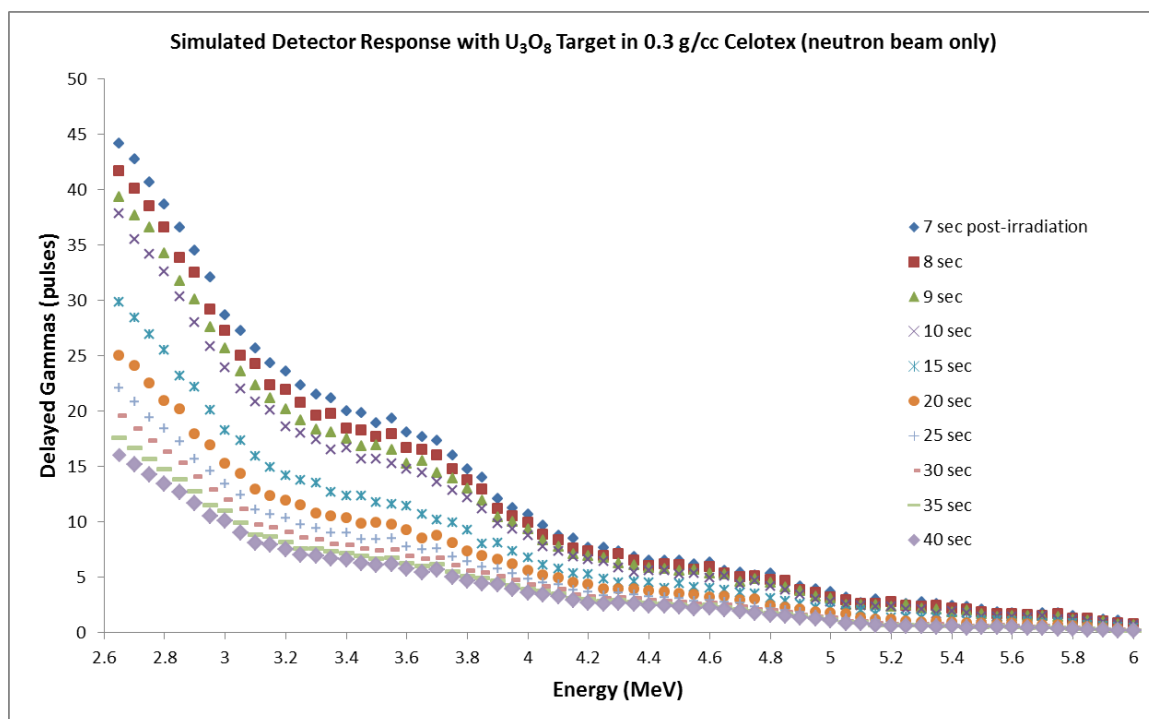


Figure 68. Simulated detector response to delayed gamma emission at one second intervals from 7-10 seconds and five second intervals from 10-40 seconds after 30 second interrogation with 7 MeV neutron beam. PVT detector adjacent to one vertical side of surrogate container cube. Rapiscan Test Object "E" in Celotex at 0.3 g/cc.

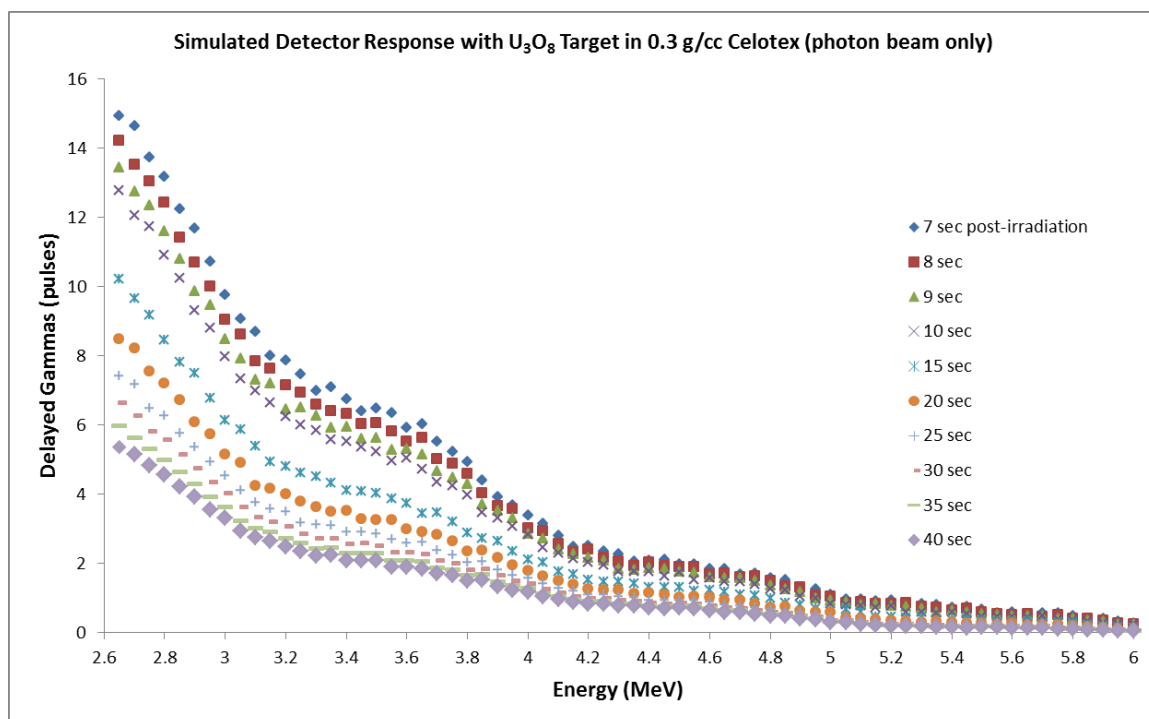


Figure 69. Simulated detector response to delayed gamma emission at one second intervals from 7-10 seconds and five second intervals from 10-40 seconds after 30 second interrogation with 12.2 MeV photon beam. PVT detector adjacent to one vertical side of surrogate container cube. Rapiscan Test Object “E” in Celotex at 0.3 g/cc.

B5. Simulated Detector Responses with U_3O_8 Target in 0.4 g/cc Celotex

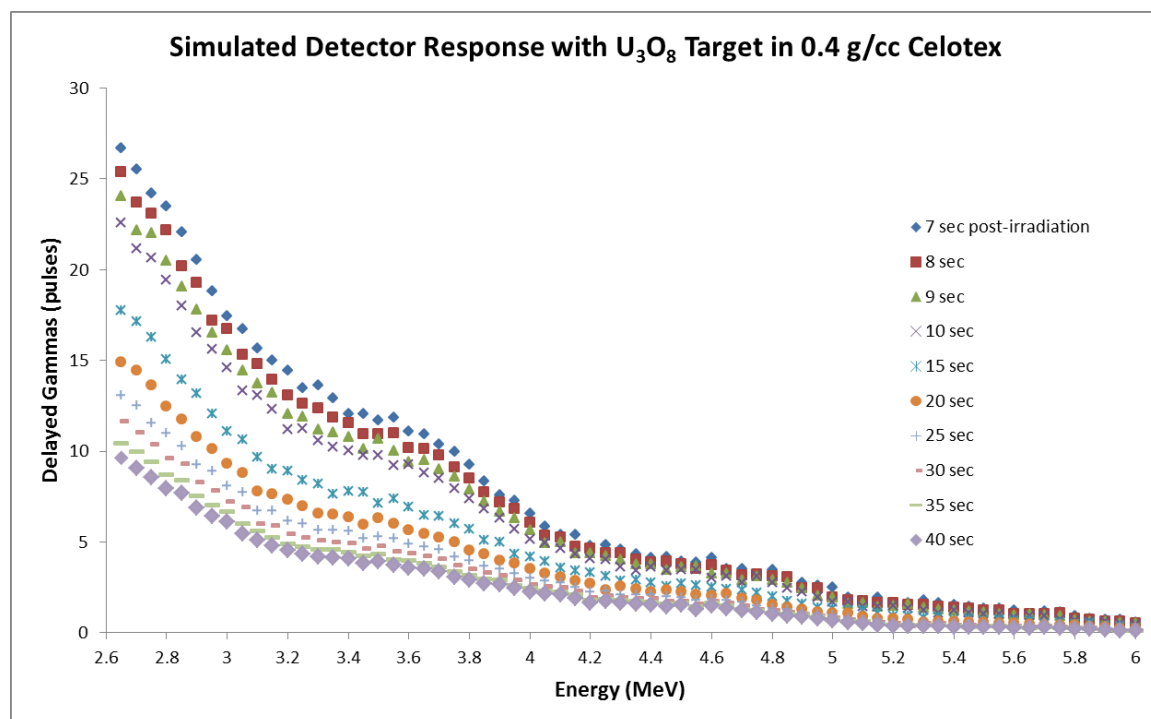


Figure 70. Simulated detector response to delayed gamma emission at one second intervals from 7-10 seconds and five second intervals from 10-40 seconds after 30 second interrogation with 7 MeV neutron and 12.2 MeV photon beams. PVT detector adjacent to one vertical side of surrogate container cube. Rapiscan Test Object "E" in Celotex at 0.4 g/cc.

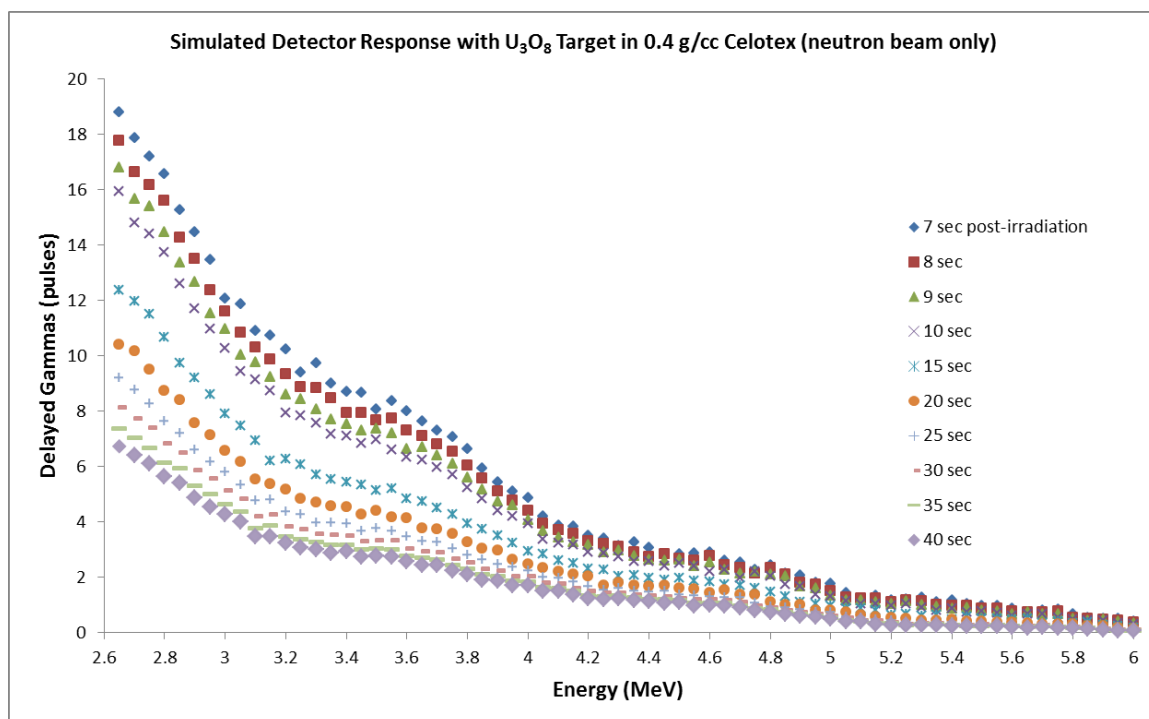


Figure 71. Simulated detector response to delayed gamma emission at one second intervals from 7-10 seconds and five second intervals from 10-40 seconds after 30 second interrogation with 7 MeV neutron beam. PVT detector adjacent to one vertical side of surrogate container cube. Rapiscan Test Object “E” in Celotex at 0.4 g/cc.

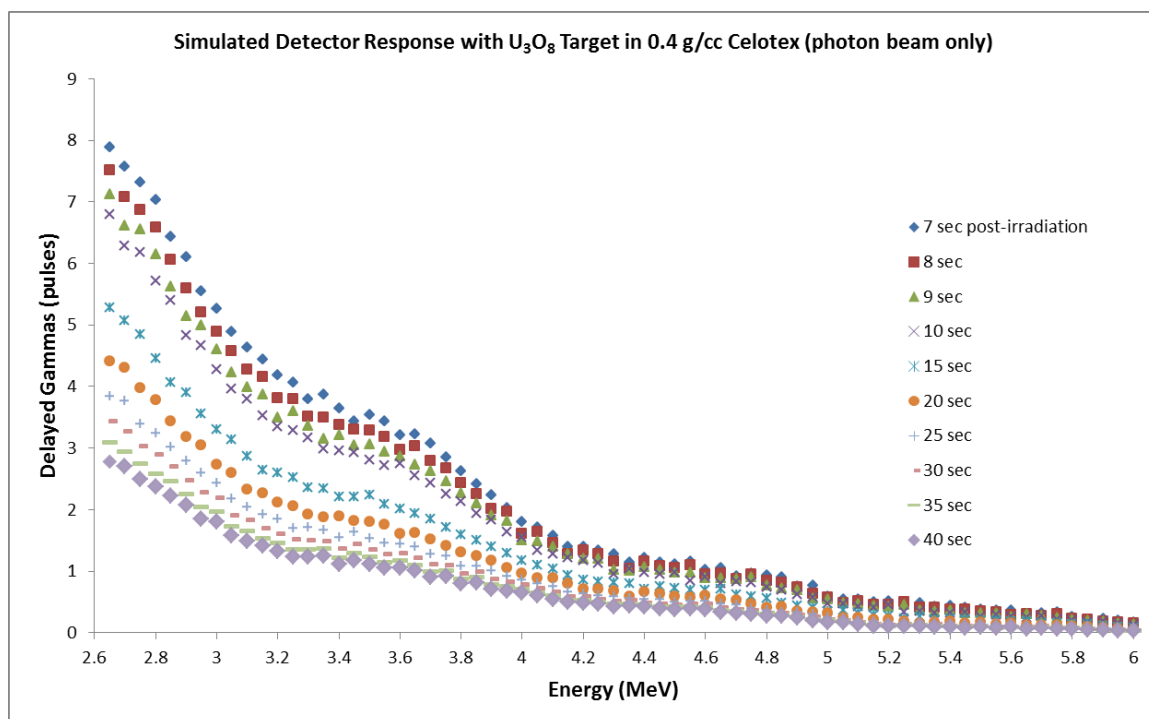


Figure 72. Simulated detector response to delayed gamma emission at one second intervals from 7-10 seconds and five second intervals from 10-40 seconds after 30 second interrogation with 12.2 MeV photon beam. PVT detector adjacent to one vertical side of surrogate container cube. Rapiscan Test Object “E” in Celotex at 0.4 g/cc.

B6. Simulated Detector Responses with U_3O_8 Target in 0.5 g/cc Celotex

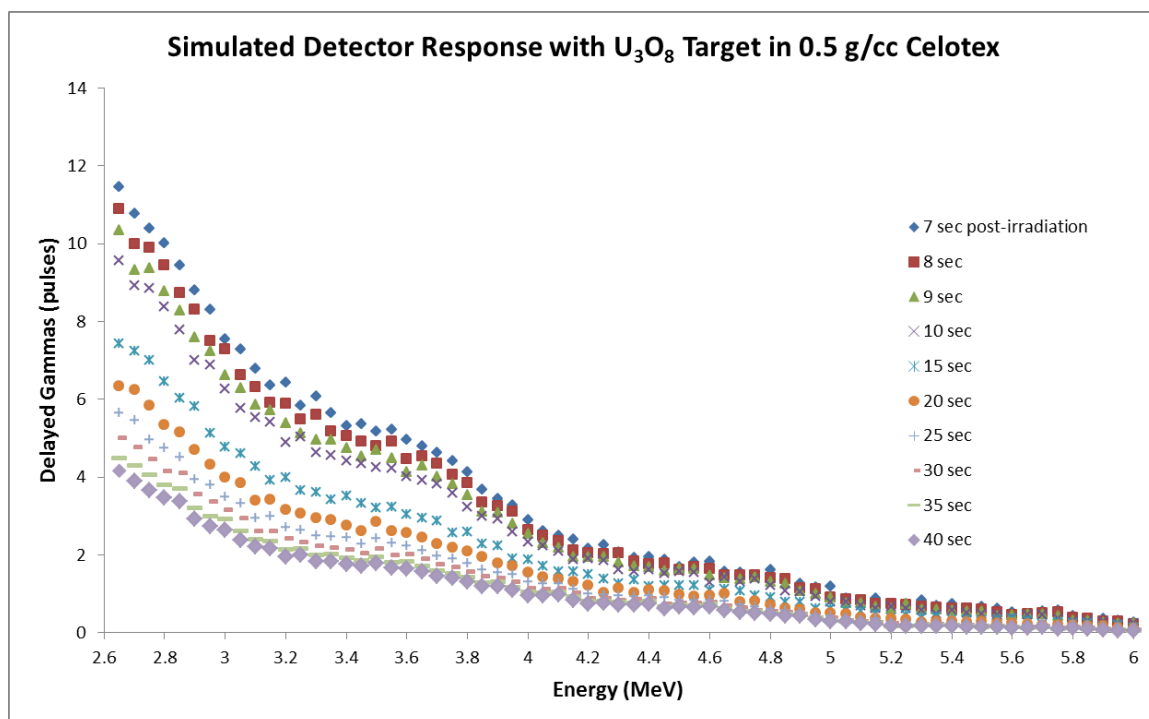


Figure 73. Simulated detector response to delayed gamma emission at one second intervals from 7-10 seconds and five second intervals from 10-40 seconds after 30 second interrogation with 7 MeV neutron and 12.2 MeV photon beams. PVT detector adjacent to one vertical side of surrogate container cube. Rapiscan Test Object "E" in Celotex at 0.5 g/cc.

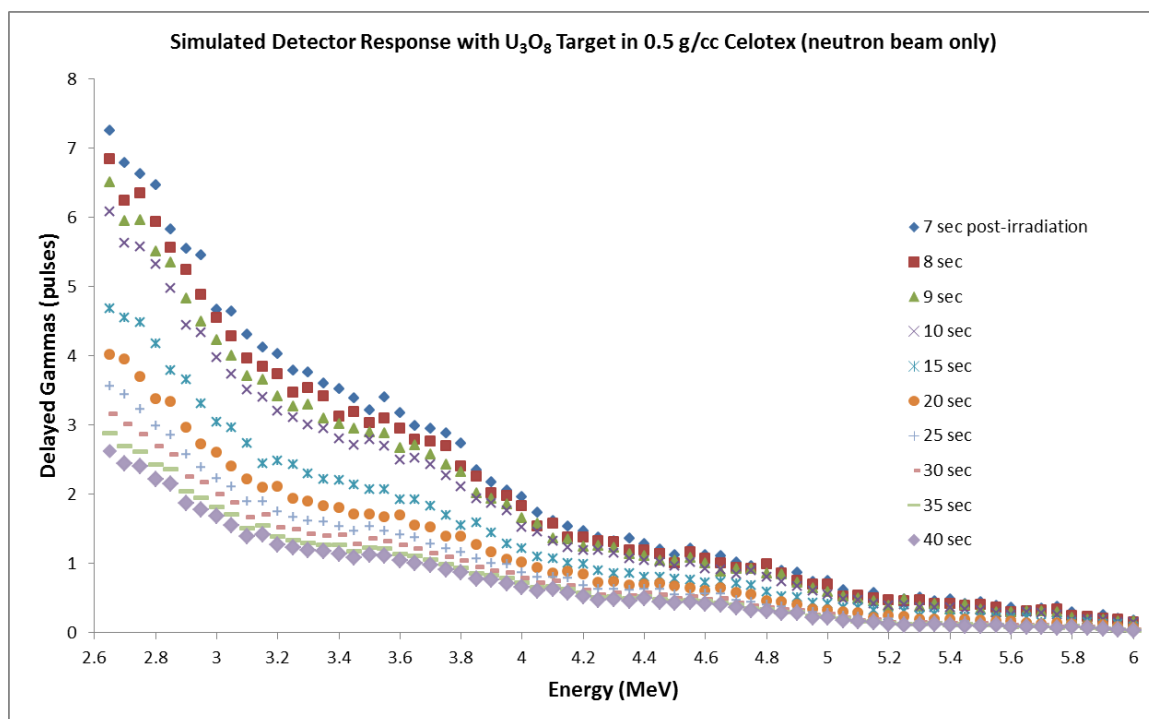


Figure 74. Simulated detector response to delayed gamma emission at one second intervals from 7-10 seconds and five second intervals from 10-40 seconds after 30 second interrogation with 7 MeV neutron beam. PVT detector adjacent to one vertical side of surrogate container cube. Rapiscan Test Object “E” in Celotex at 0.5 g/cc.

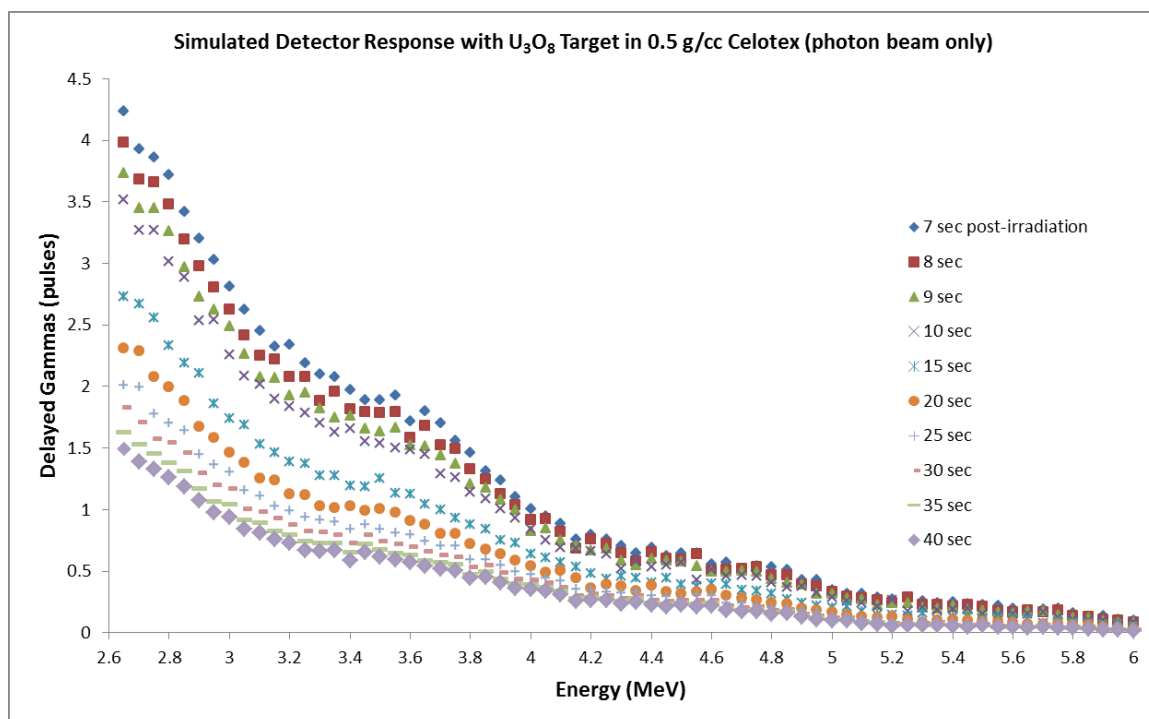


Figure 75. Simulated detector response to delayed gamma emission at one second intervals from 7-10 seconds and five second intervals from 10-40 seconds after 30 second interrogation with 12.2 MeV photon beam. PVT detector adjacent to one vertical side of surrogate container cube. Rapiscan Test Object “E” in Celotex at 0.5 g/cc.

B7. Simulated Detector Responses with U_3O_8 Target in 0.6 g/cc Celotex

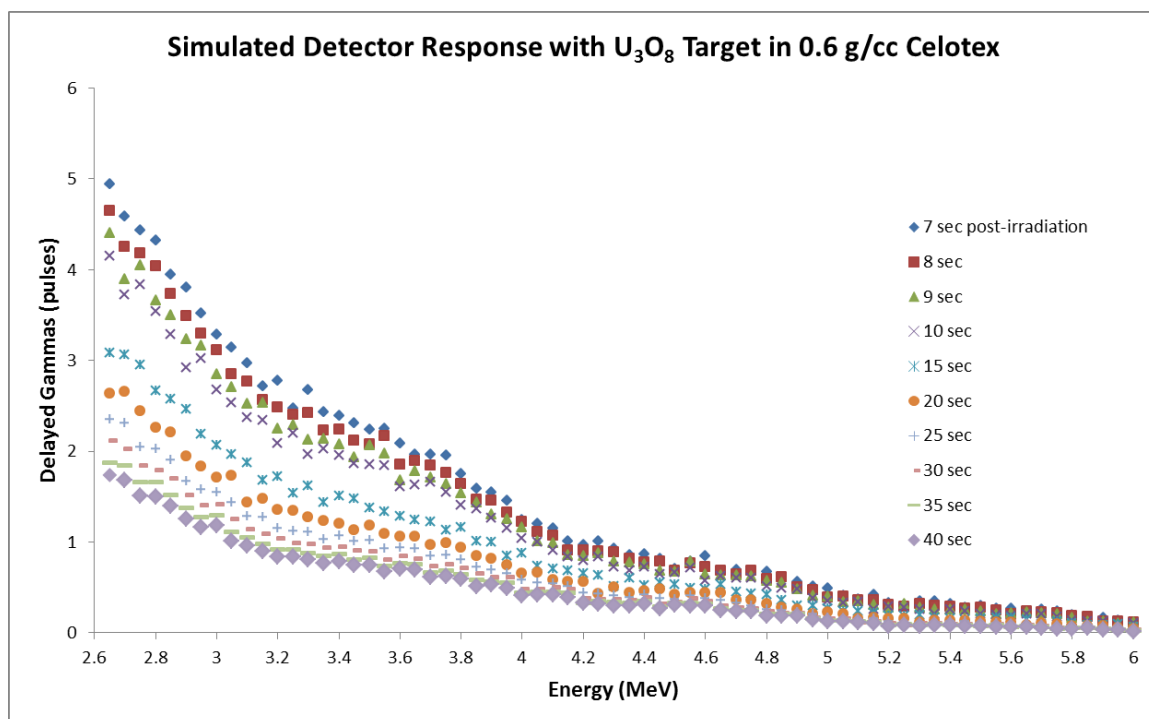


Figure 76. Simulated detector response to delayed gamma emission at one second intervals from 7-10 seconds and five second intervals from 10-40 seconds after 30 second interrogation with 7 MeV neutron and 12.2 MeV photon beams. PVT detector adjacent to one vertical side of surrogate container cube. Rapiscan Test Object "E" in Celotex at 0.6 g/cc.

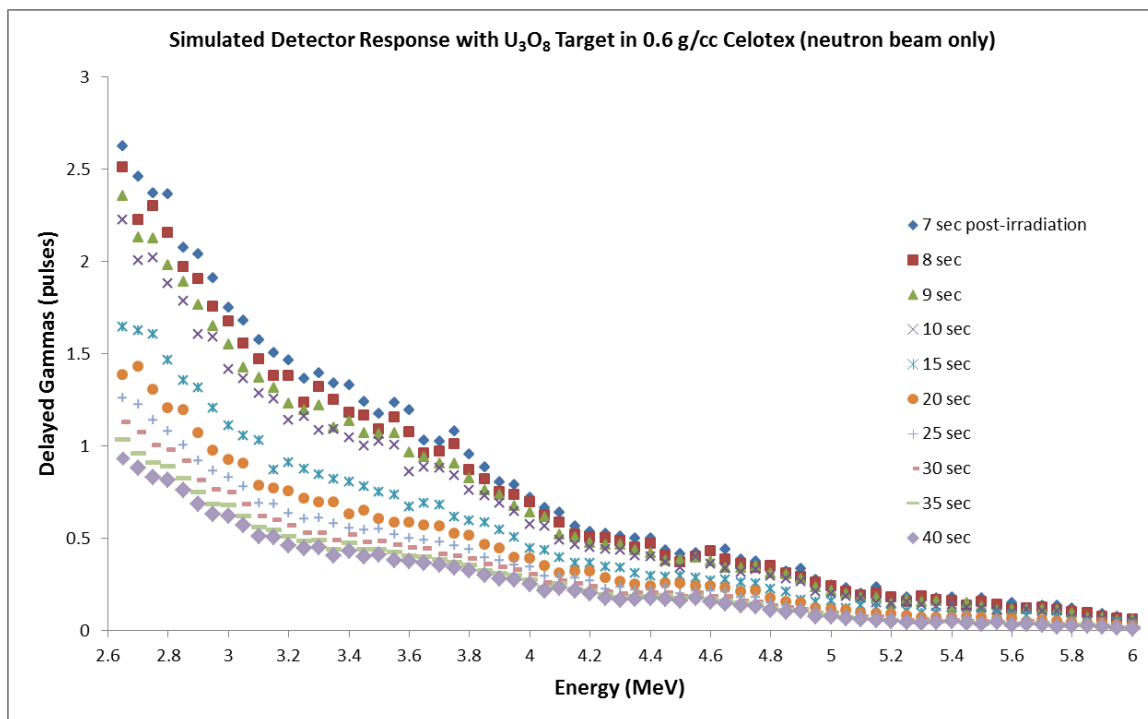


Figure 77. Simulated detector response to delayed gamma emission at one second intervals from 7-10 seconds and five second intervals from 10-40 seconds after 30 second interrogation with 7 MeV neutron beam. PVT detector adjacent to one vertical side of surrogate container cube. Rapiscan Test Object "E" in Celotex at 0.6 g/cc.

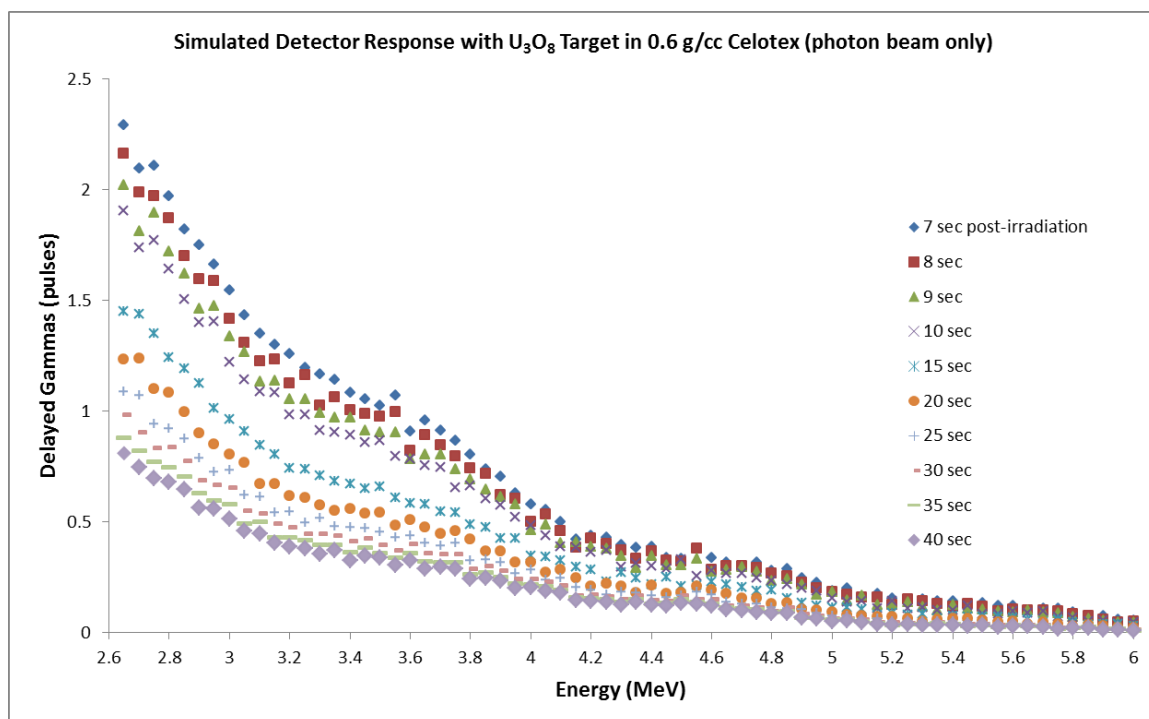


Figure 78. Simulated detector response to delayed gamma emission at one second intervals from 7-10 seconds and five second intervals from 10-40 seconds after 30 second interrogation with 12.2 MeV photon beam. PVT detector adjacent to one vertical side of surrogate container cube. Rapiscan Test Object “E” in Celotex at 0.6 g/cc.

B8. Simulated Detector Responses with U_3O_8 Target in 0.65 g/cc Celotex

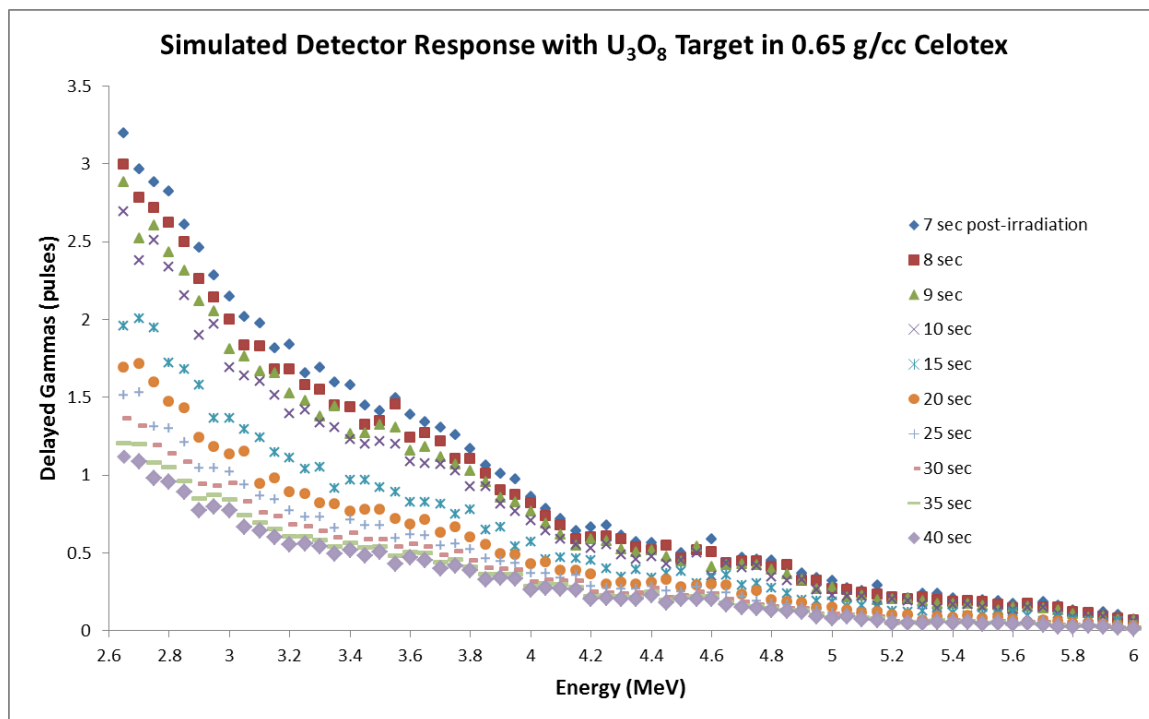


Figure 79. Simulated detector response to delayed gamma emission at one second intervals from 7-10 seconds and five second intervals from 10-40 seconds after 30 second interrogation with 7 MeV neutron and 12.2 MeV photon beams. PVT detector adjacent to one vertical side of surrogate container cube. Rapiscan Test Object "E" in Celotex at 0.65 g/cc.

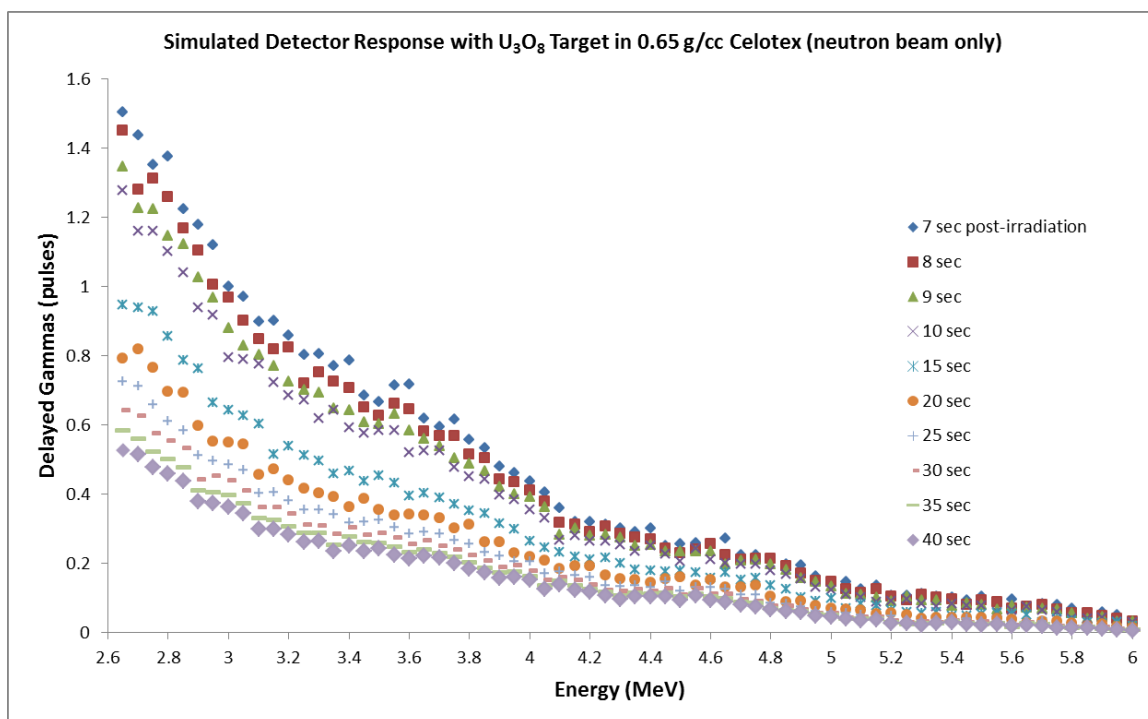


Figure 80. Simulated detector response to delayed gamma emission at one second intervals from 7-10 seconds and five second intervals from 10-40 seconds after 30 second interrogation with 7 MeV neutron beam. PVT detector adjacent to one vertical side of surrogate container cube. Rapiscan Test Object “E” in Celotex at 0.65 g/cc.

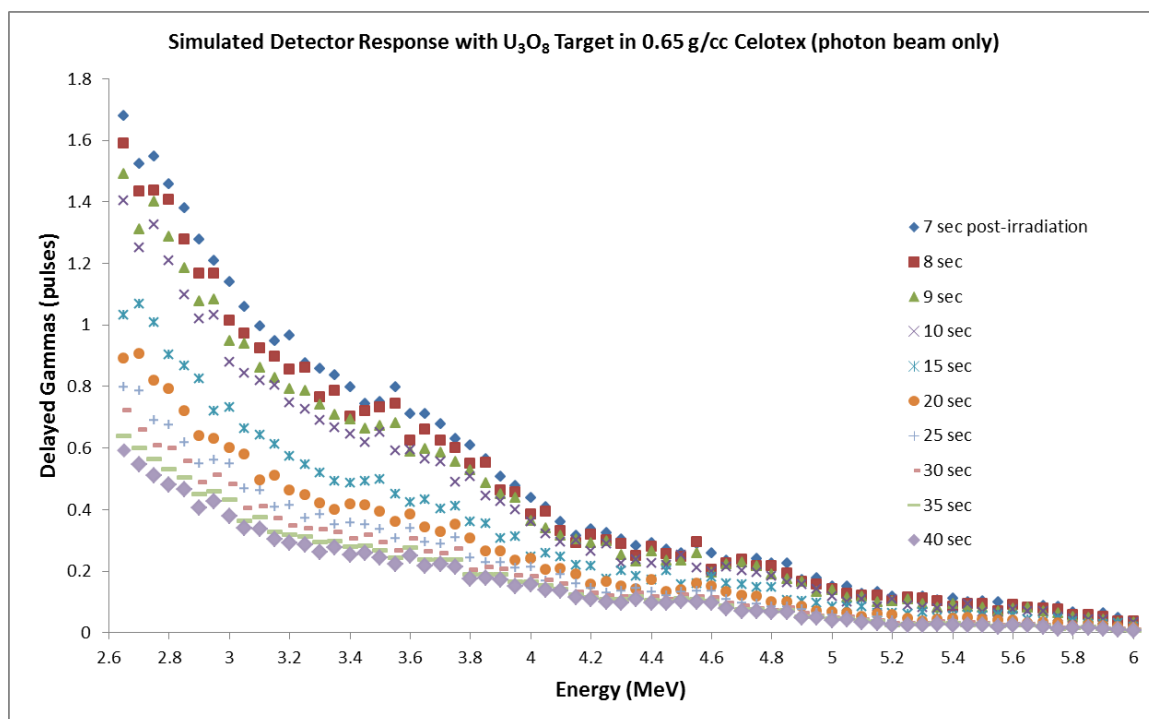


Figure 81. Simulated detector response to delayed gamma emission at one second intervals from 7-10 seconds and five second intervals from 10-40 seconds after 30 second interrogation with 12.2 MeV photon beam. PVT detector adjacent to one vertical side of surrogate container cube. Rapiscan Test Object “E” in Celotex at 0.65 g/cc.

APPENDIX C

Simulated Detector Responses with U_3O_8 Target in Aluminum

C1. Simulated Detector Responses with U_3O_8 Target in 0.05 g/cc Aluminum

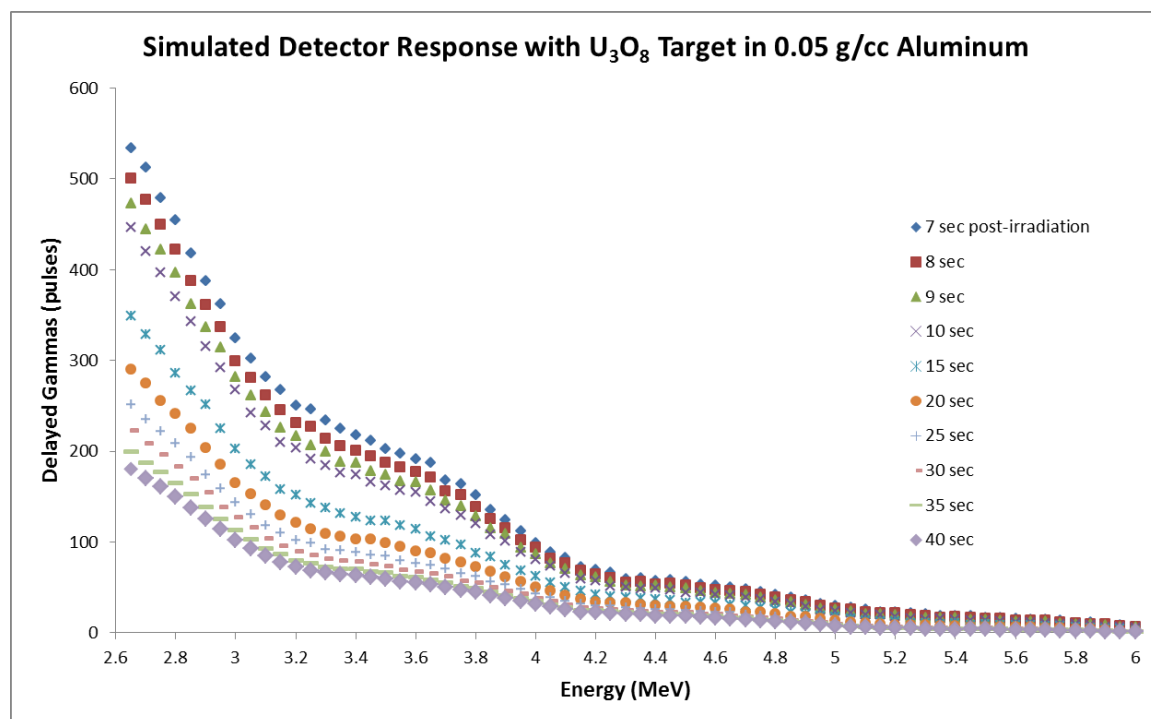


Figure 82. Simulated detector response to delayed gamma emission at one second intervals from 7-10 seconds and five second intervals from 10-40 seconds after 30 second interrogation with 7 MeV neutron and 12.2 MeV photon beams. PVT detector adjacent to one vertical side of surrogate container cube. Rapiscan Test Object "E" in aluminum at 0.05 g/cc.

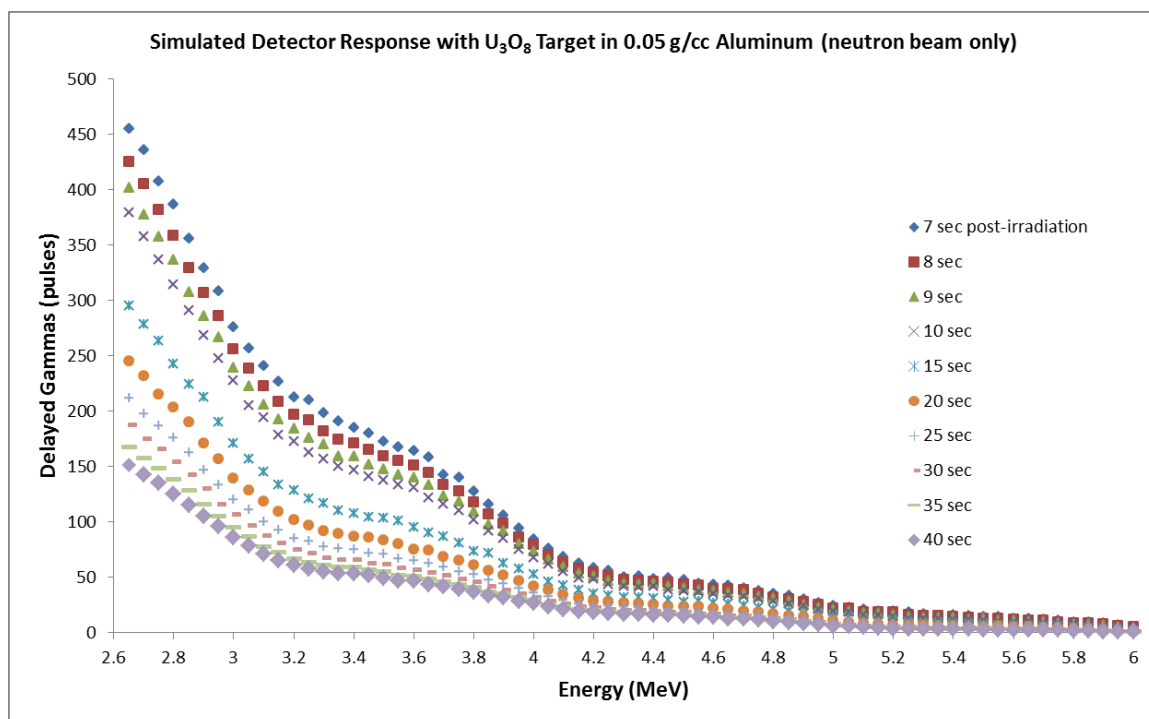


Figure 83. Simulated detector response to delayed gamma emission at one second intervals from 7-10 seconds and five second intervals from 10-40 seconds after 30 second interrogation with 7 MeV neutron beam. PVT detector adjacent to one vertical side of surrogate container cube. Rapiscan Test Object “E” in aluminum at 0.05 g/cc.

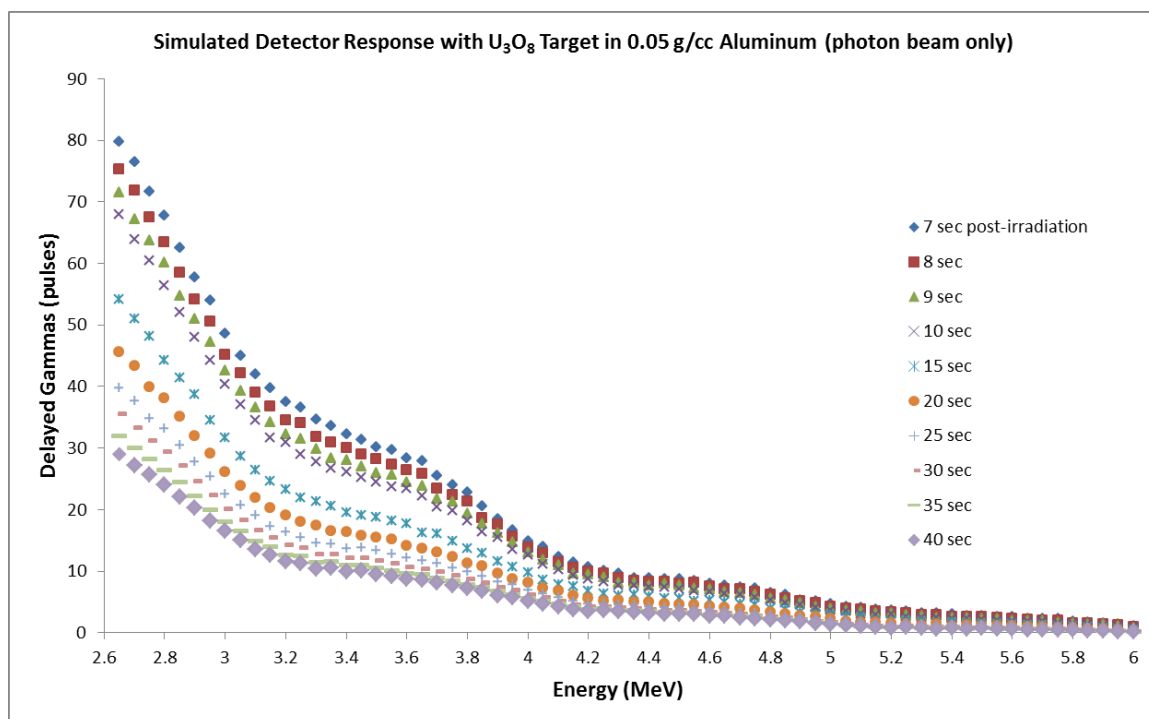


Figure 84. Simulated detector response to delayed gamma emission at one second intervals from 7-10 seconds and five second intervals from 10-40 seconds after 30 second interrogation with 12.2 MeV photon beam. PVT detector adjacent to one vertical side of surrogate container cube. Rapiscan Test Object “E” in aluminum at 0.05 g/cc.

C2. Simulated Detector Responses with U_3O_8 Target in 0.1 g/cc Aluminum

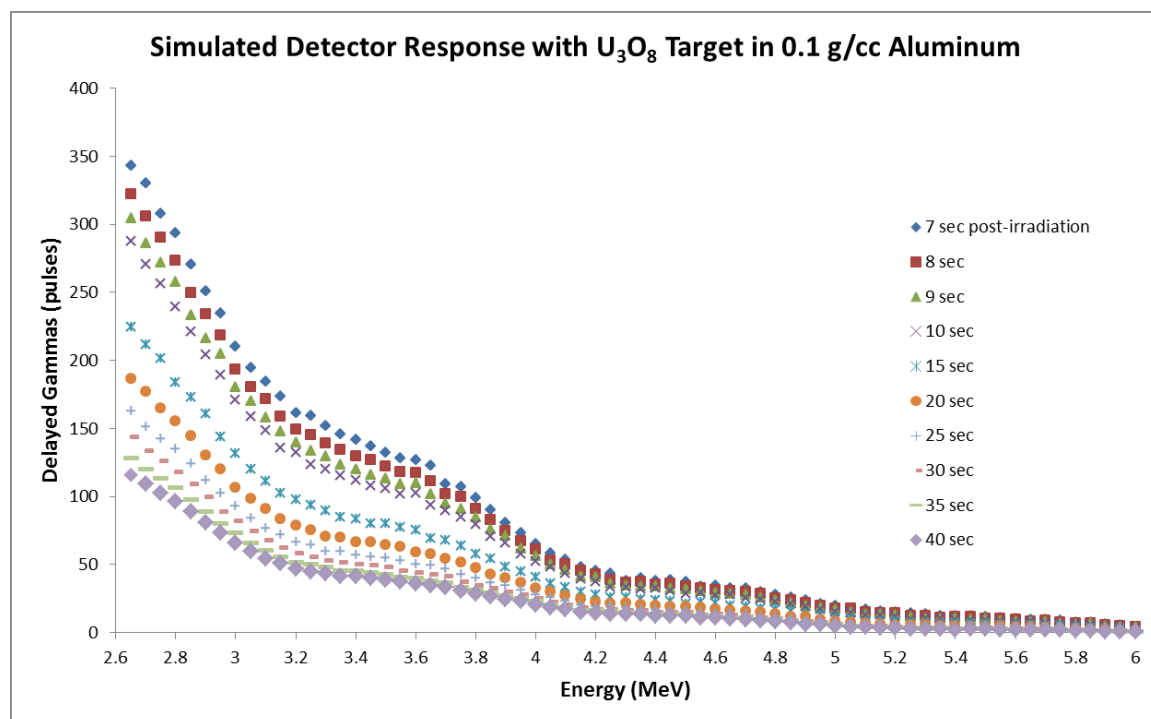


Figure 85. Simulated detector response to delayed gamma emission at one second intervals from 7-10 seconds and five second intervals from 10-40 seconds after 30 second interrogation with 7 MeV neutron and 12.2 MeV photon beams. PVT detector adjacent to one vertical side of surrogate container cube. Rapiscan Test Object "E" in aluminum at 0.1 g/cc.

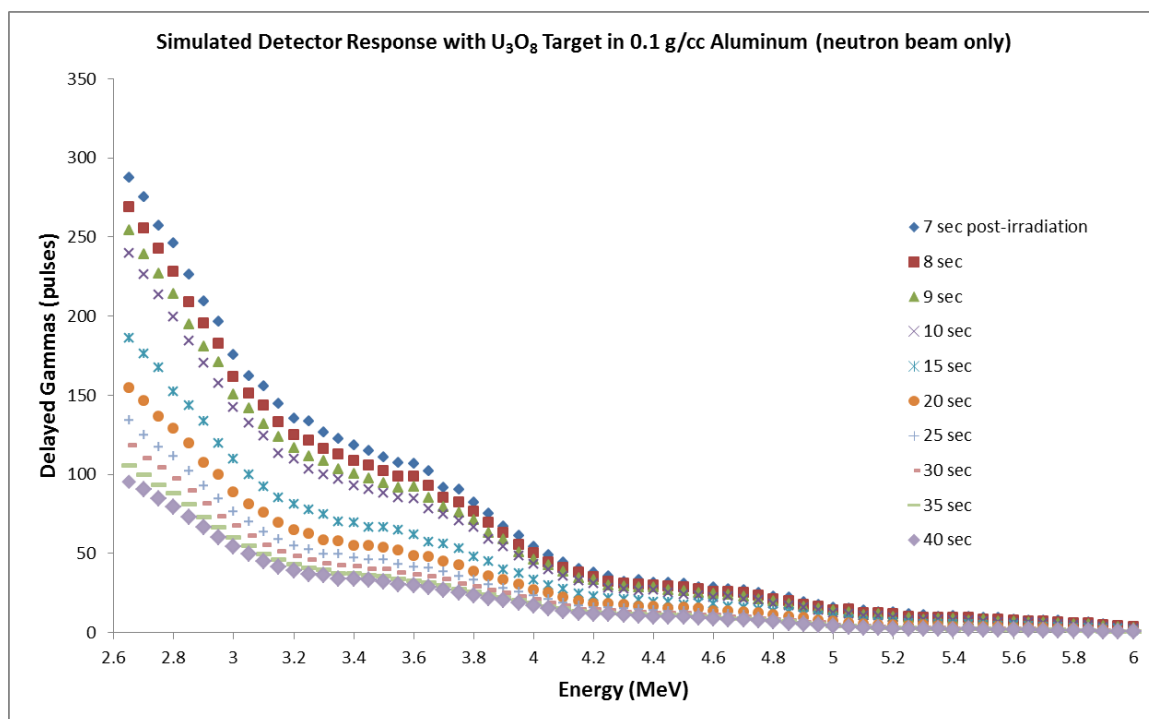


Figure 86. Simulated detector response to delayed gamma emission at one second intervals from 7-10 seconds and five second intervals from 10-40 seconds after 30 second interrogation with 7 MeV neutron beam. PVT detector adjacent to one vertical side of surrogate container cube. Rapiscan Test Object “E” in aluminum at 0.1 g/cc.

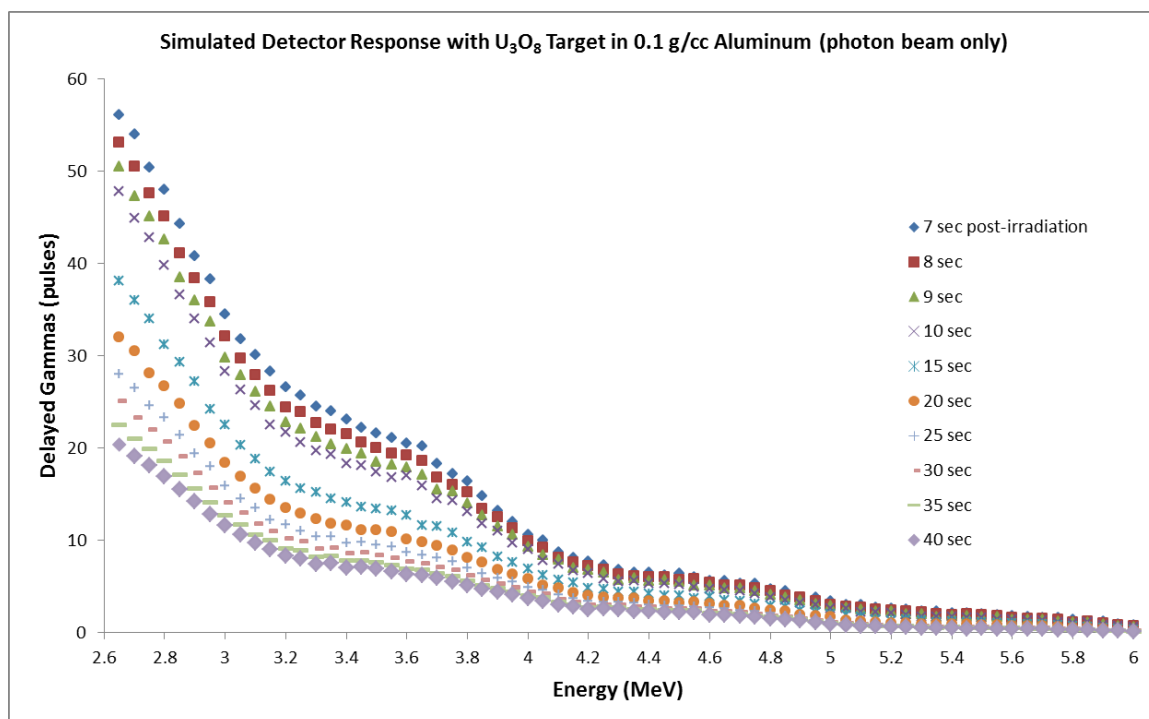


Figure 87. Simulated detector response to delayed gamma emission at one second intervals from 7-10 seconds and five second intervals from 10-40 seconds after 30 second interrogation with 12.2 MeV photon beam. PVT detector adjacent to one vertical side of surrogate container cube. Rapiscan Test Object “E” in aluminum at 0.1 g/cc.

C3. Simulated Detector Responses with U_3O_8 Target in 0.2 g/cc Aluminum

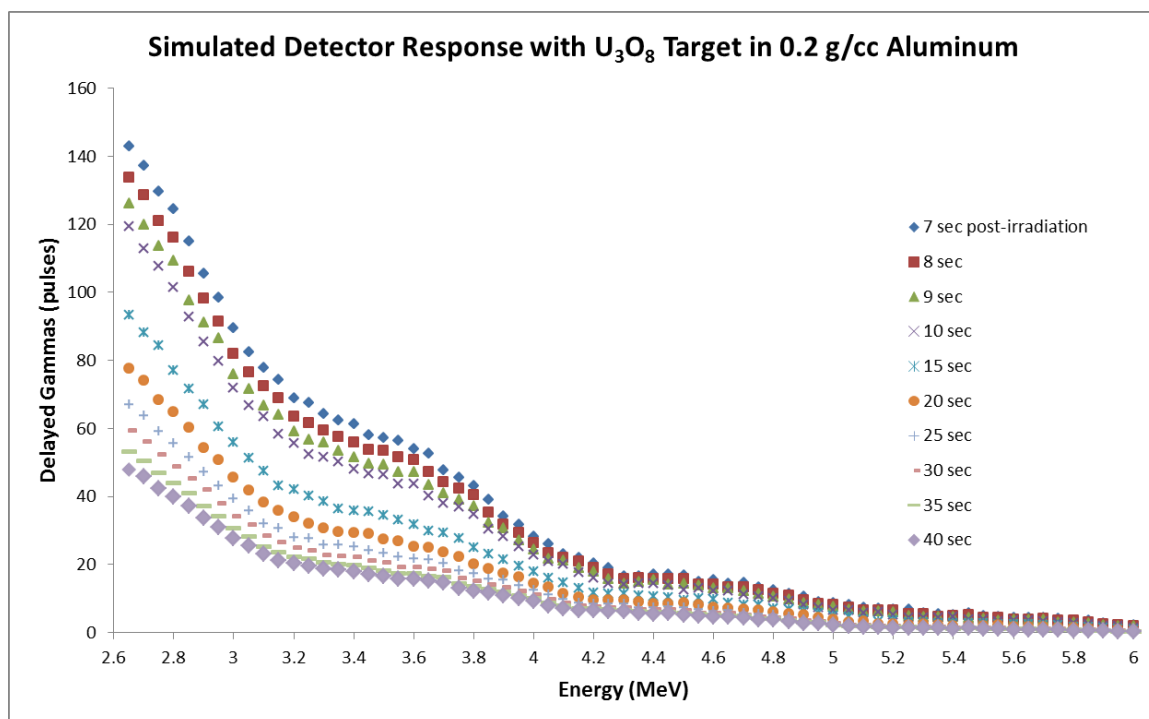


Figure 88. Simulated detector response to delayed gamma emission at one second intervals from 7-10 seconds and five second intervals from 10-40 seconds after 30 second interrogation with 7 MeV neutron and 12.2 MeV photon beams. PVT detector adjacent to one vertical side of surrogate container cube. Rapiscan Test Object “E” in aluminum at 0.2 g/cc.

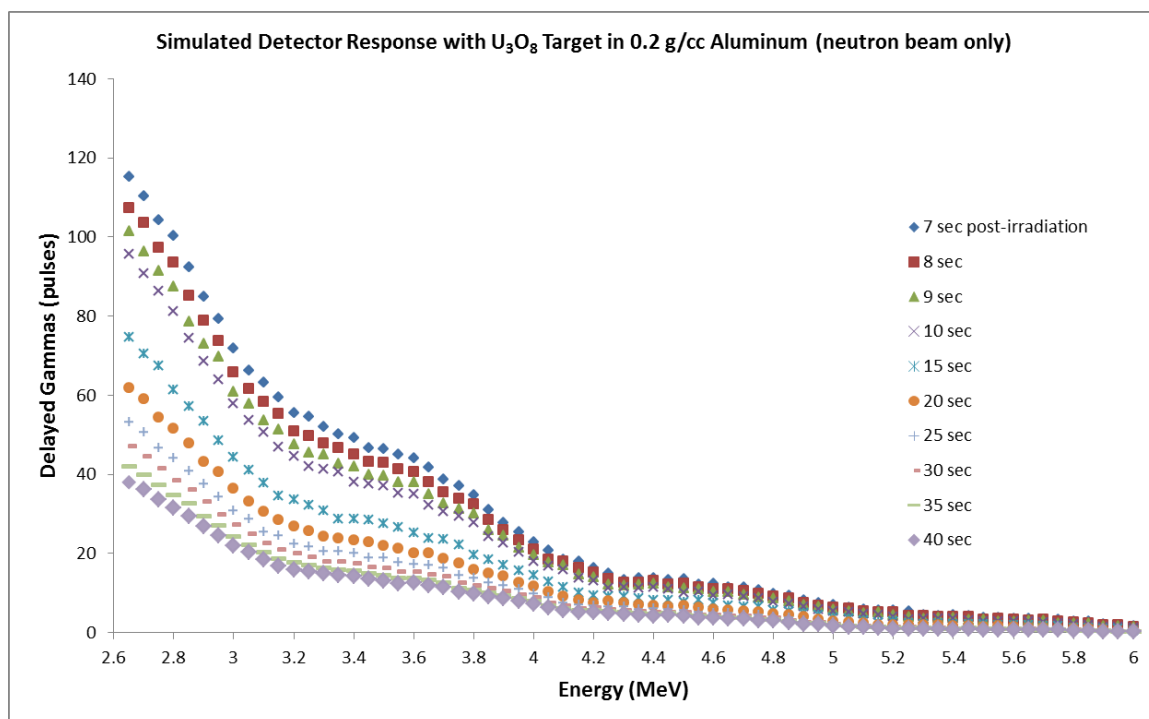


Figure 89. Simulated detector response to delayed gamma emission at one second intervals from 7-10 seconds and five second intervals from 10-40 seconds after 30 second interrogation with 7 MeV neutron beam. PVT detector adjacent to one vertical side of surrogate container cube. Rapiscan Test Object “E” in aluminum at 0.2 g/cc.

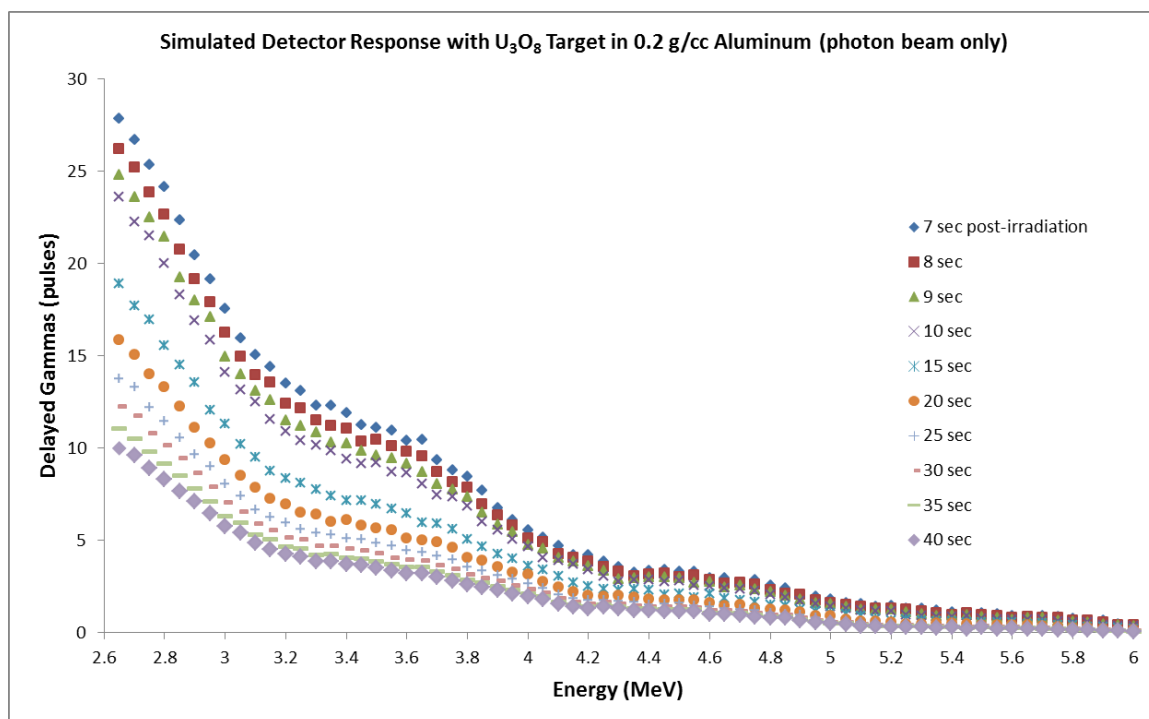


Figure 90. Simulated detector response to delayed gamma emission at one second intervals from 7-10 seconds and five second intervals from 10-40 seconds after 30 second interrogation with 12.2 MeV photon beam. PVT detector adjacent to one vertical side of surrogate container cube. Rapiscan Test Object "E" in aluminum at 0.2 g/cc.

C4. Simulated Detector Responses with U_3O_8 Target in 0.3 g/cc Aluminum

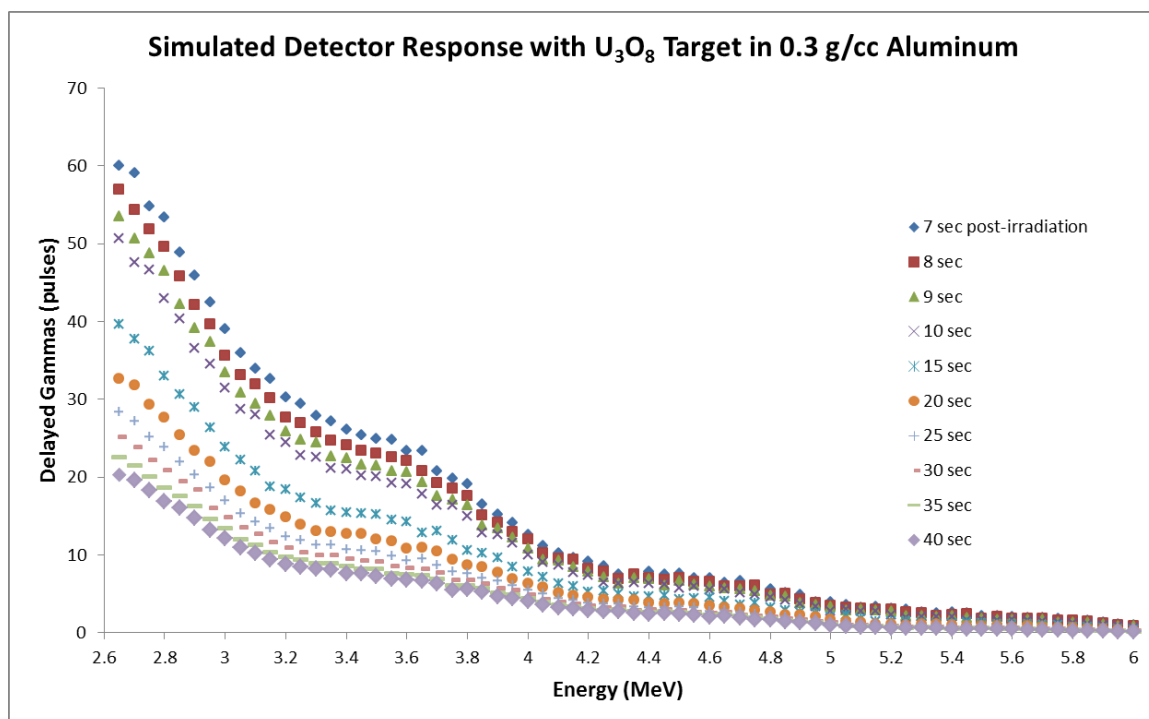


Figure 91. Simulated detector response to delayed gamma emission at one second intervals from 7-10 seconds and five second intervals from 10-40 seconds after 30 second interrogation with 7 MeV neutron and 12.2 MeV photon beams. PVT detector adjacent to one vertical side of surrogate container cube. Rapiscan Test Object "E" in aluminum at 0.3 g/cc.

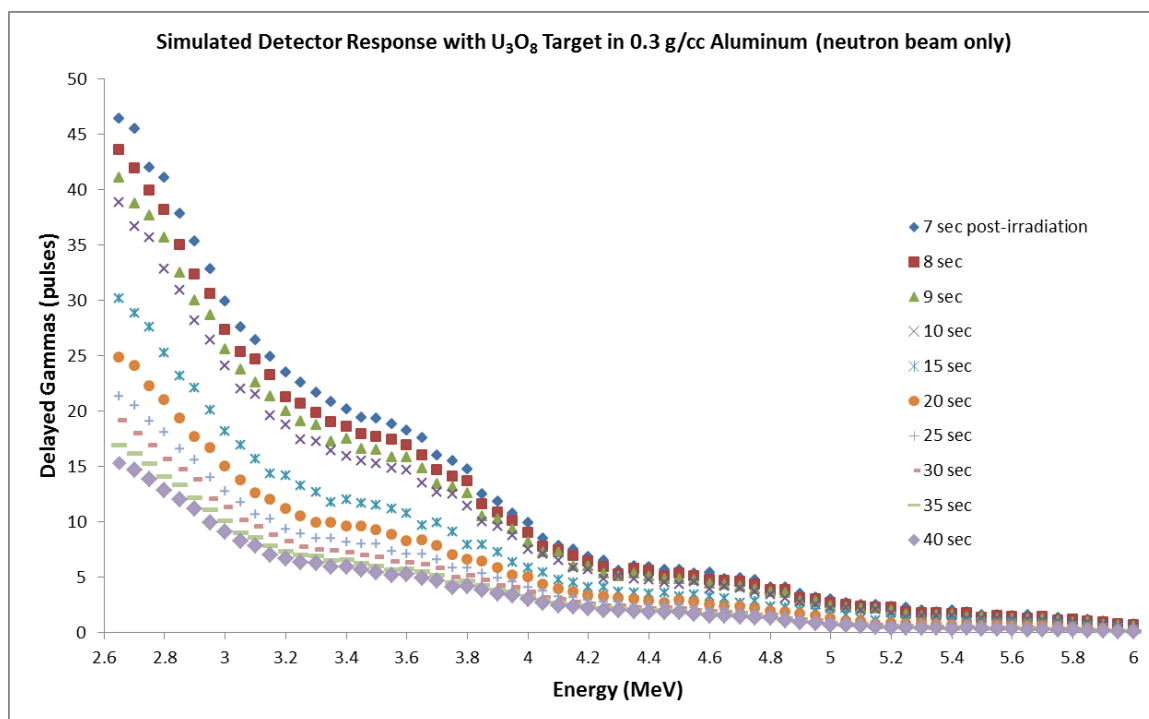


Figure 92. Simulated detector response to delayed gamma emission at one second intervals from 7-10 seconds and five second intervals from 10-40 seconds after 30 second interrogation with 7 MeV neutron beam. PVT detector adjacent to one vertical side of surrogate container cube. Rapiscan Test Object “E” in aluminum at 0.3 g/cc.

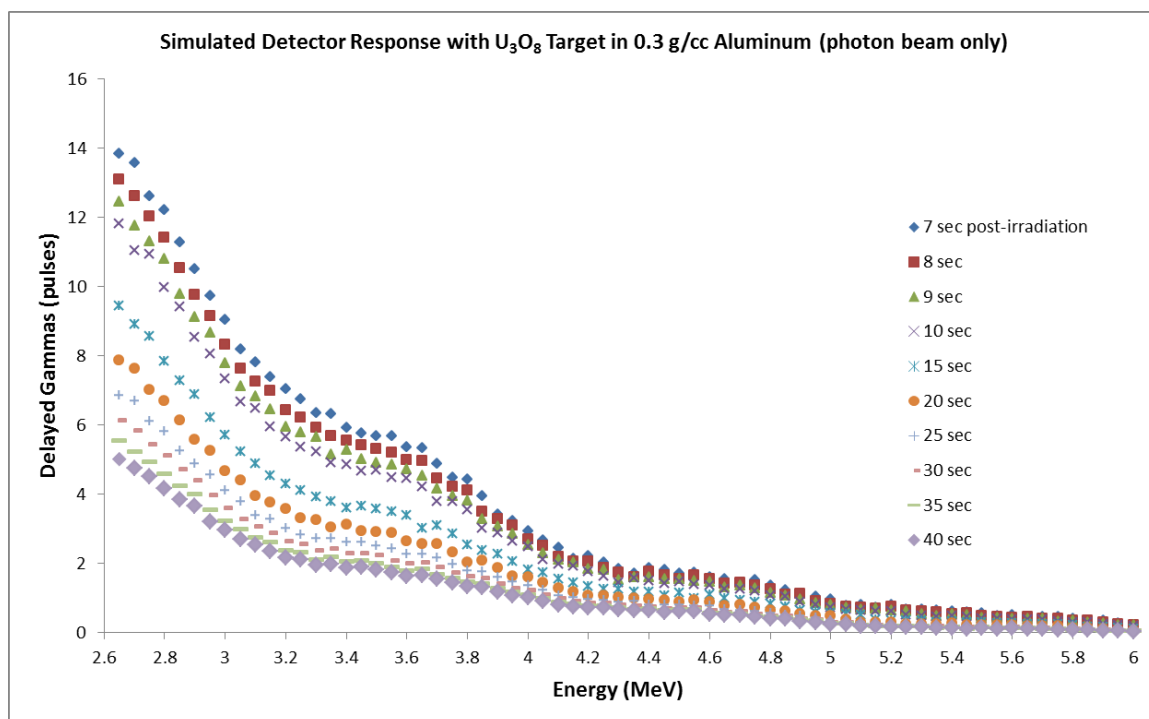


Figure 93. Simulated detector response to delayed gamma emission at one second intervals from 7-10 seconds and five second intervals from 10-40 seconds after 30 second interrogation with 12.2 MeV photon beam. PVT detector adjacent to one vertical side of surrogate container cube. Rapiscan Test Object “E” in aluminum at 0.3 g/cc.

C5. Simulated Detector Responses with U_3O_8 Target in 0.4 g/cc Aluminum

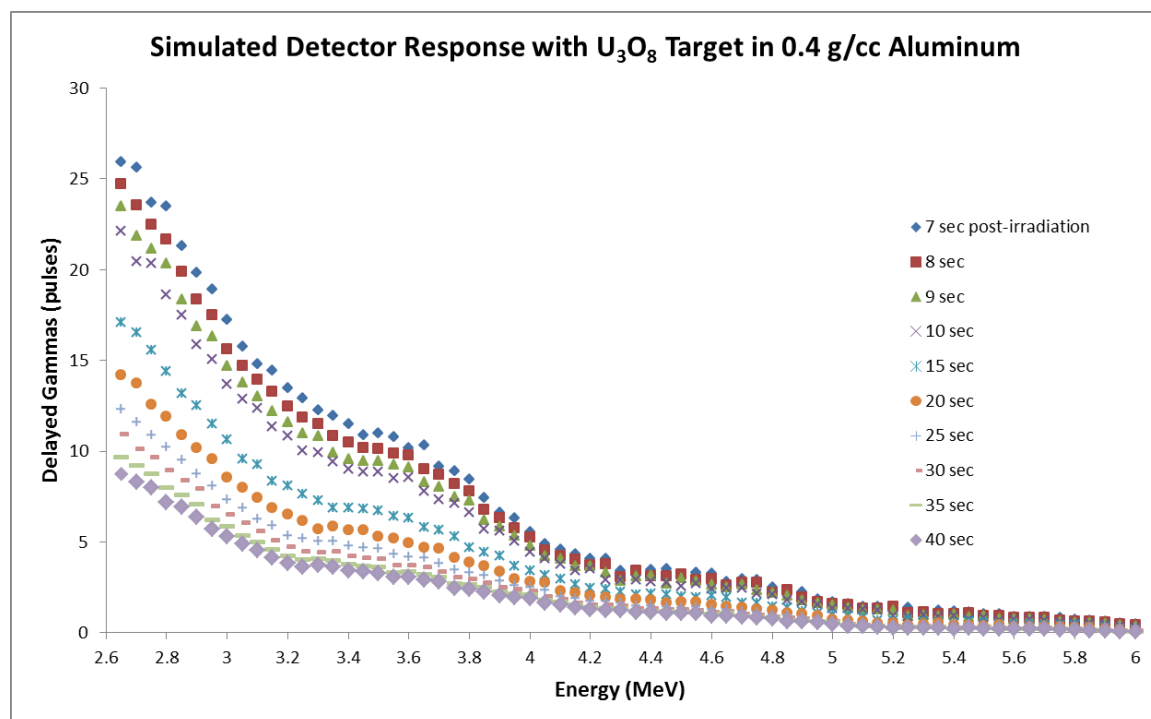


Figure 94. Simulated detector response to delayed gamma emission at one second intervals from 7-10 seconds and five second intervals from 10-40 seconds after 30 second interrogation with 7 MeV neutron and 12.2 MeV photon beams. PVT detector adjacent to one vertical side of surrogate container cube. Rapiscan Test Object "E" in aluminum at 0.4 g/cc.

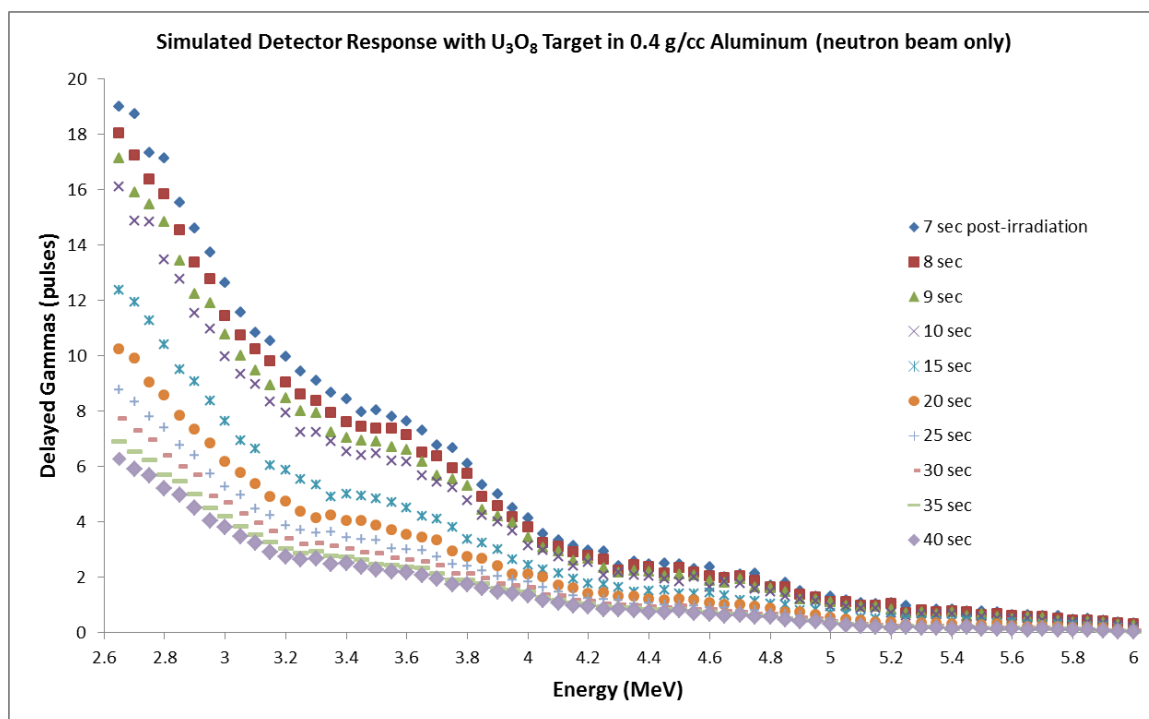


Figure 95. Simulated detector response to delayed gamma emission at one second intervals from 7-10 seconds and five second intervals from 10-40 seconds after 30 second interrogation with 7 MeV neutron beam. PVT detector adjacent to one vertical side of surrogate container cube. Rapiscan Test Object “E” in aluminum at 0.4 g/cc.

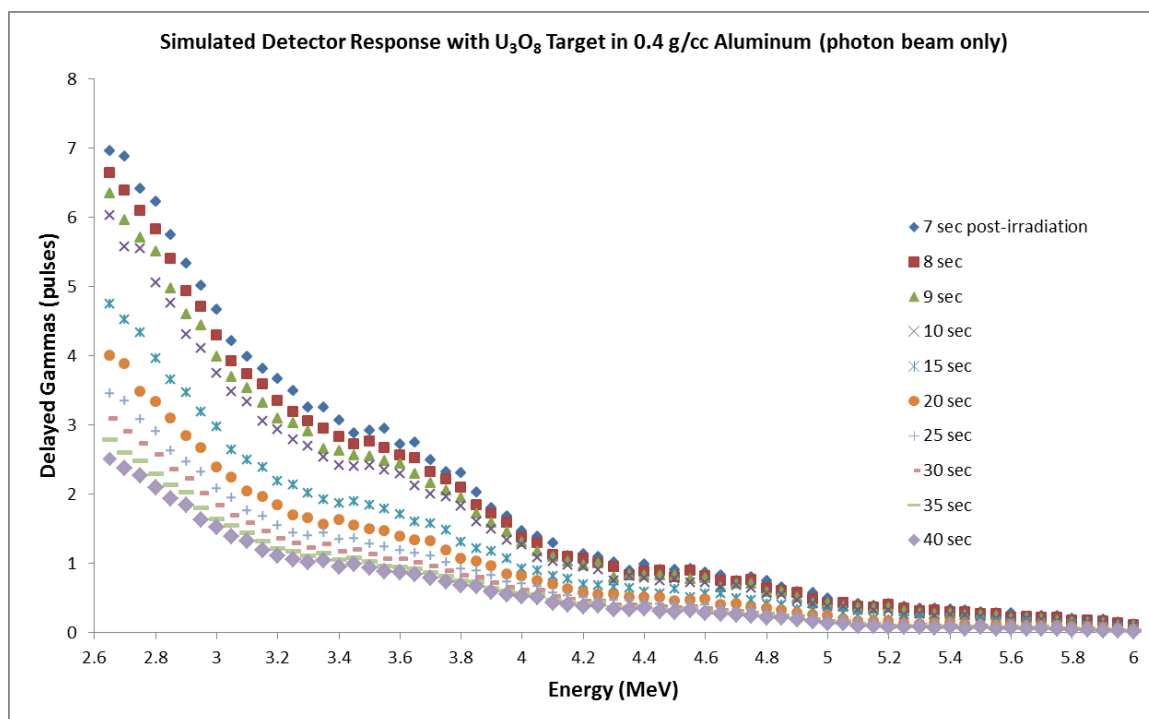


Figure 96. Simulated detector response to delayed gamma emission at one second intervals from 7-10 seconds and five second intervals from 10-40 seconds after 30 second interrogation with 12.2 MeV photon beam. PVT detector adjacent to one vertical side of surrogate container cube. Rapiscan Test Object “E” in aluminum at 0.4 g/cc.

C6. Simulated Detector Responses with U_3O_8 Target in 0.5 g/cc Aluminum

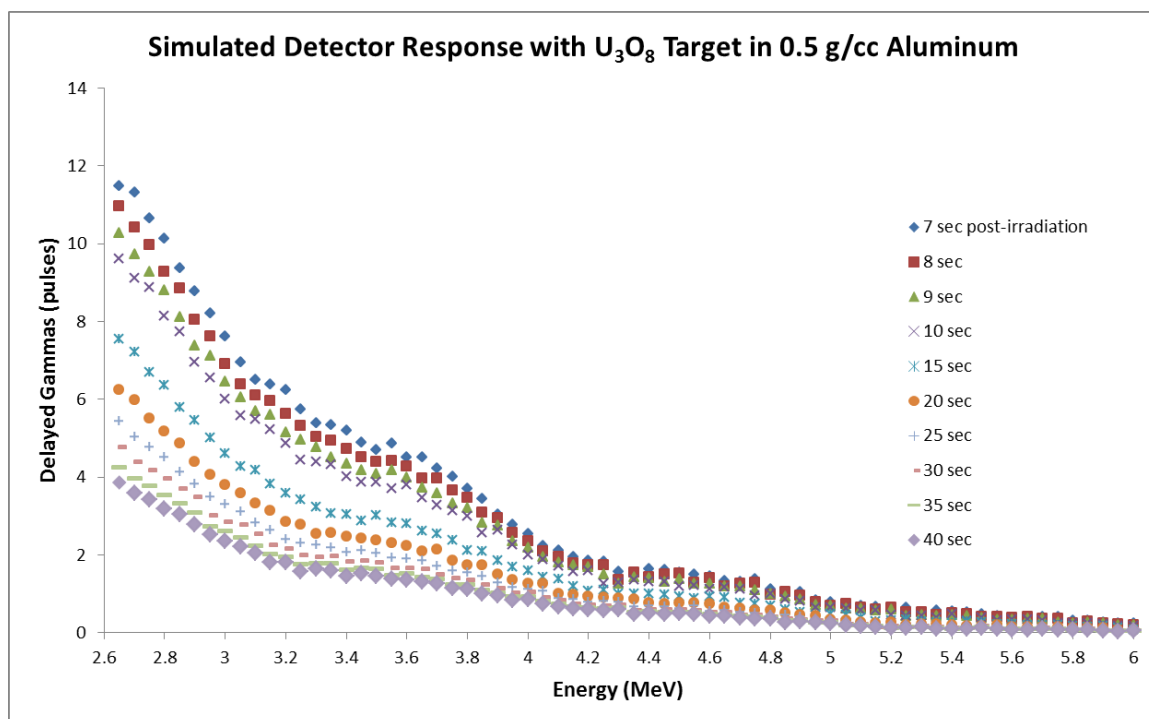


Figure 97. Simulated detector response to delayed gamma emission at one second intervals from 7-10 seconds and five second intervals from 10-40 seconds after 30 second interrogation with 7 MeV neutron and 12.2 MeV photon beams. PVT detector adjacent to one vertical side of surrogate container cube. Rapiscan Test Object “E” in aluminum at 0.5 g/cc.

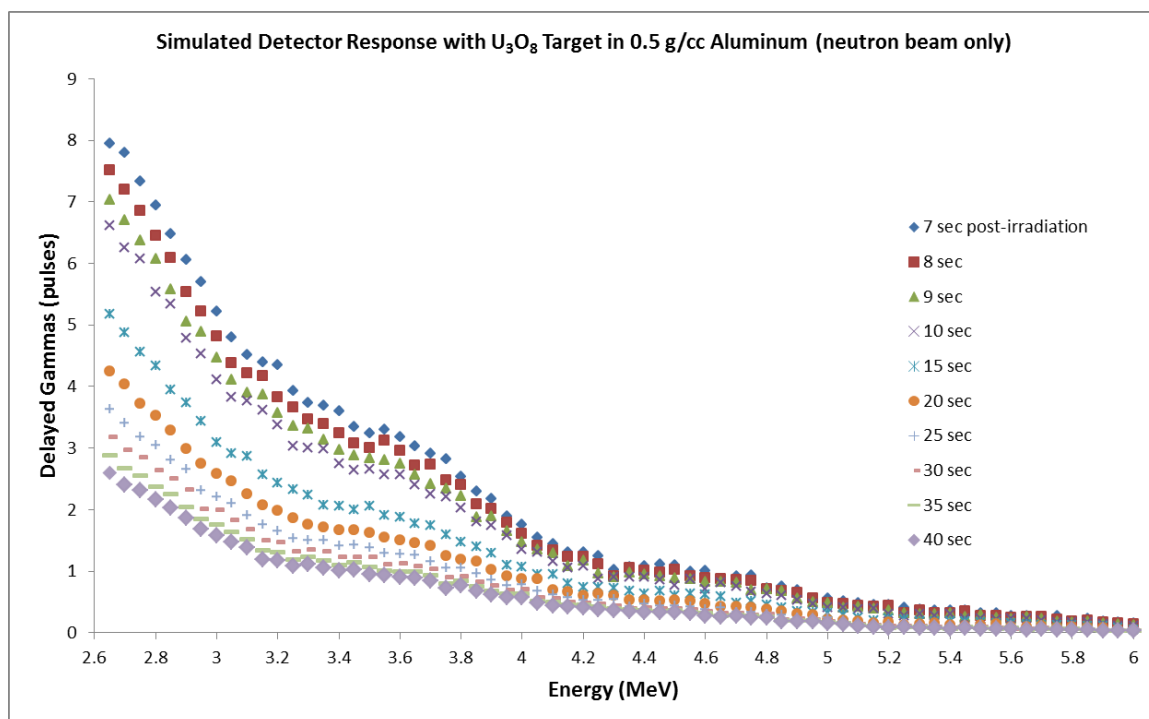


Figure 98. Simulated detector response to delayed gamma emission at one second intervals from 7-10 seconds and five second intervals from 10-40 seconds after 30 second interrogation with 7 MeV neutron beam. PVT detector adjacent to one vertical side of surrogate container cube. Rapiscan Test Object “E” in aluminum at 0.5 g/cc.

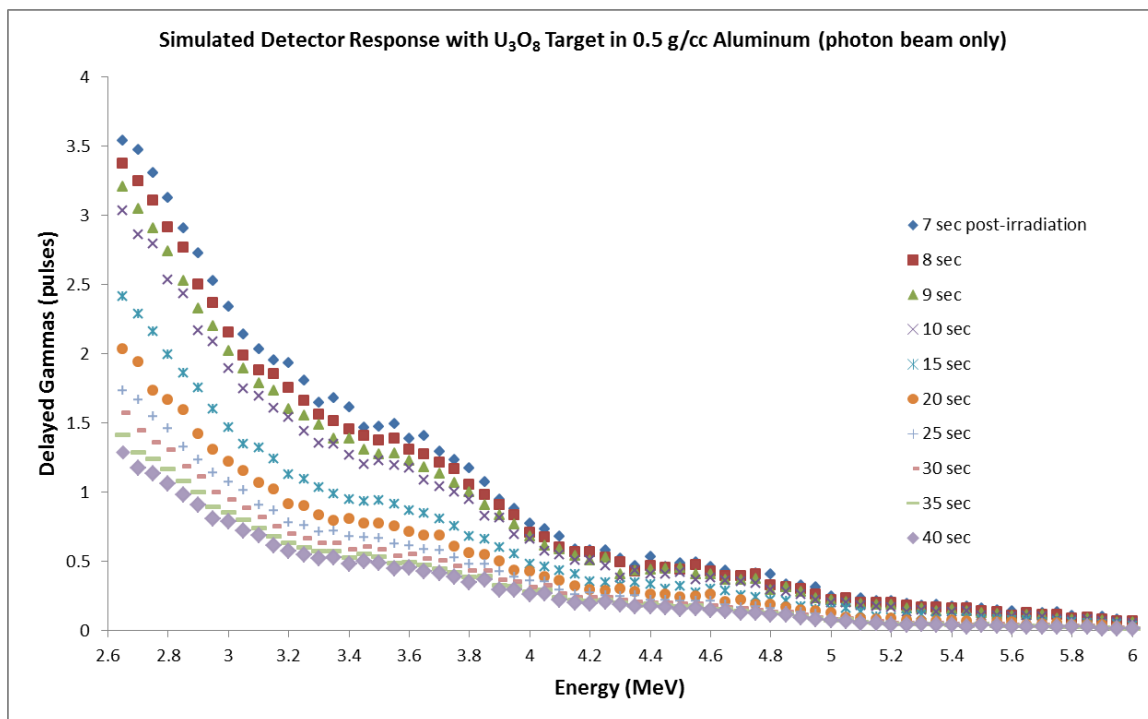


Figure 99. Simulated detector response to delayed gamma emission at one second intervals from 7-10 seconds and five second intervals from 10-40 seconds after 30 second interrogation with 12.2 MeV photon beam. PVT detector adjacent to one vertical side of surrogate container cube. Rapiscan Test Object "E" in aluminum at 0.5 g/cc.

C7. Simulated Detector Responses with U_3O_8 Target in 0.6 g/cc Aluminum

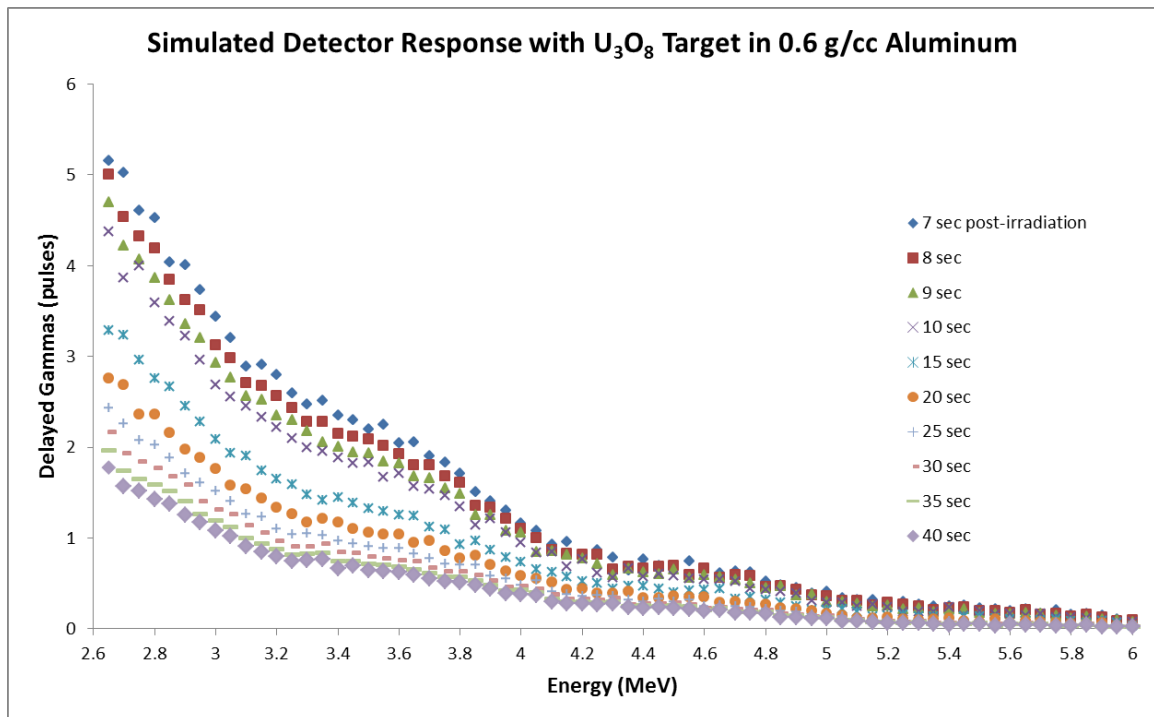


Figure 100. Simulated detector response to delayed gamma emission at one second intervals from 7-10 seconds and five second intervals from 10-40 seconds after 30 second interrogation with 7 MeV neutron and 12.2 MeV photon beams. PVT detector adjacent to one vertical side of surrogate container cube. Rapiscan Test Object "E" in aluminum at 0.6 g/cc.

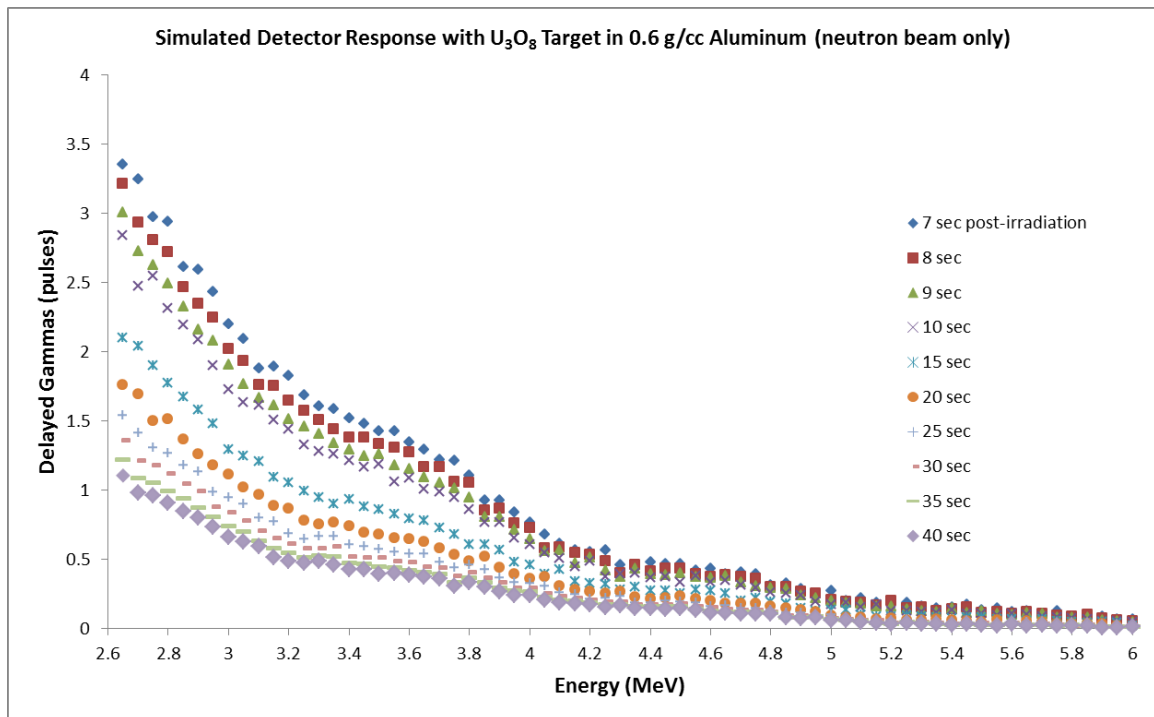


Figure 101. Simulated detector response to delayed gamma emission at one second intervals from 7-10 seconds and five second intervals from 10-40 seconds after 30 second interrogation with 7 MeV neutron beam. PVT detector adjacent to one vertical side of surrogate container cube. Rapiscan Test Object “E” in aluminum at 0.6 g/cc.

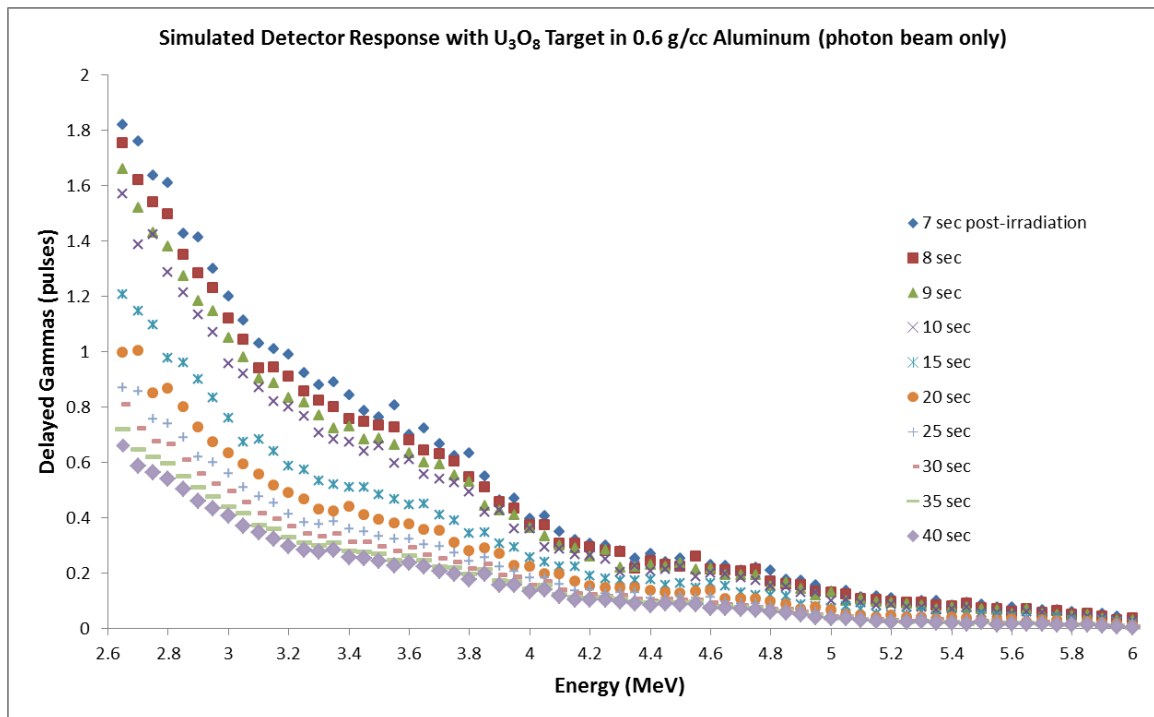


Figure 102. Simulated detector response to delayed gamma emission at one second intervals from 7-10 seconds and five second intervals from 10-40 seconds after 30 second interrogation with 12.2 MeV photon beam. PVT detector adjacent to one vertical side of surrogate container cube. Rapiscan Test Object “E” in aluminum at 0.6 g/cc.

C8. Simulated Detector Responses with U_3O_8 Target in 0.65 g/cc Aluminum

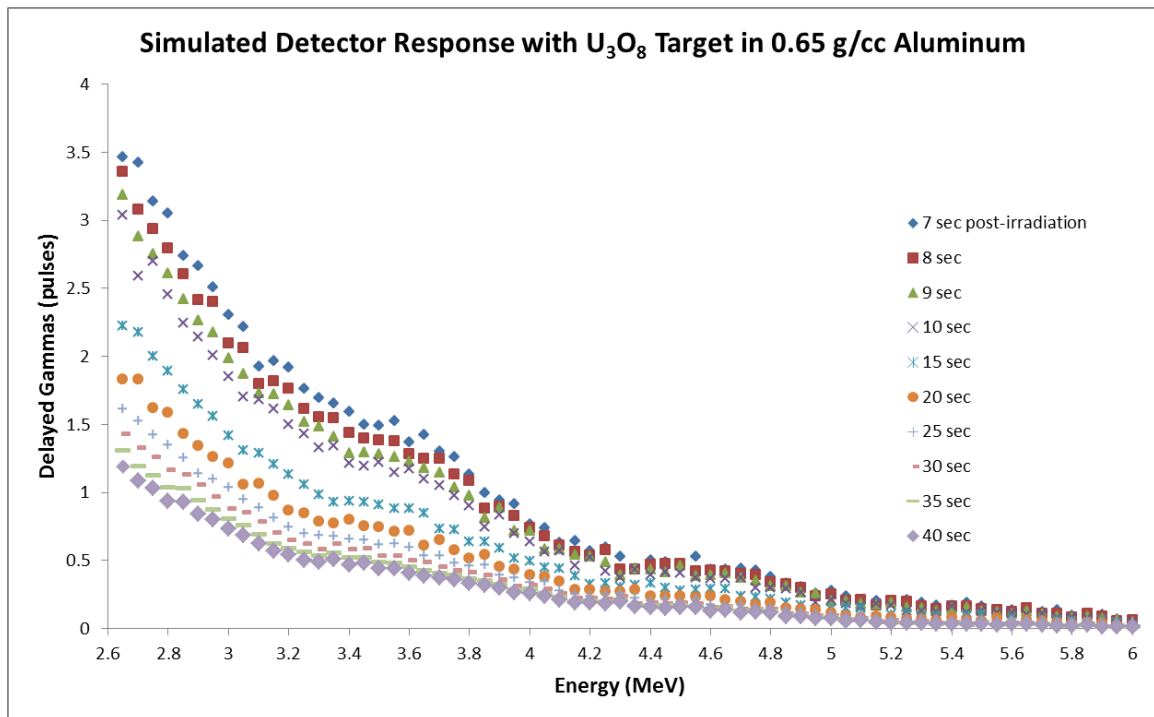


Figure 103. Simulated detector response to delayed gamma emission at one second intervals from 7-10 seconds and five second intervals from 10-40 seconds after 30 second interrogation with 7 MeV neutron and 12.2 MeV photon beams. PVT detector adjacent to one vertical side of surrogate container cube. Rapiscan Test Object "E" in aluminum at 0.65 g/cc.

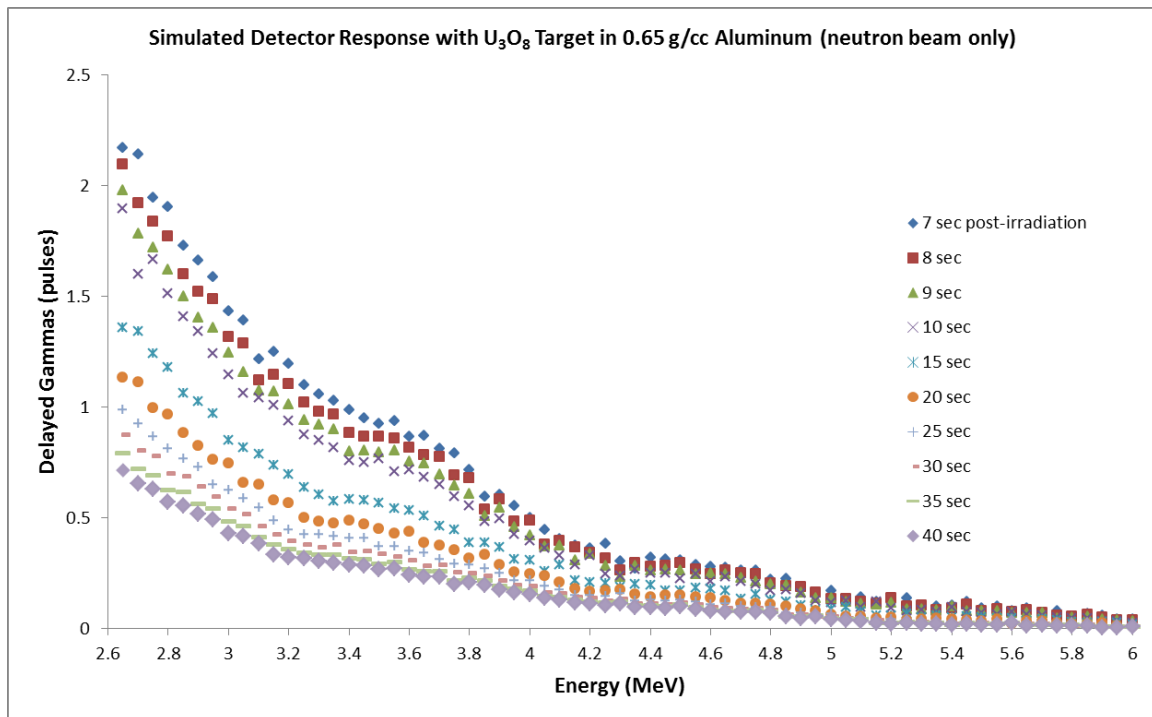


Figure 104. Simulated detector response to delayed gamma emission at one second intervals from 7-10 seconds and five second intervals from 10-40 seconds after 30 second interrogation with 7 MeV neutron beam. PVT detector adjacent to one vertical side of surrogate container cube. Rapiscan Test Object “E” in aluminum at 0.65 g/cc.

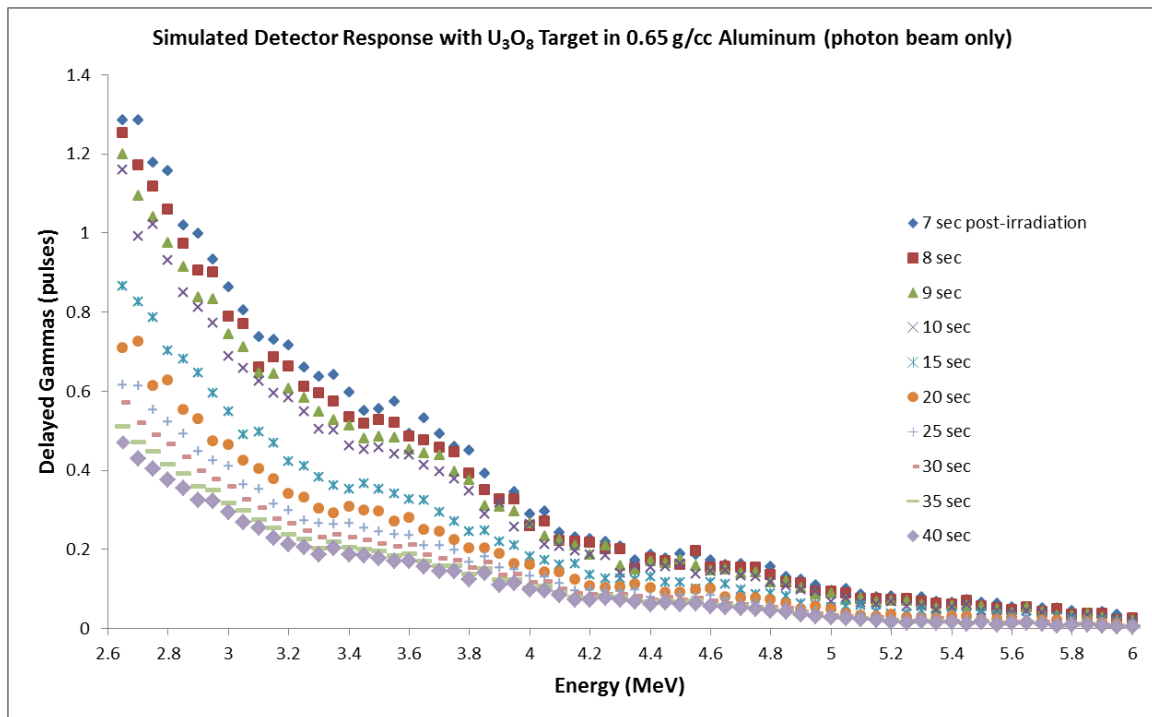


Figure 105. Simulated detector response to delayed gamma emission at one second intervals from 7-10 seconds and five second intervals from 10-40 seconds after 30 second interrogation with 12.2 MeV photon beam. PVT detector adjacent to one vertical side of surrogate container cube. Rapiscan Test Object “E” in aluminum at 0.65 g/cc.

APPENDIX D

Simulated Detector Responses with U_3O_8 Target in Clay

D1. Simulated Detector Responses with U_3O_8 Target in 0.05 g/cc Clay

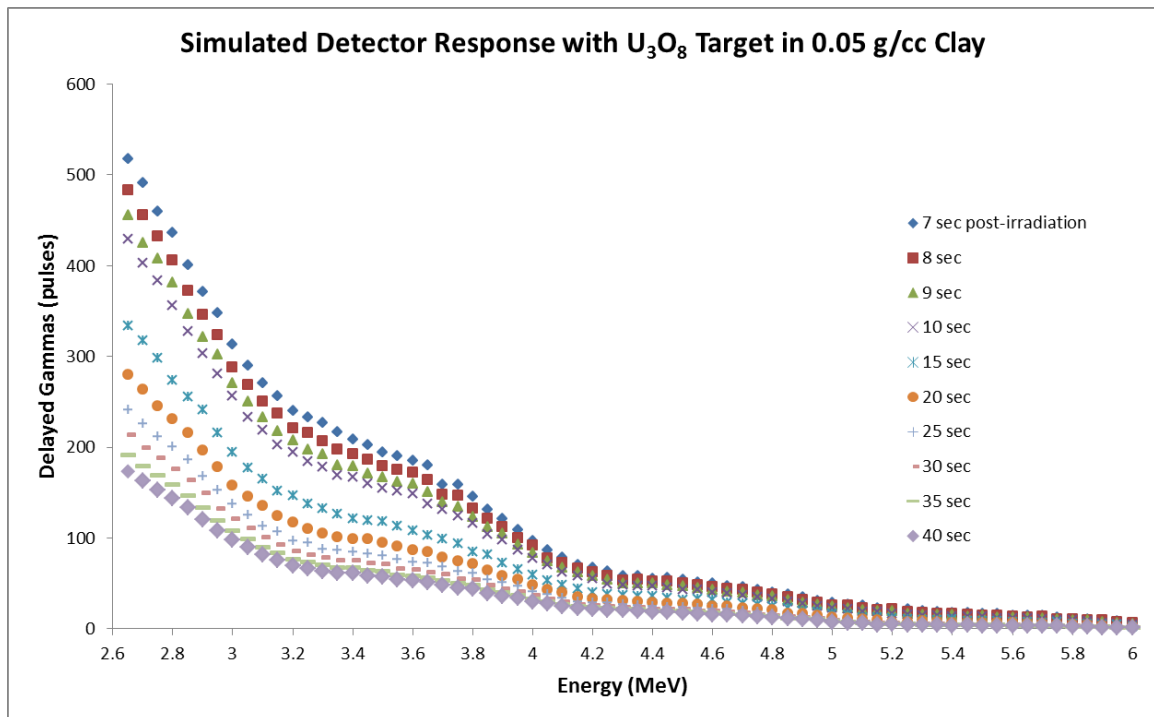


Figure 106. Simulated detector response to delayed gamma emission at one second intervals from 7-10 seconds and five second intervals from 10-40 seconds after 30 second interrogation with 7 MeV neutron and 12.2 MeV photon beams. PVT detector adjacent to one vertical side of surrogate container cube. Rapiscan Test Object "E" in clay at 0.05 g/cc.

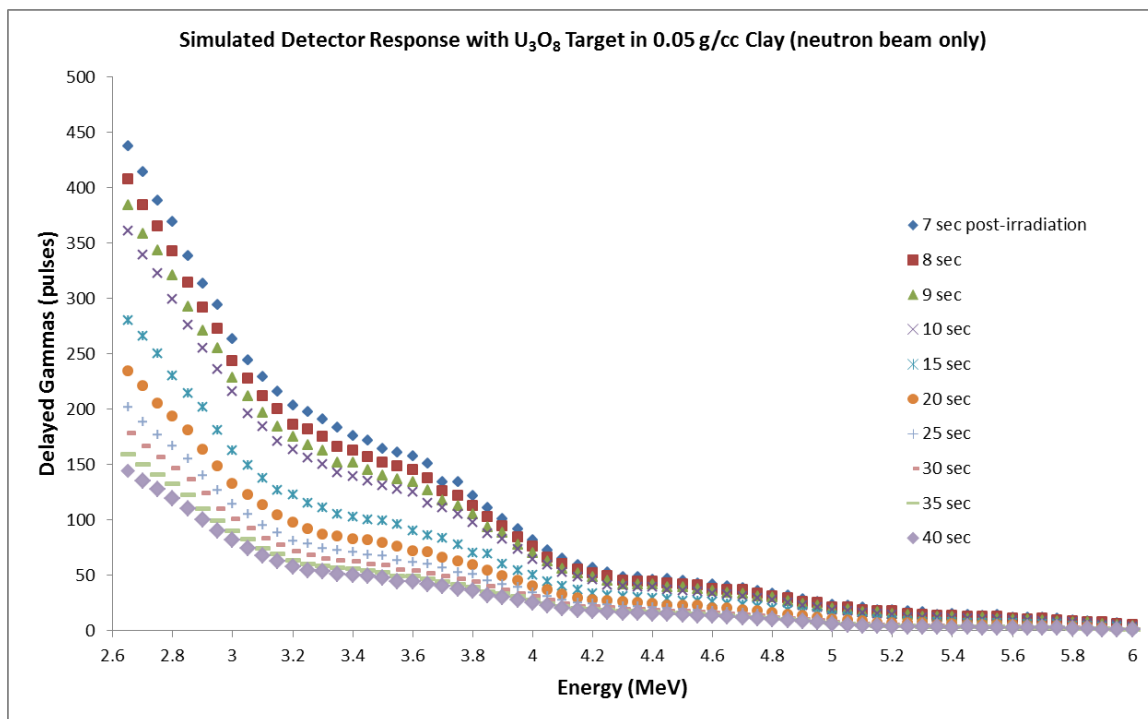


Figure 107. Simulated detector response to delayed gamma emission at one second intervals from 7-10 seconds and five second intervals from 10-40 seconds after 30 second interrogation with 7 MeV neutron beam. PVT detector adjacent to one vertical side of surrogate container cube. Rapiscan Test Object “E” in clay at 0.05 g/cc.

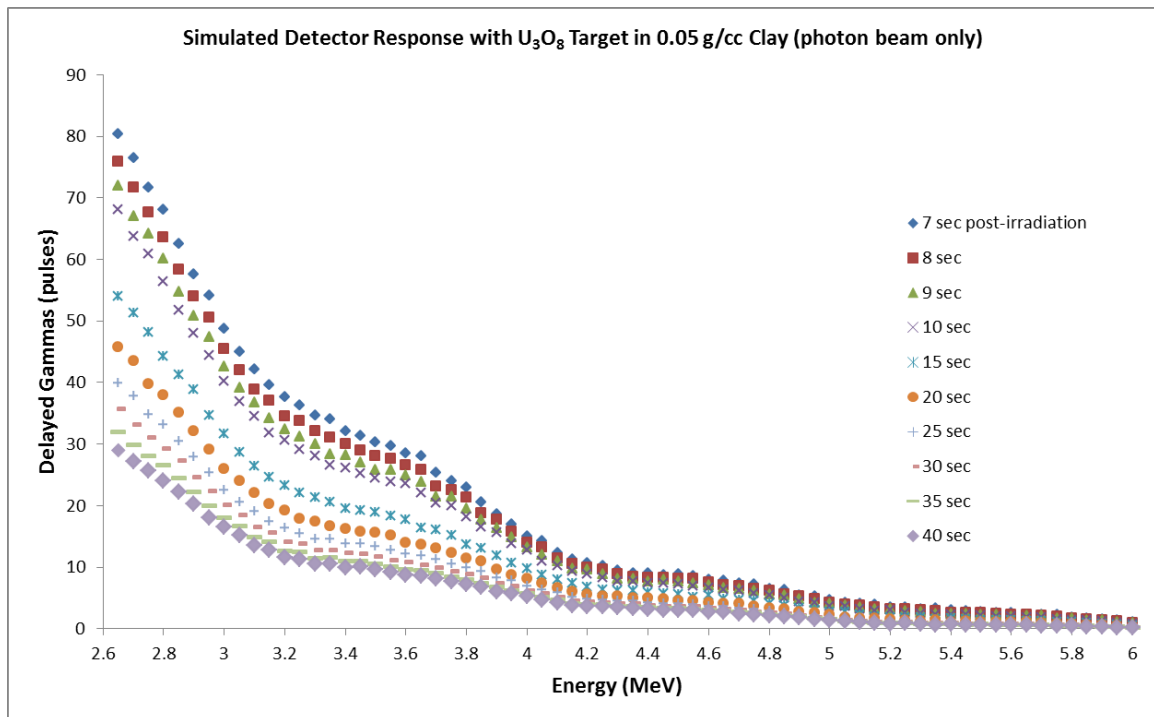


Figure 108. Simulated detector response to delayed gamma emission at one second intervals from 7-10 seconds and five second intervals from 10-40 seconds after 30 second interrogation with 12.2 MeV photon beam. PVT detector adjacent to one vertical side of surrogate container cube. Rapiscan Test Object “E” in clay at 0.05 g/cc.

D2. Simulated Detector Responses with U_3O_8 Target in 0.1 g/cc Clay

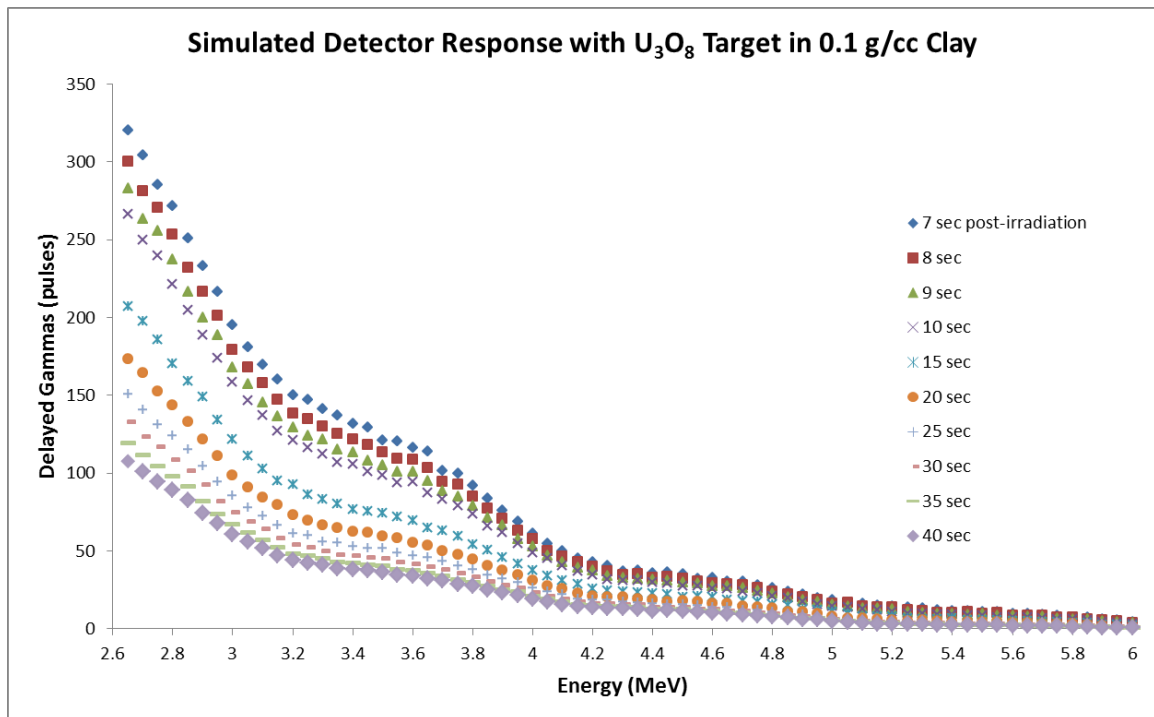


Figure 109. Simulated detector response to delayed gamma emission at one second intervals from 7-10 seconds and five second intervals from 10-40 seconds after 30 second interrogation with 7 MeV neutron and 12.2 MeV photon beams. PVT detector adjacent to one vertical side of surrogate container cube. Rapiscan Test Object "E" in clay at 0.1 g/cc.

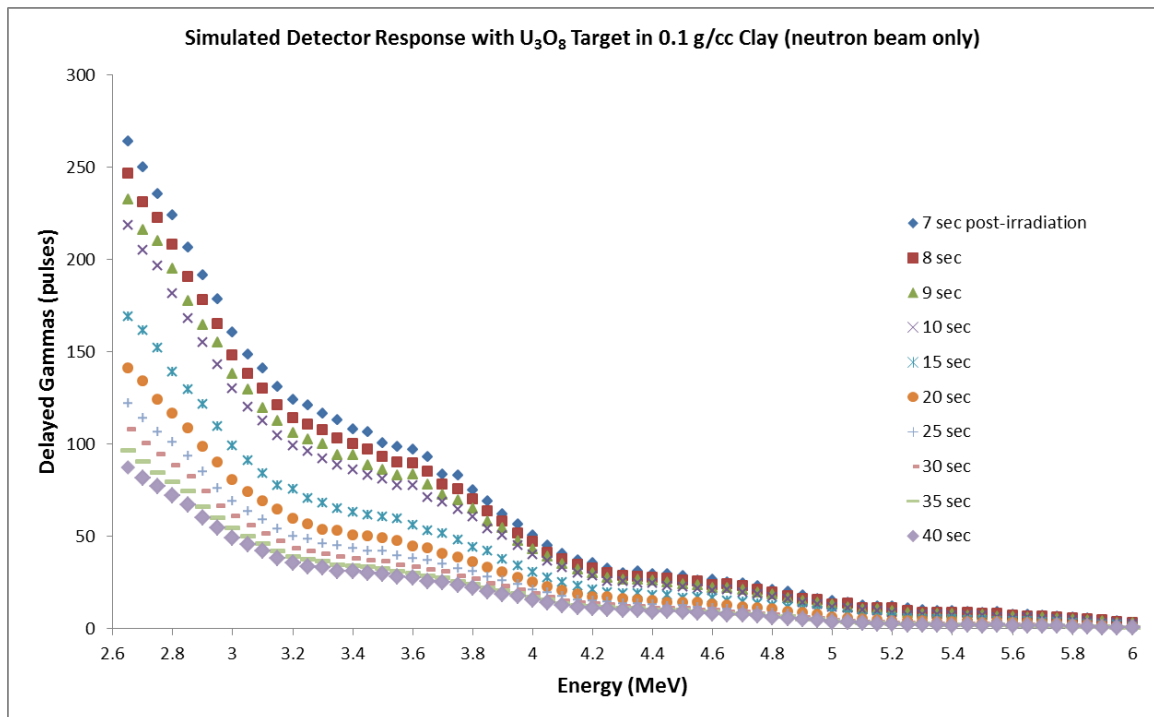


Figure 110. Simulated detector response to delayed gamma emission at one second intervals from 7-10 seconds and five second intervals from 10-40 seconds after 30 second interrogation with 7 MeV neutron beam. PVT detector adjacent to one vertical side of surrogate container cube. Rapiscan Test Object “E” in clay at 0.1 g/cc.

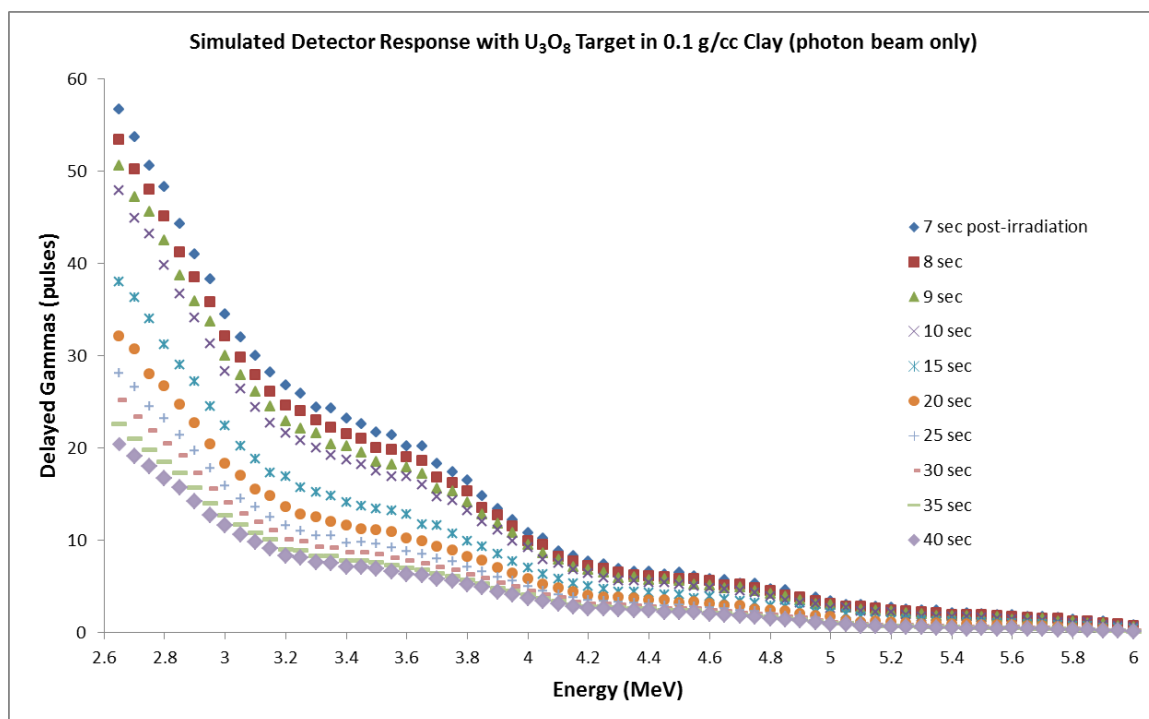


Figure 111. Simulated detector response to delayed gamma emission at one second intervals from 7-10 seconds and five second intervals from 10-40 seconds after 30 second interrogation with 12.2 MeV photon beam. PVT detector adjacent to one vertical side of surrogate container cube. Rapiscan Test Object “E” in clay at 0.1 g/cc.

D3. Simulated Detector Responses with U_3O_8 Target in 0.2 g/cc Clay

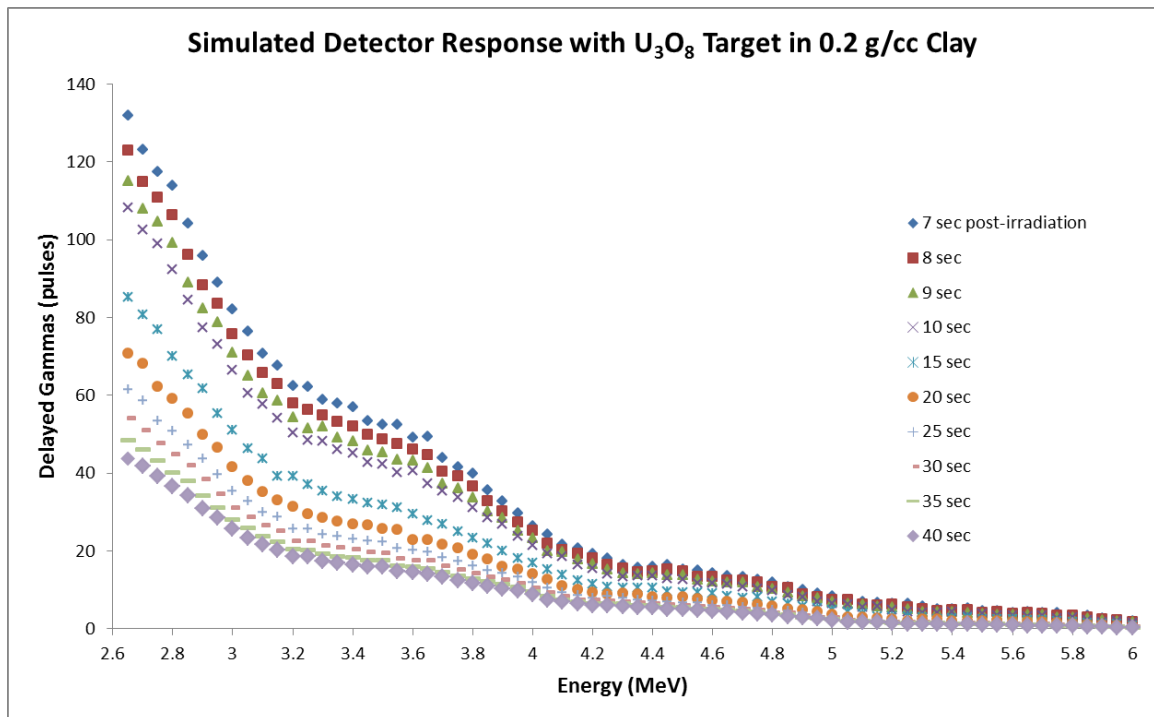


Figure 112. Simulated detector response to delayed gamma emission at one second intervals from 7-10 seconds and five second intervals from 10-40 seconds after 30 second interrogation with 7 MeV neutron and 12.2 MeV photon beams. PVT detector adjacent to one vertical side of surrogate container cube. Rapiscan Test Object "E" in clay at 0.2 g/cc.

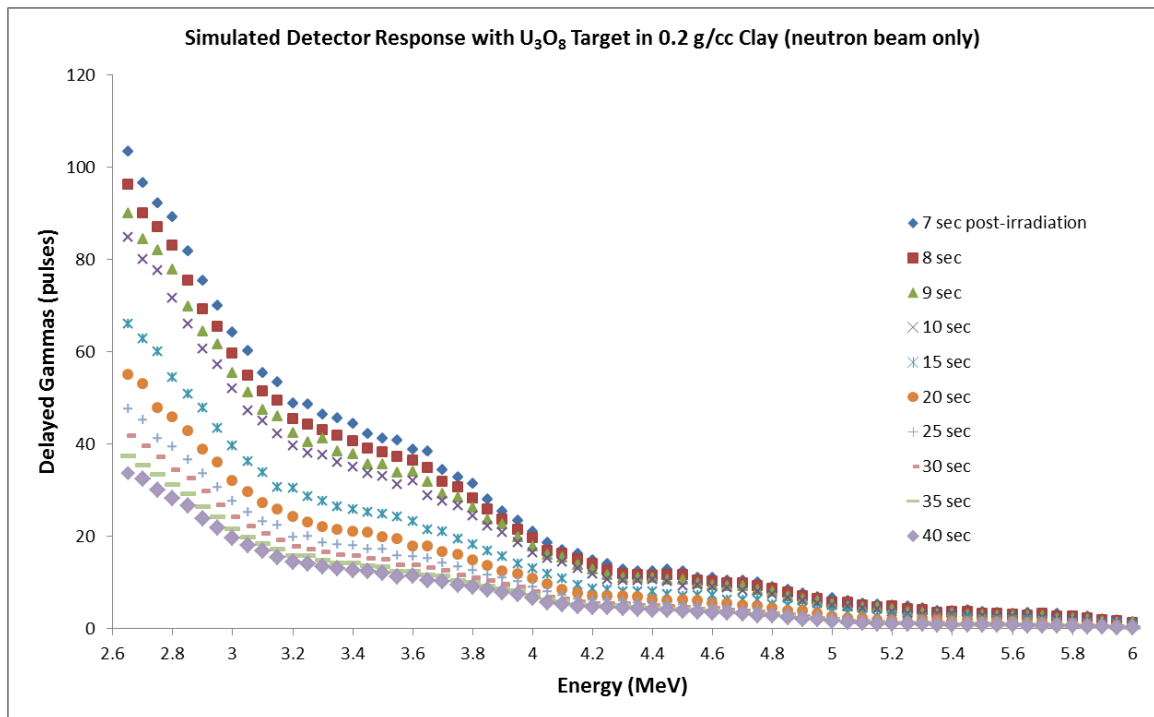


Figure 113. Simulated detector response to delayed gamma emission at one second intervals from 7-10 seconds and five second intervals from 10-40 seconds after 30 second interrogation with 7 MeV neutron beam. PVT detector adjacent to one vertical side of surrogate container cube. Rapiscan Test Object “E” in clay at 0.2 g/cc.

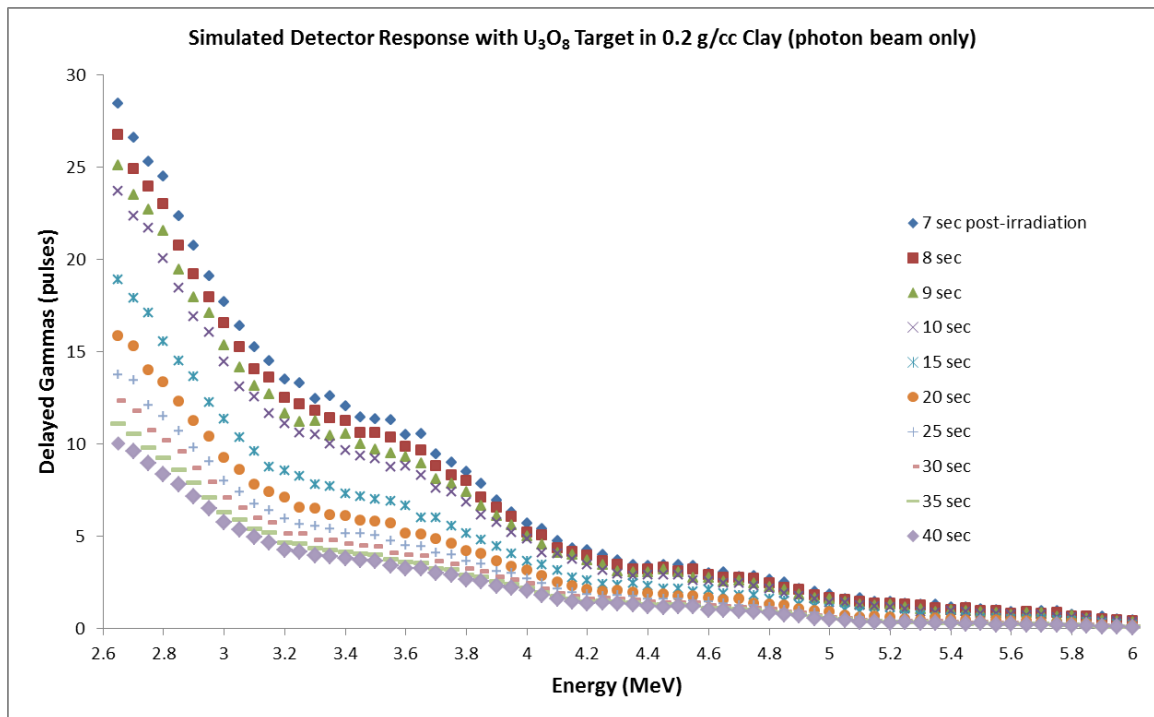


Figure 114. Simulated detector response to delayed gamma emission at one second intervals from 7-10 seconds and five second intervals from 10-40 seconds after 30 second interrogation with 12.2 MeV photon beam. PVT detector adjacent to one vertical side of surrogate container cube. Rapiscan Test Object “E” in clay at 0.2 g/cc.

D4. Simulated Detector Responses with U_3O_8 Target in 0.3 g/cc Clay

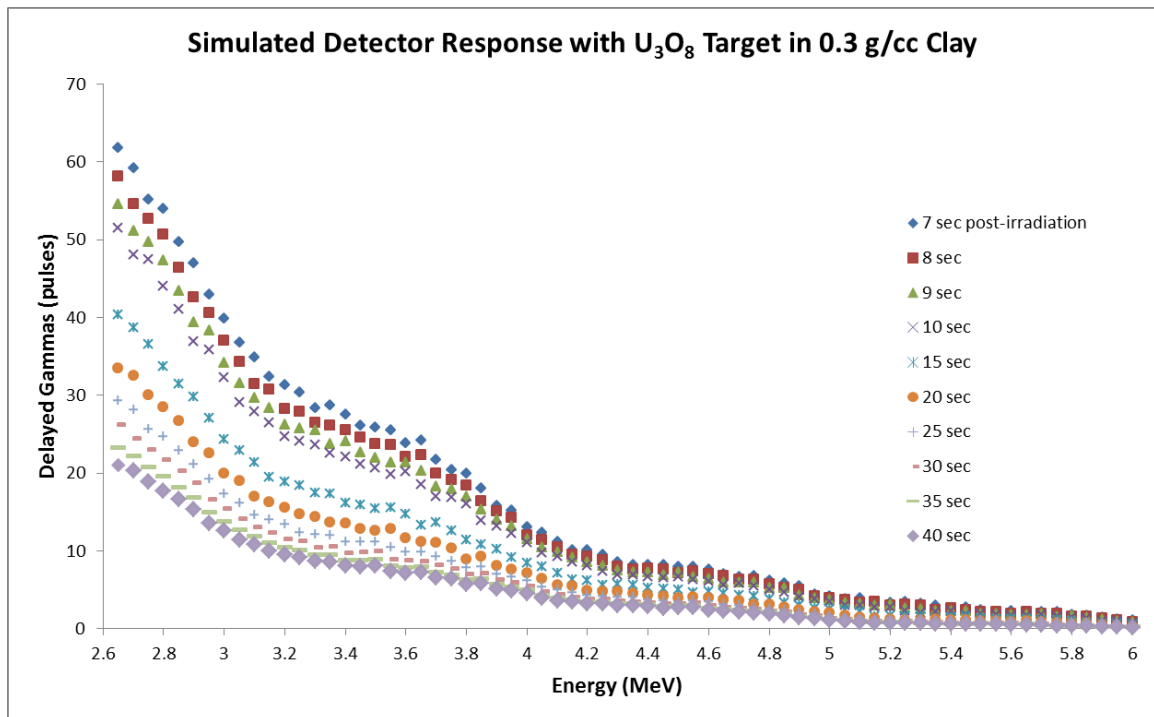


Figure 115. Simulated detector response to delayed gamma emission at one second intervals from 7-10 seconds and five second intervals from 10-40 seconds after 30 second interrogation with 7 MeV neutron and 12.2 MeV photon beams. PVT detector adjacent to one vertical side of surrogate container cube. Rapiscan Test Object "E" in clay at 0.3 g/cc.

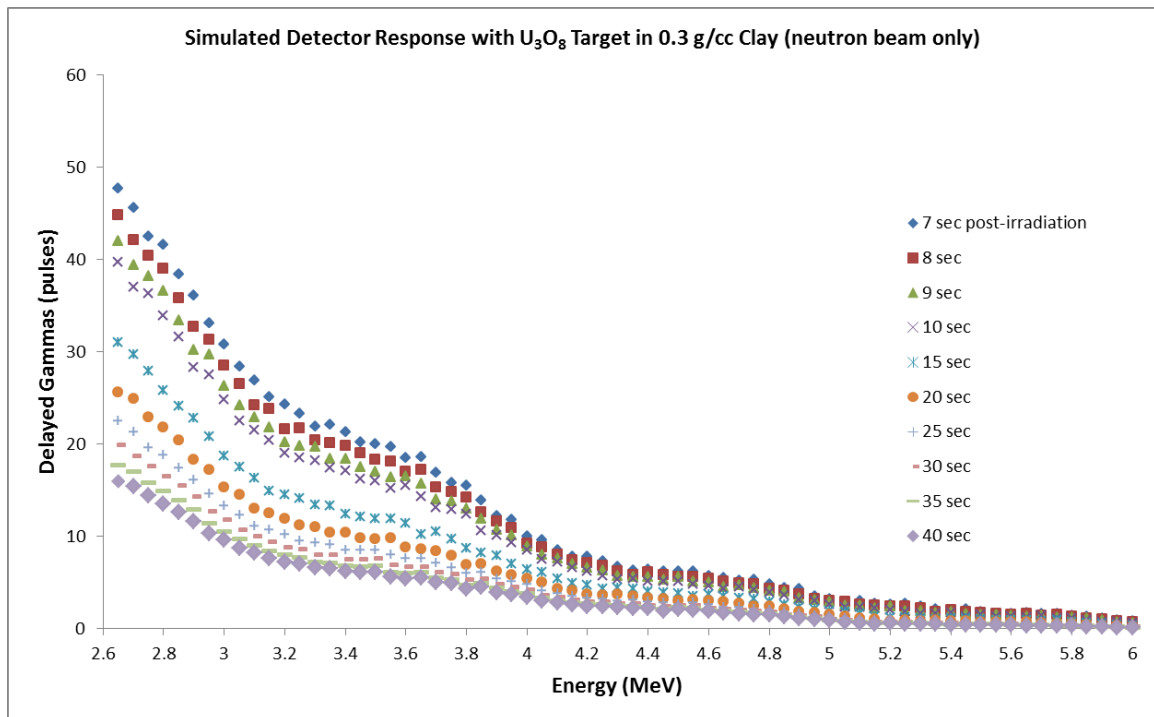


Figure 116. Simulated detector response to delayed gamma emission at one second intervals from 7-10 seconds and five second intervals from 10-40 seconds after 30 second interrogation with 7 MeV neutron beam. PVT detector adjacent to one vertical side of surrogate container cube. Rapiscan Test Object “E” in clay at 0.3 g/cc.

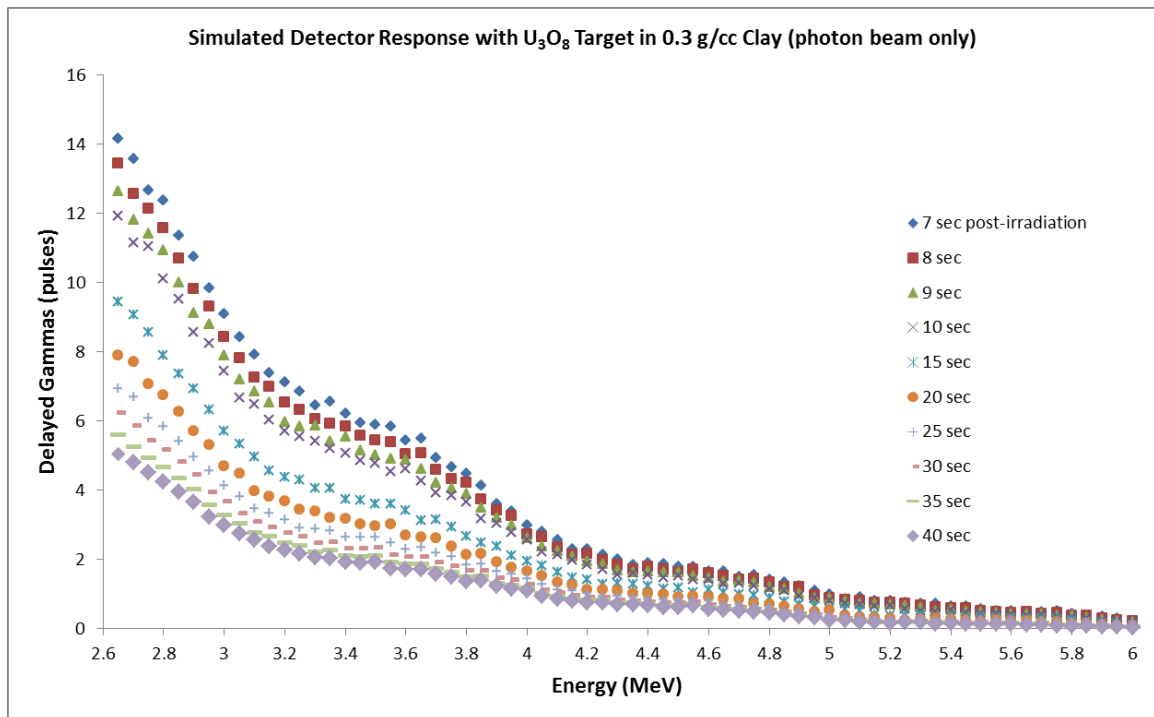


Figure 117. Simulated detector response to delayed gamma emission at one second intervals from 7-10 seconds and five second intervals from 10-40 seconds after 30 second interrogation with 12.2 MeV photon beam. PVT detector adjacent to one vertical side of surrogate container cube. Rapiscan Test Object “E” in clay at 0.3 g/cc.

D5. Simulated Detector Responses with U_3O_8 Target in 0.4 g/cc Clay

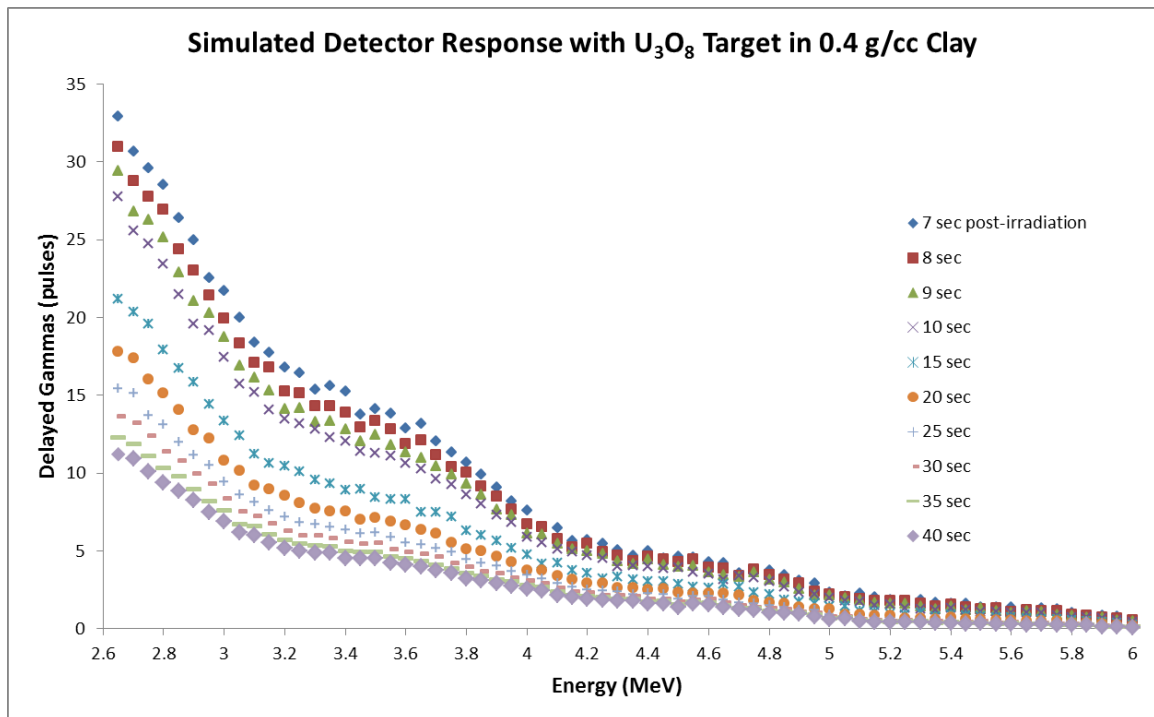


Figure 118. Simulated detector response to delayed gamma emission at one second intervals from 7-10 seconds and five second intervals from 10-40 seconds after 30 second interrogation with 7 MeV neutron and 12.2 MeV photon beams. PVT detector adjacent to one vertical side of surrogate container cube. Rapiscan Test Object "E" in clay at 0.4 g/cc.

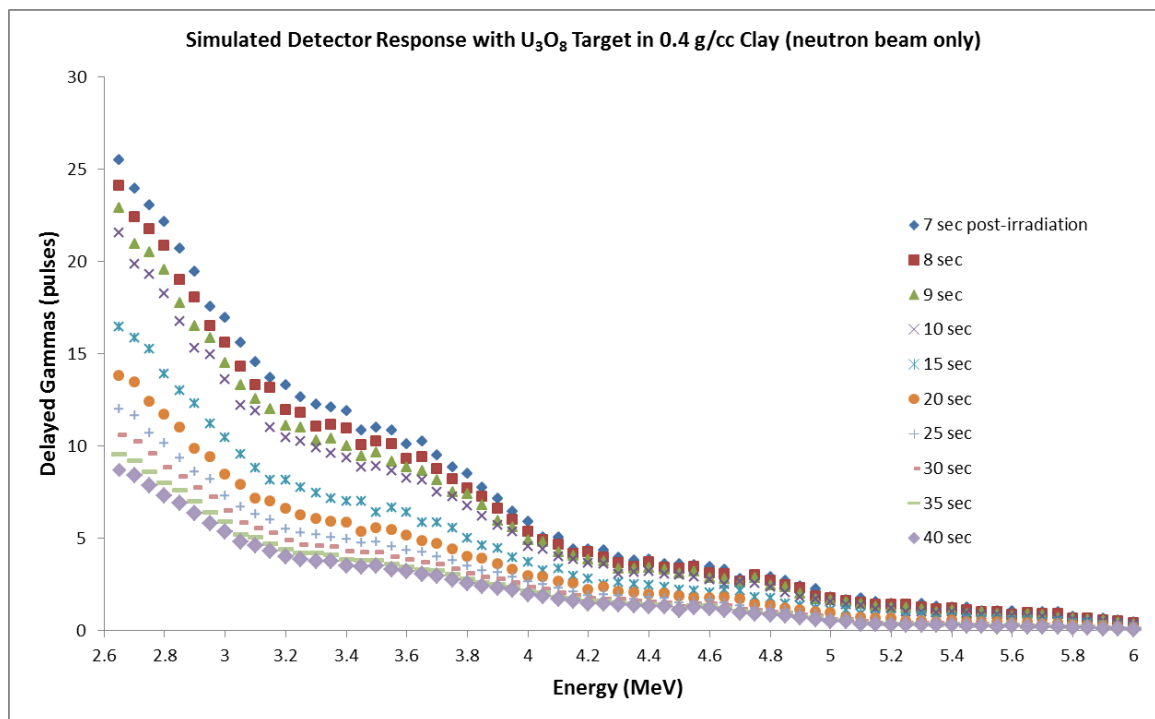


Figure 119. Simulated detector response to delayed gamma emission at one second intervals from 7-10 seconds and five second intervals from 10-40 seconds after 30 second interrogation with 7 MeV neutron beam. PVT detector adjacent to one vertical side of surrogate container cube. Rapiscan Test Object “E” in clay at 0.4 g/cc.

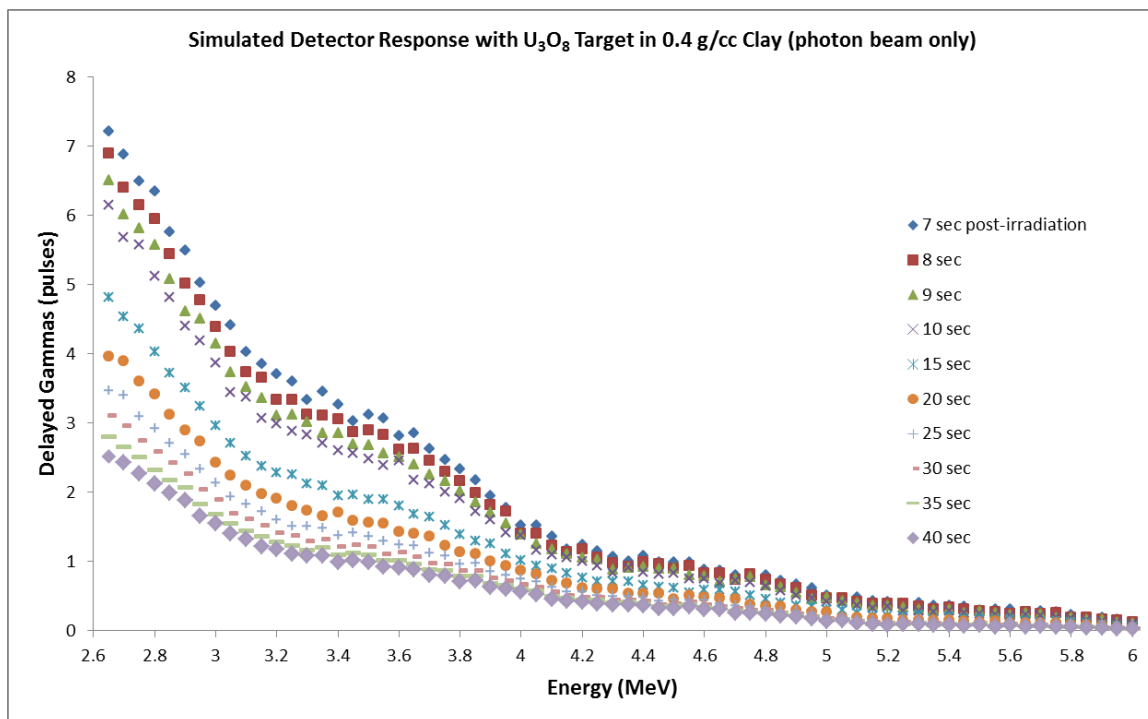


Figure 120. Simulated detector response to delayed gamma emission at one second intervals from 7-10 seconds and five second intervals from 10-40 seconds after 30 second interrogation with 12.2 MeV photon beam. PVT detector adjacent to one vertical side of surrogate container cube. Rapiscan Test Object “E” in clay at 0.4 g/cc.

D6. Simulated Detector Responses with U_3O_8 Target in 0.5 g/cc Clay

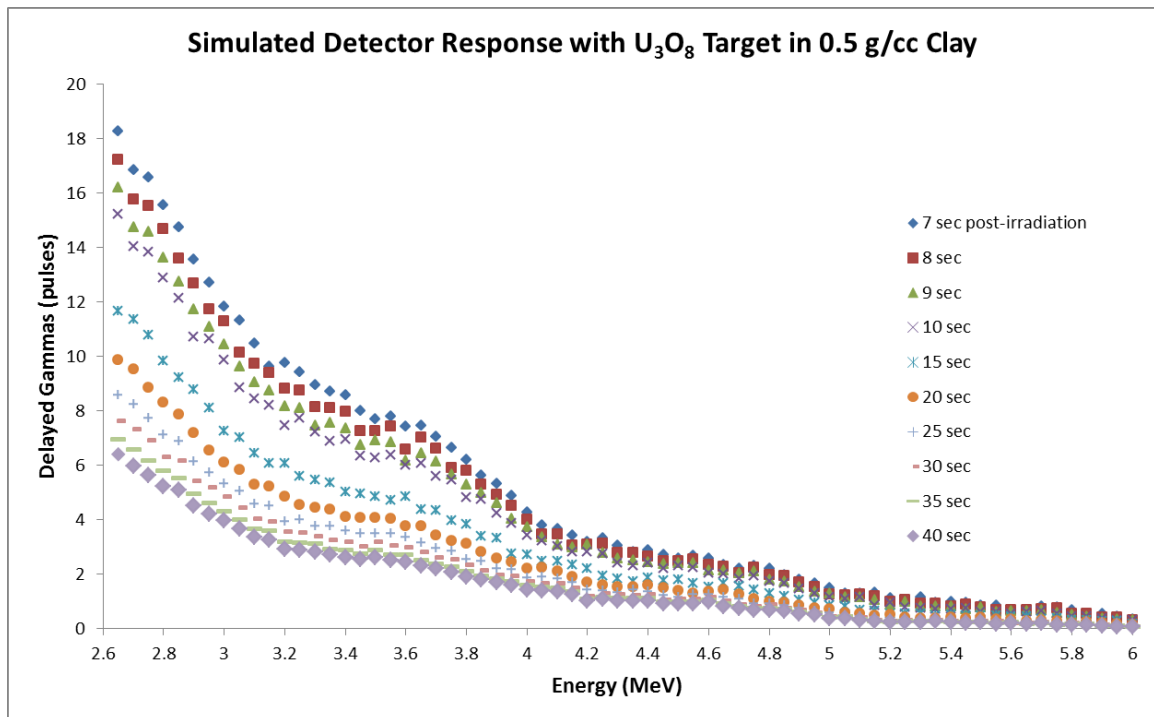


Figure 121. Simulated detector response to delayed gamma emission at one second intervals from 7-10 seconds and five second intervals from 10-40 seconds after 30 second interrogation with 7 MeV neutron and 12.2 MeV photon beams. PVT detector adjacent to one vertical side of surrogate container cube. Rapiscan Test Object "E" in clay at 0.5 g/cc.

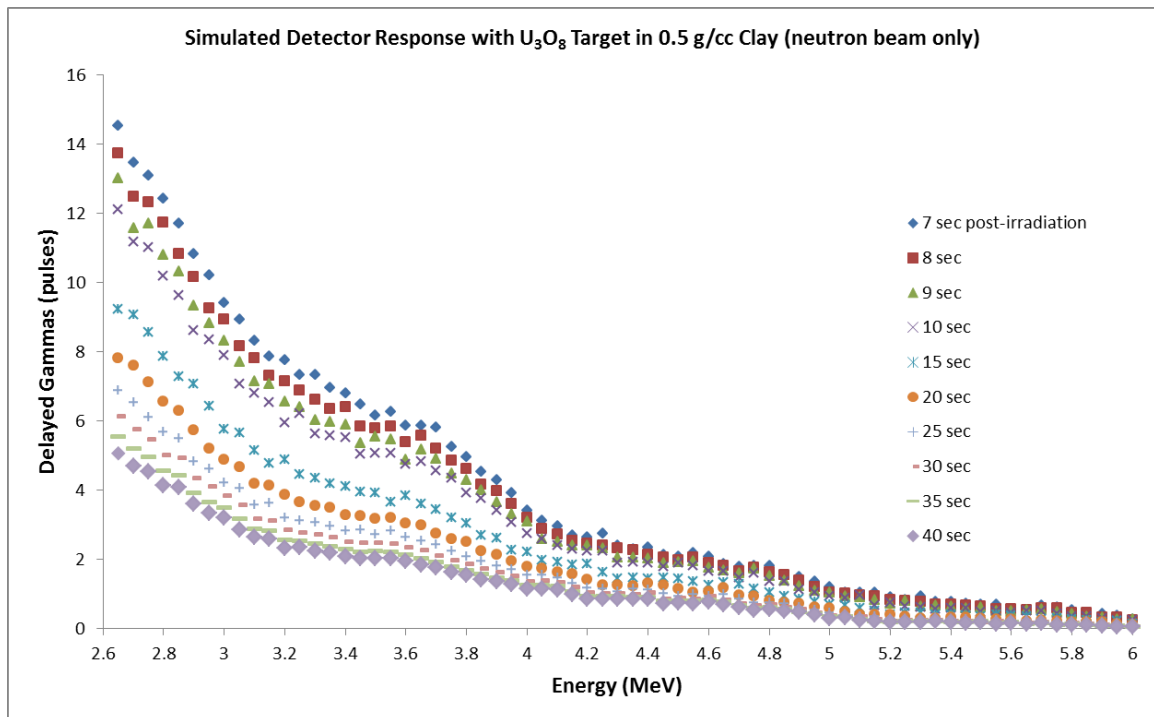


Figure 122. Simulated detector response to delayed gamma emission at one second intervals from 7-10 seconds and five second intervals from 10-40 seconds after 30 second interrogation with 7 MeV neutron beam. PVT detector adjacent to one vertical side of surrogate container cube. Rapiscan Test Object “E” in clay at 0.5 g/cc.

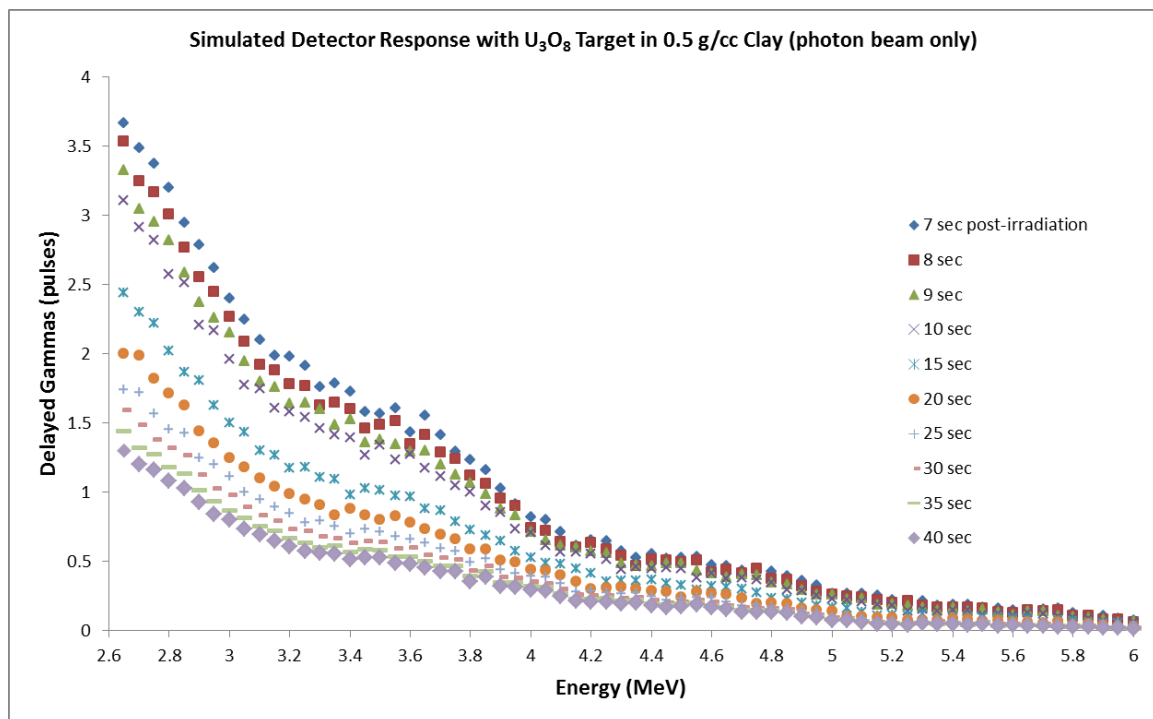


Figure 123. Simulated detector response to delayed gamma emission at one second intervals from 7-10 seconds and five second intervals from 10-40 seconds after 30 second interrogation with 12.2 MeV photon beam. PVT detector adjacent to one vertical side of surrogate container cube. Rapiscan Test Object “E” in clay at 0.5 g/cc.

D7. Simulated Detector Responses with U_3O_8 Target in 0.6 g/cc Clay

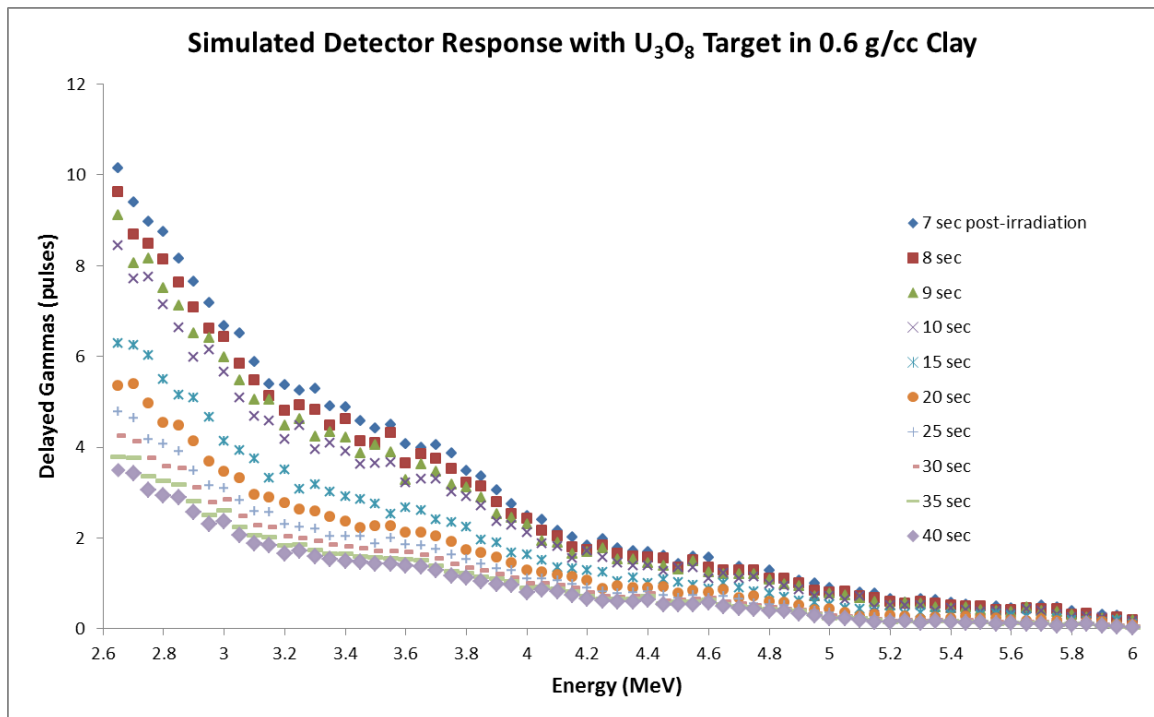


Figure 124. Simulated detector response to delayed gamma emission at one second intervals from 7-10 seconds and five second intervals from 10-40 seconds after 30 second interrogation with 7 MeV neutron and 12.2 MeV photon beams. PVT detector adjacent to one vertical side of surrogate container cube. Rapiscan Test Object "E" in clay at 0.6 g/cc.

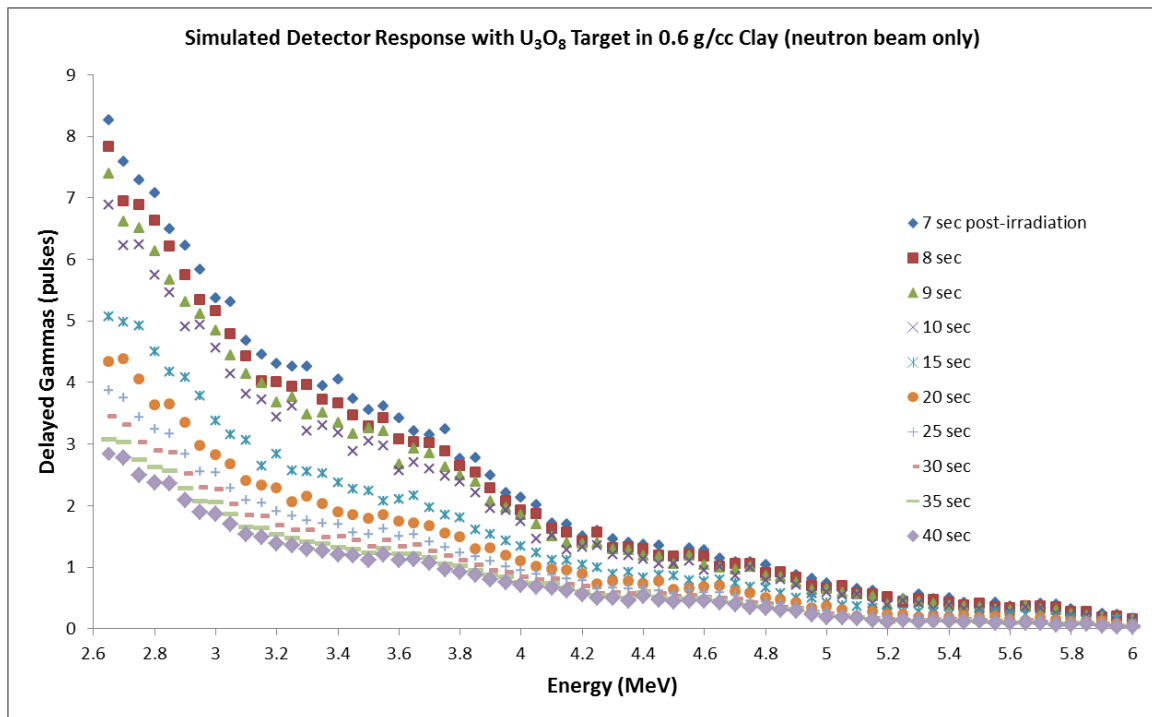


Figure 125. Simulated detector response to delayed gamma emission at one second intervals from 7-10 seconds and five second intervals from 10-40 seconds after 30 second interrogation with 7 MeV neutron beam. PVT detector adjacent to one vertical side of surrogate container cube. Rapiscan Test Object “E” in clay at 0.6 g/cc.

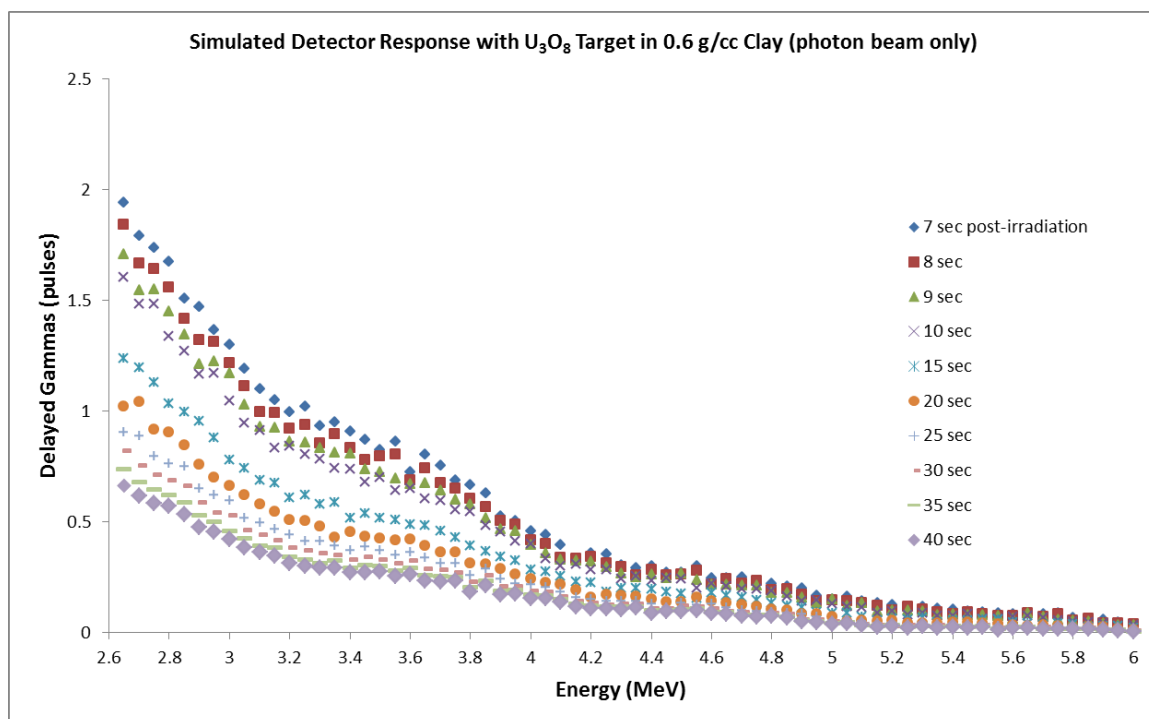


Figure 126. Simulated detector response to delayed gamma emission at one second intervals from 7-10 seconds and five second intervals from 10-40 seconds after 30 second interrogation with 12.2 MeV photon beam. PVT detector adjacent to one vertical side of surrogate container cube. Rapiscan Test Object “E” in clay at 0.6 g/cc.

D8. Simulated Detector Responses with U_3O_8 Target in 0.65 g/cc Clay

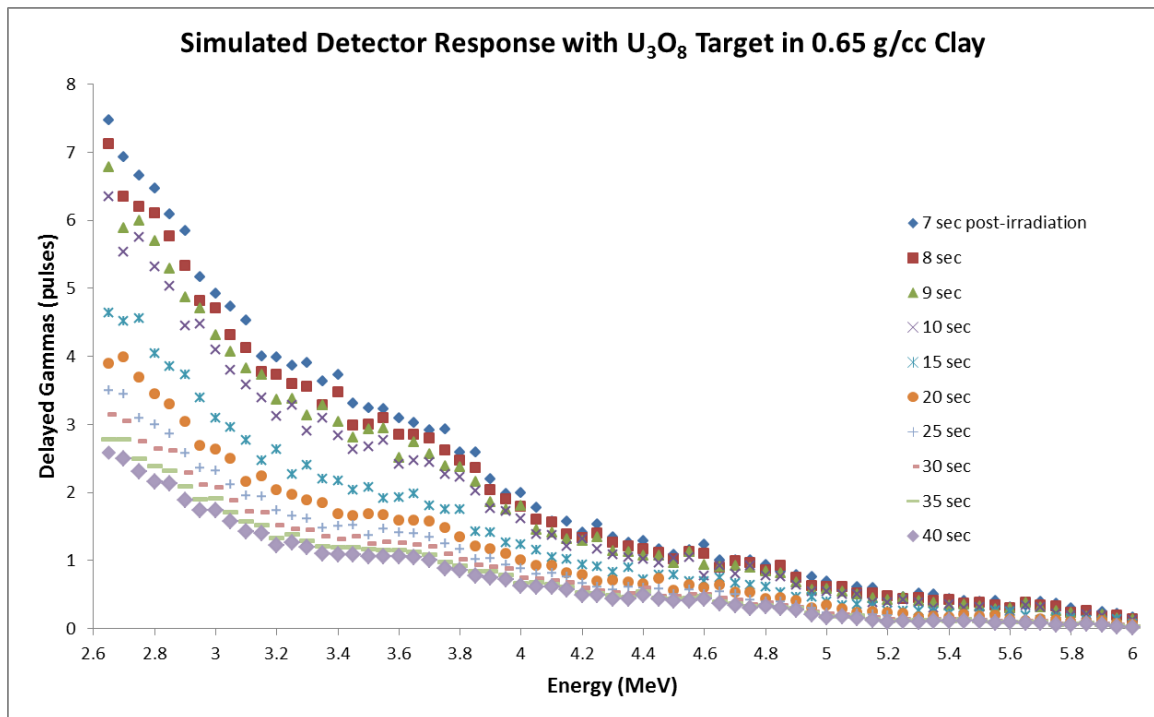


Figure 127. Simulated detector response to delayed gamma emission at one second intervals from 7-10 seconds and five second intervals from 10-40 seconds after 30 second interrogation with 7 MeV neutron and 12.2 MeV photon beams. PVT detector adjacent to one vertical side of surrogate container cube. Rapiscan Test Object "E" in clay at 0.65 g/cc.

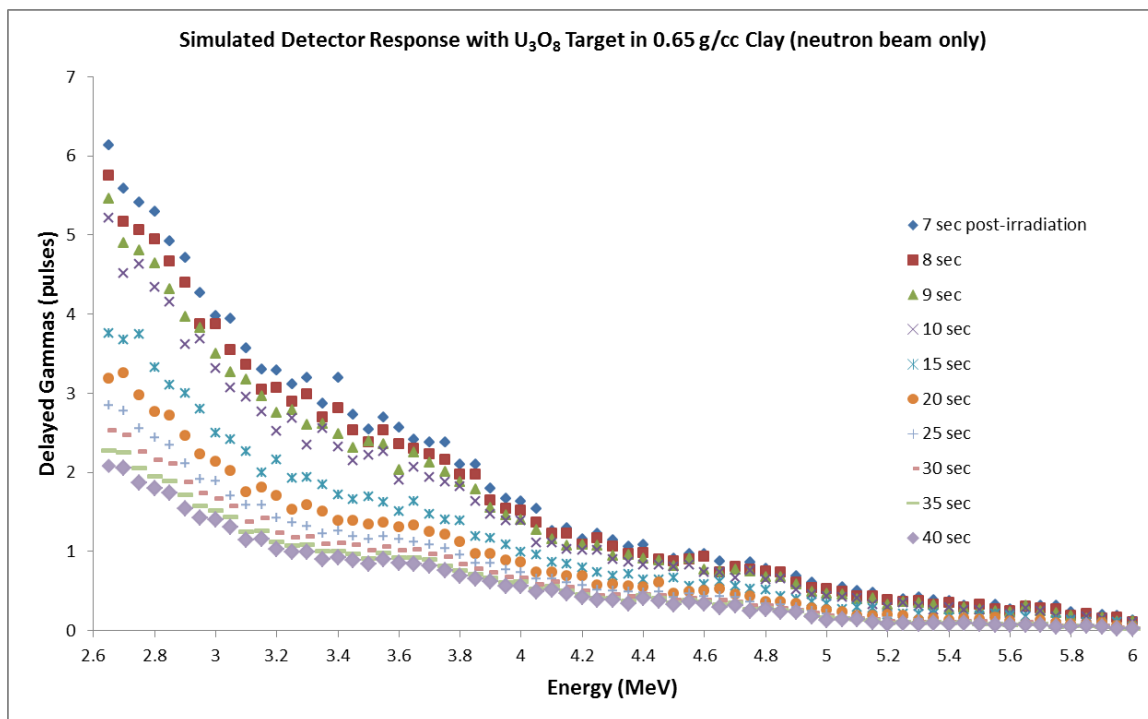


Figure 128. Simulated detector response to delayed gamma emission at one second intervals from 7-10 seconds and five second intervals from 10-40 seconds after 30 second interrogation with 7 MeV neutron beam. PVT detector adjacent to one vertical side of surrogate container cube. Rapiscan Test Object “E” in clay at 0.65 g/cc.

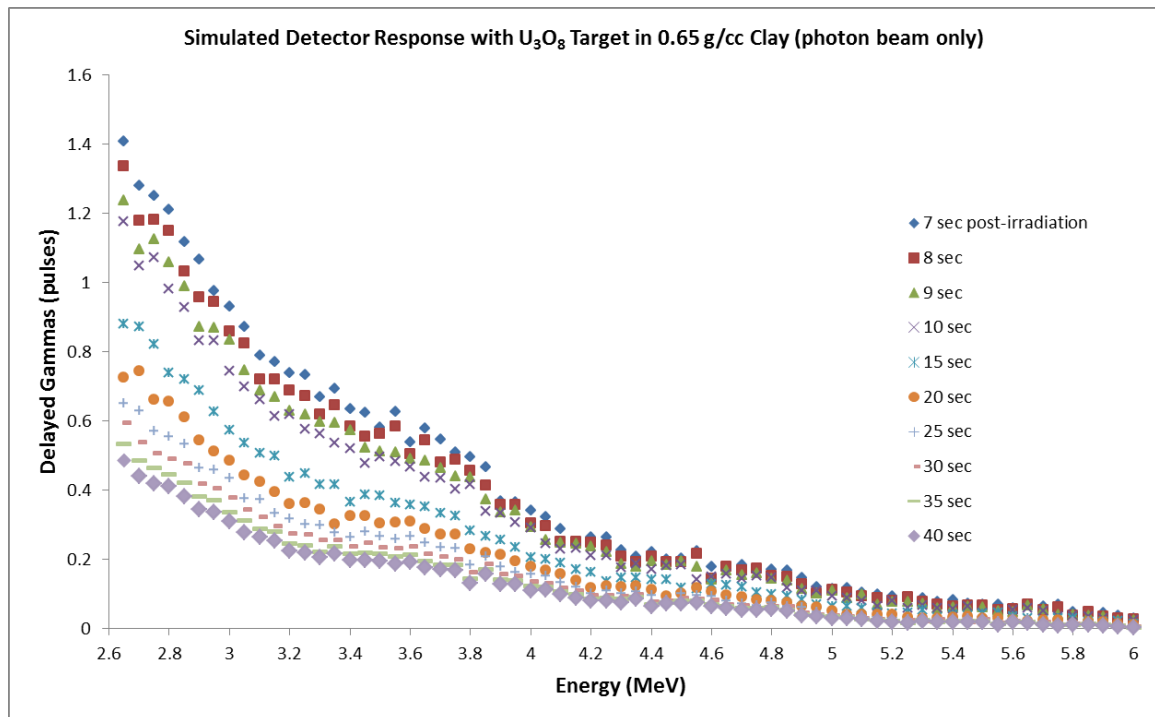


Figure 129. Simulated detector response to delayed gamma emission at one second intervals from 7-10 seconds and five second intervals from 10-40 seconds after 30 second interrogation with 12.2 MeV photon beam. PVT detector adjacent to one vertical side of surrogate container cube. Rapiscan Test Object “E” in clay at 0.65 g/cc.

APPENDIX E

Simulated Detector Responses with U_3O_8 Target in Iron

E1. Simulated Detector Responses with U_3O_8 Target in 0.05 g/cc Iron

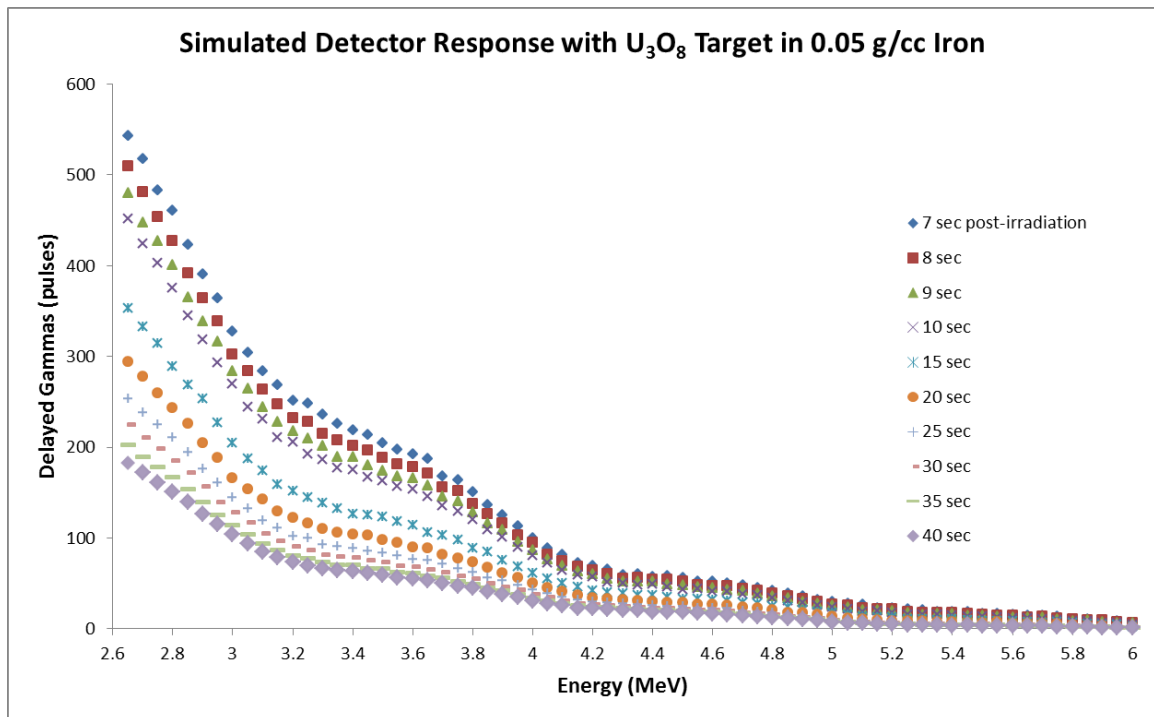


Figure 130. Simulated detector response to delayed gamma emission at one second intervals from 7-10 seconds and five second intervals from 10-40 seconds after 30 second interrogation with 7 MeV neutron and 12.2 MeV photon beams. PVT detector adjacent to one vertical side of surrogate container cube. Rapiscan Test Object "E" in iron at 0.05 g/cc.

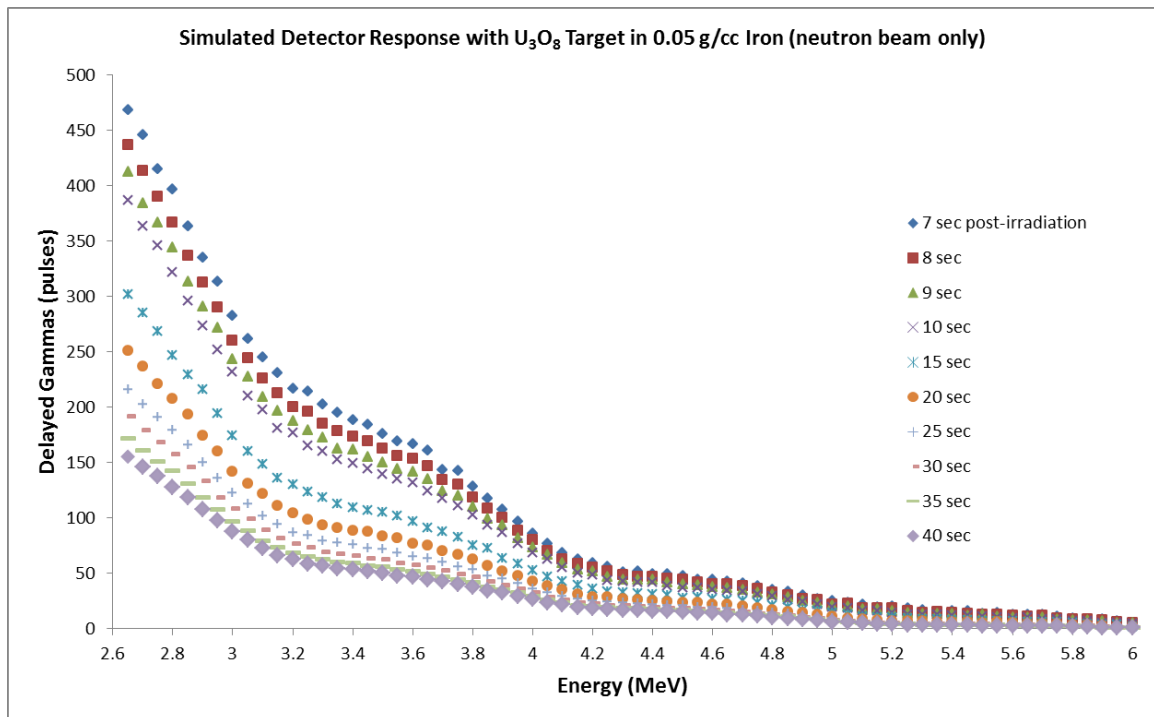


Figure 131. Simulated detector response to delayed gamma emission at one second intervals from 7-10 seconds and five second intervals from 10-40 seconds after 30 second interrogation with 7 MeV neutron beam. PVT detector adjacent to one vertical side of surrogate container cube. Rapiscan Test Object “E” in iron at 0.05 g/cc.

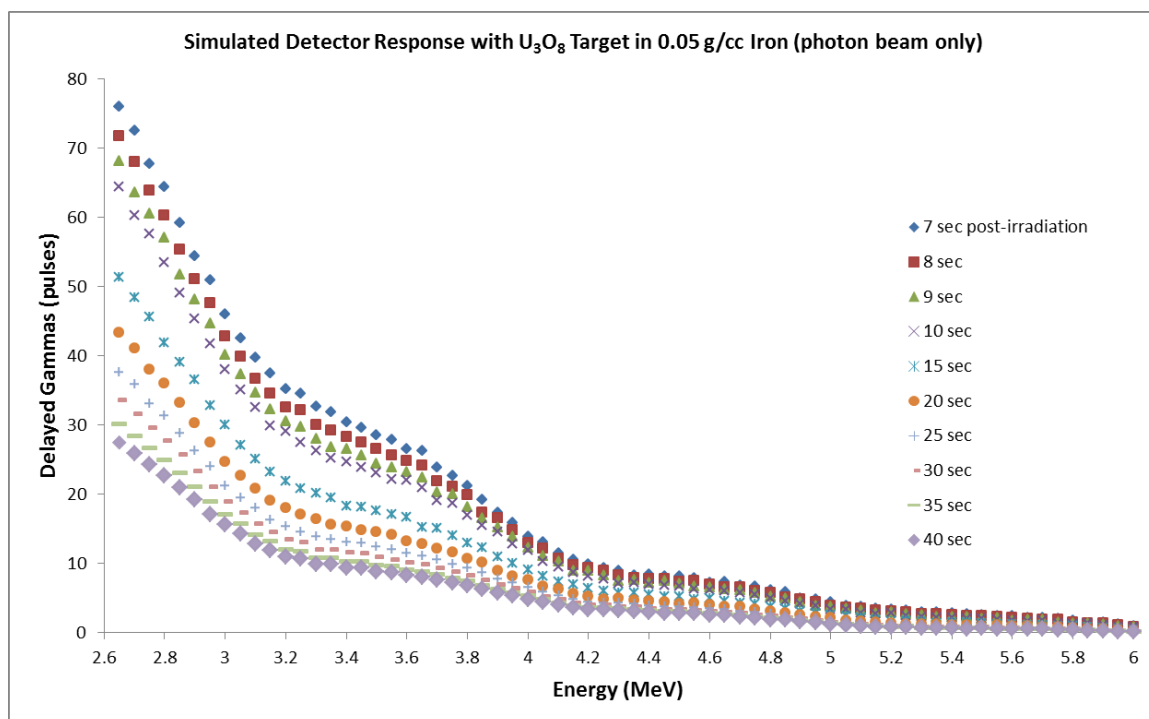


Figure 132. Simulated detector response to delayed gamma emission at one second intervals from 7-10 seconds and five second intervals from 10-40 seconds after 30 second interrogation with 12.2 MeV photon beam. PVT detector adjacent to one vertical side of surrogate container cube. Rapiscan Test Object “E” in iron at 0.05 g/cc.

E2. Simulated Detector Responses with U_3O_8 Target in 0.1 g/cc Iron

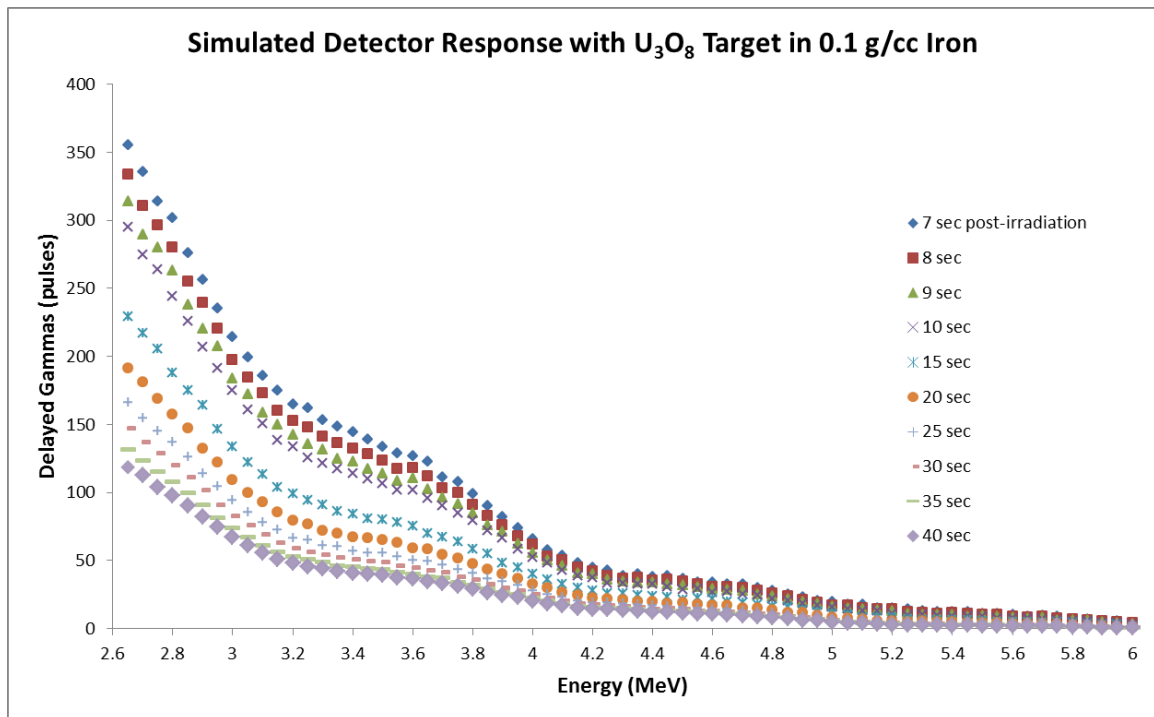


Figure 133. Simulated detector response to delayed gamma emission at one second intervals from 7-10 seconds and five second intervals from 10-40 seconds after 30 second interrogation with 7 MeV neutron and 12.2 MeV photon beams. PVT detector adjacent to one vertical side of surrogate container cube. Rapiscan Test Object "E" in iron at 0.1 g/cc.

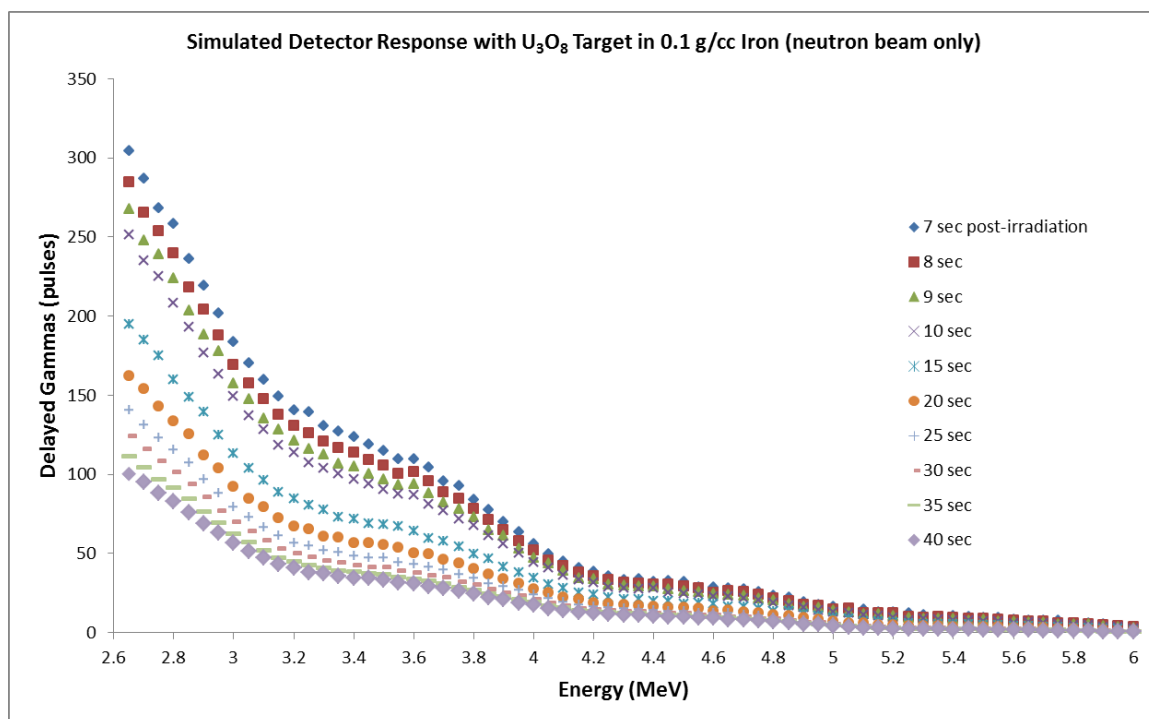


Figure 134. Simulated detector response to delayed gamma emission at one second intervals from 7-10 seconds and five second intervals from 10-40 seconds after 30 second interrogation with 7 MeV neutron beam. PVT detector adjacent to one vertical side of surrogate container cube. Rapiscan Test Object “E” in iron at 0.1 g/cc.

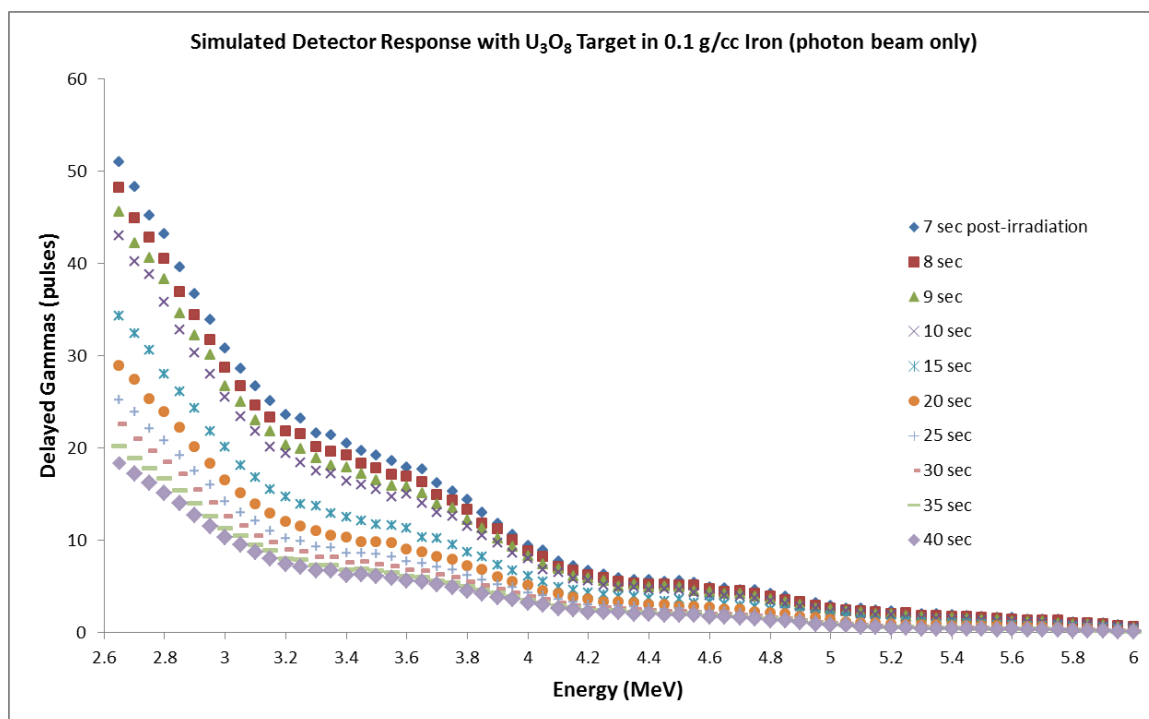


Figure 135. Simulated detector response to delayed gamma emission at one second intervals from 7-10 seconds and five second intervals from 10-40 seconds after 30 second interrogation with 12.2 MeV photon beam. PVT detector adjacent to one vertical side of surrogate container cube. Rapiscan Test Object “E” in iron at 0.1 g/cc.

E3. Simulated Detector Responses with U_3O_8 Target in 0.2 g/cc Iron

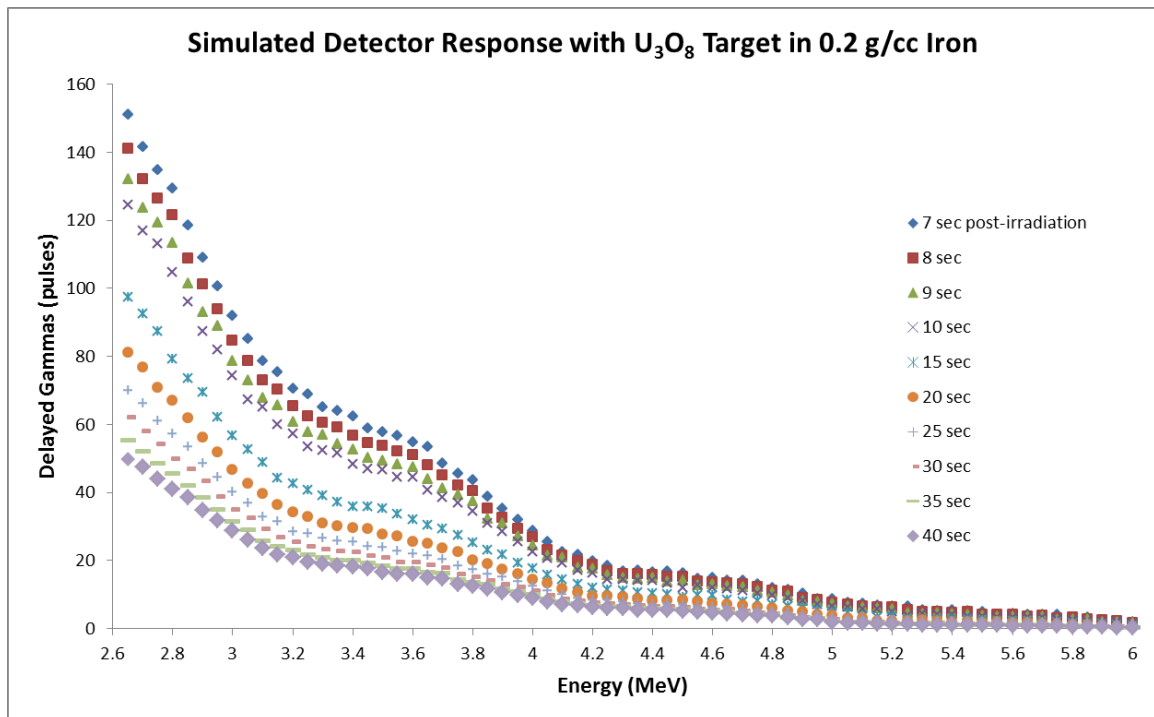


Figure 136. Simulated detector response to delayed gamma emission at one second intervals from 7-10 seconds and five second intervals from 10-40 seconds after 30 second interrogation with 7 MeV neutron and 12.2 MeV photon beams. PVT detector adjacent to one vertical side of surrogate container cube. Rapiscan Test Object "E" in iron at 0.2 g/cc.

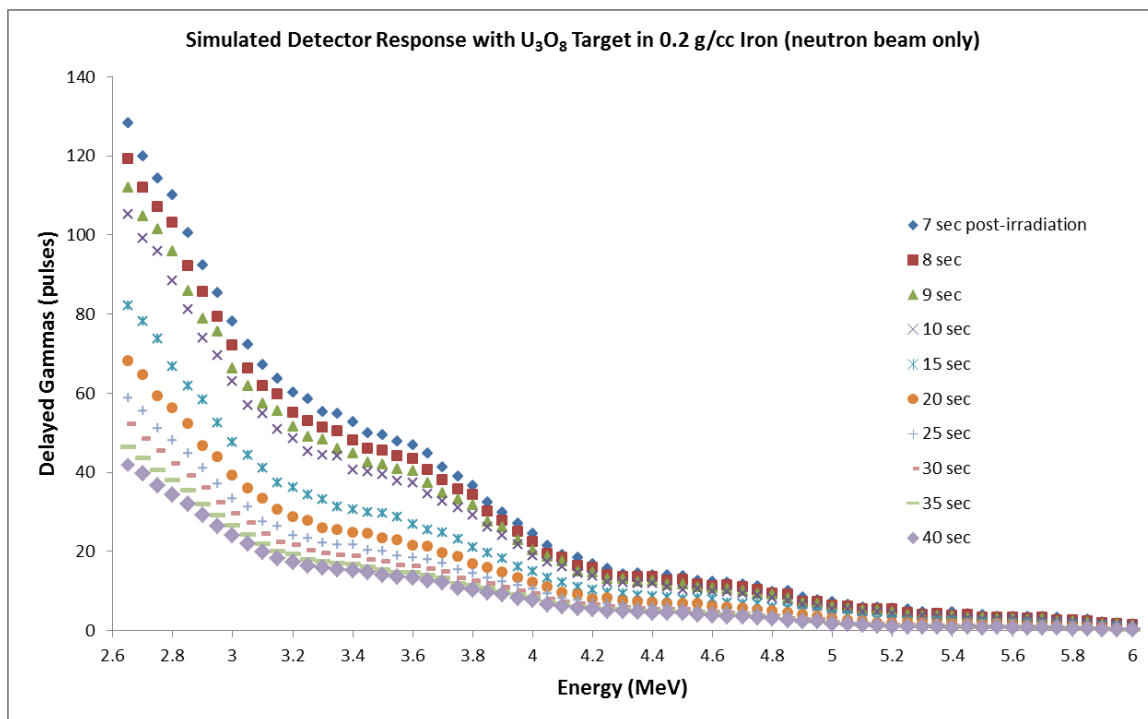


Figure 137. Simulated detector response to delayed gamma emission at one second intervals from 7-10 seconds and five second intervals from 10-40 seconds after 30 second interrogation with 7 MeV neutron beam. PVT detector adjacent to one vertical side of surrogate container cube. Rapiscan Test Object “E” in iron at 0.2 g/cc.

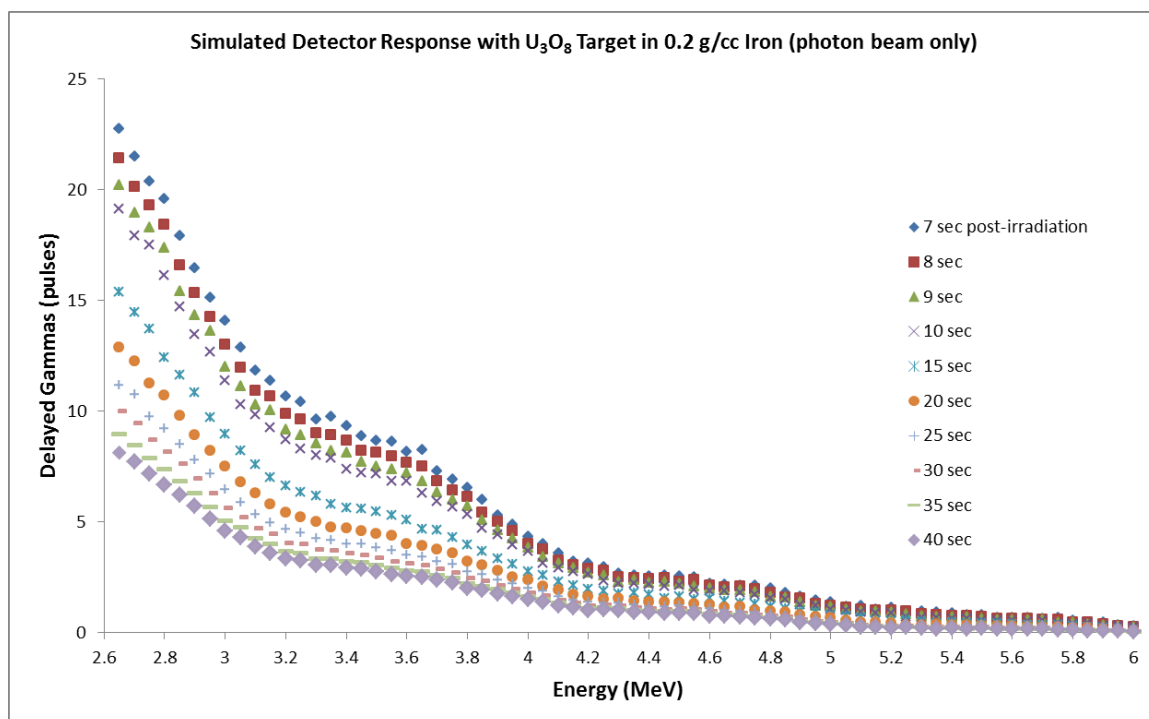


Figure 138. Simulated detector response to delayed gamma emission at one second intervals from 7-10 seconds and five second intervals from 10-40 seconds after 30 second interrogation with 12.2 MeV photon beam. PVT detector adjacent to one vertical side of surrogate container cube. Rapiscan Test Object “E” in iron at 0.2 g/cc.

E4. Simulated Detector Responses with U_3O_8 Target in 0.3 g/cc Iron

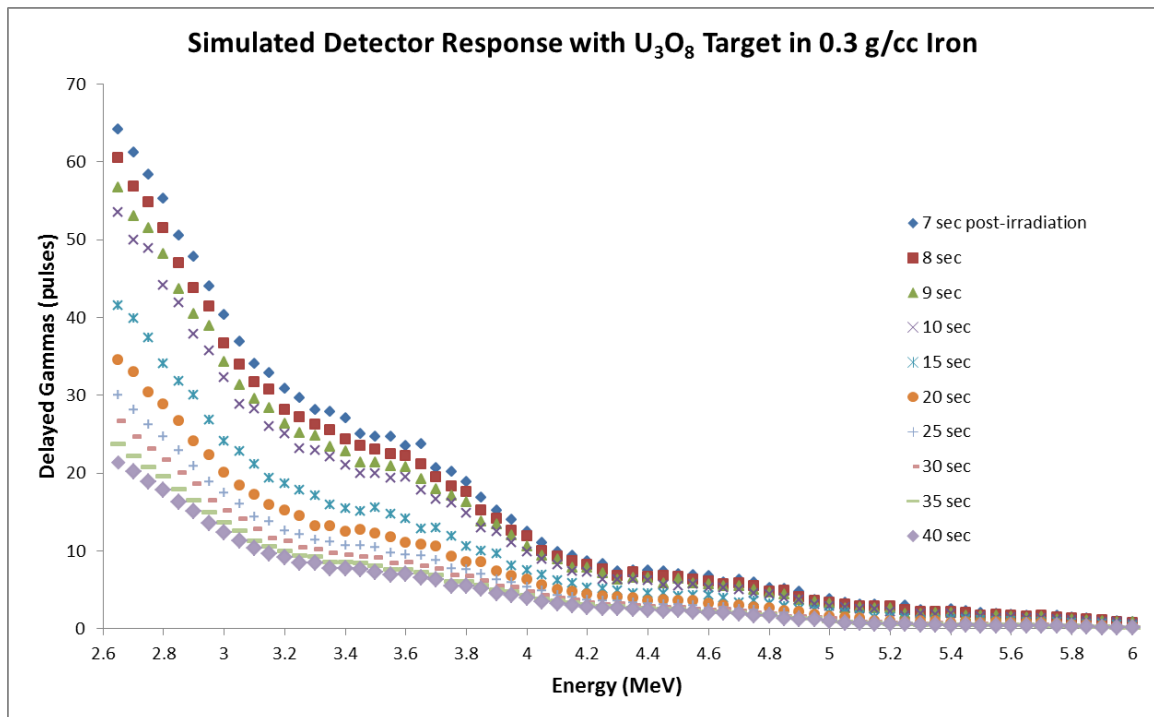


Figure 139. Simulated detector response to delayed gamma emission at one second intervals from 7-10 seconds and five second intervals from 10-40 seconds after 30 second interrogation with 7 MeV neutron and 12.2 MeV photon beams. PVT detector adjacent to one vertical side of surrogate container cube. Rapiscan Test Object “E” in iron at 0.3 g/cc.

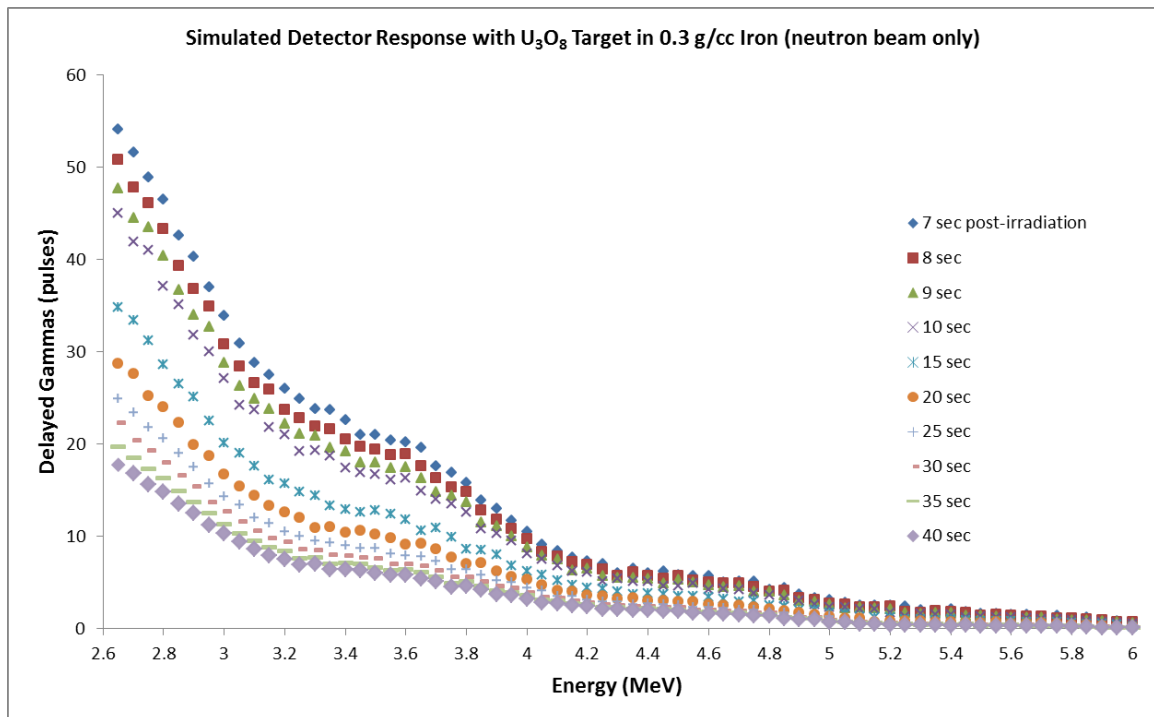


Figure 140. Simulated detector response to delayed gamma emission at one second intervals from 7-10 seconds and five second intervals from 10-40 seconds after 30 second interrogation with 7 MeV neutron beam. PVT detector adjacent to one vertical side of surrogate container cube. Rapiscan Test Object “E” in iron at 0.3 g/cc.

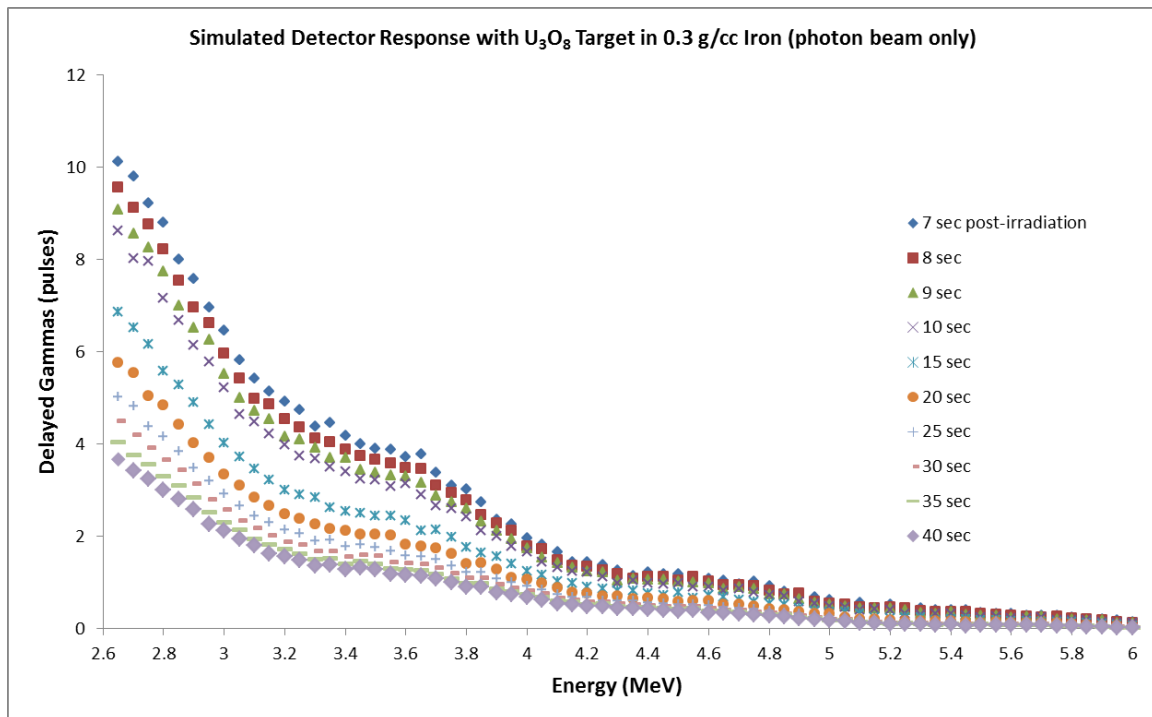


Figure 141. Simulated detector response to delayed gamma emission at one second intervals from 7-10 seconds and five second intervals from 10-40 seconds after 30 second interrogation with 12.2 MeV photon beam. PVT detector adjacent to one vertical side of surrogate container cube. Rapiscan Test Object “E” in iron at 0.3 g/cc.

E5. Simulated Detector Responses with U_3O_8 Target in 0.4 g/cc Iron

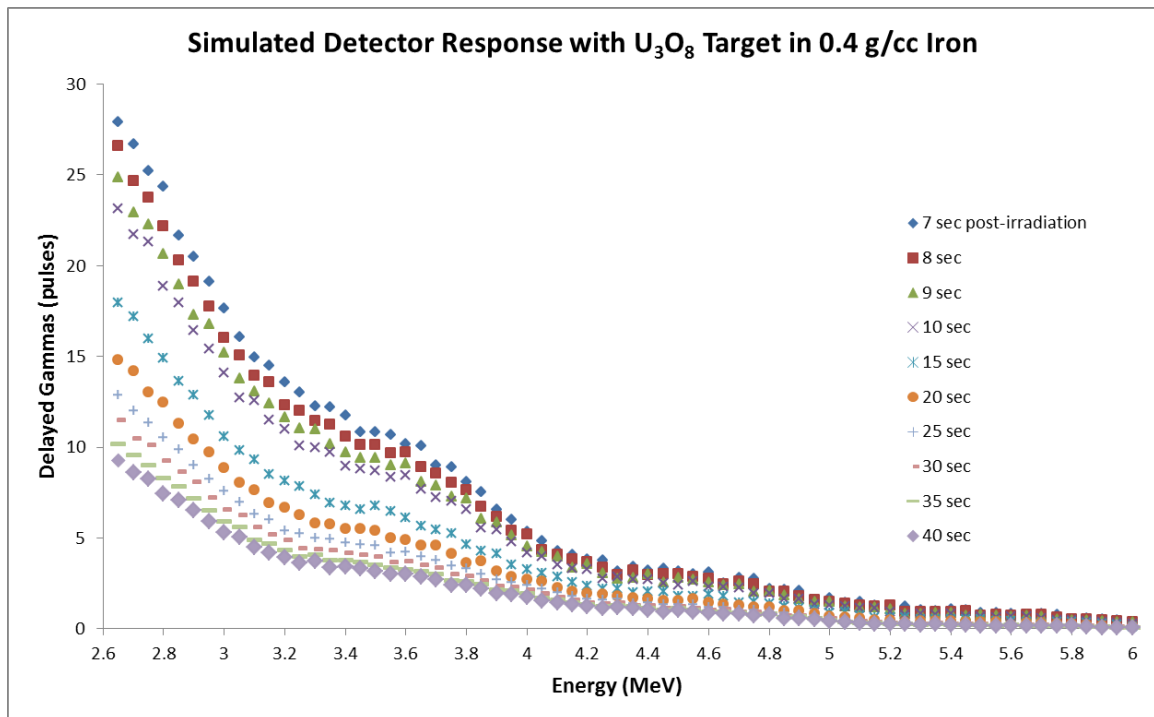


Figure 142. Simulated detector response to delayed gamma emission at one second intervals from 7-10 seconds and five second intervals from 10-40 seconds after 30 second interrogation with 7 MeV neutron and 12.2 MeV photon beams. PVT detector adjacent to one vertical side of surrogate container cube. Rapiscan Test Object "E" in iron at 0.4 g/cc.

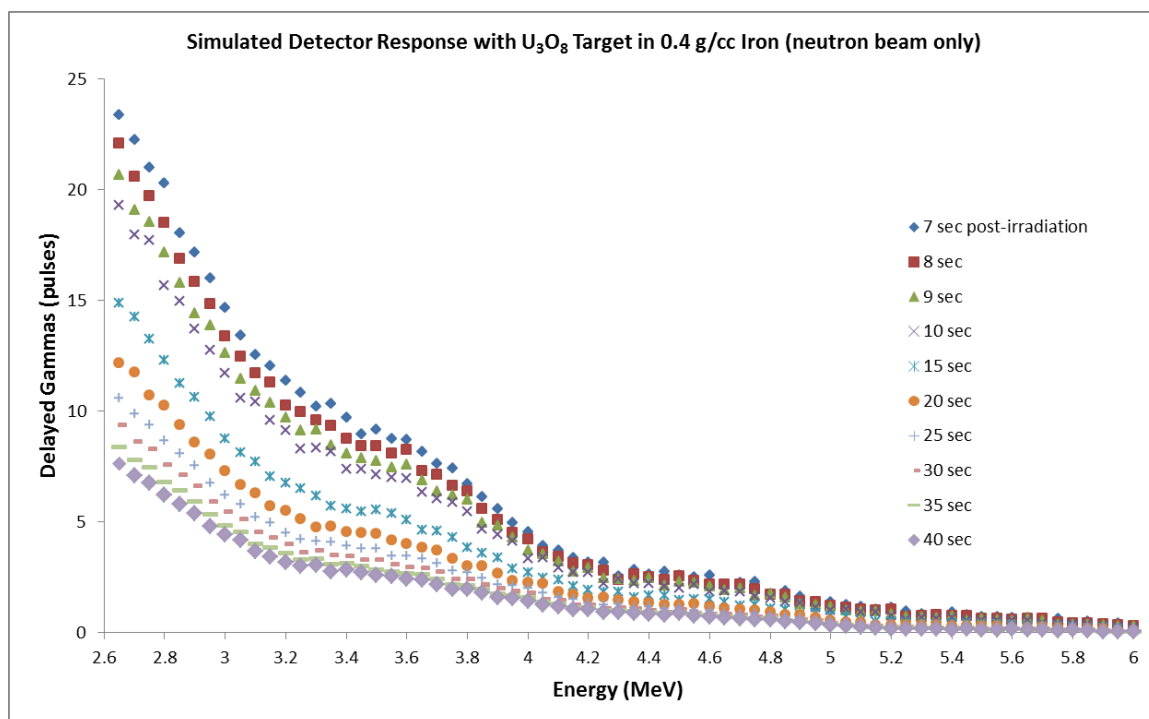


Figure 143. Simulated detector response to delayed gamma emission at one second intervals from 7-10 seconds and five second intervals from 10-40 seconds after 30 second interrogation with 7 MeV neutron beam. PVT detector adjacent to one vertical side of surrogate container cube. Rapiscan Test Object “E” in iron at 0.4 g/cc.

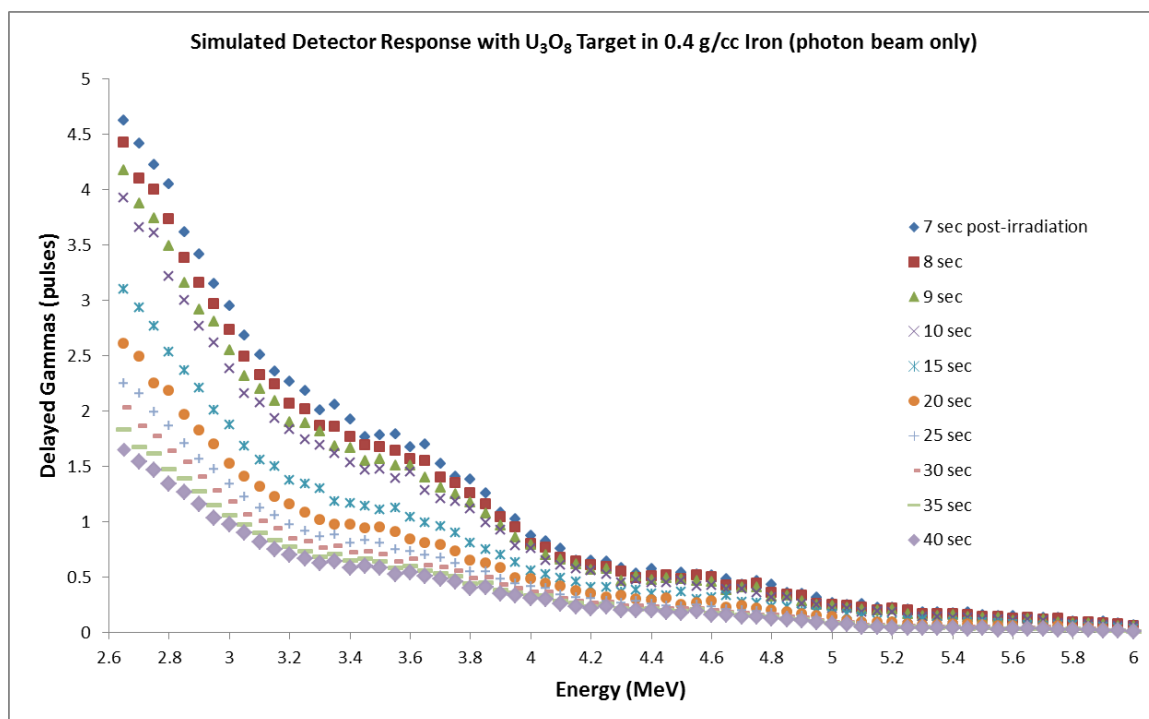


Figure 144. Simulated detector response to delayed gamma emission at one second intervals from 7-10 seconds and five second intervals from 10-40 seconds after 30 second interrogation with 12.2 MeV photon beam. PVT detector adjacent to one vertical side of surrogate container cube. Rapiscan Test Object “E” in iron at 0.4 g/cc.

E6. Simulated Detector Responses with U_3O_8 Target in 0.5 g/cc Iron

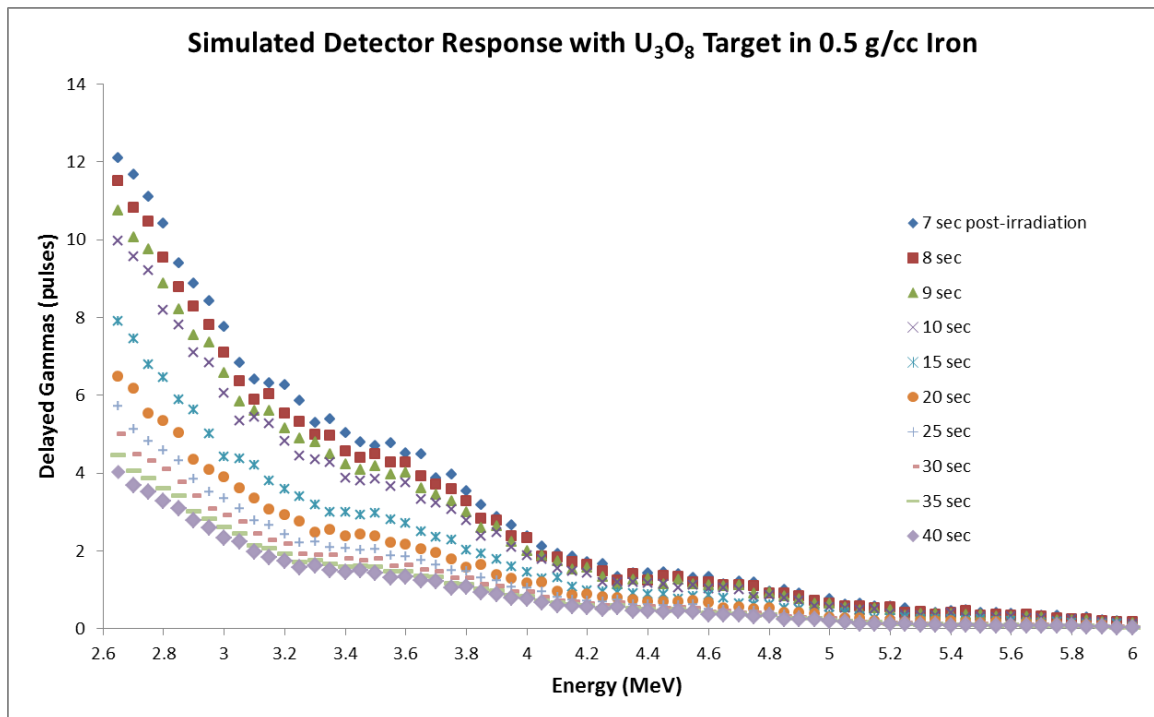


Figure 145. Simulated detector response to delayed gamma emission at one second intervals from 7-10 seconds and five second intervals from 10-40 seconds after 30 second interrogation with 7 MeV neutron and 12.2 MeV photon beams. PVT detector adjacent to one vertical side of surrogate container cube. Rapiscan Test Object "E" in iron at 0.5 g/cc.

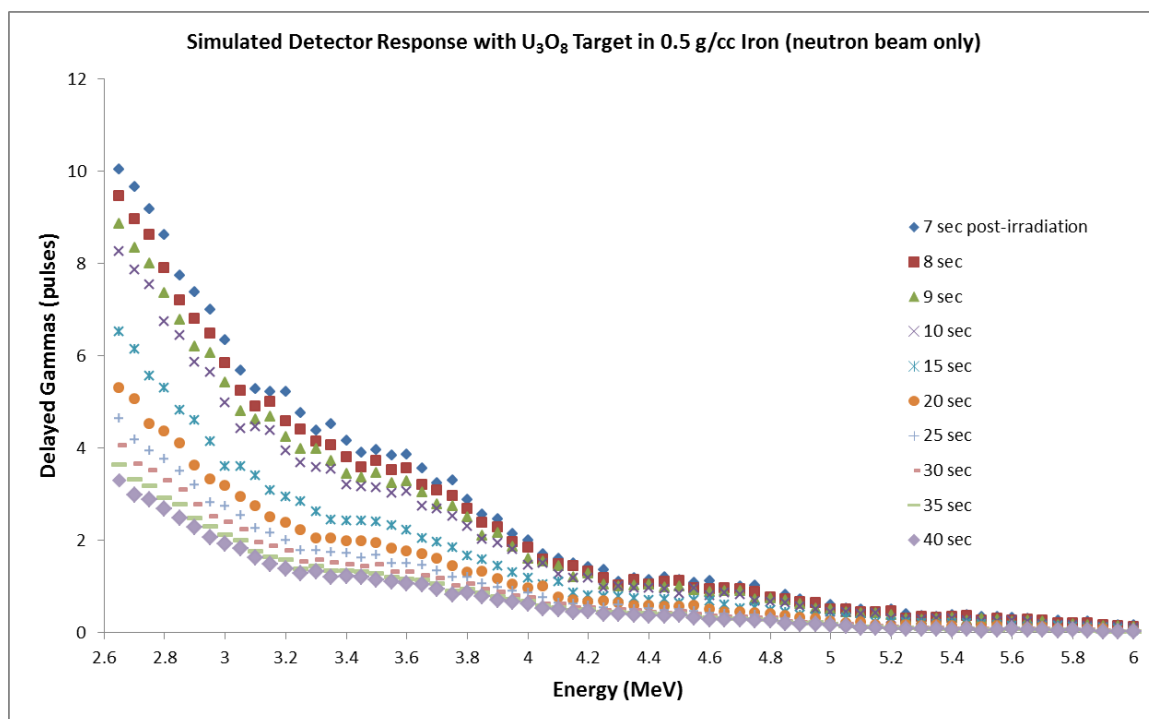


Figure 146. Simulated detector response to delayed gamma emission at one second intervals from 7-10 seconds and five second intervals from 10-40 seconds after 30 second interrogation with 7 MeV neutron beam. PVT detector adjacent to one vertical side of surrogate container cube. Rapiscan Test Object “E” in iron at 0.5 g/cc.

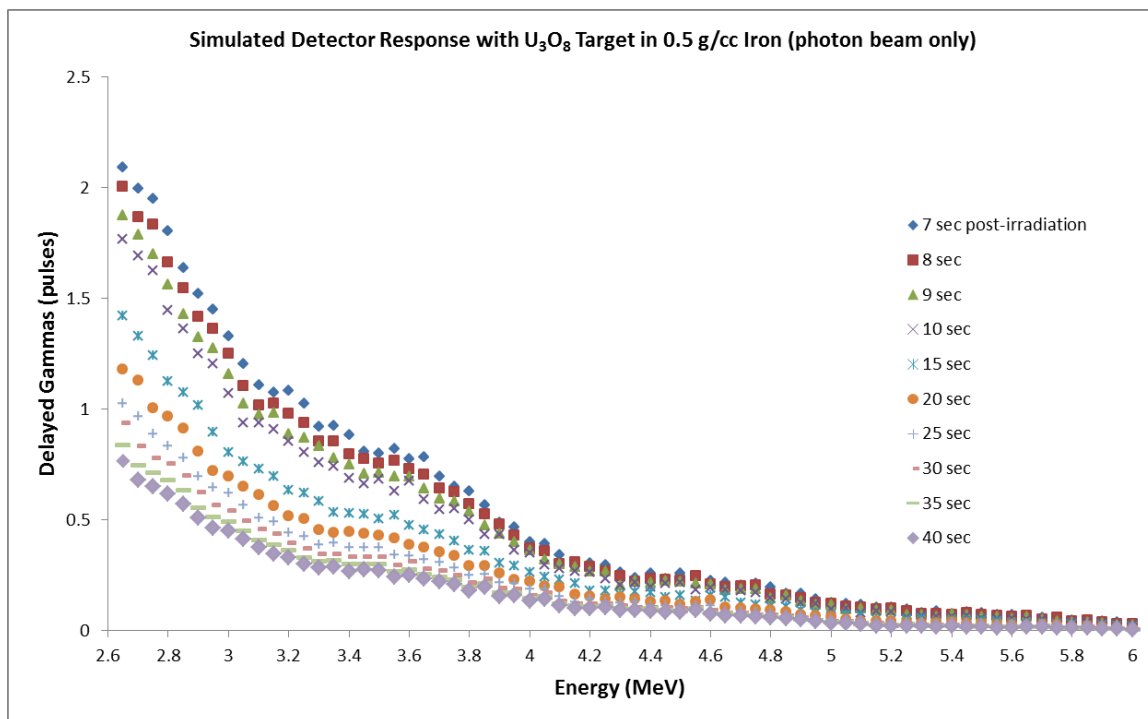


Figure 147. Simulated detector response to delayed gamma emission at one second intervals from 7-10 seconds and five second intervals from 10-40 seconds after 30 second interrogation with 12.2 MeV photon beam. PVT detector adjacent to one vertical side of surrogate container cube. Rapiscan Test Object “E” in iron at 0.5 g/cc.

E7. Simulated Detector Responses with U_3O_8 Target in 0.6 g/cc Iron

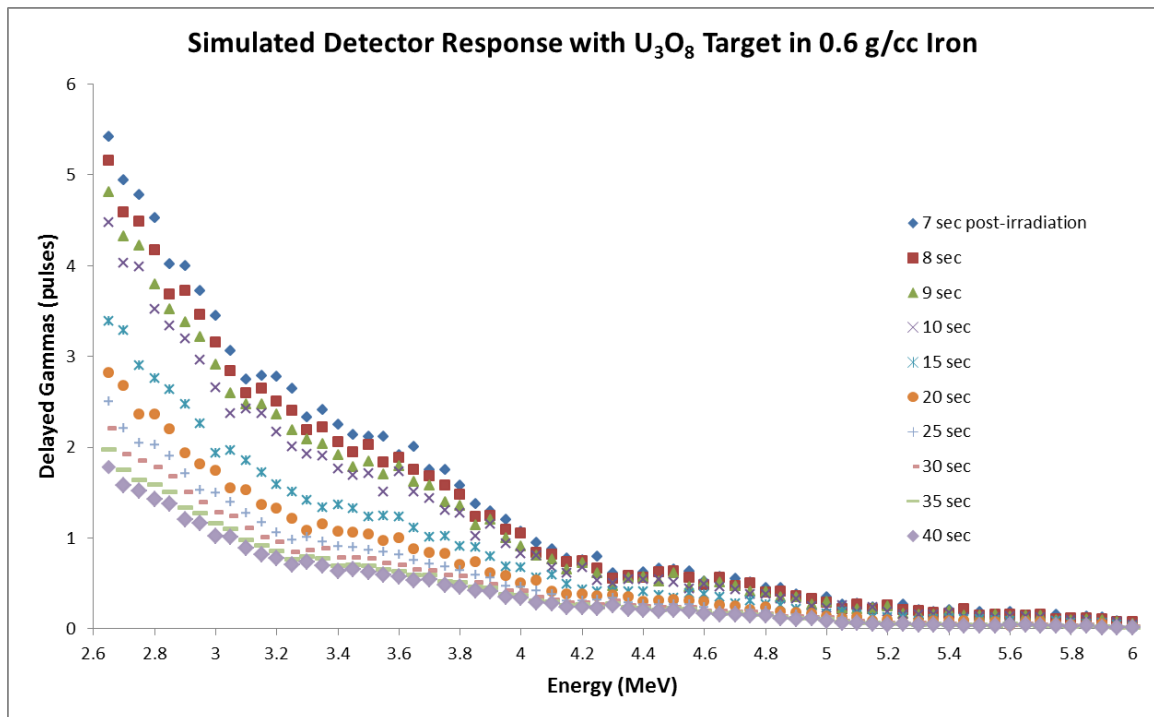


Figure 148. Simulated detector response to delayed gamma emission at one second intervals from 7-10 seconds and five second intervals from 10-40 seconds after 30 second interrogation with 7 MeV neutron and 12.2 MeV photon beams. PVT detector adjacent to one vertical side of surrogate container cube. Rapiscan Test Object "E" in iron at 0.6 g/cc.

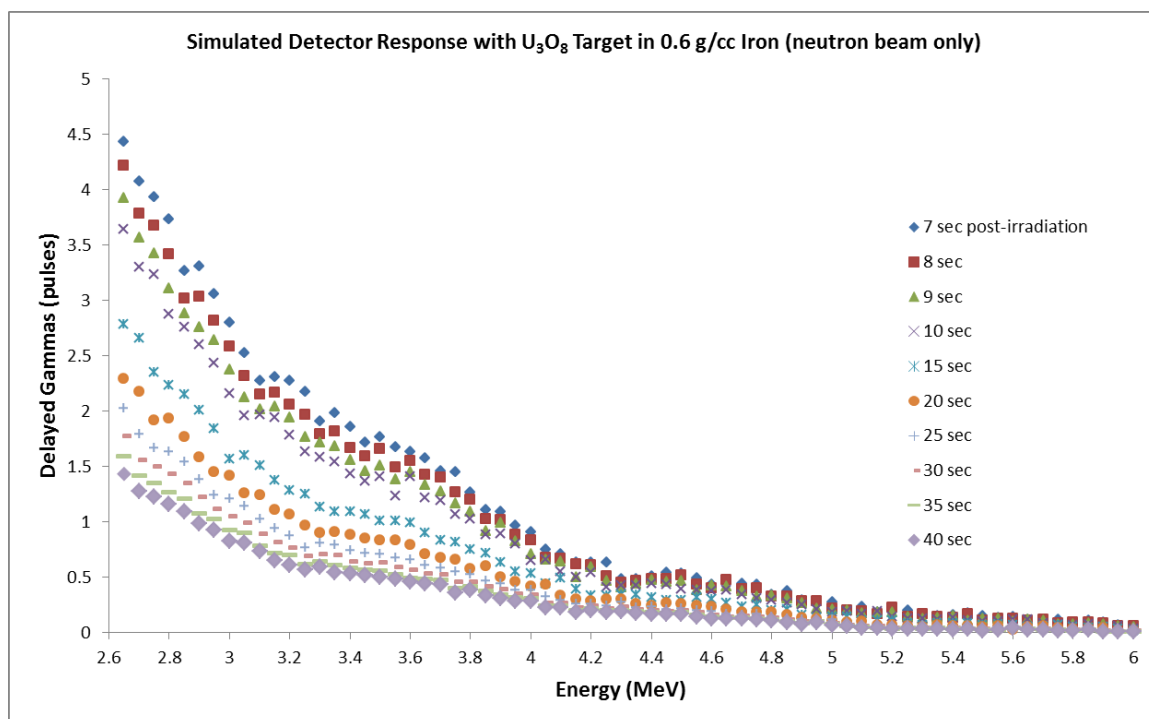


Figure 149. Simulated detector response to delayed gamma emission at one second intervals from 7-10 seconds and five second intervals from 10-40 seconds after 30 second interrogation with 7 MeV neutron beam. PVT detector adjacent to one vertical side of surrogate container cube. Rapiscan Test Object “E” in iron at 0.6 g/cc.

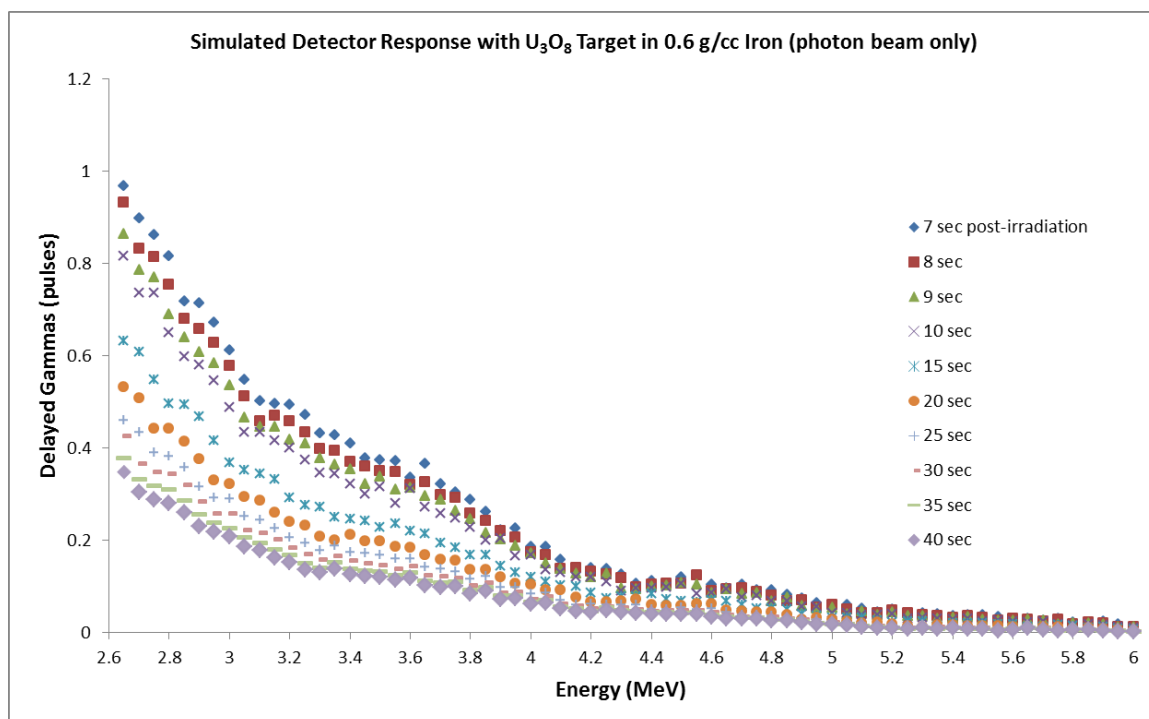


Figure 150. Simulated detector response to delayed gamma emission at one second intervals from 7-10 seconds and five second intervals from 10-40 seconds after 30 second interrogation with 12.2 MeV photon beam. PVT detector adjacent to one vertical side of surrogate container cube. Rapiscan Test Object “E” in iron at 0.6 g/cc.

E8. Simulated Detector Responses with U_3O_8 Target in 0.65 g/cc Iron

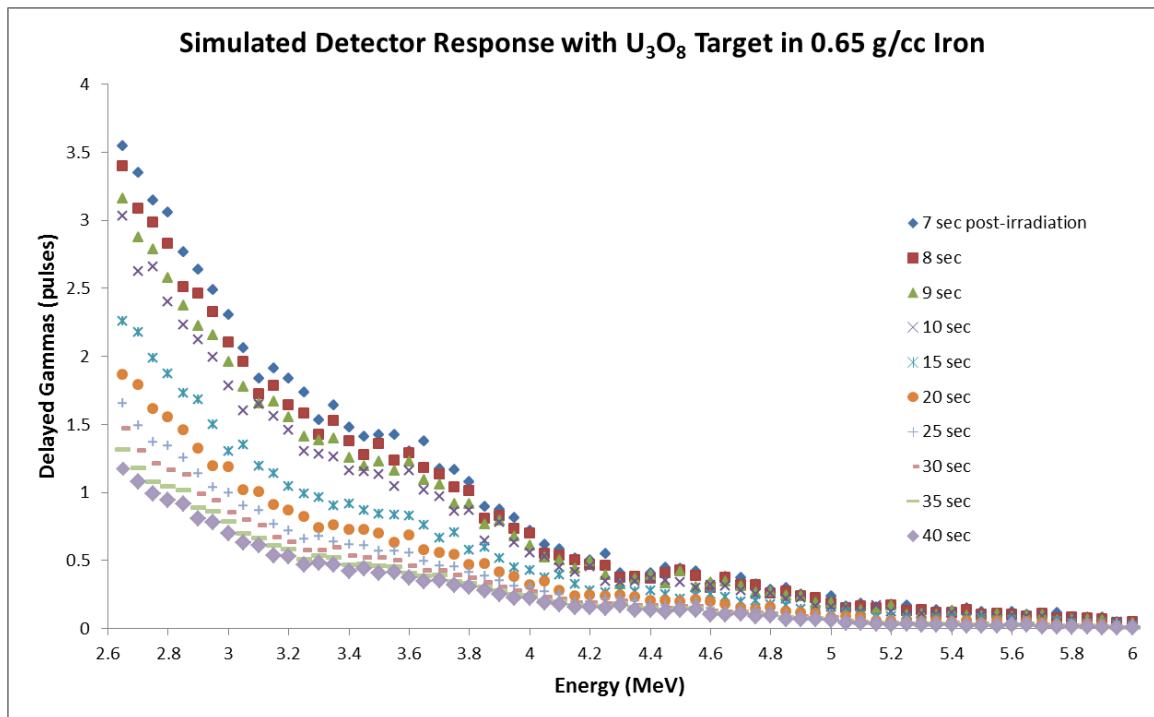


Figure 151. Simulated detector response to delayed gamma emission at one second intervals from 7-10 seconds and five second intervals from 10-40 seconds after 30 second interrogation with 7 MeV neutron and 12.2 MeV photon beams. PVT detector adjacent to one vertical side of surrogate container cube. Rapiscan Test Object "E" in iron at 0.65 g/cc.

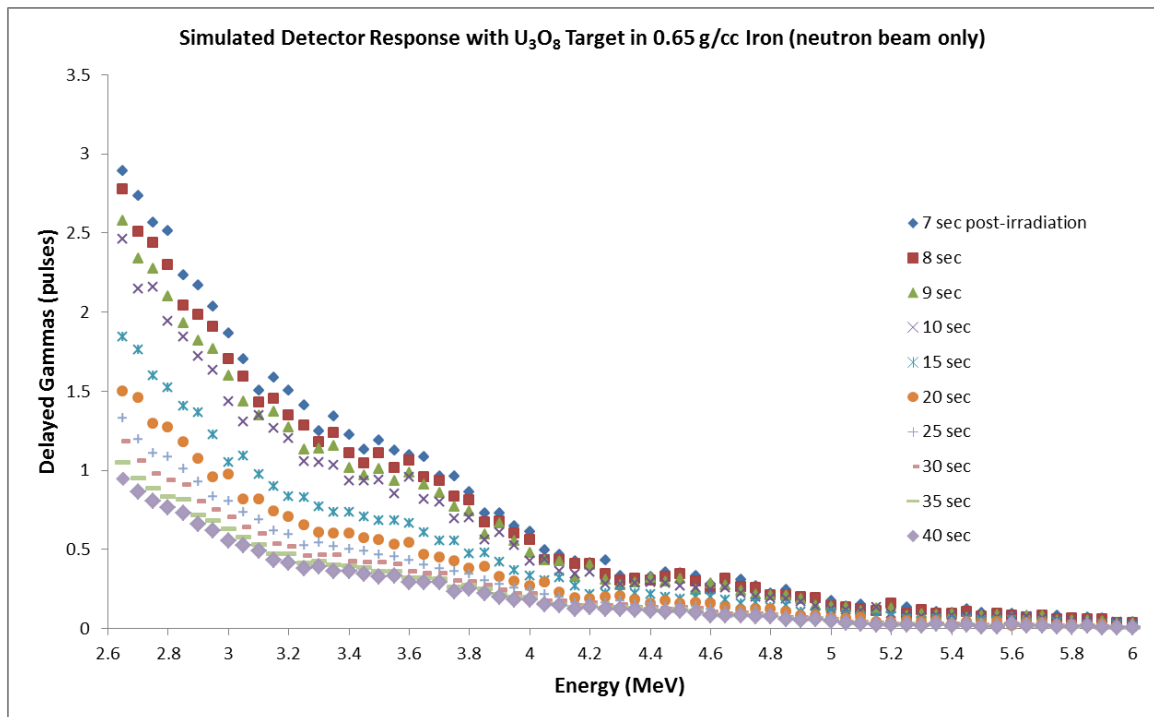


Figure 152. Simulated detector response to delayed gamma emission at one second intervals from 7-10 seconds and five second intervals from 10-40 seconds after 30 second interrogation with 7 MeV neutron beam. PVT detector adjacent to one vertical side of surrogate container cube. Rapiscan Test Object “E” in iron at 0.65 g/cc.

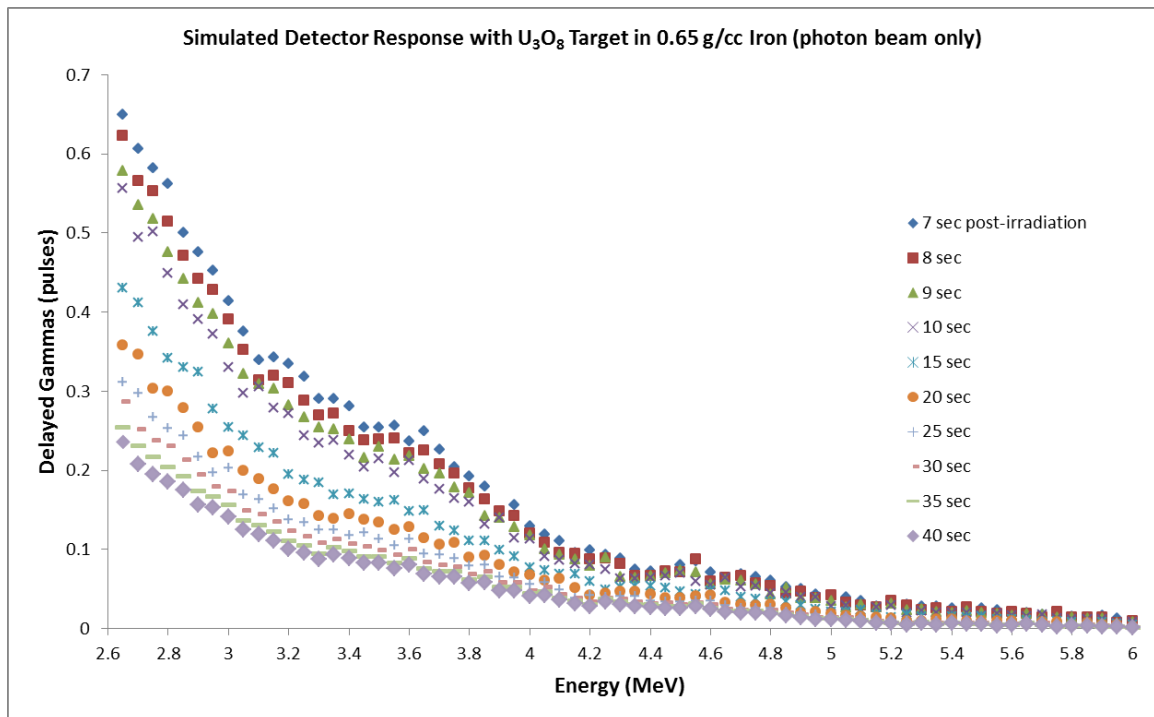


Figure 153. Simulated detector response to delayed gamma emission at one second intervals from 7-10 seconds and five second intervals from 10-40 seconds after 30 second interrogation with 12.2 MeV photon beam. PVT detector adjacent to one vertical side of surrogate container cube. Rapiscan Test Object “E” in iron at 0.65 g/cc.

APPENDIX F

EJ-200 PLASTIC SCINTILLATOR

This plastic scintillator combines the two important properties of long optical attenuation length and fast timing and is therefore particularly useful for time-of-flight systems using scintillators greater than one meter long. Typical measurements of 4 meter optical attenuation length are achieved in strips of cast sheet in which a representative size is 2 cm x 20 cm x 300 cm.

The combination of long attenuation length, high light output and an emission spectrum well matched to the common photomultipliers recommends EJ-200 as the detector of choice for many industrial applications such as gauging and environmental protection where high sensitivity of signal uniformity are critical operating requirements.

Physical and Scintillation Constants:

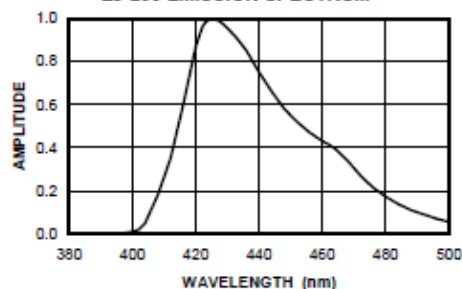
Light Output, % Anthracene	64
Scintillation Efficiency, photons/1 MeV e ⁻	10,000
Wavelength of Max. Emission, nm	425
Rise Time, ns	0.9
Decay Time, ns	2.1
Pulse Width, FWHM, ns	~2.5
No. of H Atoms per cm ³ , x 10 ²³	5.17
No. of C Atoms per cm ³ , x 10 ²³	4.69
No. of Electrons per cm ³ , x 10 ²³	3.33
Density, g/cc:	1.023

Polymer Base: Polyvinyltoluene
 Refractive Index: 1.58
 Vapor Pressure: Is vacuum-compatible
 Coefficient of Linear
 Expansion: 7.8 x 10⁻⁶ below +67°C

Light Output vs. Temperature:
 At +60°C, L.O. = 95% of that at +20°C
 No change from +20°C to -60°C

Chemical Compatibility: Is attacked by aromatic solvents, chlorinated solvents, ketones, solvent bonding cements, etc. It is stable in water, dilute acids and alkalis, lower alcohols and silicone greases. It is safe to use most epoxies and "super glues" with EJ-200.

EJ-200 EMISSION SPECTRUM



ELJEN TECHNOLOGY
 1300 W. Broadway
 Sweetwater TX 79556 USA

Tel: (325) 235-4276 or (888) 800-8771
 Fax: (325) 235-0701
 Website: www.eljentechnology.com

APPENDIX G

Sample Input Decks – U₃O₈ Target in 0.1 g/cc Aluminum

G1. TINDER Input Deck

```

&input
  cinderexec= 'cinder2008',
  debug=0,
  transexec= './tinder_mcnpx_act.pl',
  ngrps= 66,
  ggrps= 25,
  burnlibn= "/usr/local/cinder/CINDER2008/Data/C08lib_fission",
  burnlibg= "/usr/local/cinder/CINDER2008/Data/C08lib_gamma_OK",
  burnlibgl= "/usr/local/cinder/CINDER2008/Data/cindergl.dat",
  burnlocin= "/home/rlkeith/work/cinder/",
  spectraFile= "spectra_l"
/

```

```

&materials
  umix
  u-235 2350920 8.710941E-04
  u-238 2380920 3.536092E-03
  o-16 160080 1.175411E-02

```

```

&burnup
  calculation= "u3o8 puck in aluminum",
  volcc=2.92075E+02,
  flxmt=5e8,
  flosig=1.000e-21,
  signif=1.000e-21,
  epsm=0,
  epsn=0,
  exponmax=0,
  kchn=0,
  klib=0,
  nfe=2,
  ltsdnz=-1,
  nlintl=0,
  nosame=0,
  gasopt=1,

```

```

run_tab=1,
suffix="",
fine_dg=1000,
coarse_dg=10000,
fine_dn=1000,
coarse_dn=10000,
flxmtg=5e8,
nfeg=2,
description="u3o8 puck",
fluxname="tally 14",
gfluxname="tally 24",
ncamp = 11
/
1 1.0 1.0
  30.0 's'
2 0.0E+00 0.0
  6.0 's'
 -7.0 's'
1 0.0 0.0
  1.0 's'
1 0.0 0.0
  1.0 's'
1 0.0 0.0
  1.0 's'
1 0.0 0.0
  5.0 's'
1 0.0 0.0
  5.0 's'
1 0.0 0.0
  5.0 's'
1 0.0 0.0
  5.0 's'
1 0.0 0.0
  5.0 's'
1 0.0 0.0
  5.0 's'
/

```

G2. MCNPX.X1 Neutron Beam Input Deck

Test Object E (U3O8 disk) surrounded by low density aluminum

C Cell Cards

```
1 1 -2.05 -1 imp:n=1 imp:p=1 $ target
2 2 -0.1 1 -2 imp:n=1 imp:p=1 $ L-density
3 3 -7.82 2 -3 imp:n=1 imp:p=1 $ 4.76mm (3/16") of c-steel
4 0 3 imp:n=0 imp:p=0
```

C Surface Cards

```
1 RCC 0 -1.27 0 0 2.54 0 6.05 $ 600g total mass
2 RPP -121.524 121.524 -121.524 121.524 -121.524 121.524
3 RPP -122.0 122.0 -122.0 122.0 -122.0 122.0 $ cm - 8x8x8 ft
```

C Data Cards

```
m1 92235 0.0539 92238 0.2188 8016 0.7273 $ 19.75% enriched
m2 13027 1.0 $ aluminum
m3 6000 -0.005 26000 -0.995 $ wall
```

MODE N P

F14:N 1

c

C 66 group CINDER2008g neutron energy group structure

```
E14 1.0000E-11 5.0000E-10 1.0000E-09 2.0000E-09 5.0000E-09 1.0000E-08 &
1.5000E-08 2.0000E-08 2.5000E-08 3.0000E-08 3.5000E-08 4.2000E-08 &
5.0000E-08 5.8000E-08 6.7000E-08 8.0000E-08 1.0000E-07 1.5200E-07 &
2.5100E-07 4.1400E-07 6.8300E-07 1.1250E-06 1.8550E-06 3.0590E-06 &
5.0430E-06 8.3150E-06 1.3710E-05 2.2600E-05 3.7270E-05 6.1440E-05 &
1.0130E-04 1.6700E-04 2.7540E-04 4.5400E-04 7.4850E-04 1.2340E-03 &
2.0350E-03 2.4040E-03 2.8400E-03 3.3550E-03 5.5310E-03 9.1190E-03 &
1.5030E-02 1.9890E-02 2.5540E-02 4.0870E-02 6.7380E-02 1.1110E-01 &
1.8320E-01 3.0200E-01 3.8870E-01 4.9790E-01 6.39279E-01 8.2085E-01 &
1.10803E+00 1.35335E+00 1.73774E+00 2.23130E+00 2.86505E+00 &
3.67879E+00 4.96585E+00 6.06500E+00 1.00000E+01 1.49182E+01 &
1.69046E+01 2.00000E+01 2.50000E+01
```

C

F24:P 1

c

C 25 group CINDER gamma energy group structure

E24 1.00e-03 1.00e-02 3.00e-02 6.00e-02 1.00e-01 2.00e-01 &
 3.00e-01 5.00e-01 5.250e-01 7.500e-01 1.0 1.330 1.660 &
 2.0 2.5 3.0 4.0 5.0 6.0 7.0 8.0 9.0 10.0 12.0 17.0 30.0

C

F11:P 3.1

c

C 2.6-7 MeV Check

E11 2.6 3.0 4.0 5.0 6.0 7.0 30.0

C

VOL j 14.3574e6 2j \$ cargo volume

C 7 MeV neutron source

c This is for initial irradiation transport step

{SRC1:SDEF SUR=3.4 POS=0 -122.0 0 AXS=0 1 0 RAD=D1 PAR=1 ERG=7.0 VEC=0 1 0 DIR=1
 SI1 0 6.05

SP1 -21 1}

c This is for any other re-transport step

{SRC2:SDEF CEL=1 PAR=2 ERG=d3

si3 [ERG]

sp3 [SRC] }

PHYS:N 25.0 2j -1 j 5

PHYS:P 30.0 2j -1 2j 1

NPS 1.4e7

PRINT

G3. MCNPX.X2 Photon Beam/Re-Transport Input Deck

Test Object E (U3O8 disk) surrounded by low density aluminum

C Cell Cards

```
1 1 -2.05 -1 imp:n=1 imp:p=1 $ target
2 2 -0.1 1 -2 imp:n=1 imp:p=1 $ L-density
3 3 -7.82 2 -3 imp:n=1 imp:p=1 $ 4.76mm (3/16") of c-steel
4 4 -1.023 3 -4 imp:n=1 imp:p=1 $ plastic scintillator
5 0 4 imp:n=0 imp:p=0
```

C Surface Cards

```
1 RCC 0 -1.27 0 0 2.54 0 6.05 $ 600g total mass
2 RPP -121.524 121.524 -121.524 121.524 -121.524 121.524
3 RPP -122.0 122.0 -122.0 122.0 -122.0 122.0 $ cm - 8x8x8 ft
4 RPP -122.0 147.4 -122.0 122.0 -122.0 122.0 $ 10" thick detector
```

C Data Cards

```
m1 92235 0.0539 92238 0.2188 8016 0.7273 $ 19.75% enriched
m2 13027 1.0 $ aluminum
m3 6000 -0.005 26000 -0.995 $ wall
m4 1001 -0.0841 6000 -0.9159 $ EJ-200 PVT detector
{SRC1:MODE N P}
{SRC2:MODE P}
F14:N 1
```

c

C 66 group CINDER2008g neutron energy group structure

```
E14 1.0000E-11 5.0000E-10 1.0000E-09 2.0000E-09 5.0000E-09 1.0000E-08 &
1.5000E-08 2.0000E-08 2.5000E-08 3.0000E-08 3.5000E-08 4.2000E-08 &
5.0000E-08 5.8000E-08 6.7000E-08 8.0000E-08 1.0000E-07 1.5200E-07 &
2.5100E-07 4.1400E-07 6.8300E-07 1.1250E-06 1.8550E-06 3.0590E-06 &
5.0430E-06 8.3150E-06 1.3710E-05 2.2600E-05 3.7270E-05 6.1440E-05 &
1.0130E-04 1.6700E-04 2.7540E-04 4.5400E-04 7.4850E-04 1.2340E-03 &
2.0350E-03 2.4040E-03 2.8400E-03 3.3550E-03 5.5310E-03 9.1190E-03 &
1.5030E-02 1.9890E-02 2.5540E-02 4.0870E-02 6.7380E-02 1.1110E-01 &
1.8320E-01 3.0200E-01 3.8870E-01 4.9790E-01 6.39279E-01 8.2085E-01 &
1.10803E+00 1.35335E+00 1.73774E+00 2.23130E+00 2.86505E+00 &
3.67879E+00 4.96585E+00 6.06500E+00 1.00000E+01 1.49182E+01 &
1.69046E+01 2.00000E+01 2.50000E+01
```

```

C
F24:P 1
c
C 25 group CINDER gamma energy group structure
E24 1.00e-03 1.00e-02 3.00e-02 6.00e-02 1.00e-01 2.00e-01 &
    3.00e-01 5.00e-01 5.250e-01 7.500e-01 1.0 1.330 1.660 &
    2.0 2.5 3.0 4.0 5.0 6.0 7.0 8.0 9.0 10.0 12.0 17.0 30.0
C
F11:P 3.1
{SRC2:FM11 [SRCTOT]}
c
C 2.6-7 MeV Check
E11 2.6 3.0 4.0 5.0 6.0 7.0 30.0
c
C Detector
{SRC2:F18:P 4
E18 0 1e-5 2.0 99i 7.0 30.0}
c
C Gaussian Energy Broadening is FWHM=0.35 MeV per Knoll
{SRC2:FT18 GEB 0.35 0 0 }
C
VOL j 14.3574e6 3j $ cargo volume
C 12.2 MeV photon source
c This is for initial irradiation transport step
{SRC1:SDEF SUR=3.4 POS=0 -122.0 0 AXS=0 1 0 RAD=D1 PAR=2 ERG=12.2 VEC=0 1 0
DIR=1
SI1 0 6.05
SP1 -21 1}
c This is for any other re-transport step
{SRC2:SDEF CEL=1 PAR=2 ERG=d3
si3 [ERG]
sp3 [SRC] }
PHYS:N 25.0 2j -1 j 5
PHYS:P 30.0 2j -1 2j 1
NPS 6.3e7
PRINT

```

REFERENCES

Aloise, G., (2009) "Combating Nuclear Smuggling – Recent Testing Raises Issues about the Potential Effectiveness of Advanced Radiation Detection Portal Monitors," Government Accountability Office testimony, GAO-10-252T.

Aloise, G., Caldwell, S.L., (2010) "Combating Nuclear Smuggling - Inadequate Communication and Oversight Hampered DHS Efforts to Develop an Advanced Radiography System to Detect Nuclear Materials," Government Accountability Office testimony, GAO-10-1041T.

ANSI, (2007) "American National Standard Minimum Performance Criteria for Active Interrogation Systems Used for Homeland Security," American National Standards Institute, ANSI N42.41-2007.

Bjorkholm P.J., (2003) "Detection of Weapons of Mass Destruction," *Port Technology International*, ed. 19, pp. 1-4.

Bjorkholm P.J., Boeh, L.D., (2006) "The Economics of Cargo Screening," *Port Technology International*, ed. 31, pp. 146-148.

Buck, R.M., Hall, J.M., (1999) "Applications of the COG Multiparticle Monte Carlo Transport Code to Simulated Imaging of Complex Objects," Lawrence Livermore National Laboratory report, UCRL-JC-134630.

Buffler, A., Tickner, J., (2010) "Detecting Contraband Using Neutrons: Challenges and Future Directions," *Radiation Measurements*, vol. 45, pp.1186-1192.

Buck, R.M., Lent, E.M., Wilcox, T., Hadjimarkos, S., (2002) "COG – A Multiparticle Monte Carlo Transport Code, User's Manual, Fifth Edition," Lawrence Livermore National Laboratory report, UCRL-TM-202590.

Church, J.A., Slaughter, D.R., Asztalos, S., Bilotto, P., Descalle, M.-A., Hall, J., Luu, T., Manatt, D., Mauger, J., Norman, E.B., Petersen, D., Prussin, S., (2007a) "Signals and Interferences in the Nuclear Car Wash," *Nuclear Instruments and Methods in Physics Research B*, vol. 261, pp. 351-355.

Church, J.A., Slaughter, D.R., Norman, E.B., Asztalos, S., Bilotto, P., Descalle, M.-A., Hall, J., Luu, T., Manatt, D.R., Mauger, G.J., Petersen, D., Prussin, S., (2007b) "Experimental Study of Variations in Background Radiation and the Effect on Nuclear Car Wash Sensitivity," Lawrence Livermore National Laboratory report, UCRL-TR-229157.

Church, J.A., Slaughter, D.R., Asztalos, S., Bilotto, P., Descalle, M.-A., Hall, J., Manatt, D., Mauger, J., Norman, E.B., Petersen, D., Prussin, S., (2006) "Nuclear Car Wash Sensitivity in Varying Thicknesses of Wood and Steel Cargo," Lawrence Livermore National Laboratory report, UCRL-TR-225709.

Cochran, T.B., Paine, C.E., (1995) "The Amount of Plutonium and Highly-Enriched Uranium Needed for Pure Fission Nuclear Weapons." National Resources Defense Council, Inc.

CTaSC, (2012) "Ceramic Tile Statistics," Ceramic Tile and Stone Consultants, www.ctasc.com.

Cutmore, N.G., Liu, Y., Tickner, J.R., (2010) "Development and Commercialization of a Fast-Neutron/X-ray Cargo Scanner," *2010 IEEE International Conference on Technologies for Homeland Security (HST)*, conference publication, pp. 330-336.

Danagouliau, A., Bertozzi, W., Hicks, C.L., Klimenko, A.V., Korbly, S.E., Ledoux, R.J., Wilson, C.M., (2010) "Prompt Neutrons from Photofission and its Use in Homeland Security Applications," *2010 IEEE International Conference on Technologies for Homeland Security (HST)*, conference publication, pp. 379-384.

Descalle, M.-A., Manatt, D., Slaughter D., (2006) "Analysis of Recent Manifests for Goods Imported through US Ports," Lawrence Livermore National Laboratory report, UCRL-TR-225708.

de Oliveira, C.R.E., Prinja, A.K., Hecht, A., Arthur, E., (2009) "Modeling and Simulation to Support Systems Development and Assessment for Standoff Detection of Nuclear Materials," Defense Threat Reduction Agency (DTRA), contract DTRA01-03-D-0009-0025.

de Oliveira, C.R.E., Ross, T.J., Booker, J.M., Arthur E.D., (2011) "Active Nuclear Interrogation Systems Modeling, Simulation and Uncertainty Quantification," proposal to DNDO-NSF ARI Solicitation NSF 11-530 (National Science Foundation).

DNDO, (2011) "Technical Capability Standard for Handheld Instruments Used for the Detection and Identification of Radionuclides," Domestic Nuclear Detection Office, Document #: 500-DNDO-117250v0.00.

DOE, (1993) "DOE Fundamentals Handbook, Nuclear Physics and Reactor Theory, Volume 1 of 2," Department of Energy (DOE), DOE-HDBK-1019/1-93.

DuPont, (2012) "Fluoropolymer Comparison – Typical Properties,"
www2.dupont.com/Teflon_Industrial/en_US/tech_info/.

Durkee, J.W., James, M.R., McKinney, G.W., Trelue, H.R., Waters, L.S., Wilson, W.B., (2009) "Delayed-Gamma Signature Calculation for Neutron-Induced Fission and Activation Using MCNPX. Part II: Simulations," *Progress in Nuclear Energy*, vol. 51, pp.828-836.

ELG, (2012) "Shipping Containers," Export Logistics Guide,
<http://exportlogisticsguide.com>.

Ely, J., Kouzes, R., Schweppe, J., Siciliano, E., Strachan, D., Weier, D., (2006) "The Use of Energy Windowing to Discriminate SNM from NORM in Radiation Portal Monitors," *Nuclear Instruments and Methods in Physics Research A*, vol. 560, pp. 373-387.

Entergy, (2011) "Arkansas Nuclear One: Tungsten Shielding," corporate news release, Entergy Nuclear, May 12.

ET, (2012) "EJ-200 Plastic Scintillator," Eljen Technology,
www.eljentechnology.com.

FDA, (2001) "Irradiation in the Production, Processing and Handling of Food," US Food and Drug Administration, *Federal Register*, vol. 66, pp. 18537-18539.

Gallmeier, F.X., (2005) "An Improved Photo-Absorption Cross Section Model for the Physics Models Regime in MCNPX," *Radiation Protection Dosimetry*, vol. 116, pp. 264-269.

Gmar, M., Capdevila J.M., (1999) "Use of Delayed Gamma Spectra for Detection of Actinides (U,Pu) by Photofission," *Nuclear Instruments and Methods in Physics Research A*, vol. 422, pp. 841-845.

Gozani, T., (2009) "Fission Signatures for Nuclear Material Detection," *IEEE Transactions on Nuclear Science*, vol. 56, pp. 736-741.

GSN, (2011) "Homeland Security Cancels Troubled Radiation Detector Effort," *Global Security Newswire*, July 26, www.nti.org/gsn.

Hall, J.M., Asztalos, S., Bilotto, P., Church, J., Descalle, M.-A., Luu, T., Manatt, D., Mauger, G., Norman, E., Petersen, D., Pruet, J., Prussin, S., Slaughter, D., (2007) "The Nuclear Car Wash: Neutron Interrogation of Cargo Containers to

Detect Hidden SNM,” *Nuclear Instruments and Methods in Physics Research B*, vol. 261, pp. 337-340.

Haxby, R.O., Shoupp, W.E., Stephens, W.E., Wells, W.H., (1941) “Photo-Fission of Uranium and Thorium,” *Physical Review*, vol. 59, pp. 57-61.

Hilton, J., (2010) “Phosphogypsum (PG): Uses and Current Handling Practices Worldwide,” presentation, The 25th Annual Regional Phosphate Conference, Lakeland, Florida, October 13-14, www.stackfree.com.

Hollas, C.L., Close, D.A., Moss, C.E., (1987) “Analysis of Fissionable Material Using Delayed Gamma Rays From Photofission,” *Nuclear Instruments and Methods in Physics Research B*, vol. 24/25, pp. 503-505.

Holloway, S.T., Wilson, W.B., Kelsey, C.T., Little, H., Mozin, V., (2011) “A Manual for CINDER2008 Codes and Data,” Los Alamos National Laboratory report, LA-UR-11-00006.

Hosenball, M., (2008) “A Hassle at the Border,” *Newsweek*, via The Daily Beast, ed. August 8, www.thedailybeast.com/newsweek.

IAEA, (1993) "Against the Spread of Nuclear Weapons: IAEA Safeguards in the 1990s," International Atomic Energy Agency, 93-04459, IAEA/PI/A38E, December.

Jacobs, E., De Clercq, A., Thierens, H., De Frenne, D., D'hondt, P., De Gelder, P., Deruytter, A.J., (1979) "Fragment Mass and Kinetic Energy Distributions for the Photofission of U-238 with 12-, 15-, 20-, 30-, and 70-MeV Bremsstrahlung," *Physical Review C*, vol. 20, pp. 2249-2256.

Jones, J.L., Blackburn, B.W., Watson, S.M., Norman, D.R., Hunt, A.W., (2007) "High-Energy Photon Interrogation for Nonproliferation Applications," *Nuclear Instruments and Methods in Physics Research B*, vol. 261, pp. 326-330.

Jones, J.L., Yoon, W.Y., Harker, Y.D., Hoggan, J.M., Haskell, K.J., VanAusdeln, L.A., (2000) "Proof-of-Concept Assessment of a Photofission-Based Interrogation System for the Detection of Shielded Nuclear Material," Idaho National Engineering and Environmental Laboratory report, INEEL/EXT-2000-01523.

Kelly, R.W., (2007) "Containing the Threat: Protecting the Global Supply Chain through Enhanced Cargo Container Security," The Reform Institute, ed. October, www.reforminstitute.org.

Knoll, F.G., (1989) Radiation Detection and Measurement, Second Edition, New York: John Wiley & Sons.

Kouzes, R., Ely, J., Evans, W., Hensley, W., Lepel, E., McDonald, J., Schweppe, J., Siciliano, E., Strom, D., Woodring, M., (2006) "Naturally Occurring Radioactive Materials in Cargo at US Borders," *Packaging, Transport, Storage and Security of Radioactive Materials*, vol. 17, pp. 11-17.

Kraemer, S., Carayon, P., Sanquist, T.F., (2009) "Human and Organizational Factors in Security Screening and Inspection Systems: Conceptual Framework and Key Research Needs," *Cognition, Technology & Work*, vol. 11, pp. 29-41.

Langenbrunner, J.R., Booker, J.M., Hemez, F.M., Ross, T.J., (2008) "Inference Uncertainty Quantification Instead of Full-scale Testing" Los Alamos National Laboratory report, LA-UR-08-1669.

Langenbrunner, J.R., Booker, J.M., Hemez, F.M., Ross, T.J., Salazar, I.F., (2009) "An Uncertainty Inventory Demonstration—A Primary Step in Uncertainty Quantification," Los Alamos National Laboratory report, LA-UR-09-5161.

Langenbrunner, J.R., Booker, J.M., Ross, T.J., Hemez, F.M., (2010a) "Evolving Desiderata for Validating Engineered-Physics Systems without Full-Scale Testing," Los Alamos National Laboratory report, LA-UR-10-1494.

Langenbrunner, J.R., Hemez, F.M., Booker, J.M., Ross, T.J., (2010b) "Model Choice Considerations and Information Integration Using Analytical Hierarchy Process," Los Alamos National Laboratory report, LA-UR-10-0398.

Lichtenwald, T.G., Perri, F.S., MacKenzie, P., (2009) "Smuggling Multi-Consignment Contraband: Isolated Incidents or a New Trend?" *Inside Homeland Security*, ed. Summer.

Lin, G., Engel, D.W., Eslinger, P.W., (2012) "Survey and Evaluate Uncertainty Quantification Methodologies," Pacific Northwest National Laboratory report, PNNL- 20914.

Linfoot, E.H., (1957) "An Informational Measure of Correlation," *Information and Control*, vol. 1, pp. 85-89.

Luu, T., Bilotto, P., Church J., Descalle, M.-A., Hall, J., Manatt, D., Mauger, J., Norman E., Petersen, D., Pruet, J., Prussin, S., Slaughter, D., (2007)

“Description of ALARMA: The Alarm Algorithm Developed for the Nuclear Car Wash,” Lawrence Livermore National Laboratory report, UCRL-TR-227515.

Maienschein, F.C., Peelle, R.W., Zobel, W., Love, T.A., (1958) “Gamma-Rays Associated with Fission,” Second United Nations International Conference on the Peaceful Uses of Atomic Energy, A/CONF.15/P/670, June.

Martin, W.J., (2012) “Dual Neutral Particle Induced Transmutation,” Ph.D. Dissertation, Department of Chemical and Nuclear Engineering, The University of New Mexico.

Moss, C.E., Hollas, C.L., McKinney, G.W., Myers, W.L., (2006) “Comparison of Active Interrogation Techniques,” *IEEE Transactions on Nuclear Science*, vol. 53, pp. 2242-2246.

Myers, W.L., Goulding, C.A., Hollas, C.L., Moss, C.E., (2004) “Photon and Neutron Active Interrogation of Highly Enriched Uranium,” Los Alamos National Laboratory report, LA-UR-04-6565.

Navy, (2009) “JUSTIFICATION AND APPROVAL FOR USE OF OTHER THAN FULL AND OPEN COMPETITION,” Department of the Navy document, N00406-09-T-0593.

Nelson K., Sokkappa, P., (2008) “A Statistical Model for Generating a Population of Unclassified Objects and Radiation Signatures Spanning Nuclear Threats,” Lawrence Livermore National Laboratory report, LLNL-TR-408407.

NNDC, (2012) “Reaction-code F-19 (N,A) N-16, SIG,” Evaluated Nuclear Data File (ENDF/B-VII.0), Brookhaven National Laboratory, National Nuclear Data Center, www.nndc.bnl.gov.

NORM, (2011) “Naturally-Occurring Radioactive Materials (NORM),” World Nuclear Association, <http://world-nuclear.org/info/inf30.html>.

Norman, E.B., Prussin, S.G., Larimer, R.-M., Shugart, H., Browne, E., Smith, A.R., McDonald, R.J., Nitsche, H., Gupta, P., Frank, M.I., Gosnell, T.B., (2004) “Signatures of Fissile Materials: High-Energy Gamma Rays Following Fission,” *Nuclear Instruments and Methods in Physics Research A*, vol. 521, pp. 608–610.

Pelowitz, D.B., Durkee, J.W., Elson, J.S., Fensin, M.L., Hendricks, J.S., James, M.R., Johns, R.C., McKinney, G.W., Mashnik, S.G., Verbeke, J.M., Waters, L.S., Wilcox, T.A., (2011) "MCNPX 2.7.0 Extensions," Los Alamos National Laboratory report, LA-UR-11-02295.

Pelowitz, D.B., editor, (2011) "MCNPX User's Manual Version 2.7.0," Los Alamos National Laboratory report, LA-CP-11-00438.

Port of Oakland, (2005) "Port of Oakland: First Major US Container Port with Radiation Portal Monitors at Every International Terminal," *Port Technology International*, ed. 27, pp. 143-145.

Proctor, A., Gabriel, T.A., Hunt, A.W., Manges, J., Handler, T., (2012) "Detecting Fissionable Materials in a Variety of Shielding Matrices via Delayed Gamma and Neutron Photofission Signatures - Part 2: Experimental Results," *Nuclear Instruments and Methods in Physics Research A*, vol. 662, pp. 71-80.

Pruet, J., Descalle, M.-A., Hall, J., Pohl, B., Prussin, S.G., (2005) "Neutron and Photon Transport in Sea-Going Cargo Containers," Lawrence Livermore National Laboratory report, UCRL-JRNL-209546.

Prussin, S., Slaughter, D., Pruet, J., Descalle, M., Bernstein, A., Hall, J., Accatino, M., Alford, O., Asztalos, S., Church, J., Loshak, A., Madden, N., Manatt, D., Moore, T., Norman, E., Petersen D., (2005) "Nuclear Car Wash Status Report, August 2005," Lawrence Livermore National Laboratory report, UCRL-TR-214636.

Prussin, S.G., Descalle, M.-A., Hall, J.M., Pruet, J.A., Slaughter, D.R., Accatino, M.R., Alford, O.J., Asztalos, S.J., Bernstein, A., Church, J.A., Gosnell, T., Loshak, A., Madden, N.W., Manatt, D.R., Mauger, G.J., Meyer, A.W., Moore, T.L., Norman, E.B., Pohl, B.A., Petersen, D.C., Rusnak, B., Sundsmo, T.B., Tembrook, W.K., Walling, R.S., (2006) "A Monte Carlo Model for Interrogation of Thick Cargos for Clandestine Fissionable Materials; Tests with 14-MeV Neutrons," Lawrence Livermore National Laboratory report, UCRL-JRNL-222153.

PTG, (2010) "The following is a brief overview of what you can expect if your shipment has been selected for examination by Customs and Border Protection or the U.S. Government," Price Transfer Group, www.pricetransfer.com.

Quiter, B.J., Prussin, S.G., Pohl, B., Hall, J., Trebes, J., Stone G., Descalle, M.-A., (2008) "A Method for High-Resolution X-Ray Imaging of Intermodal Cargo

Containers for Fissionable Materials,” *Journal of Applied Physics*, vol. 103, 064910.

Rath E., (1973) Container Systems, New York: John Wiley & Sons.

Reed, W.A., (2007) “X-ray Cargo Screening Systems: The Technology Behind Image Quality,” *Port Technology International*, ed. 35, pp. 101-103.

Rennhofer, H., Crochemore, J.-M., Roesgen, E., Pedersen, B., (2010) “Detection of SNM by Delayed Gamma Rays From Induced Fission,” *Nuclear Instruments and Methods in Physics Research A*, vol. 652, pp. 140-142.

Reshef, D.N., Reshef, Y.A., Finucane, H.K., Grossman, S.R., McVean, G., Turnbaugh, P.J., Lander, E.S., Mitzenmacher, M., Sabeti, P.C., (2011) “Detecting Novel Associations in Large Data Sets,” *Science*, vol. 334, pp.1518-1524.

Reynolds, K.R., Dusina, J., (2010) “The Next Step in Radiation Monitoring for Ports,” *Port Technology International*, ed. 45, pp. 109-111.

Saaty, T.L., (1980) Analytic Hierarchy Process: Planning, Priority Setting, and Resource Allocation, New York: McGraw-Hill.

Sanquist, T.F., Doctor, P., Parasuraman, R., (2008) "Designing Effective Alarms for Radiation Detection in Homeland Security Screening," *IEEE Transactions on Systems, Man, and Cybernetics - Part C: Applications and Reviews*, vol. 38, no. 6, pp. 856-860.

Schwarz, A.L., Schwarz, R.A., Carter, L.L., (2011) "MCNP/MCNPX Visual Editor Computer Code Manual for Vised Version 24E," <http://www.mcnpvised.com>, Visual Editor Consultants, Richland, WA.

Shahabidin, M., (2011) "Request for an Exemption from the Requirement for a Criticality Monitoring System," Rapiscan Systems communication to Marilyn Diaz, Office of Nuclear Material Safety and Safeguards, U.S. Nuclear Regulatory Commission, <http://pbadupws.nrc.gov/docs/ML110890380.pdf>.

Slaughter, D.R., Accatino, M.R., Bernstein, A., Church, J.A., Descalle, M.-A., Gosnell, T.B., Hall, J.M., Loshak, A., Manatt, D.R., Mauger G.J., McDowell, M., Moore, T.M., Norman, E.B., Pohl, B.A., Pruet, J.A., Petersen, D.C., Walling, R.S., Weirup, D.L., Prussin, S.G., (2004) "Early Results Utilizing High-Energy Fission Product (Gamma) Rays to Detect Fissionable Material in Cargo," Lawrence Livermore National Laboratory report, UCRL-JRNL-207073.

Slaughter, D.R., Asztalos, S., Church, J.A., Bilotto, P., Descalle, M.-A., Hall, J., Manatt, D., Mauger J., Moore, T.L., Norman, E.B., Petersen, D., Pruet, J.A., Prussin, S.G., (2007a) "Detection of Well Shielded SNM Using Medium Energy Neutron Interrogation Followed by Observing High-Energy Delayed Fission Product γ -rays: A Final Report," Domestic Nuclear Detection Office report, CFP06-TA02-LL10.

Slaughter, D.R., Asztalos, S.J., Bilotto, P.J., Church, J.A., Descalle, M.-A., Hall, J.M., Luu, T.C., Manatt, D.R., Mauger J.G., Norman, E.B., Petersen, D.C., Pruet, J.A., Prussin, S.G., (2007b) "Optimized Performance for Neutron Interrogation to Detect SNM," Lawrence Livermore National Laboratory report, UCRL-TR-228924.

Smalling, J., (2004) "New Technology Gives Bombs Squads the Upper Hand in the Fight Against Radiological or Nuclear Terrorism," *The Detonator*, vol. 31, no. 5, pp. 48-52.

Sokkappa, P., Lange, D., Nelson, K., Wheeler, R., (2009) "Nuisance Source Population Modeling for Radiation Detection System Analysis," Lawrence Livermore National Laboratory report, LLNL-TR-418342.

Sowerby, B.D., Cutmore, N.G., Liu Y., Peng, H., Tickner, J.R., Xie, Y., Zong, C., (2009) "Recent Developments in Fast Neutron Radiography for the Interrogation of Air Cargo Containers," IAEA Conference, Vienna, Austria, 4-8 May.

Steinecker, (2010) "Technical Specification for Steel Dry Cargo Container, 20' x 8' x 9'6" High Cube," Steinecker Containerhandel, www.steinecker-container.de.

Stevenson, D., (2005) "High-Energy X-Ray Technology Expands its Global Reach to US Customs," *Port Technology International*, ed. 27, pp. 151-153.

TSA, (2012) "AM-270," TSA Systems, Ltd., Longmont, Colorado, http://tsasystems.com/products/portal_AM-270.html.

USDOT, (2009) "America's Container Ports: Freight Hubs That Connect Our Nation to Global Markets," United States Department of Transportation, Bureau of Transportation Statistics, June.

Verbeke, J.M., Hagmann, C., Wright, D., (2010) "Simulation of Neutron and Gamma Ray Emission from Fission and Photofission," Lawrence Livermore National Laboratory report, UCRL-AR-228518.

Weinberg, G.M., (1972) "A Computer Approach to General Systems Theory," in Trends in General Systems Theory, Klir, G.J., editor, New York: Wiley-Interscience.

Wilson, W.B., Cowell, S.T., England, T.R., Hayes, A.C., Moller, P., (2007) "A Manual for CINDER'90 Version 07.4 Codes and Data," Los Alamos National Laboratory report, LA-UR-07-8412 (revised 2007).

WRRC, (1990) "Load Wt. Estimation," Wire Rope & Rigging Consultants, Inc., *The Professional Rigger*, vol. 5, no. 3.

WSC, (2012) "Trade Statistics," World Shipping Council, www.worldshipping.org.